SANDIA REPORT

SAND96–2611 • UC–~~706~~ 406
Unlimited Release
Printed November 1996

Experimental Time To Burnout of A Prototypical ITER Divertor Plate During a Simulated Loss of Flow Accident

T. D. Marshall, R. D. Watson, J. M. McDonald, L. S. Wold, D. L. Youchison, L. C. Cadwallader

Prepared by
Sandia National Laboratories
Albuquerque, New Mexico 87185 and Livermore, California 94550
for the United States Department of Energy
under Contract DE-AC04-94AL85000

Issued by Sandia National Laboratories, operated for the United States Department of Energy by Sandia Corporation.

Available to DOE and DOE contractors from
Office of Scientific and Technical Information
PO Box 62
Oak Ridge, TN 37831

Prices available from (615) 576-8401, FTS 626-8401

Available to the public from
National Technical Information Service
US Department of Commerce
5285 Port Royal Rd
Springfield, VA 22161

NTIS price codes
Printed copy: A08
Microfiche copy: A01

SAND96-2611
Unlimited Release
Printed February 1997

Distribution
Category UC - ~~706~~ 406

Experimental Time To Burnout of A Prototypical ITER Divertor Plate During a Simulated Loss of Flow Accident

T. D. Marshall
Department of Nuclear Engineering
Rensselaer Polytechnic Institute
Troy, NY 12180

R. D. Watson, J. M. McDonald, L. S. Wold, D. L. Youchison
Fusion Technology Department
Sandia National Laboratories
Albuquerque, NM 87185-1129

L. C. Cadwallader
Fusion Safety Program
Idaho National Engineering Laboratory,
Idaho Falls, ID 83415

Abstract

The Loss of Flow Accident (LOFA) is a serious safety concern for the International Thermonuclear Experimental Reactor (ITER) because it has been suggested that greater than 100 s are necessary to safely shut down the plasma when ITER is operating at full power. In this experiment, the thermal response of a prototypical ITER divertor tube during a simulated LOFA was studied. The divertor tube is fabricated from oxygen-free high-conductivity copper to have a square geometry with a circular coolant channel. The inner diameter of the coolant channel is 0.77 cm, the heated length is 4.0 cm, and the heated width is 1.6 cm. The mockup does not feature any flow enhancement techniques, i.e., swirl tape, porous coating, or internal fins. One-sided surface heating of the mockup is accomplished through the use of the 30-kW Sandia Electron Beam Test System. After reaching steady-state temperatures in the mockup, as determined by two K-type thermocouples embedded 0.5 mm beneath the heated surface, the circulation pump for the high temperature, high pressure coolant loop is manually tripped off and the coolant flow allowed to naturally coast down. Electron beam heating continues after the pump trip until the divertor plate's heated surface exhibits the high-temperature transient normally indicative of rapidly approaching "burnout." Experimental data show that time-to-burnout increases proportionally with increases in the initial (before the pump trip) inlet velocity and decreases proportionally with increases in the incident heat flux.

Acknowledgments

The authors would like to thank K. Troncosa and F. Bauer for their assistance in producing and verifying the experimental data. The authors would especially like to thank M. Ulrickson of Sandia National Laboratories, M. Cohen of the Department Of Energy, D. Petti and G. Longhurst of the Idaho National Engineering Laboratory, and D. Steiner of Rensselaer Polytechnic Institute for their support of this project. Finally, the authors issue a most heartfelt thank you to P. Stevens and D. Youso for their invaluable contributions toward the completion of this report.

Preface

This report is an excerpt from doctoral research being performed by Theron Marshall at Sandia National Laboratories. Two additional LOFA experiments are expected to complete the research. These experiments will focus on the thermalhydraulic operating parameters relevant to ITER and next-generation fusion reactors. Robert Watson, as research advisor and ITER Task 221 Leader, is ensuring that the experimental data are applicable to the research and design needs of ITER. In addition, he brings to the project 15 years of experience with finite element analyses. Jimmie McDonald and Dennis Youchison (ITER Task 232 Leader) have an intimate knowledge of Sandia's 30 kW and 1200 kW electron beam test facilities. Their input and efforts are ensuring that the desired experimental data are attainable. LaWanda Wold, as system administrator of the electron beams' software and data acquisition systems, is providing the data sampling rates, sensor controls, and software configuration required to enable the simulation of a LOFA. Lee Cadwallader, as principal investigator of the ITER Failure Rate Database Task (SAE-3), contributes 12 years of experience in safety and risk assessment. He is also ensuring that the project is consistent with the safety-related research and design needs of ITER.

Executive Summary

As the fusion discipline continues its steadfast march towards highly efficient and environmentally benign commercial fusion power, with the International Thermonuclear Experimental Reactor (ITER) as one of the intermediate steps, designers and analysts must address practical operating issues in addition to the physics and material issues normally associated with fusion machines. Nuclear fission engineers recognized that certain off-normal events could seriously threaten the integrity of their reactors and these events were defined as reactor design basis accidents (DBAs). That is, during the design of the reactor, precautions such as installing passively and actively controlled safety systems, were incorporated to lessen the cumulative damage potential of the DBAs. While a licensing and/or regulatory agency has not yet been defined for commercial fusion, in time, fusion designers will have to follow the path of fission designers and prove that fusion machines can safely recover from all postulated accident conditions.

Marshall, Cadwallader, and others have identified three off-normal events that can be considered as DBAs for fusion machines: Loss of Vacuum Accident (LOVA), Loss of Coolant Accident (LOCA), and Loss of Flow Accident (LOFA). Considering the LOFA to be a subset of the LOCA, the referenced authors gave the following LOFA definition:

> "The LOFA is similar to an external LOCA, the difference being that coolant is not lost from the system. A LOFA normally occurs from either a pump trip or an obstruction in the coolant tubing. The major concern with a LOFA is the reactor's inability to remove heat from part or the whole of the vacuum vessel. As the temperature rises inside the vessel, the PFCs may lose their structural integrity. The elevated temperatures may also release activation products and tritium normally contained within the PFCs."

During normal operations, ITER plasma facing components (PFCs) are expected to absorb an average heat load of 2 MW/m^2 while the divertor plates will be designed to absorb average heat loads of 5 MW/m^2. To meet such design specifications, the divertor plates will be actively cooled by subcooled water (50 - 150 °C inlet) at moderate pressure (1 - 4 MPa) and velocity (5 - 10 m/s). In an off-normal event, the divertor plates may experience a maximum heat load of 20 MW/m^2 for a time period of 10 s. During a LOFA, the divertor plates may have to remove normal or off-normal heat loads while simultaneously experiencing decreases in the water coolant pressure and/or velocity. Until the research discussed in this report, there has not been a published comprehensive investigation on the LOFA issue, complete with experimental data for verification of derived calculations and/or hypotheses.

The objective of this experiment is to generate time-to-burnout data for a simulated LOFA. Time-to-burnout is the amount of time the divertor plate can withstand continual one-sided surface heating while simultaneously experiencing a loss of coolant flow. These data are intended to give fusion designers an approximate idea of the response time ITER plant engineers and operators will have to successfully detect the onset of a LOFA and safely shut down the plasma. This information is critical to ensure that the typical ITER divertor plate can safely handle the thermal challenges of a LOFA.

One-sided heating of the prototypical ITER divertor plate is provided by the Sandia 30-kW Electron Beam Test System (EBTS). The EBTS is a multipurpose device for studying the surface modification, thermal response, and failure modes of high heat flux materials and components. Targets of all shapes and sizes, up to 30 cm by 60 cm can be tested. A large variety of ports as well as vacuum feed-throughs in the 70 cm diameter by 100 cm length stainless steel vacuum chamber are available for diagnostics and utility connections. Discharge of the electron beam gun is controlled by a VAX computer system. The electron source is typically a tungsten or tantalum filament with maximum operating parameters of 30-kV and 30-kW. Magnetic lenses and deflection coils are used to focus, position, and raster the electron beam to cover a variety of sample surfaces with either a finely tuned or defocused beam. For most experiments, the beam is operated with a full-width, half-maximum beam diameter of 5 mm. Various scenarios can be simulated with the electron gun since it provides a variable directed heat source. In a chamber pressure of 130 Pa, average beam rise time is 1 ms and pulse duration can be adjusted from 2 ms to continuous operation over a heated area from 1 to 100 cm^2. With 30-kV acceleration, the beam electrons have an approximate penetration depth of 1×10^{-3} mm in copper, which produces what is essentially a surface heat flux.

The experimental divertor plate mockup, as shown in Figure 1, is a one-piece assembly of oxygen-free high-conductivity copper bar stock and tubing. The square bar stock has a length of 133.4 mm and a 15.7 mm cross-section. A circular coolant channel with a 7.5 mm diameter is center drilled, axially, through the length of the bar stock. The coolant channel entrance and exit are counterbored 3.175 mm to allow a slip fit of the 98.4 mm long copper tubes (9.5 mm o.d., 7.5 mm i.d.), which are silver brazed into place. Each side of the mockup includes three 13 mm long and 1 mm square cross-sectional grooves, positioned 1 cm from either end and at the center of the mockup. These grooves house the wires for the 0.5 mm diameter K-type thermocouples, preventing them from damage by the electron beam. The thermocouple sensor tips are positioned 0.5 mm from the top surface (heated surface) of the mockup. Since the thermocouples sensing tips are so close to the heated surface, the recorded temperatures are assumed to be indicative of the surface temperature.

The primary objective of the experiment is to determine the time-to-burnout of the prototypical fusion reactor divertor plate mockup after a simulated coolant pump failure. This objective is achieved by removing the power to the pump after steady-state heating by the electron beam is reached. The electron beam continues supplying one-sided surface heating to the mockup until a high-temperature trip signal from the embedded thermocouples in the heated area of the mockup shut down the electron beam. The difference between the time at which the electron beam is tripped and the time when the pump is tripped is defined as the time-to-burnout.

Eight experimental cases are run to generate time-to-burnout data. The eight cases are devised to examine the characteristics of the time-to-burnout for two scenarios:

1. constant inlet pressure, temperature, and incident heat flux, with the initial inlet velocity as the experimental variable,
2. constant inlet pressure, temperature, and initial inlet velocity, with the incident heat flux as the experimental variable.

The time-to-burnout data, plotted in Figures 2 and 3, behaves as expected for both scenarios: increasing parabolically in scenario 1 and decreasing parabolically in scenario 2. The experimental

time-to-burnout data listed in Table 1 show a strong correlation of the time-to-burnout response to the initial inlet water velocity and the incident heat flux.

At normal ITER divertor operating conditions (1 MPa, 10 m/s, 68 °C, 6 MW/m^2 - the 1994 EDA specifications), EBTS shot 144201 has an approximate time-to-burnout of 32 s. This result suggests that if the plant engineers and operators require more than 32 s for response time, then additional active circulation devices, such as standby emergency pumps, are necessary to ensure that the typical ITER divertor plate will not reach burnout temperatures and release water into the vacuum vessel. Further tests are necessary to verify this 32 s time for the given inlet conditions.

The LOFA data indicate that the strongest influence upon the time-to-burnout of a divertor plate design is the steady-state inlet water velocity prior to the LOFA. As one might imagine, if some sort of flow, even in a reduced state, continues through the divertor plate during the LOFA, the time-to-burnout could be increased. This means that flow-continuation devices such as inertial flywheels on the pump shafts or fast-acting backup pumps for the primary coolant pump can be employed to safely extend the time-to-burnout for a given divertor plate design.

Finite element modeling of the simulated LOFA is attempted using the ABAQUS code. The heat transfer coefficient during the LOFA is calculated using a user-written "film" subroutine. Currently, this subroutine contains only two correlations: Sieder-Tate for single-phase heat transfer and Thom for nucleate boiling heat transfer. Two different techniques are employed to model the LOFA:

1. setting the heat transfer coefficient equal to zero (adiabatic case) at the time of the pump trip,
2. using the experimentally-measured velocity coast down in the film subroutine.

The predicted surface temperatures for these two techniques are shown in Figure 4. Neither of the techniques predicted surface temperatures that are consistent with the experimental temperatures. Figures 5 and 6 show the ratio of the experimental time-to-burnout to the predicted time-to-burnout. From the two figures, the predicted time-to-burnout underpredicted the experimental time-to-burnout by a factor of four to fourteen when the adiabatic model was used.

The principal conclusion of the report is that experimentally measured burnout times can exceed the predicted adiabatic value by as much as an order of magnitude. One could thus conclude that the adiabatic model is too conservative. Further LOFA experiments and improved heat transfer models are necessary to increase understanding of the mockup thermal response during a LOFA.

Table 1. Times of Pump Trip, High Temperature Trip, and Time-to-Burnout Data

	Water Inlet Conditions			Experimental					Predicted	
EBTS Shot	Pressure (MPa)	Velocity (m/s)	Temp. (°C)	$q_{incident}$ (MW/m^2)	T_{trip} (°C)	$t_{pump\ trip}$ (s)	$t_{ebeam\ trip}$ (s)	TBO[b] (s)	TBO[c] (s)	CHF[a] (MW/m^2)
144198	1	1	68	6	700.0	122.8	134.5	11.8	3.0	4.0
144201	1	10	68	6	750.0	135.0	167.0	32.0	3.5	12.0
144205	1	5	68	6	700.0	122.0	136.0	14.0	3.1	8.7
144318	1	10	11	16	750.0	130.5	139.3	8.8	0.6	21.5
144319	1	10	11	15	750.0	132.0	142.0	10.0	1.0	21.5
144320	1	10	11	10	700.0	121.0	134.3	13.3	1.5	21.5
144321	1	10	11	7	750.0	123.0	140.8	17.8	2.5	21.5
144322	1	10	11	3	750.0	135.0	170.0	35.0	8.0	21.5

[a] incident critical heat flux predicted by Tong-75 correlation.
[b] experimental time-to-burnout.
[c] adiabatic case in finite element analysis.

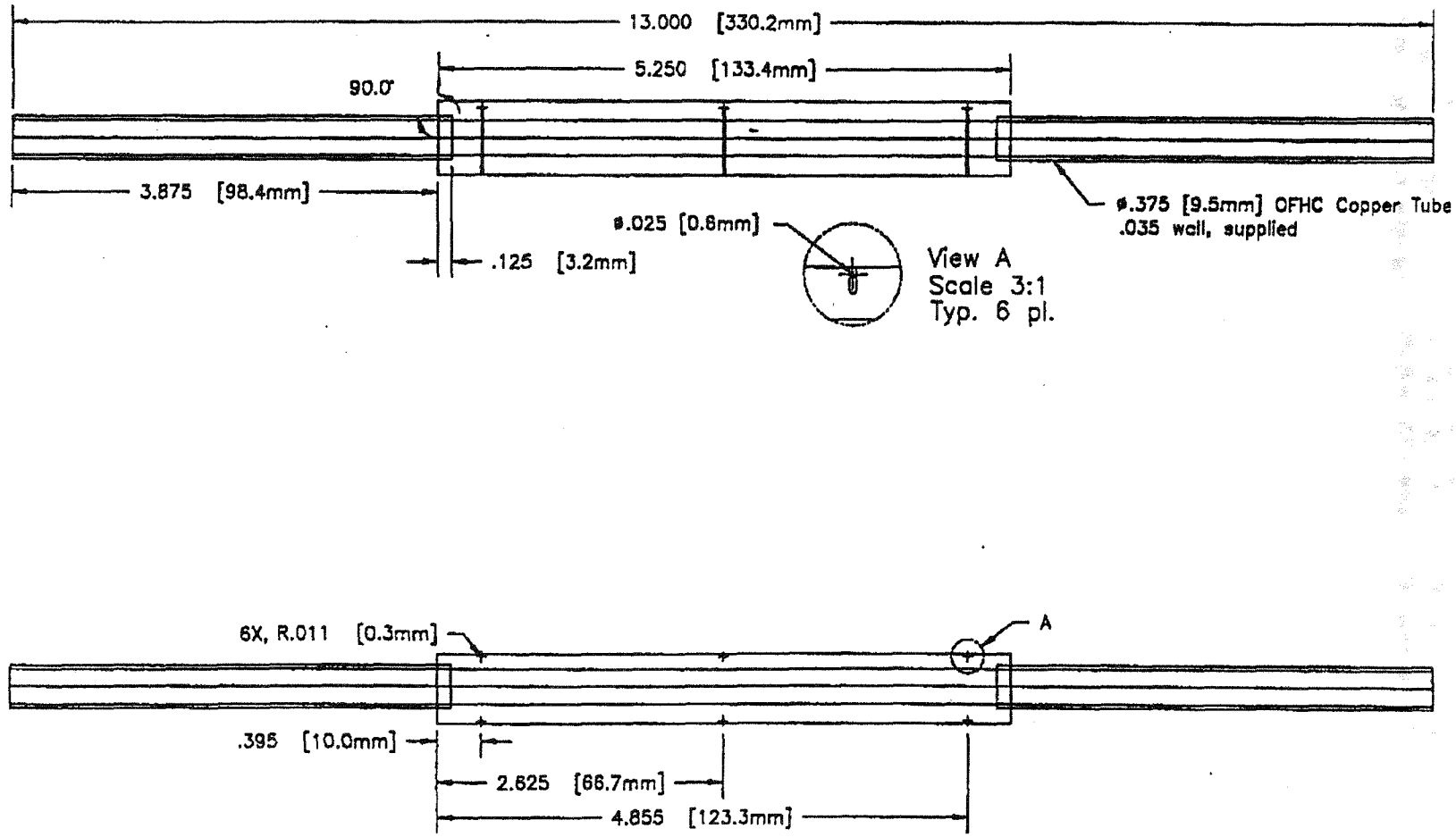

Figure 1a. Axial Dimensions of Mockup.

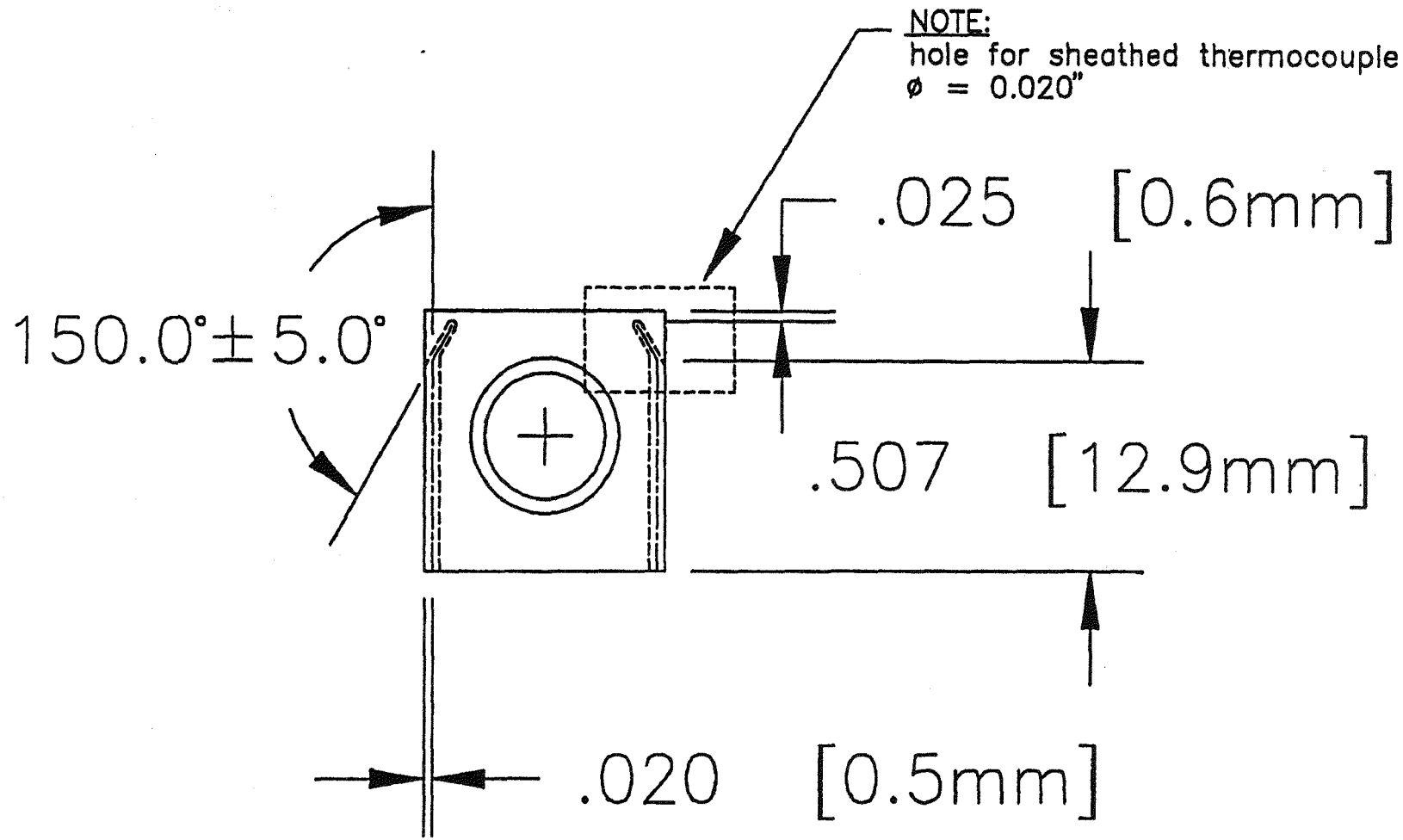

Figure 1b. Thermocouple Positioning in Mockup.

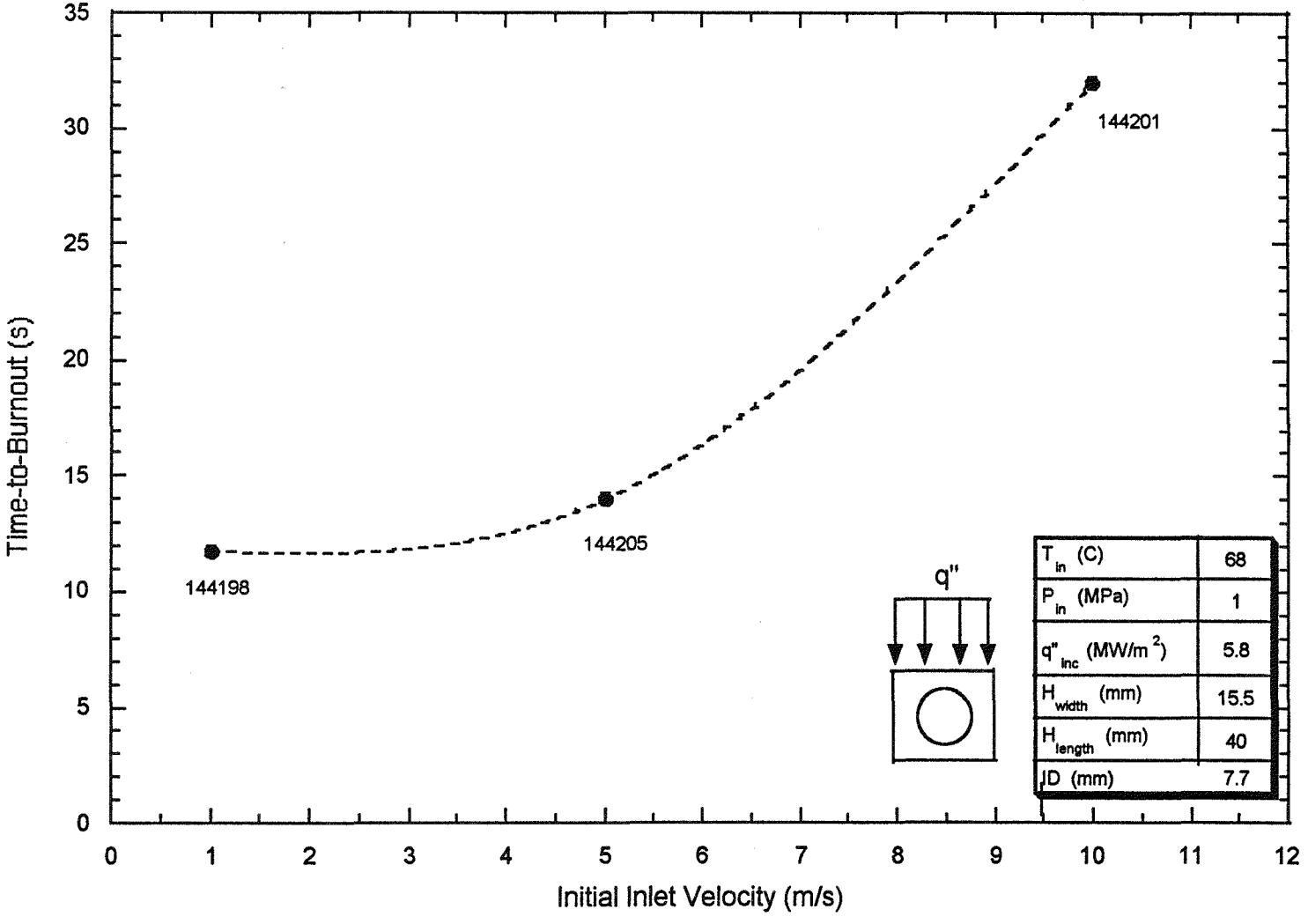

Figure 2: Influence of Initial Inlet Velocity on the Experimental Time-to-Burnout Data.

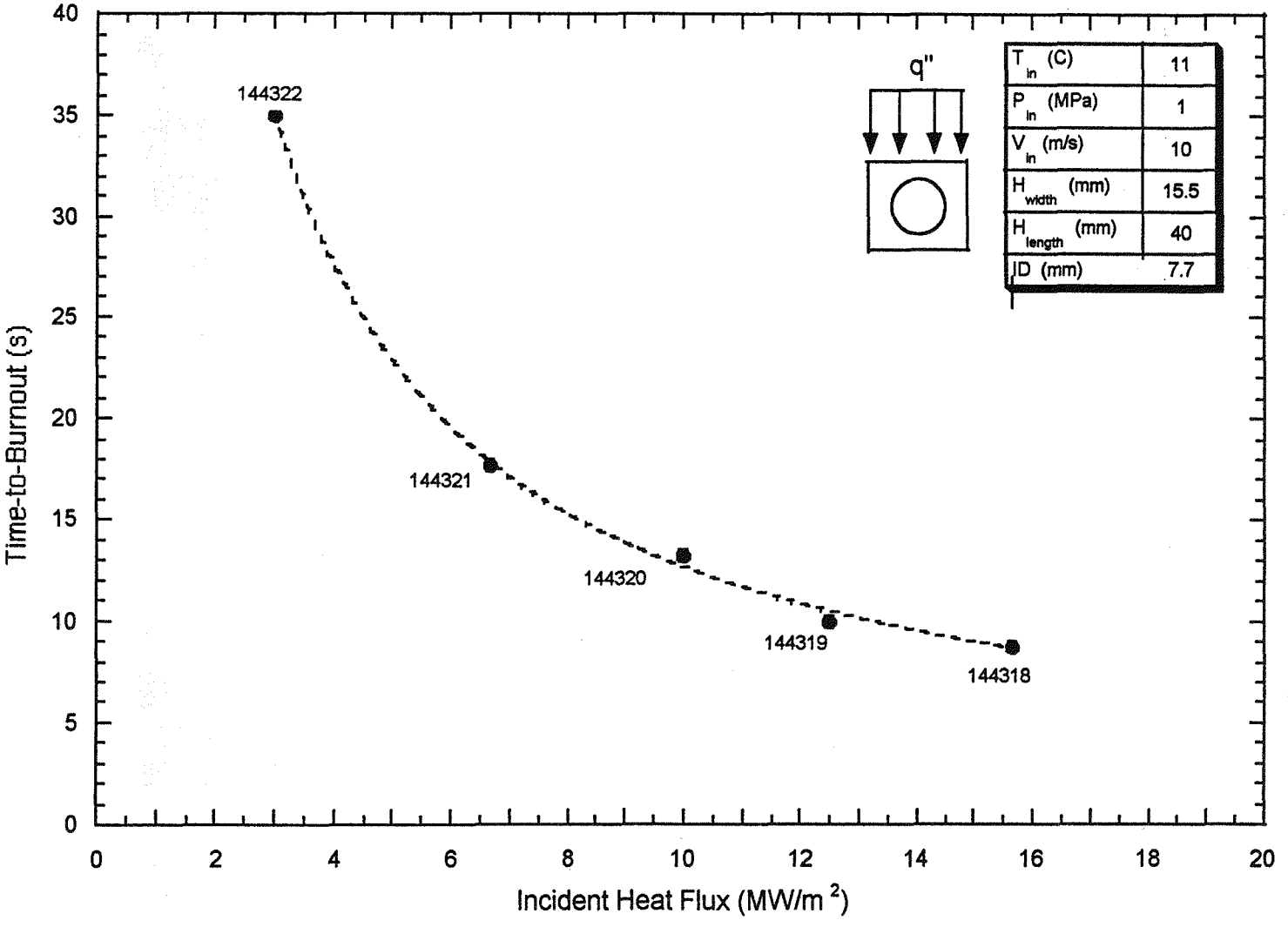

Figure 3: Influence of Incident Heat flux on the Experiment Time-to-Burnout Data.

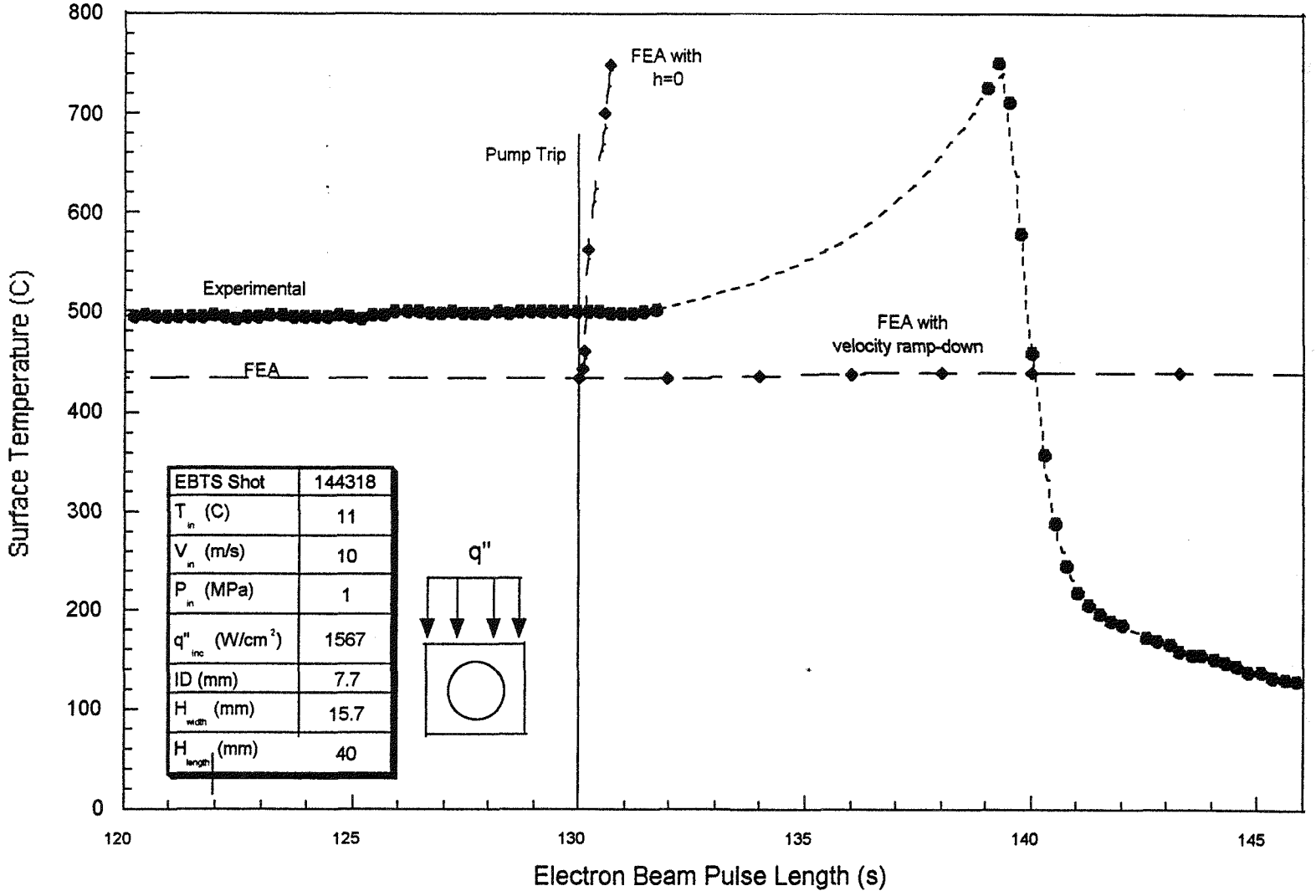

Figure 4: Prediction of Surface Temperature by Finite Element Analysis using the Adiabatic and Velocity Coast Down Techniques.

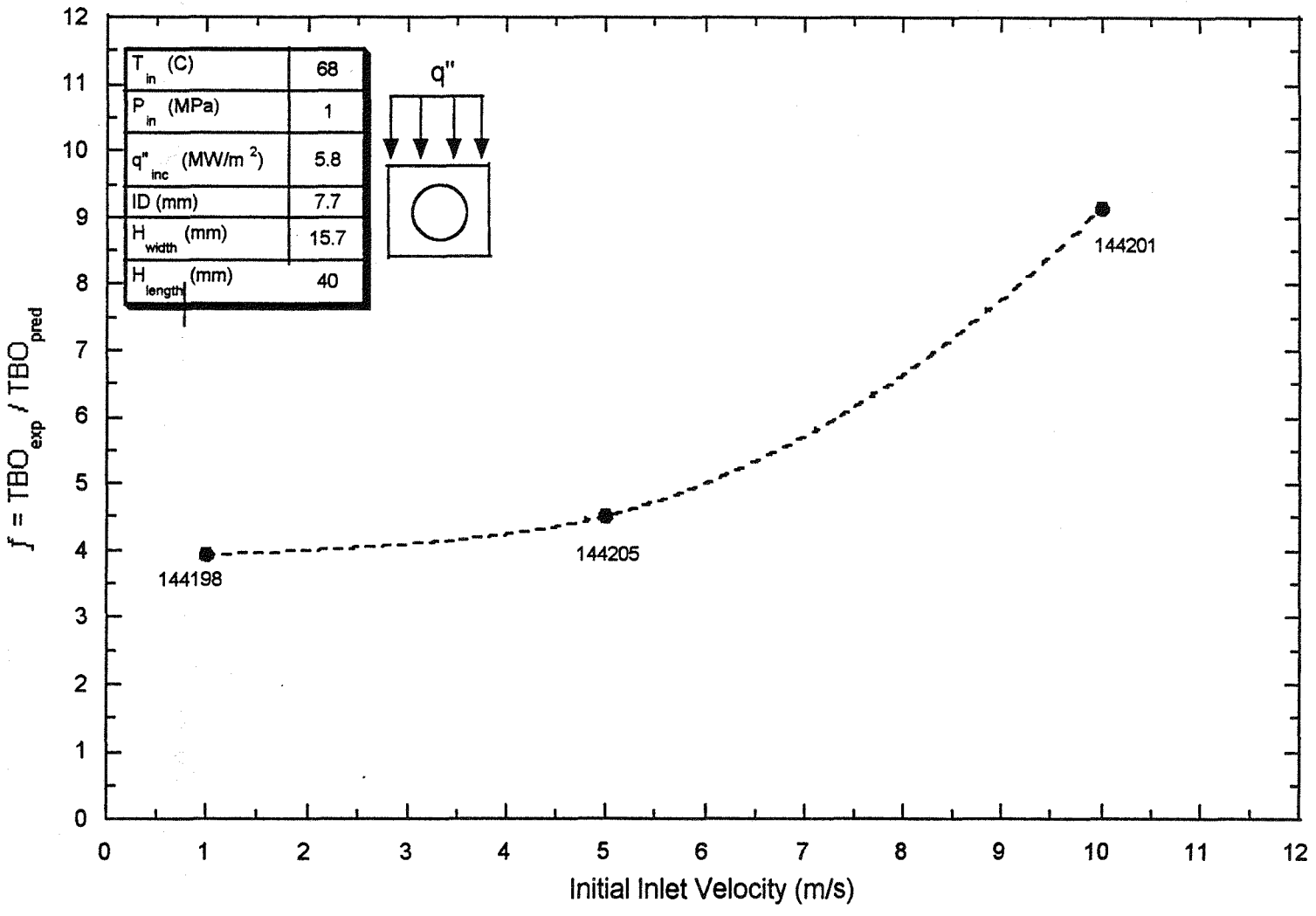

Figure 5: Ratio of Experimental to Finite Element Analysis Time-to-Burnout as a Function of Initial Inlet Velocity.

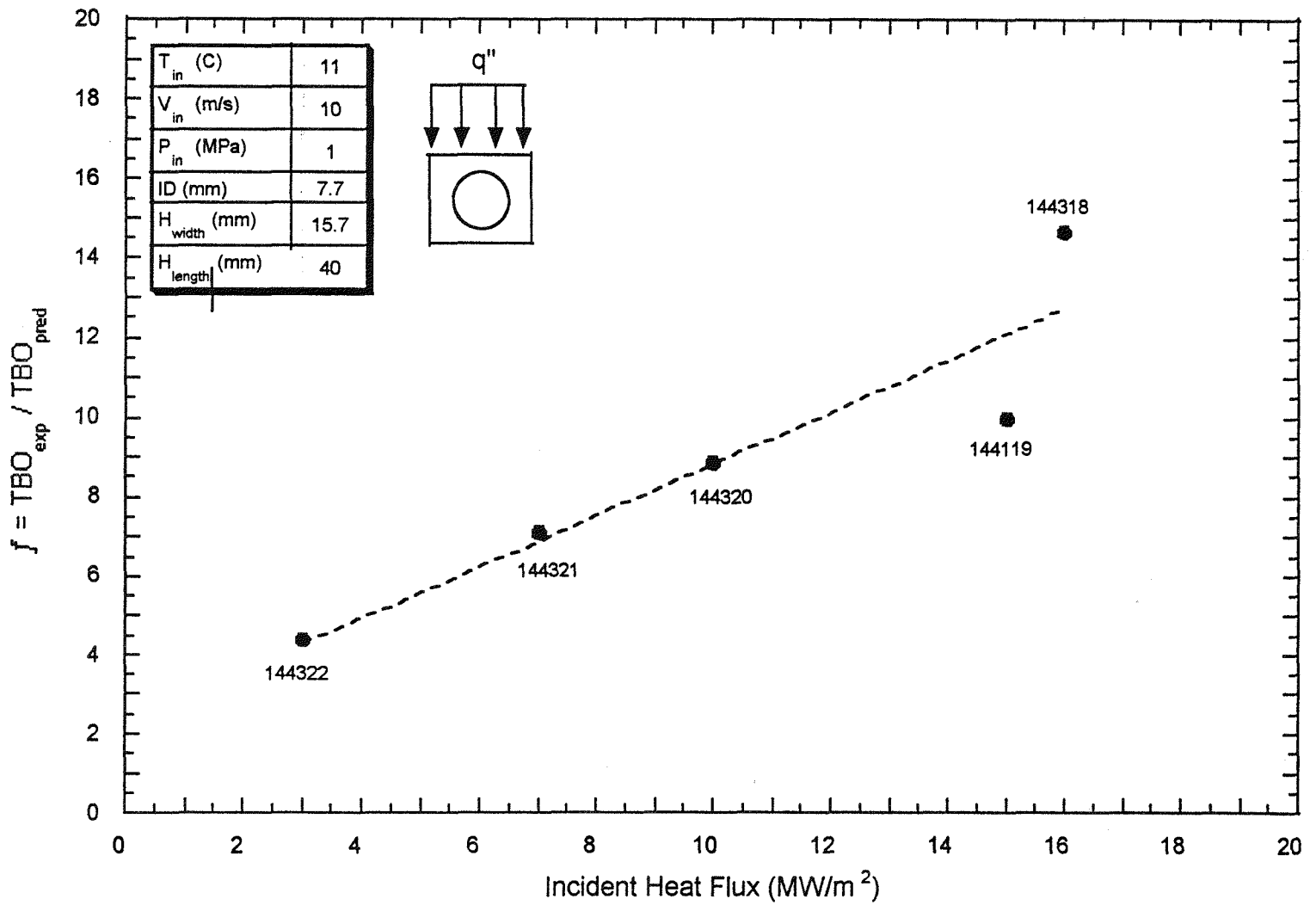

Figure 6: Ratio of Experimental to Finite Element Analysis Time-to-Burnout as a Function of Incident Heat Flux.

Units

atm-cm^3/s	atmosphere per cubic centimeter per second
°C	degrees Celsius
cm	centimeter
g.p.m.	gallon per minute
hp	horsepower
hr	hour
K	degree Kelvin
kV	kilovolt
kW	kilowatt
m/s	meter per second
mbar	millibar
ml	milliliter
mm	millimeter
MPa	megapascal
ms	millisecond
rpm	revolutions per minute
s	seconds
W/cm^2	Watts per square centimeter

Table of Contents

Acknowledgments ii

Preface ii

Executive Summary iii

1.0 Introduction 1
1.1 Thermalhydraulic Scaling 2
1.2 Off-normal Events 3

2.0 Electron Beam Test System 6
2.1 Introduction 6
2.2 Basic Operating Capabilities 6
2.3 Standard Diagnostics 6
2.4 Water Flow Loop 7
2.4.1 General Description 7
2.4.2 Temperature Control 7
2.4.3 Flow Control 8
2.4.4 Pressure Control 8
2.4.5 Water Chemistry Control 8
2.4.6 Surge Tank 8
2.4.7 Circulation Pump 8
2.4.8 Low-Pressure Clean-up Pump 9
2.4.9 Pressure Control Pump 9
2.4.10 Chemical Injection Pumps 9
2.4.11 Heat Exchanger 9
2.4.12 Surge Tank 10

3.0 Prototypical Divertor Plate Mockup 14
3.1 Introduction 14
3.2 General Description 14
3.3 Pre-Test Procedures 15
3.4 Leak Check 15
3.5 Pressure Test 15

4.0 Experimental Procedure 22
4.1 Introduction 22
4.2 Instrumentation 22
4.3 Calibration Procedure 22
4.3.1 Bulk Temperature 22
4.3.2 Surface Temperature 22
4.3.3 Water Calorimetry 23
4.3.4 Beam Alignment 23
4.4 Test Prerequisites 24

4.5 Test Procedures 24

5.0 Experimental Results 26
5.1 Introduction 26
5.2 Time-to-Burnout Plots 26
5.3 Experimental Data 26

6.0 Modeling Results 36
6.1 Introduction 36
6.2 ABAQUS Calculations 36
6.2.1 Steady State Temperatures 36
6.2.3 Peaking Factors 37
6.2.4 Finite Element Analysis Time-to-Burnout 38
6.3 Critical Heat Fluxes 38
6.4 Burnout Safety Margin 39

7.0 Discussion 59
7.1 Introduction 59
7.2 Time-to-Burnout Data 59
7.3 LOFA Modeling 60
7.3.1 Finite Element Modeling: Adiabatic Case 60
7.3.2 Finite Element Modeling: Velocity Coastdown 62

7.4 Thermal Responses 63
7.4 Burnout Safety Margin 63
7.5 Error Analysis 64
7.5.1 Water Calorimetry 64
7.5.2 Heated Area 65
7.5.3 Heated Area 65
7.6 Thermalhydraulic Scaling 66

8.0 Conclusions 90
8.1 Time-to-Burnout Data 90
8.2 Heat Transfer Coefficient 90

References 92

Appendix A: Experimental Data 95

List of Figures

Figure 1a. Axial Dimensions of Mockup. vii
Figure 1b. Thermocouple Positioning in Mockup. viii
Figure 2: Influence of Initial Inlet Velocity on the Experimental Time-to-Burnout Data. ix
Figure 3: Influence of Incident Heat flux on the Experiment Time-to-Burnout Data. x
Figure 4: Prediction of Surface Temperature by Finite Element Analysis using the Adiabatic and Velocity Coast Down Techniques. xi
Figure 5: Ratio of Experimental to Finite Element Analysis Time-to-Burnout as a Function of Initial Inlet Velocity. xii
Figure 6: Ratio of Experimental to Finite Element Analysis Time-to-Burnout as a Function of Incident Heat Flux. xiii
Figure 2-1. Sandia 30-kW Electron Beam Test System 12
Figure 2-2: Schematic of Sandia EBTS Water Loop 13
Figure 3-1. Axial Dimensions of Mockup. 17
Figure 3-2. Face Dimensions of Mockup. 18
Figure 3-3. Thermocouple Positioning in Mockup. 19
Figure 5-1: Surface (thermocouple) Temperature and Inlet Velocity Responses Used to Calculate TBO for EBTS Shot 144198. 28
Figure 5-2: Surface (thermocouple) Temperature and Inlet Velocity Responses Used to Calculate TBO for EBTS Shot 144201. 29
Figure 5-3: Surface (thermocouple) Temperature and Inlet Velocity Responses Used to Calculate TBO for EBTS Shot 144205. 30
Figure 5-4: Surface (thermocouple) Temperature and Inlet Velocity Responses Used to Calculate TBO for EBTS Shot 144381. 31
Figure 5-5: Surface (thermocouple) Temperature and Inlet Velocity Responses Used to Calculate TBO for EBTS Shot 144319. 32
Figure 5-6: Surface (thermocouple) Temperature and Inlet Velocity Responses Used to Calculate TBO for EBTS Shot 144320. 33
Figure 5-7: Surface (thermocouple) Temperature and Inlet Velocity Responses Used to Calculate TBO for EBTS Shot 144321. 34
Figure 5-8: Surface (thermocouple) Temperature and Inlet Velocity Responses Used to Calculate TBO for EBTS Shot 144322. 35
Figure 6-1. PATRAN Finite Element Mesh of Mockup - 200 Elements and 760 Nodes. 42
Figure 6-2: Predicted Angular Temperature and Heat Flux Distributions at the Channel Wall for EBTS Shot 144198. 43
Figure 6-3: Predicted Angular Temperature and Heat Flux Distributions at the Channel Wall for EBTS Shot 144201. 44
Figure 6-4: Predicted Angular Temperature and Heat Flux Distributions at the Channel Wall for EBTS Shot 144205. 45
Figure 6-5: Predicted Angular Temperature and Heat Flux Distributions at the Channel Wall for EBTS Shot 144318. 46
Figure 6-6: Predicted Angular Temperature and Heat Flux Distributions at the Channel Wall for EBTS Shot 144319. 47
Figure 6-7: Predicted Angular Temperature and Heat Flux Distributions at the Channel Wall for

EBTS Shot 144320. 48
Figure 6-8: Predicted Angular Temperature and Heat Flux Distributions at the Channel Wall for EBTS Shot 144321. 49
Figure 6-9: Predicted Angular Temperature and Heat Flux Distributions at the Channel Wall for EBTS Shot 144322. 50
Figure 6-10: Comparison of the Burnout Safety Margin Decline and the Surface Temperature Rise During the Experimental Pump Trip for EBTS Shot 144198. 51
Figure 6-11: Comparison of the Burnout Safety Margin Decline and the Surface Temperature Rise During the Experimental Pump Trip for EBTS Shot 144201. 52
Figure 6-12: Comparison of the Burnout Safety Margin Decline and the Surface Temperature Rise During the Experimental Pump Trip for EBTS Shot 144205. 53
Figure 6-13: Comparison of the Burnout Safety Margin Decline and the Surface Temperature Rise During the Experimental Pump Trip for EBTS Shot 144318. 54
Figure 6-14: Comparison of the Burnout Safety Margin Decline and the Surface Temperature Rise During the Experimental Pump Trip for EBTS Shot 144319. 55
Figure 6-15: Comparison of the Burnout Safety Margin Decline and the Surface Temperature Rise During the Experimental Pump Trip for EBTS Shot 144320. 56
Figure 6-16: Comparison of the Burnout Safety Margin Decline and the Surface Temperature Rise During the Experimental Pump Trip for EBTS Shot 144321. 57
Figure 6-17: Comparison of the Burnout Safety Margin Decline and the Surface Temperature Rise During the Experimental Pump Trip for EBTS Shot 144322. 58
Figure 7-1: Influence of Initial Inlet Velocity on the Experimental Time-to-Burnout Data 70
Figure 7-2: Influence of Incident Heat Flux on the Experimental Time-to-Burnout Data. 71
Figure 7-3: Finite Element Analysis Predicted vs. Experimental Time-to-Burnout as a Function of Initial Inlet Velocity. 72
Figure 7-4: Finite Element Analysis Predicted vs. Experimental Time-to-Burnout as a Function of Incident Heat Flux. 73
Figure 7-5: Ratio of the Experimental Time-to-Burnout to the Finite Element Analysis Predicted Time-to-Burnout as a Function of Initial Inlet Velocity. 74
Figure 7-6: Ratio of the Experimental Time-to-Burnout to the Finite Element Analysis Predicted Time-to-Burnout as a Function of Incident Heat Flux. 75
Figure 7-7: Finite Element Analysis (adiabatic) Predicted vs. Experimental Surface (thermocouple) Temperatures after Pump Trip for EBTS Shot 144198. 76
Figure 7-8: Finite Element Analysis (adiabatic) Predicted vs. Experimental Surface (thermocouple) Temperatures after Pump Trip for EBTS Shot 144201. 77
Figure 7-9: Finite Element Analysis (adiabatic) Predicted vs. Experimental Surface (thermocouple) Temperatures after Pump Trip for EBTS Shot 144205. 78
Figure 7-10: Finite Element Analysis (adiabatic) Predicted vs. Experimental Surface (thermocouple) Temperatures after Pump Trip for EBTS Shot 144318. 79
Figure 7-11: Finite Element Analysis (adiabatic) Predicted vs. Experimental Surface (thermocouple) Temperatures after Pump Trip for EBTS Shot 144319. 80
Figure 7-12: Finite Element Analysis (adiabatic) Predicted vs. Experimental Surface (thermocouple) Temperatures after Pump Trip for EBTS Shot 144320. 81
Figure 7-13: Finite Element Analysis (adiabatic) Predicted vs. Experimental Surface (thermocouple) Temperatures after Pump Trip for EBTS Shot 144321. 82
Figure 7-14: Finite Element Analysis (adiabatic) Predicted vs. Experimental Surface (thermocouple)

Temperatures after Pump Trip for EBTS Shot 144322. 83
Figure 7-15: Influence of Initial Inlet Velocity on the Surface (thermocouple) Temperature Rate of Increase Following the Coolant Pump Trip. 84
Figure 7-16: Influence of Incident Heat Flux on the Surface (thermocouple) Temperature Rate of Increase Following the Coolant Pump Trip. 85
Figure 7-17: Surface (thermocouple) Temperature Response During Finite Element Analysis Simulated LOFA with Experimental Velocity Coast down. 86
Figure 7-18: Results of Finite Element Analysis Modeling of Simulated LOFA using the Adiabatic and Experimental Velocity Coast Down Techniques. 87
Figure 7-19: Comparison of Predicted and Experimental Thermocouple Temperature as a Function of Initial Inlet Velocity. 88
Figure 7-20: Comparison of Predicted and Experimental Thermocouple Temperature as a Function of Incident Heat Flux. 89
Figure 7-18: Results of Finite Element Analysis Modeling of Simulated LOFA using the Adiabatic and Experimental Velocity Coast Down Techniques. 95
Figure 7-18: Results of Finite Element Analysis Modeling of Simulated LOFA using the Adiabatic and Experimental Velocity Coast Down Techniques. 95

List of Tables

Table 1. Times of Pump Trip, High Temperature Trip, and Time-to-Burnout Data vi
Table 2-1. Operating Ranges of EBTS Diagnostics 10
Table 2-2. Accuracy of EBTS Diagnostics 11
Table 2-3. EBTS Heat Exchanger Operating Parameters 11
Table 3-1. Mockup Measurements (Pre-test) 16
Table 4-1. LOFA Test Matrix 25
Table 5-1. Coolant Pump and Electron-Beam Trip Times 27
Table 6-1. ABAQUS Predicted Thermocouple Temperatures 40
Table 6-2. Finite Element Peaking Factor Calculated by ABAQUS 40
Table 6-3. ABAQUS Predicted Time-to-Burnout with $h_{film} = 0$ at Pump Trip 41
Table 6-4. Predicted CHF Limits 41
Table 7-1. Definition of Inlet Conditions for Experimental Cases 68
Table 7-2. Times of Pump Trip, High Temperature Trip, and Time-to-Burnout Data 68
Table 7-3. ABAQUS Predicted TBO with $h_{film} = 0$ at Pump Trip vs. Experimental TBO 69
Table 7-4. Comparison of Predicted and Actual Thermocouple Temperatures 69

Acronyms and Abbreviations

ANSI	American National Standards Institute
ASME	American Society of Mechanical Engineers
BSM	burnout safety margin
CFC	carbon fiber composite
CHF	critical heat flux
DBA	design basis accident
EBTS	electron beam test facility
FCV	flow control valve
FEPF	finite element peaking factor
IBHF	incident burnout heat flux
I.D.	inner diameter
IR	infrared
ITER	International Thermonuclear Experimental Reactor
JET	Joint European Torus
LOCA	loss of coolant accident
LOFA	loss of flow accident
LOVA	loss of vacuum accident
LS	nitrogen level switch
O.D.	outer diameter
OFHC	oxygen-free high-conductivity copper
PCV	pressure control valve
PFC	plasma facing component
PIC	pressure instrument/controller
PT	pressure transmitter
SOFE	symposium on fusion engineering
SOFT	symposium on fusion technology
SV	nitrogen vent valve
TBO	time to burnout, seconds
TC2	thermocouple 2
TC5	thermocouple 5
TCV	temperature control valve
TE	temperature measurement
TEMA	Tubular Exchanger Manufacturer's Association
TFTR	Tokamak Fusion Test Reactor
TIC	temperature instrument/controller
TT	temperature transmitter
TV	television
V-I	voltage to current measurement
WCHF	wall critical heat flux

Variables

h	heat transfer coefficient (MW/m^2-K)
p	pressure (MPa)
q"	heat flux (MW/m^2)
t	time (s)
T	temperature (°C)
v	velocity (m/s)

Subscripts

q''_{inc}	heat flux at the heated surface
q''_{wall}	heat flux at the channel wall
t_{ebeam}	time that the electron beam was tripped off
t_{pump}	time that the flow loop coolant pump was tripped off
T_{trip}	high-temperature trip for the electron beam

Experimental Time to Burnout of a Prototypical ITER Divertor Plate During a Simulated Loss of Flow Accident

1.0 Introduction

This report describes an experimental investigation of the thermal response of a prototypical fusion reactor divertor plate during a simulated Loss of Flow Accident (LOFA) with steady-state heating. The experimental data presented are the first published results of their kind and should provide valuable information to fusion system designers, finite element modelers, and safety analysts. In addition, the simulated plasma heating (one-sided heating) of the divertor plate during the experiment ensures that the data are applicable to both inertial confinement and magnetic confinement approaches to fusion. Accordingly, the report should be of interest to a wide group of fusion personnel.

Fusion technology has made significant progress during the past 15 years with record performances by the Joint European Torus (JET) [1], JT-60U, T-15, DIII-D [2], Tore Supra [3], and the Tokamak Fusion Test Reactor (TFTR) [4]. Experiences with these fusion machines have substantially increased our knowledge and competence in the areas of:

1. material selection for high heat flux performance,
2. plasma control systems,
3. tritium handling systems.

This experience is now being applied to new challenges as the United States, the European Union, Japan, and the Russian Federation have formed a collaboration to design, construct, and operate the next-generation fusion machine, the International Thermonuclear Experimental Reactor (ITER).

As the fusion discipline continues its steadfast march towards highly efficient and environmentally benign commercial fusion power with ITER being an interim step, designers and analysts must answer practical operating issues in addition to the physics and materials issues normally associated with fusion machines. The nuclear fission industry had to develop sophisticated techniques for the detection and prevention of off-normal events during reactor operation [5][6] before it could become a licensed industry, and so must fusion. Fission engineers recognized that certain off-normal events could seriously threaten the integrity of their reactors and these events were defined as reactor design basis accidents (DBAs) [7]. That is, fission reactors have been designed to incorporate passively and actively actuated safety systems to lessen the cumulative damage potential of the DBAs. While a licensing and/or regulatory agency has not yet been defined for commercial fusion, in time fusion designers will have to follow the path of fission designers and prove that fusion machines can safely recover from known and postulated accident conditions.

1.1 Thermalhydraulic Scaling

One way that fusion designers can research DBAs for next-generation reactors is through the use of scale models to evaluate the reactor performance during accident conditions. The concept of using a scale model to predict the performance of a full-sized unit has a large history in the automotive, aviation, marine, chemical engineering, and nuclear fission industries. This approach is particularly useful when tests of full-scale models are impractical due to cost, safety, or technological constraints. However, while scale models are useful, inherent imperfections, or distortions, are unavoidable.

The process of selecting the proper parameters (dimensions of the model, etc.) to obtain the maximum useful information from a scale model is called scaling analysis [8]. In assessments of fission reactor safety, scaling analysis has been very important for benchmarking the thermalhydraulic computer codes that predict a plant's response to transients, and for understanding the predicted trends in full-sized plant responses to transient events.

Scaling analysis is approached by using engineering similitude. Dimension-less groups of variables are formed and applied to the scale model and the expected full-sized plant or facility. Similitude can be in the form of geometry or kinematics [9] [10]. The dimension-less groups can also be formed from the basic conservation equations for mass, energy, and momentum.

If a scale model system is geometrically similar to the full-sized (prototype) system, and the dimension-less numbers describing parameters of operation are equal to those of the prototype system, then the scale model is said to be dynamically similar to the prototype. Potential dimension-less numbers are:

1. Biot, ratio of conductive resistance to convective resistance,
2. Euler, ratio of pressure force to inertia,
3. Froude, ratio of inertia to gravity force,
4. Richardson, ratio of buoyancy force to inertia,
5. Reynolds, ratio of inertia to viscous force,

It is common to use five or more dimension-less groups in scale model predictions for fission power plants when the primary coolant system enters into two-phase flow accident situations [11]. However, it may not be possible to satisfy all the dimension-less groups simultaneously.

Dimension-less numbers in scale models are made equivalent to those for the prototype system [12]. There are also fixed ratios from the full-sized system, such as length, coolant channel diameter, flow velocity, and heat flux, that are applied to the scaled down model. These ratios may additionally be used to design testing facilities.

Thermalhydraulicists have spent the past three decades attempting to identify which of the many available engineering ratios are more important for making the scale model data applicable to the prototype system. The best method for answering this question is by applying the dimension-less numbers to empirical data from scale model experiments and prototype system operational data, if such exists.

from the system. A LOFA normally occurs from either a pump trip or an obstruction in the coolant tubing. The major concern with a LOFA is the reactor's inability to remove heat from part or the whole of the vacuum vessel. As the temperature rises inside the vessel, the PFCs may lose their structural integrity. The elevated temperatures may also release activation products and tritium normally contained within the PFCs.

This definition suggests that all three accidents threaten not only the reactor's integrity, but may also have environmental repercussions if the off-normal event causes radioactive isotopes to be released to the atmosphere.

Within the vacuum vessel, the primary barrier to a coolant leak during a LOFA is the divertor plate. In a tokamak reactor, the divertor is one of the most important components because it removes plasma exhaust, that would otherwise contaminate the plasma as ash and eventually cause the plasma to disrupt. The divertor is partially extended into the null point of the burning plasma and is consequently exposed to the charged ions, electrons, and particles of the plasma, which strike the divertor surface and create high heat loads. These heat loads, if not properly removed, can challenge divertor material limits, and consequently lower the safety margins of operation. In order to increase the heat removal capability of the divertor, the device may have several individual coolant channels, defined here as divertor plates, that run parallel to each other and are assembled as a single unit.

During the evolution of ITER, many divertor plate design concepts have been explored. The most basic of the concepts is the bare tube design, which is essentially a section of tubing with coolant flowing through it. While operational, the bare tube is a lackluster divertor plate option since it has a rather limited critical heat flux (CHF) performance. The CHF performance of a divertor plate is a measure of the ultimate surface heat load that the plate can withstand before failing. Variations on the bare tube divertor plate include use of a swirl tape, porous coating, and screw thread to enhance heat transfer and CHF. These design concepts promote coolant turbulence within the tube, which correspondingly increases the concept component's CHF performance. Other prominent ITER divertor plate design concepts are the internally finned (or "ribbed") channel and the hypervapotron.

In all cases, the divertor plates have a tile of armor, such as a carbon fiber composite (CFC), beryllium, or tungsten to help protect the copper plates from plasma erosion. In this experiment, the armor tile was omitted because the primary interest was the heat transfer performance of the divertor plate mockup. Since the armor tile affects only the distribution and not the intensity of the divertor plate's incident heat flux, omitting the tile does not constrain the applicability of the experimental data. The remainder of the discussion focuses on the LOFA phenomena, however any readers who would like more detail on the various divertor plate geometries are encouraged to review the articles by J. Schlosser [14], M. Araki [15], G. Celata [16], R. Watson [17], and others, that are available in the *Fusion Technology* journal and the proceedings of the biennial *Symposium on Fusion Technology* (SOFT), the biennial *Symposium on Fusion Engineering* (SOFE), and the annual *Thermalhydraulics Specialist Workshop* conferences.

During normal operations, ITER PFCs are expected to absorb an average heat load of 2 MW/m^2 while the divertor plates are being designed to absorb heat loads of 5 MW/m^2. To meet such design specifications, the divertor plates will be actively cooled by subcooled water (50 - 150 °C inlet) at

The semiscale experiment (a scaled primary coolant system for a fission power plant that uses electrical resistance heating instead of nuclear fuel, with 1/1700th of the coolant inventory of a full-sized plant), the Loss of Fluid Test Facility (LOFT) in Idaho, and the Multi-loop Integral System Test (MIST) facility in Virginia, have provided much data for analysis and prediction of power plant transient responses. Unfortunately, this work has dwelt upon overcooling, undercooling, loss of cooling water inventory, and anticipated transients without scram as being the most potentially significant to fission reactor safety - while fusion's interest is in loss of flow events.

For scaling, the parameters of interest will be the physical parameters of the model and the prototype system. These parameters include the pipe lengths, diameters, fittings, heated surface areas, and height changes. The physical size and performance parameters of the pump, pressurizer, and heat exchanger must also be known. The parameters of the fluid are also needed, including the pressure, temperature, flow rate, heat and pump energy added to the fluid, and pressure drops in the flow system. In normal scaling practice, the model system is built to specifications based on the full-sized system design and the specifications are set by careful consideration of the trade-offs and distortions that are introduced when building the model.

1.2 Off-normal Events

Marshall and Cadwallader [13] have cited three off-normal events that can be considered as DBAs for fusion machines: Loss of Vacuum Accident (LOVA), Loss of Coolant Accident (LOCA), and Loss of Flow Accident (LOFA). The LOVA and LOCA were summarized by Marshall and Cadwallader as follows:

> A LOVA normally results from a breach in the vacuum vessel or one of its ports. This breach allows air to enter the plasma chamber and disrupt the plasma, causing the plasma energy to be deposited in a localized area within the chamber. This sudden, intense deposition of energy and ensuing chemical reactions with air may release activation products and tritium formerly contained within the plasma facing components (PFCs), increase on-site dose levels, and damage or destroy the PFCs. The higher on-site dose levels may threaten the safety of operations personnel while the damaged PFCs will decrease the reactor's availability.
>
> A LOCA is the consequence of a leak or rupture in the tubing and allows coolant to enter the vacuum vessel. The LOCA can be internal or external, depending on the location of the leak or rupture in reference to the vacuum vessel. While both internal and external LOCAs pose significant threats to the reactor through the loss of a heat removing medium, the internal LOCA also allows coolant to react with the PFCs. These reactions release activation products that are normally contained within the PFCs.

Considering a LOFA as a subset of the LOCA, Marshall and Cadwallader gave the following definition:

> The LOFA is similar to an external LOCA, the difference being that coolant is not lost

moderate pressure (1 - 4 MPa) and velocity (5 - 10 m/s). In an off-normal event, the divertor plates may experience a maximum heat load of 20 MW/m^2 for a maximum time period of 10 seconds. During a LOFA, the divertor plates may have to remove normal or off-normal heat loads while simultaneously experiencing decreases in the water coolant pressure and/or velocity. Until this report, there has not been a comprehensive investigation of the LOFA issue, complete with experimental data for verification of derived calculations and/or hypotheses.

The question can be logically raised of why resources should be committed to researching off-normal, if not abstract, events such as a LOFA at this juncture of ITER development. The answer is straightforward: LOFAs are already a reality. In 1991, Tore Supra reported that during normal operations, a copper PFC cooling tube lost flow, exceeded its critical heat flux, and ruptured, sending 0.5 liter of water into the vacuum vessel [18]. This real-life experience, combined with the estimated $1x10^{-3}$ events/year frequency for LOFAs in a fusion water coolant system [19], indicates that the phenomenon be analyzed and this report is an initial effort in that direction.

The discussion in this report is not intended to be a complete discussion on LOFAs. Rather, it is a first order approximation on the time-to-burnout (TBO) of a prototypical divertor plate during a simulated LOFA. Time-to-burnout can be used as a figure of merit for comparing potential divertor plate geometries and/or determining if reactor safety systems and operations personnel will have sufficient time to shut down the plasma if a LOFA is detected. Perhaps the most important value of this report lies in its experimental TBO data. Prior to the experiments documented here, fusion designers relied primarily on the thermal calculations of finite element codes such as ABAQUS, COSMOS, and RELAP, to predict the thermal response of divertor plates during an off-normal event. As with any model, experimental data are necessary to verify that the model accurately depicts the physical situation. This is especially the case when modeling a LOFA for a fusion machine since heat transfer during the event may be extremely complex as a result of the simultaneous coexistence of all regions of the boiling curve (single phase, fully developed nucleate boiling, critical heat flux, transition boiling, and film boiling) [20].

This report is organized to first discuss the Sandia 30-kW Electron Beam Test System (EBTS) that was used to generate fusion-relevant one-sided heating on the mockup. The following chapter discusses the manufacture and instrumentation of the experimental mockup of a prototypical divertor plate. Chapter 4 presents the experimental procedure and Chapter 5 presents the experimental results. An extensive modeling effort on the LOFA phenomenon was performed and the results are presented in Chapter 6. Chapter 7 is a discussion on the experimental and modeling results and thermalhydraulic scaling to make the TBO data applicable to ITER. Finally, Chapter 8 contains the major conclusions, including suggestions for future work, that would be essential to understand and characterize fully the LOFA phenomenon.

2.0 Electron Beam Test System

2.1 Introduction

This chapter discusses the 30 kW Electron Beam Test System (EBTS) located at Sandia National Laboratories in Albuquerque, New Mexico. The EBTS is a multipurpose device for studying the surface modification, thermal response, and failure modes of high heat flux materials and components [21]. The following discussion includes basic operating capabilities, available diagnostics, and the water flow loop.

For completeness, the discussion on the EBTS diagnostics includes a table of known errors for each of the sensors, instruments, and readings. A rather intensive discussion is given on the EBTS water flow loop since its characteristics inherently influence the experimental LOFA data.

2.2 Basic Operating Capabilities

The EBTS, shown in Figure 2-1, can accommodate targets of all shapes. The only restriction that the EBTS imposes on the mockup physical dimension is that the size is limited to 30 cm by 60 cm. A large variety of ports and vacuum feed-throughs in the 70 cm diameter by 100 cm length stainless steel vacuum chamber are available for diagnostics and utility connections.

The electron source is typically a tungsten or tantalum filament with maximum operating parameters of 30-kV and 30-kW. Magnetic lenses and deflection coils are used to focus, position, and raster the electron beam to cover a variety of sample surfaces with a range of focusing options, from finely tuned to defocused. For most experiments, the beam is operated with a beam full-width, half-maximum diameter of 5 mm.

A dedicated VAX cluster controls the discharge of the electron gun. The use of the EBTS as a variable directed heat source allows many scenarios of heat flux distributions. In a chamber pressure of 130 Pa, average beam rise time is 1 ms and pulse duration can be adjusted from 2 ms to continuous operation over a heated area from 1 to 100 cm^2. With 30-kV acceleration, the beam electrons have an approximate penetration depth of 1×10^{-3} mm in copper, which produces what is essentially a surface heat flux.

2.3 Standard Diagnostics

Standard diagnostics for the EBTS include a television monitoring system and an infrared camera and colorizing system. During beam pulses, both the TV video and infrared camera outputs can be recorded with a standard video cassette recorder. For water calorimetry, differential temperature (ΔT) blocks and flow meters are provided and logged two to three times per second during a beam pulse. Other routinely logged diagnostics are:

1. 1-color and 2-color pyrometers: for spot surface temperature;
2. a bank of Type-K thermocouples: for spot temperatures and infrared camera calibration;

3. pressure transducers: for measuring water inlet and exit pressures;
4. a residual gas analyzer: for target out-gassing measurements.

Table 2-1 presents the operating ranges of the diagnostic sensors and transducers.

All data are logged to a computer system via analog signals from the sensors and transducers, converted to digital signals by the data acquisition subsystem, and stored on the computer system's disk drive. Estimated accuracy, the zeroth order error [22], of the diagnostics is shown in Table 2-2.

2.4 Water Flow Loop

2.4.1 General Description

The flow loop provides demineralized water to cool the EBTS target. Water in the main cooling loop is circulated by a variable speed centrifugal pump. The system flow rate is regulated by a flow control valve, FCV-05. Water temperature is regulated by a temperature control valve, TCV-02, which diverts water around the flow loop heat exchanger, as required, to maintain the preset temperature. System hydraulic conditions may range from: 3 to 32 l/s flow rate, ambient to 282 °C temperature, and 0 to 7 MPa pressure.

The flow loop pressure is controlled by a continuous feed-and-bleed system. Up to 0.6 l/s of demineralized water may be injected into the flow loop by a positive displacement pressure control pump with pulsation dampener. The water injection rate is controlled by a bypass flow control valve, FCV-02, which directs a portion of the pump flow rate to the raw water storage tank. Flow loop pressure is controlled by a pressure control valve, PCV-04, located in the bleed line. Bleed water is discharged into a raw water storage tank through a demineralizer and back to the pressure control pump. Line-mounted oxygen and pH sensors in the bleed line control the feed rate of hydrazine and ammonia injected into the system. Minor pressure and volume changes in the loop are dampened by a surge tank. Water level in the surge tank is maintained between high and low limits via pressurizing with bottled nitrogen or by venting. A low pressure clean-up centrifugal pump is used to flush or fill the system.

2.4.2 Temperature Control

The system's temperature is controlled using a three-way control valve, TCV-02, to modulate the flow of water through the loop's heat exchanger. The main control loop temperature measurement, TE-02, is taken downstream of the circulation pump. The signal from the temperature transmitter, TT-02, is directed to the local controller, TIC-02, and to the control computer for monitoring and control. A control valve, TCV-02, in the main loop is modulated, dependent upon the difference between the present and measured variable. Operating setpoints can be entered locally or through the control computer.

An additional feature allows the temperature controller to position valve TCV-02 in response to an incoming slug of hot water from the EBTS chamber. Temperature at the outlet of the EBTS chamber is sensed by temperature transmitter TT-01 and the signal directed to controller TIC-02.

The flow rate signal from FT-05 is also directed to TIC-02 to reset the controller in response to step changes in flow.

2.4.3 Flow Control

System flow is controlled using a flow control valve, FCV-05, located downstream of the circulation pump. A flow transmitter, FT-05, is used to sense flow upstream of FCV-05. The flow signal is directed to both controller FIC-05 and the control computer for monitoring and control. The flow control valve FCV-05 is modulated by controller FIC-05, dependent upon deviations between the preset and the measured variable. The flow signal from FT-05 is also directed to reset TIC-02 in response to flow rate changes. Operating setpoints can be entered locally or through the control computer.

2.4.4 Pressure Control

Control of the system pressure is accomplished using pressure control valve PCV-04 to bleed water from the flow loop and direct it to the raw water storage tank. Pressure transmitter PT-04 senses the system pressure downstream of the circulation pump. The pressure signal is directed to both the pressure controller PIC-04 and the control computer for monitoring and control. Control valve PCV-04 is modulated by PIC-04, dependent upon the deviations between the present and the measured variable. Operating setpoints can be entered locally or through the control computer.

2.4.5 Water Chemistry Control

To monitor and control the system water chemistry, an oxygen sensor and pH sensor are installed in the bleed line. These sensors are connected to the panel-mounted oxygen-indicating transmitter AIT-09 and pH-indicating transmitter AIT-08, respectively. Signals from AIT-08 and AIT-09 are directed to the control computer for monitoring and control. The control computer regulates the injection rate by adjusting the stroke length of the hydrazine and ammonia injection pumps. Injection rates are under 500 ml/hr. Operating setpoints can be entered locally or through the control computer.

2.4.6 Surge Tank

The surge tank is installed as part of the system to dampen minor pressure and volume changes. Water level in the surge tank is maintained either by controlled venting or pressurization using nitrogen. The water level is controlled by a combination high/low level switch, LS-06. When the surge tank water level is low, the vent valve, SV-07, is energized to open by the low-level switch LS-06 and the nitrogen valve, SV-06, is closed. When the surge tank water level is high, the nitrogen valve SV-06 is energized to open by the high-level switch LS-06 and the vent valve SV-07 is closed. Nitrogen is supplied from a bottled nitrogen supply station at 17 MPa.

2.4.7 Circulation Pump

A variable-speed, vertically-oriented, in-line centrifugal pump provides flow loop circulation. This pump operates at flow rates from 3 to 32 l/s, temperatures from 37 to 271 °C, and pressures

from 0 to 7 MPa. The pump is designed for a maximum water temperature of 271 °C at 7 MPa system pressure and features a 10 cm suction and an 8 cm discharge nozzle with ANSI 672N raised face flanges. The pump also features a mechanical seal, complete with seal flush piping and cooler, and is driven by a 93-kW, 3600 rpm motor. The pump is operated using a variable-speed drive controller and located so that no special priming procedures are required.

2.4.8 Low-Pressure Clean-up Pump

A vertical, in-line centrifugal pump, rated at 3 l/s and 0.17 MPa discharge pressure, is provided to fill the flow loop or to flush the flow loop when the loop is not pressurized. The pump is designed for a maximum of 1.9 MPa at 37 °C and features 5 cm suction and 4 cm discharge nozzles with ANSI 672N flat face flanges. The pump also features a mechanical seal and is driven by a 2.2 kW, 1800 rpm motor. The pump is located so that no special priming procedures are required.

2.4.9 Pressure Control Pump

The system is pressurized with a positive displacement pump capable of pumping a maximum of 0.6 l/s against a system pressure up to 7 MPa. The pressure control pump is a horizontal, triplex, plunger power pump with a motor driven V-belt drive. The pump driver is a 7.5-kW, 1200 rpm motor having a 1.15 service factor. The pump discharge system is provided with a pulsation dampener and is protected from over-pressurization by a relief valve located just downstream of the pump discharge. Flow control is maintained by a flow bypass valve. This pump will maintain system pressures required with a 0.6 l/s bleed stream removal.

2.4.10 Chemical Injection Pumps

Two sets of positive displacement chemical injection pumps are provided, each with a 30 l stainless steel feed tank. One pump provides aqueous hydrazine injection for oxygen scavenging and the other pump provides aqueous ammonia for pH control. Each pump is capable of injecting against a 7 MPa system pressure at a flow rate of 0 to 500 ml/hr and is equipped with an electric capacity adjustment, mounted directly on the pumps, that regulates the flow rate in response to a signal from the remote control unit. The pump driver is a 0.2-kW, 1800 rpm motor. Each feed tank has a local level indicator, isolation valves, Y-strainer, and drain valve.

2.4.11 Heat Exchanger

The heat exchanger for the cooling loop is designed for the least favorable conditions from a heat transfer point of view, that is, for the minimum temperature difference between loop water and shell-side cooling water during normal operation. The heat exchanger operating parameters are provided in Table 2-3. While the heat exchanger is sized for low-temperature conditions, it is designed to operate at 282 °C maximum loop water temperature. The U-tube design facilitates thermal expansion and permits trouble-free operation through the entire operating range.

The heat exchanger is a TEMA Class R, 23-96 BEU and is designed and constructed per TEMA "R" and ASME Section VIII, Division I. The heat exchanger is 379 cm in overall length and 61 cm outside diameter. The U-tubes are 1.9 cm, 16 BWG, 304L stainless steel in a four-pass arrangement.

The channel side is constructed of carbon steel with 304L stainless steel overlay. The shell side is constructed of carbon steel with 0.3 cm corrosion allowance. Mechanical design temperature and pressure for the exchange is 1 MPa at 49 °C for the shell side and 9 MPa at 296 °C for the tube side.

The shell side of the exchanger is provided with a rupture disc, rated at 1 MPa at 49 °C, to protect the exchanger shell in the event of a high-pressure tube failure. The flow loop is provided with a relief valve set at 9 MPa to protect the system pumping and equipment from overpressure in the event of a cooling water failure with continued heat input into the system.

2.4.12 Surge Tank

A 15 l, 304 stainless steel surge tank is provided to dampen system pressure pulsations introduced by the positive displacement pump that pressurizes the loop and to compensate for minor volume changes. Pressurization is accomplished with a nitrogen cover gas. The nitrogen source is provided from a standard 14 MPa bottle and reduced to 8.6 MPa before being supplied to the system.

The surge tank has a 27 cm outer diameter and is 91 cm long, seam-to-seam. The tank is constructed of 304L stainless steel in accordance with ASME Section VIII, Division I. Design conditions are specified as 9.3 MPa at 282 °C. A corrosion allowance of 0.3 cm is allowed.

Table 2-1. Operating Ranges of EBTS Diagnostics

Diagnostics		Units	Range
ΔT blocks		°C	0 - 121
flow meter		m/s	0 - 10
1-color pyrometers	low λ	°C	150 - 550
	low range	°C	300 - 1300
	mid range	°C	1000 - 3000
	high range	°C	3000 - 6000
2-color pyrometers	low range	°C	700 - 1400
	high range	°C	1500 - 3500
pressure transducers		MPa	0 - 7

Table 2-2. Accuracy of EBTS Diagnostics

Variable	Unit	Accuracy
Velocity	m/s	± 0.02
Infrared camera surface temperature	°C	± 10
Water temperature rise through heated section	°C	± 0.1
Inlet/exit pressure	MPa	± 0.01
Inlet/exit temperature	°C	± 2
Thermocouples	°C	± 2

Table 2-3. EBTS Heat Exchanger Operating Parameters

Heat load (MW)	1.6
Inlet loop water temperature (°C)	50
Outlet loop water temperature (°C)	38
Inlet cooling water temperature (°C)	16
Outlet cooling water temperature (°C)	28
Loop water flow (l/s)	32
Cooling water flow (l/s)	32

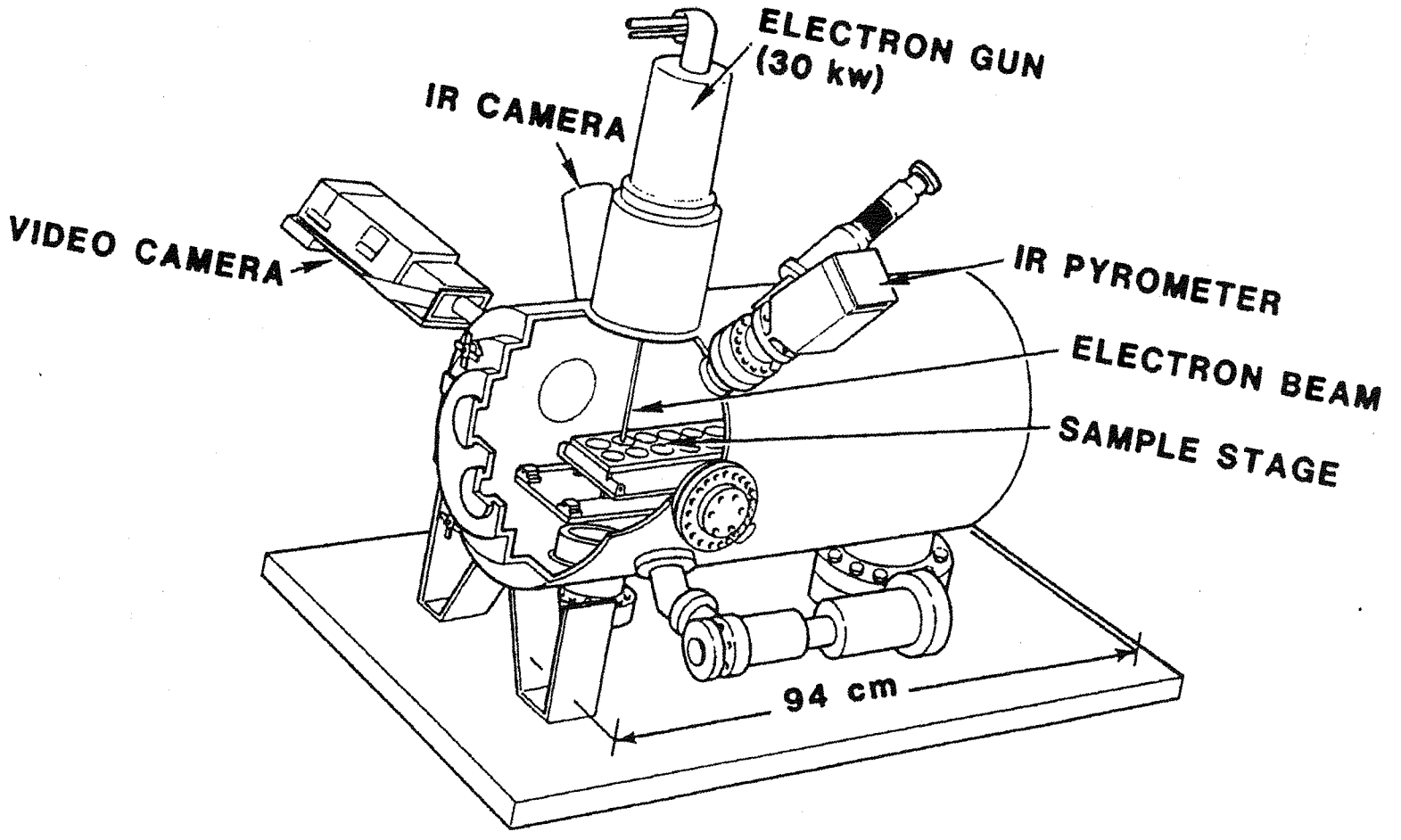

Figure 2-1. Sandia 30-kW Electron Beam Test System

Sandia National Laboratories

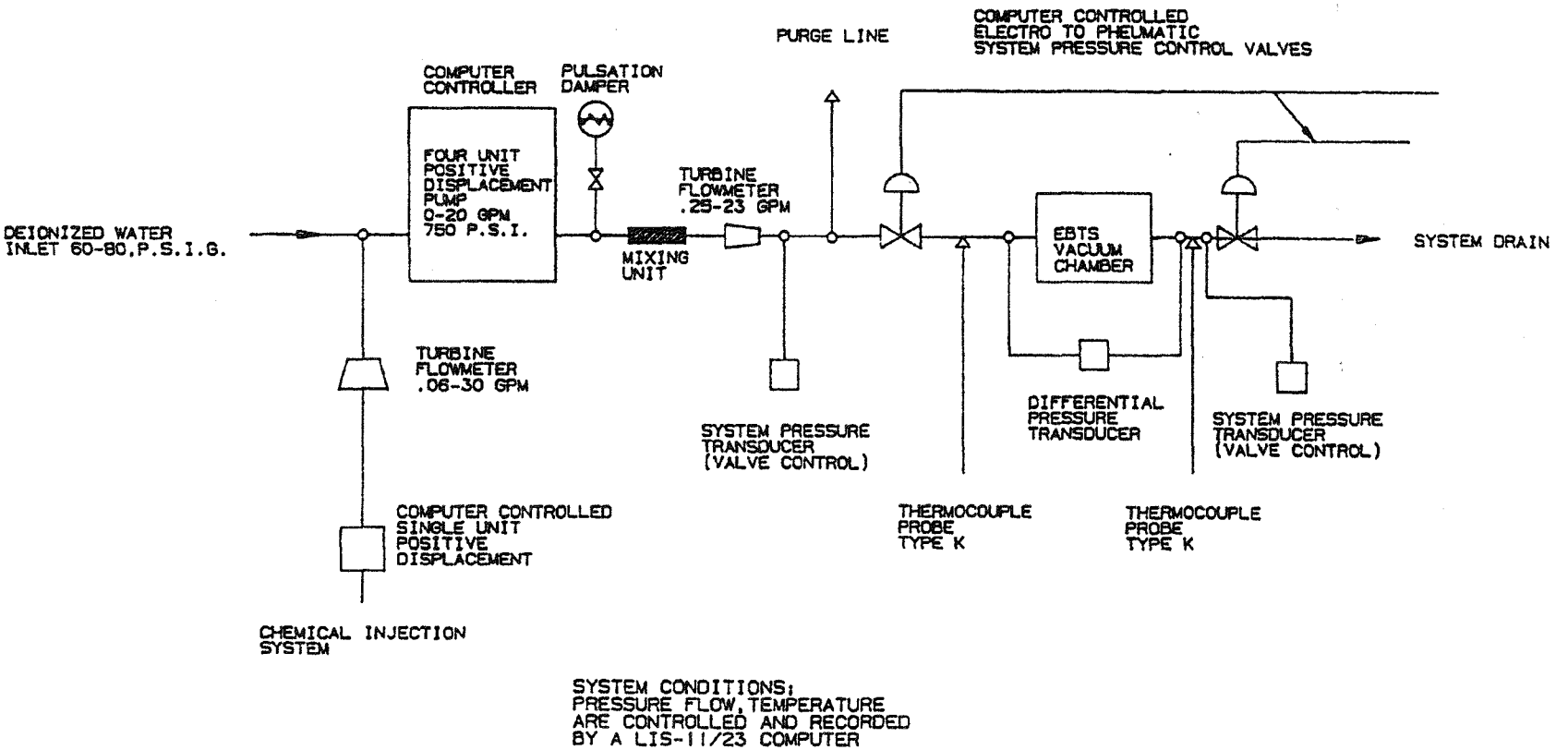

Figure 2-2: Schematic of Sandia EBTS Water Loop

3.0 Prototypical Divertor Plate Mockup

3.1 Introduction

In tokamak reactors, such as the International Thermonuclear Experimental Reactor (ITER), the plasma facing components (PFCs) are exposed to one-sided heat fluxes that are created by energetic charged and neutral particles, and photons, striking the PFC surfaces. The divertor modules in a tokamak are used to remove exhaust from the burning plasma and by design receive the highest heat loads of the PFCs. To increase the heat removal capability of the divertor, the device may have several individual coolant channels, defined here as divertor plates, that run parallel to each other and are assembled as a single unit. In all cases, actual divertor plates have a tile of armor manufactured from materials with a low atomic number, e.g., carbon fiber composite, beryllium, or tungsten, to help protect the copper heat sink from plasma damage.

The mockup used in this experiment to obtain time-to-burnout (TBO) data was designed to emulate the typical ITER divertor plate with the exception of having a protective tile of armor. The armor tile was deemed unnecessary for the experiment since the cooling channel's thermal response is not dependent on the armor material's thermal conductivity.

3.2 General Description

The divertor plate mockup is shown in Figures 3-1 through 3-3. The mockup is a one-piece assembly of oxygen-free, high-conductivity (OFHC) copper bar stock and tubing. The square bar stock has a length of 133.4 mm and a 15.7 mm x 15.7 mm square cross-section. A circular coolant channel of diameter 7.5 mm was center drilled, axially, through the bar stock. The bar stock's coolant channel entrance and exit were 3.175 mm counterbored to allow a slip fit of the 98.4 mm long copper tubes (9.5 mm o.d., 7.5 mm i.d.), which are silver brazed into place. On the two sides of the mockups are six (three each side) 13 mm long grooves, each with a 1 mm x 1 mm cross-section. These grooves (positioned 1 cm from either end and in the center of the mockup) house the wires for the 0.5 mm diameter K-type thermocouples, shielding them from damaged by the electron beam. The thermocouple sensor tips are positioned 0.5 mm from the top surface (heated surface) of the mockup. Since the thermocouples are located so close to the surface, their recorded temperatures are assumed to be indicative of the surface temperatures.

The mockup has a length of 133.4 mm, but the heated length is only 40 mm. The heated length of the top surface is scribed on the mockup so that the heated length ends 5 mm beyond the two center thermocouples (TC2 and TC5 in Figure 3-4). Prior CHF experiments performed on the EBTS have shown that burnout of the target typically occurs just prior to the heated length exit [23]. By having the heated length end 5 mm beyond the thermocouples, it is believed that the optical pyrometers will be looking at the most likely spot of burnout.

It has been noted by other experimenters [24] that the emissivity of copper divertor mockups changes considerably as a result of electron beam heating. The change in emissivity is significant because it directly impacts the optical pyrometers' calibration. To counteract this problem, a highly uniform and emissive heated surface is necessary for the mockup. Theoretically, this specially

prepared surface will limit the emissivity changes during the testing campaign.

To increase the emissivity of the copper mockup, the top surface of the mockup is sandblasted with 25 micron Al_2O_3 beads at 4.1 to 5.5 MPa air pressure for approximately 15 s. The mockup is then baked in air at 300 °C for 2 hrs and subsequently placed in a relative humidity of 100% at 70 °C for 3 days. This procedure creates an uniform layer of oxidation that increases the copper surface emissivity from less than 0.1 to approximately 0.4. The increased emissivity of the heated surface area correspondingly increases the efficiency of the low-wavelength pyrometer, and makes a more uniformly emitting surface for the infrared (IR) camera.

To assist the EBTS operators in aligning the electron beam on the mockup, beam reference marks, in 5 mm increments, are added to the top surface of the mockup as shown in Figure 3-4a. These reference marks are small nicks in the oxidation coating on the corner edge of the mockup. The nicks appear as small white spots when viewed using the IR camera.

The braze elements of the mockups are Ag, Cu, and Sn, with a braze temperature of approximately 700 °C. The brazes are applied by a hand-held torch in an atmosphere of air.

3.3 Pre-Test Procedures

Each face of the mockup is photographed using high-resolution 35 mm color film. The mockups' dimensions are measured in three places along each edge (left, right, and center) using a micrometer and calipers. The diameters and depths of all thermocouple holes are also measured and recorded. Mockup measurement data are shown in Table 3-1.

3.4 Leak Check

The mockup is leak tested with helium gas and passes a leak detection rate of 3×10^{-8} atm-cm^3/s at a vacuum of 10 mPa.

3.5 Pressure Test

A dynamic water pressure test, with the mockup installed inside of the EBTS chamber, is performed and the mockup withstands a pressure of 1.38 MPa without any visible signs of a water leak or a loss of chamber vacuum.

Table 3-1. Mockup Measurements (Pre-test)

		Divertor Mockup
Length (mm)		133.45
Width (mm)	Left edge Center edge Right edge	15.67 15.69 15.67
Thermocouple depth (mm)	TC1 - TC6	0.9
Thermocouple position (mm)	TC1 & TC4 TC2 & TC5 TC3 & TC6	10 66.54 123.59
Channel ID (mm)		7.67
Thermocouple diameter (mm)	TC1 - TC6	0.635

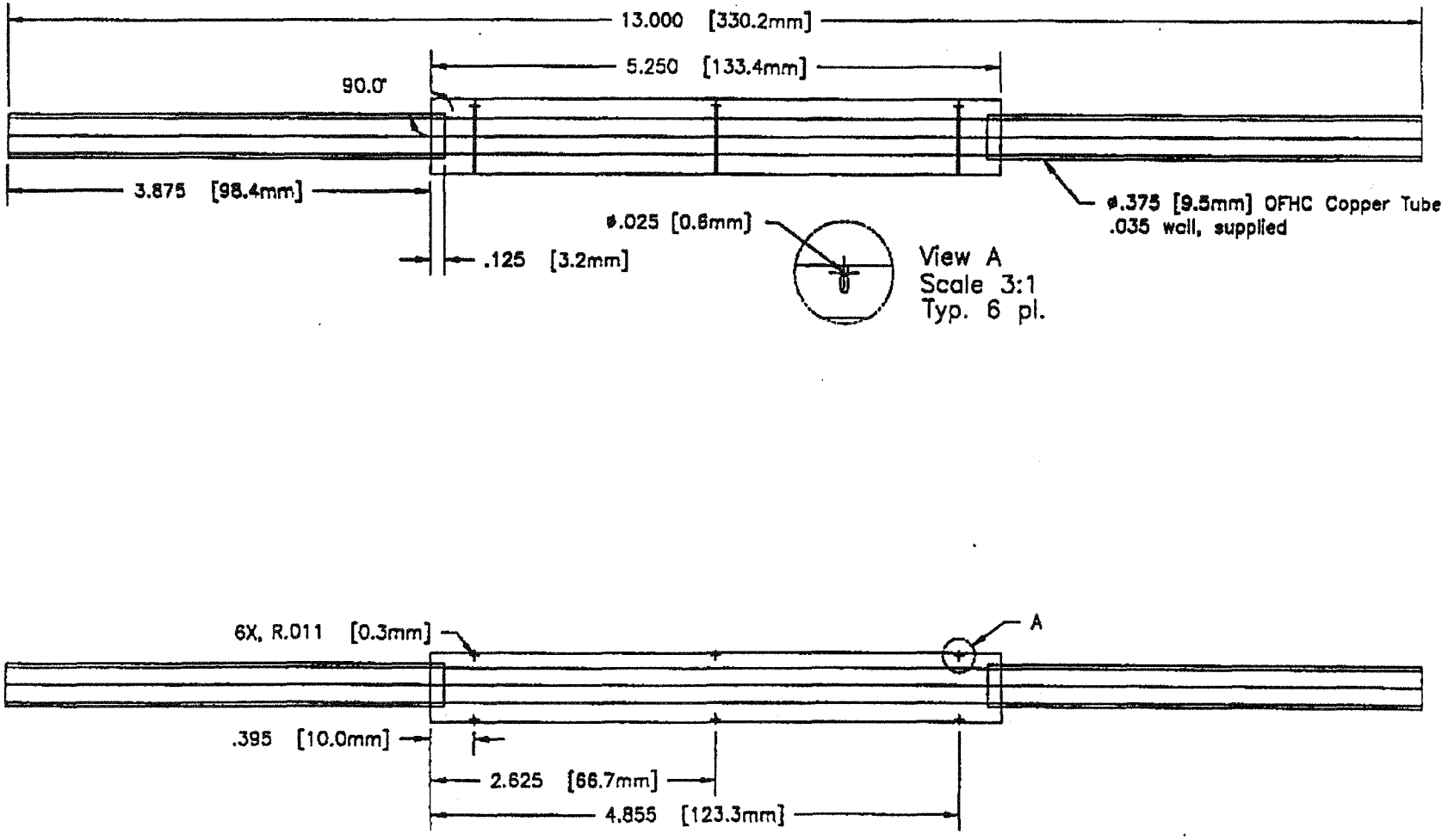

Figure 3-1: Axial Dimensions of Mockup.

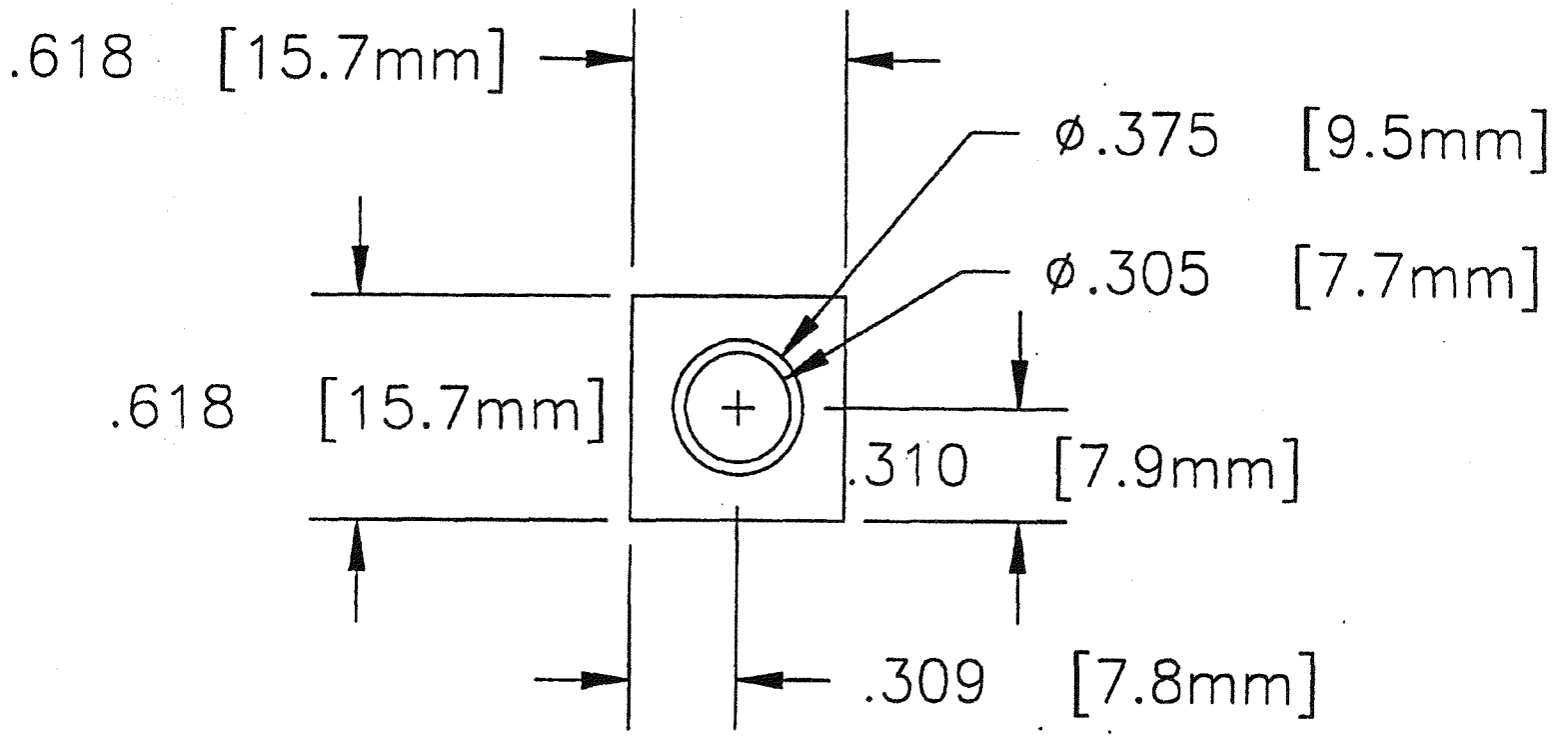

Figure 3-2. Face Dimensions of Mockup.

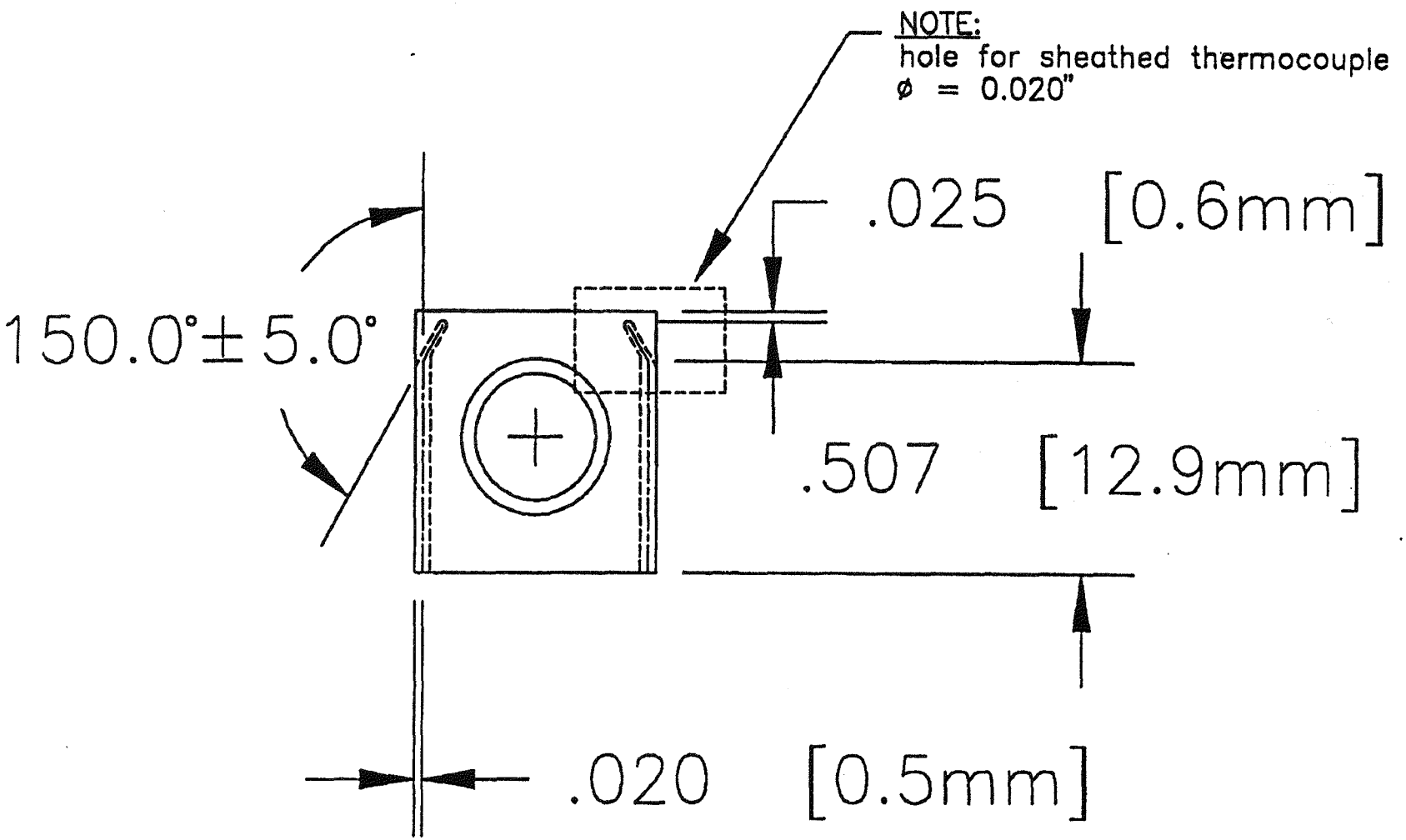

Figure 3-3. Thermocouple Positioning in Mockup.

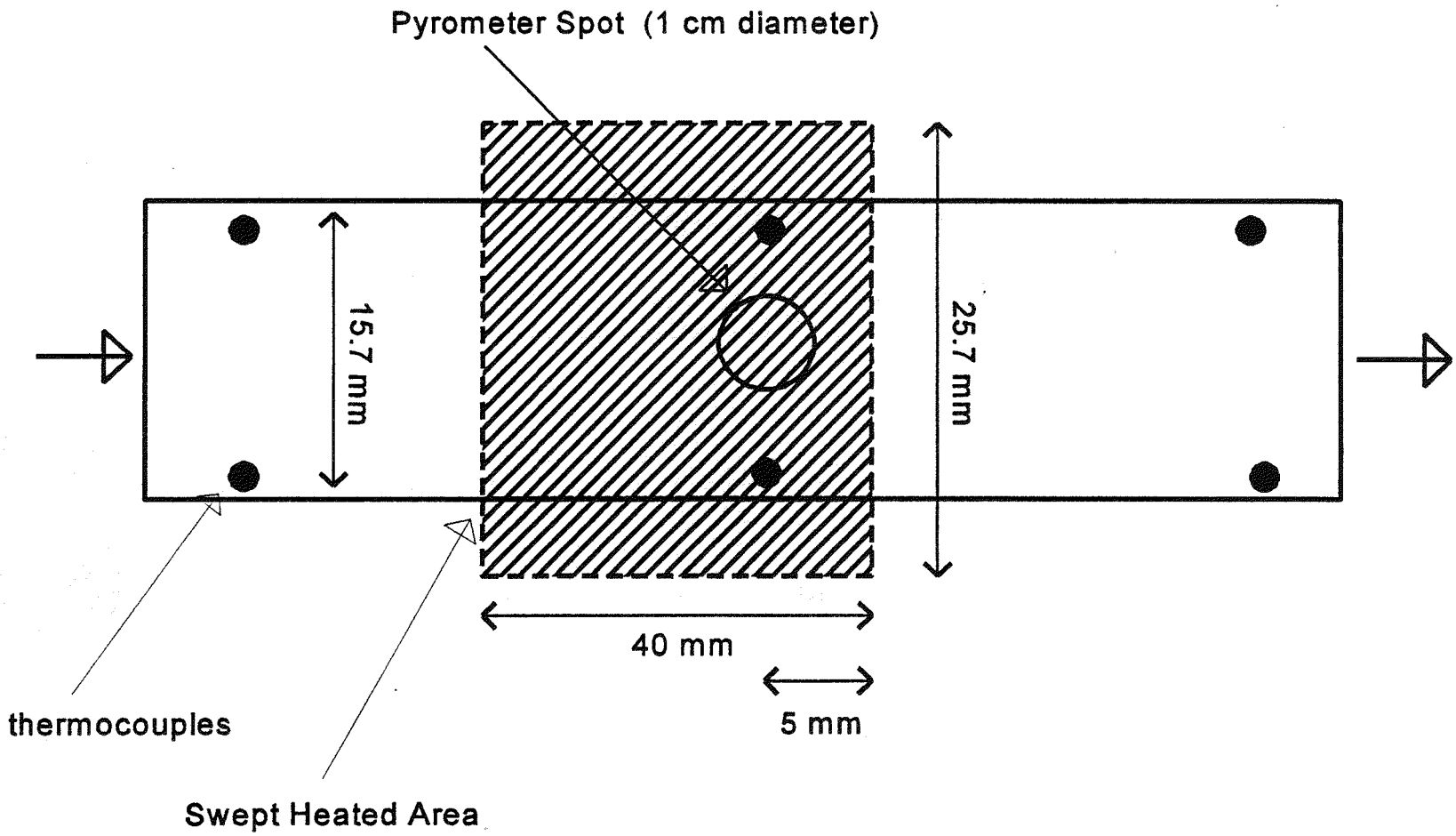

Figure 3-4. Swept Heated Area of Mockup (Top View of Mockup).

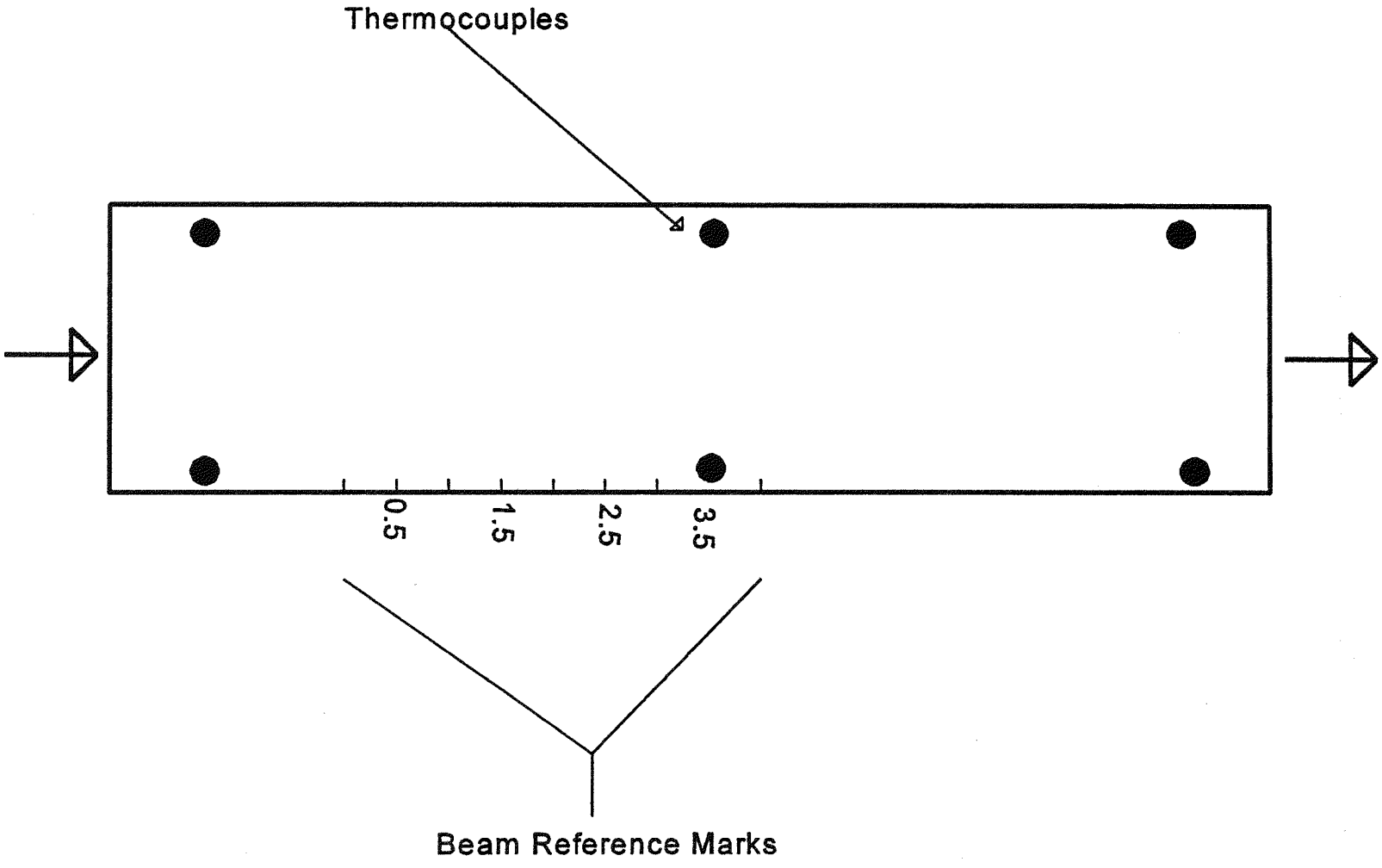

Figure 3-4a. Beam Reference Marks on Mockup (Top View of Mockup).

4.0 Experimental Procedure

4.1 Introduction

This chapter presents the procedure for obtaining the experimental LOFA data. The primary objective of the experimental procedure was to determine the time-to-burnout (TBO) of a prototypical fusion reactor divertor mockup after a simulated coolant pump failure. This objective was met by removing the power to the pump after steady-state heating by the electron beam was reached. The electron beam continued supplying one-sided heat to the mockup until a high temperature trip signal from the embedded thermocouples in the heated area of the mockup shut down the electron beam, just prior to failure of the copper tube.

4.2 Instrumentation

The following instrumentation data were required during the experiment:

1. high range coolant water flowmeter (0 - 50 g.p.m.),
2. ΔT calorimetry,
3. inlet water temperature,
4. inlet and outlet water pressure,
5. 5 Type-K target thermocouples mounted in the mockup,
6. surface temperature in the heated area, obtained with,

    1. low-wavelength optical pyrometer, 150 - 550 °C range,
    2. calibrated spot temperatures from the IR camera, 50 - 800 °C range,
    3. 1-color low range optical pyrometer, 300 - 1300 °C range

7. surface temperature distribution from calibrated IR thermography,
8. voltage-current measurement of emitted electron gun power,
9. line-scan mode for IR camera near anticipated burnout.

4.3 Calibration Procedure

4.3.1 Bulk Temperature

1. calibrated all thermocouple digital indicators and analog channels using an Omega thermocouple calibration signal.
2. verified that all computer traces agreed with calibrated visual readouts.

4.3.2 Surface Temperature

Pyrometer and IR camera calibrations were repeated often during the experiment (at least once a day or after any visual change in the mockup's heated surface) to ensure a high degree of confidence in the experimental data. The calibration procedure was as follows:

1. Water flow through the mockup was stopped.
2. The mockup was purged of water using compressed air at the coolant inlet.
3. The mockup was slowly (< 1 °C/s) heated to maximum bulk temperature of 400 °C using the electron gun "idle" filament. No large temperature gradients were created across the mockup during this heating.
4. Heating of the mockup was stopped by turning off the electron gun "idle" filament.
5. The low-wavelength spot pyrometer, low-range 1-color pyrometer, and IR camera ThermaGram© software were calibrated by adjusting the emissivity of each to obtain agreement with the Type-K thermocouples embedded in the mockup, during the mockup's cool down.
6. The pyrometer trip circuit was tested by setting the trip to 450 °C and using emission controlled electron beam heating to slowly heat the mockup to 450 °C. The circuit was considered operational if the electron beam was properly shutdown by the pyrometer software at the requested 450 °C setpoint.
7. The thermocouple trip circuit was tested by setting the trip setpoint value in the electron beam control program, EBCON, to a value equal to 50 °C greater than the inlet water temperature and running a low-power electron beam shot. The circuit was considered operational if the electron beam was properly shut down by the thermocouple software at the requested temperature setpoint.
8. The mockup was cooled by injecting compressed air through the coolant inlet until the bulk temperature reached 50 °C.
9. The low range pyrometer, 1-color pyrometer, and thermocouple trip setpoints were reset as specified in the test matrix.

4.3.3 Water Calorimetry

1. During the test matrix, the zero level of the ΔT blocks were adjusted between each shot, as necessary.
2. The computer traces from the flow meters were compared daily with the digital display to verify good agreement.
3. The flowmeter's software trip was disabled since the purpose of the experiment was to examine the mockup's thermal behavior in low flow or no flow conditions.

4.3.4 Beam Alignment

1. The axial (i.e., along length of tube) location of the beam sweep was adjusted until thermocouples TC2 and TC5 (refer to Figure 3-4) reached a maximum temperature for a long beam pulse (e.g. 2 minutes).
2. The side-to-side beam sweep pattern was adjusted so that the beam spilled over each side of the mockup by a beam diameter (5 mm). This spillover gave a swept width of (1.57 cm + 0.5 cm + 0.5 cm) = 2.57 cm. This sweeping was done to minimize the Gaussian distribution of the beam, i.e., ensure a uniform heat flux across the mockup.
3. The side-to-side beam pattern was further adjusted until thermocouple readings from TC2 and TC5 matched. The IR camera showed symmetric wings when in line scan mode and the beam pattern was balanced between the two thermocouples.

4.4 Test Prerequisites

1. The mockup was installed in the EBTS chamber centered under the electron beam. All thermocouples were checked for proper operation in the installed mockup.
2. The EBTS high pressure and high temperature loop was configured to operate with the following parameters:

Temperature:	specified value ± 3 °C
Pressure:	specified value ± 1.0 p.s.i.g
Flow rate	specified value ± 0.2 g.p.m.

The specified parameters for the test matrix are presented in Table 4-1.

4.5 Test Procedures

A summary of the test matrix is shown in Table 4-1. This table presents the general conditions of the eight test cases. The goal of the test cases was to measure the thermal response of the divertor mockup during a simulated LOFA.

The test procedures for each case was identical:

- The EBTS operator established the specified surface heat flux at the given inlet conditions of the case as specified in Table 4-1 for a beam pulse length of 120 s. The 120 s pulse length produced steady-state heating of the mockup.
- When the beam pulse length equaled 120 s, the EBTS operator removed the power to the coolant pump, but continued electron beam heating of the mockup.
- Electron beam heating of the mockup continued until either of the two thermocouples (TC2 or TC5) in the heated area or one of the two spot pyrometers registered a high-temperature trip, dependent upon the case, that shutdown the electron beam.
- The procedure was repeated for each of the eight cases.

Table 4-1. LOFA Test Matrix

	Water Inlet Conditions			CHF: Tong-75		Applied	
Case	Pressure (MPa)	Velocity (m/s)	Temp. (°C)	Surface (MW/m^2)	Wall (MW/m^2)	Surface (MW/m^2)	Predicted BSM[a]
1	1	1	68	4	8	6	0.7
2	1	10	68	12	24	6	2.0
3	1	5	68	8.7	17	6	1.5
4	1	10	11	21.5	43	16	1.3
5	1	10	11	21.5	43	15	1.4
6	1	10	11	21.5	43	10	2.1
7	1	10	11	21.5	43	7	3.1
8	1	10	11	21.5	43	3	7.2

[a] The burnout safety margin (BSM) is calculated in Chapter 6.

11. Outlet pressure, p.s.i.g,
12. Coolant water inlet temperature, °C,
13. Coolant water temperature change, °C,
14. Power: absorbed in coolant water, kW,
15. Coolant water flow rate, g.p.m..

Table 5-1. Coolant Pump and Electron-Beam Trip Times

	Water Inlet Conditions			Experimental				
EBTS Shot	Pressure (MPa)	Velocity (m/s)	Temp. (°C)	$q_{incident}$ (MW/m^2)	T_{trip} (°C)	$t_{pump\ trip}$ (s)	$t_{ebeam\ trip}$ (s)	$t_{burnout}$ (s)
144198	1	1	68	6	700.0	122.8	134.5	11.8
144201	1	10	68	6	750.0	135.0	167.0	32.0
144205	1	5	68	6	700.0	122.0	136.0	14.0
144318	1	10	11	16	750.0	130.5	139.3	8.8
144319	1	10	11	15	750.0	132.0	142.0	10.0
144320	1	10	11	10	700.0	121.0	134.3	13.3
144321	1	10	11	7	750.0	123.0	140.8	17.8
144322	1	10	11	3	750.0	135.0	170.0	35.0

5.0 Experimental Results

5.1 Introduction

Steady-state heating of the mockup was achieved with very long electron beam pulses. The pulse lengths were typically on the order of 120 s. After ensuring steady-state heating by monitoring the thermocouple readings in the heated area, the pump for the EBTS coolant loop was manually tripped off. Although the pump was tripped off, electron beam surface heating of the mockup continued until one of the two embedded thermocouples in the heated area tripped the electron beam with a predetermined high-temperature signal. After the electron beam was tripped, flow was restored to the mockup and another experimental case began.

A total of eight LOFA cases were run. The cases were chosen to demonstrate the dependence of TBO on incident heat flux and initial inlet velocity, i.e., inlet velocity prior to the pump trip. The TBO is calculated as the time difference between the pump trip and thermocouple high-temperature trip.

5.2 Time-to-Burnout Plots

Table 5-1 presents pump trip time, electron-beam trip time, and the associated TBOs for the experimental data. Plots were made for the TBO data using surface temperature and water velocity as the two y-axes and beam pulse length as the x-axis, as shown in Figure 5-1.

In Figures 5-1 through 5-8, the plots are arranged so that the beam pulse length has 120 s as the origin. This was done to increase the resolution in the area of interest, that is, the surface temperature and velocity behavior after the pump trip at 120 s. As discussed in the previous chapter, the time prior to the pump trip was used to ensure steady-state conditions, so the omission of this time period in the following plots does not affect the TBO.

5.3 Experimental Data

Appendix A contains the experimental data plots, as recorded by the EBTS data acquisition system. For each EBTS shot, there are fifteen time-dependent plots. They are:

1. Power: electron beam power during the shot, W,
2. Low-range 1-color pyrometer temperature, °C,
3. Low-wavelength pyrometer temperature, °C,
4. Thermocouple 1 temperature: inlet thermocouple, °C,
5. Thermocouple 2 temperature: heated area thermocouple, °C,
6. Thermocouple 3 temperature: exit thermocouple, °C,
7. Thermocouple 5 temperature: heated area thermocouple, °C,
8. Thermocouple 6 temperature: exit thermocouple, °C,
9. Thermocouple 7 temperature: bottom of mockup (in heated area) thermocouple, °C,
10. Inlet pressure, p.s.i.g,

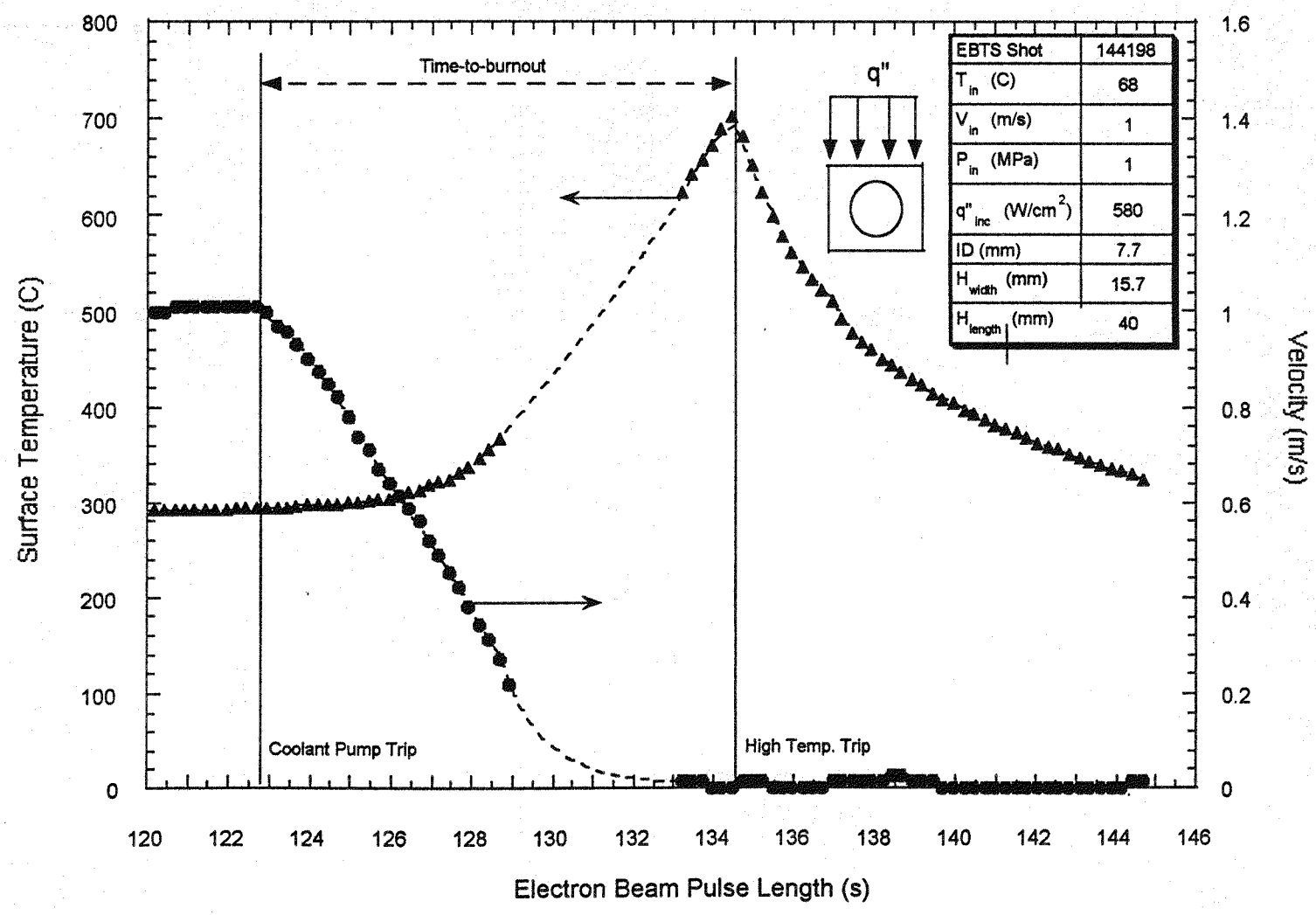

Figure 5-1: Surface (thermocouple) Temperature and Inlet Velocity Responses Used to Calculate TBO for EBTS Shot 144198.

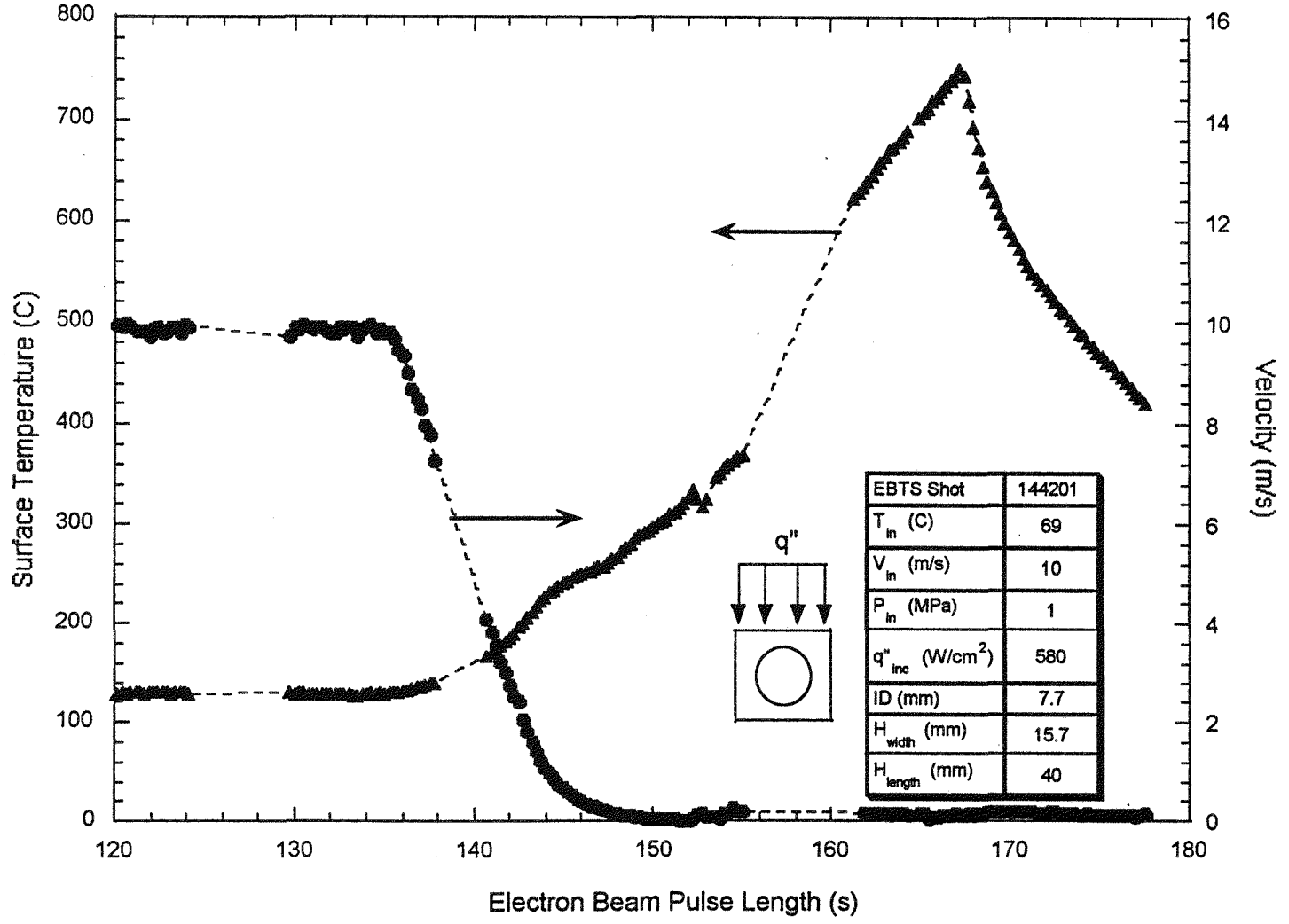

Figure 5-2: Surface (thermocouple) Temperature and Inlet Velocity Responses Used to Calculate TBO for EBTS Shot 144201.

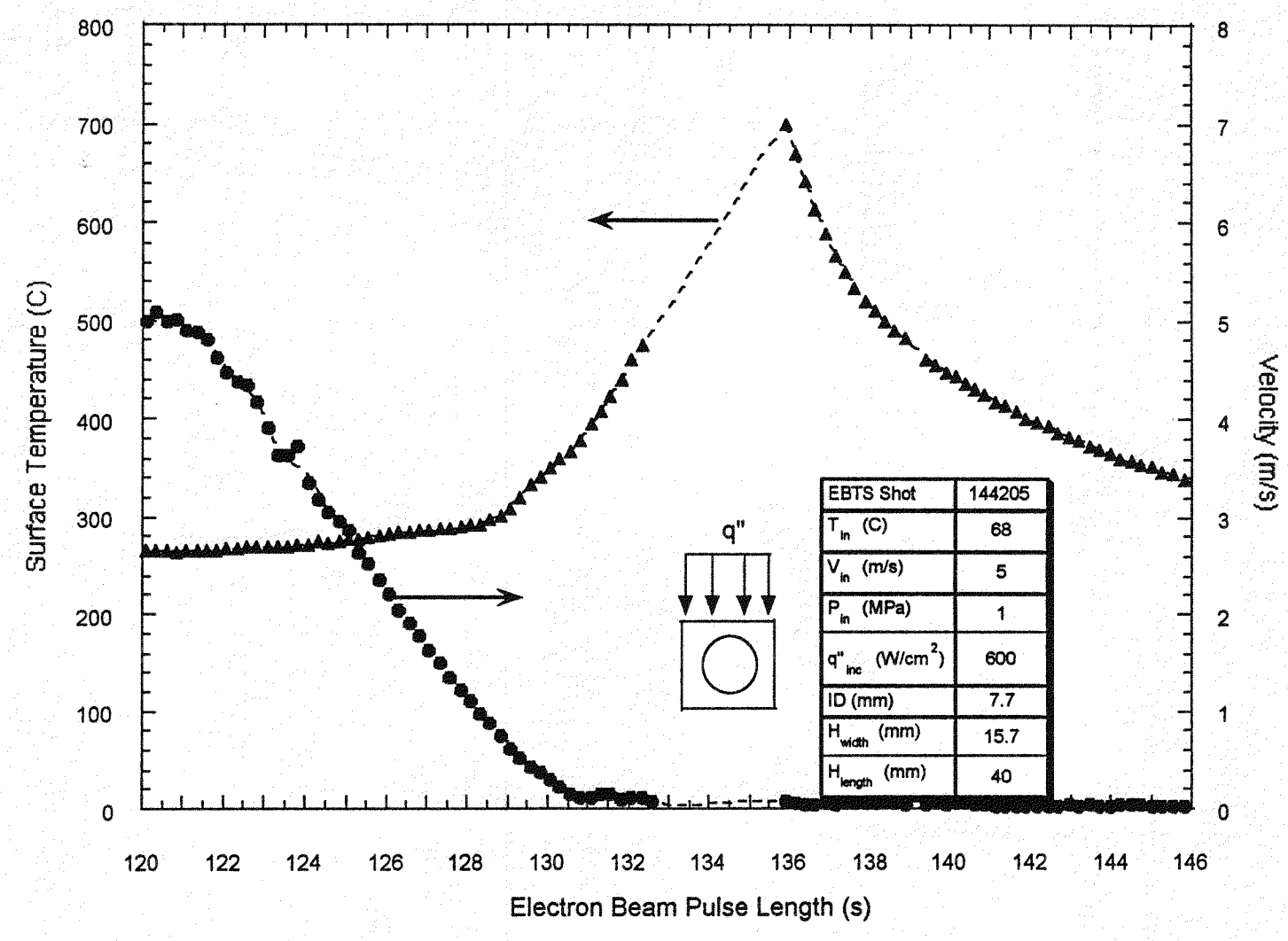

Figure 5-3: Surface (thermocouple) Temperature and Inlet Velocity Responses Used to Calculate TBO for EBTS Shot 144205.

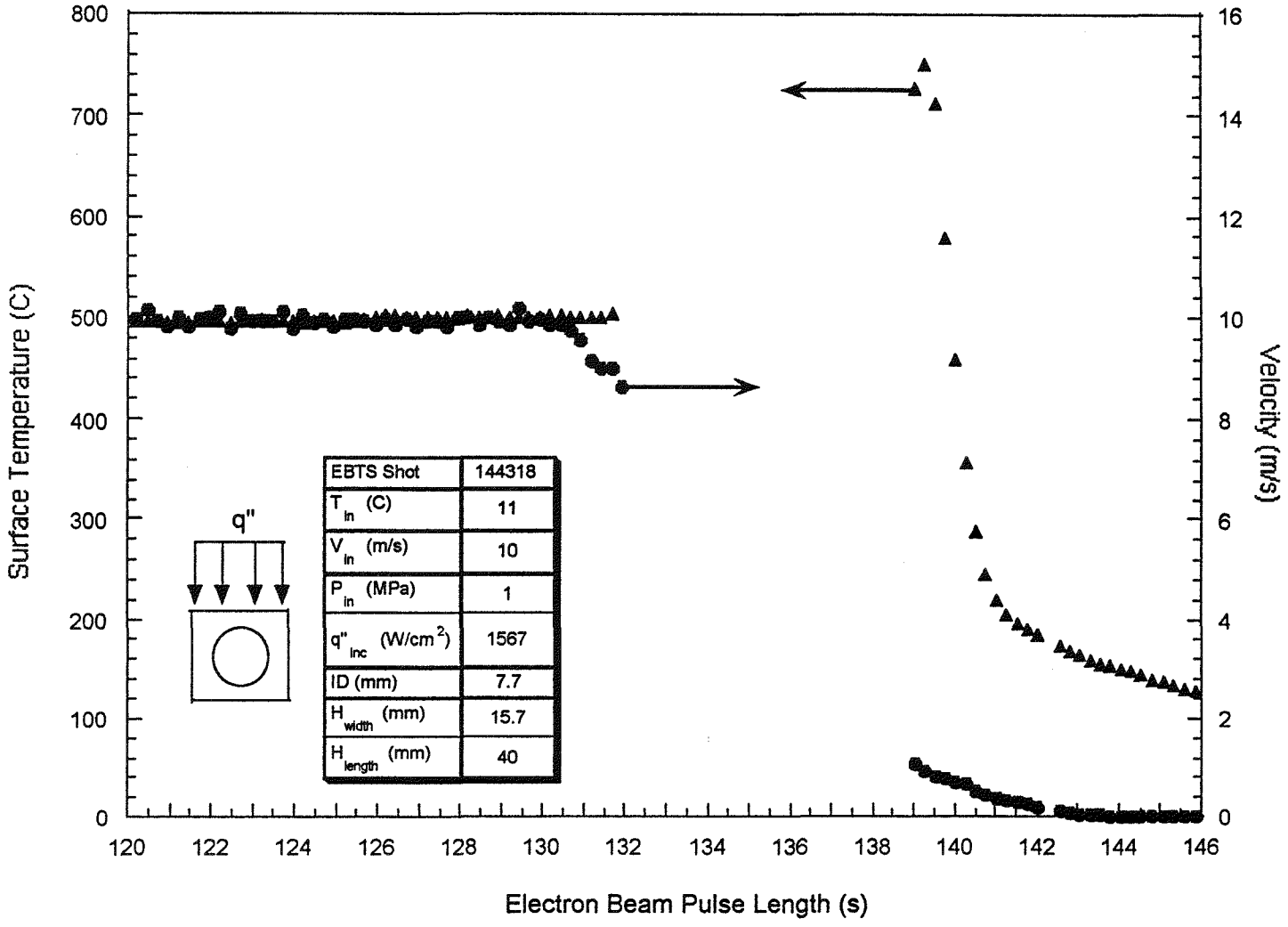

Figure 5-4: Surface (thermocouple) Temperature and Inlet Velocity Responses Used to Calculate TBO for EBTS Shot 144381.

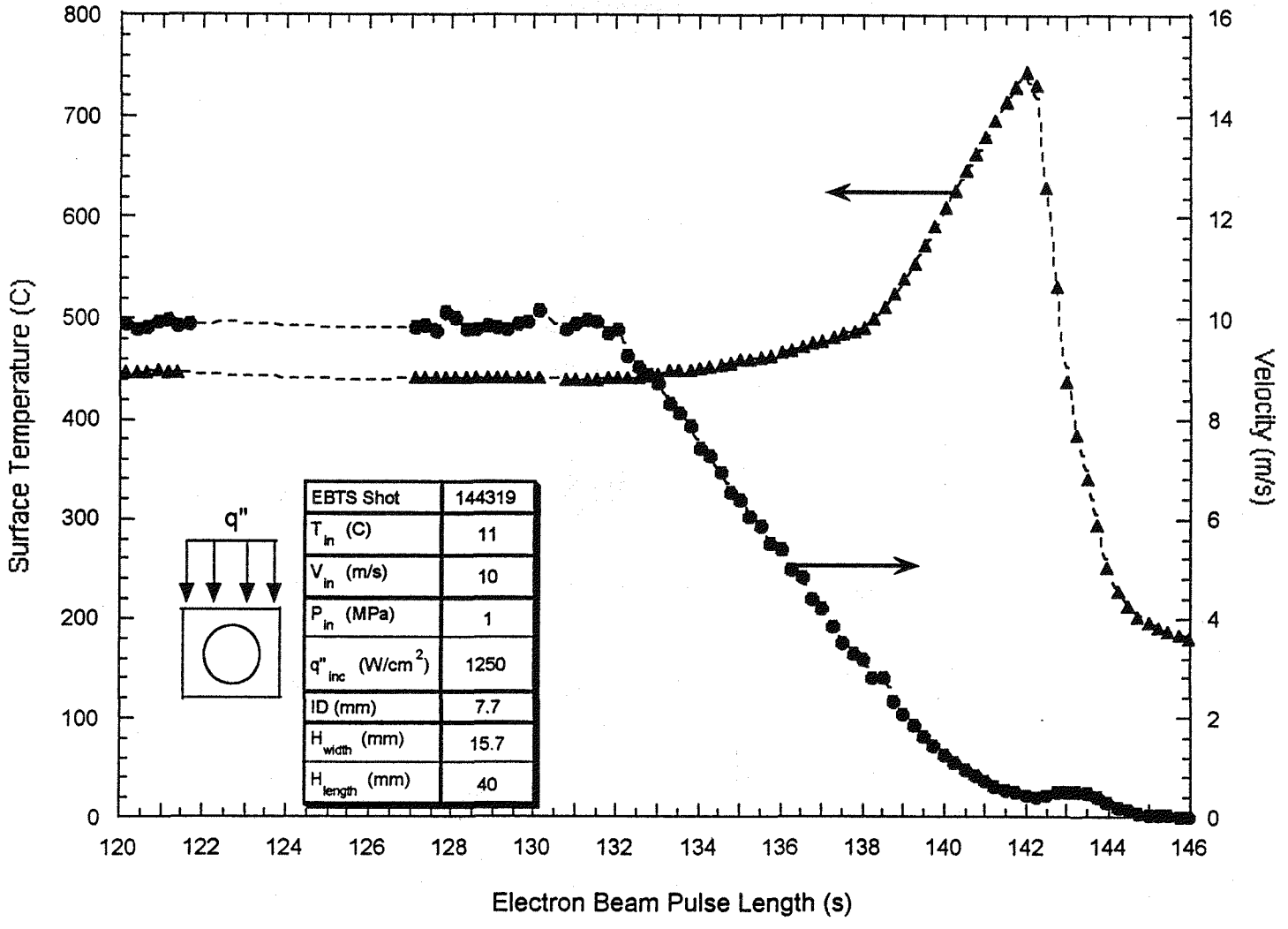

Figure 5-5: Surface (thermocouple) Temperature and Inlet Velocity Responses Used to Calculate TBO for EBTS Shot 144319.

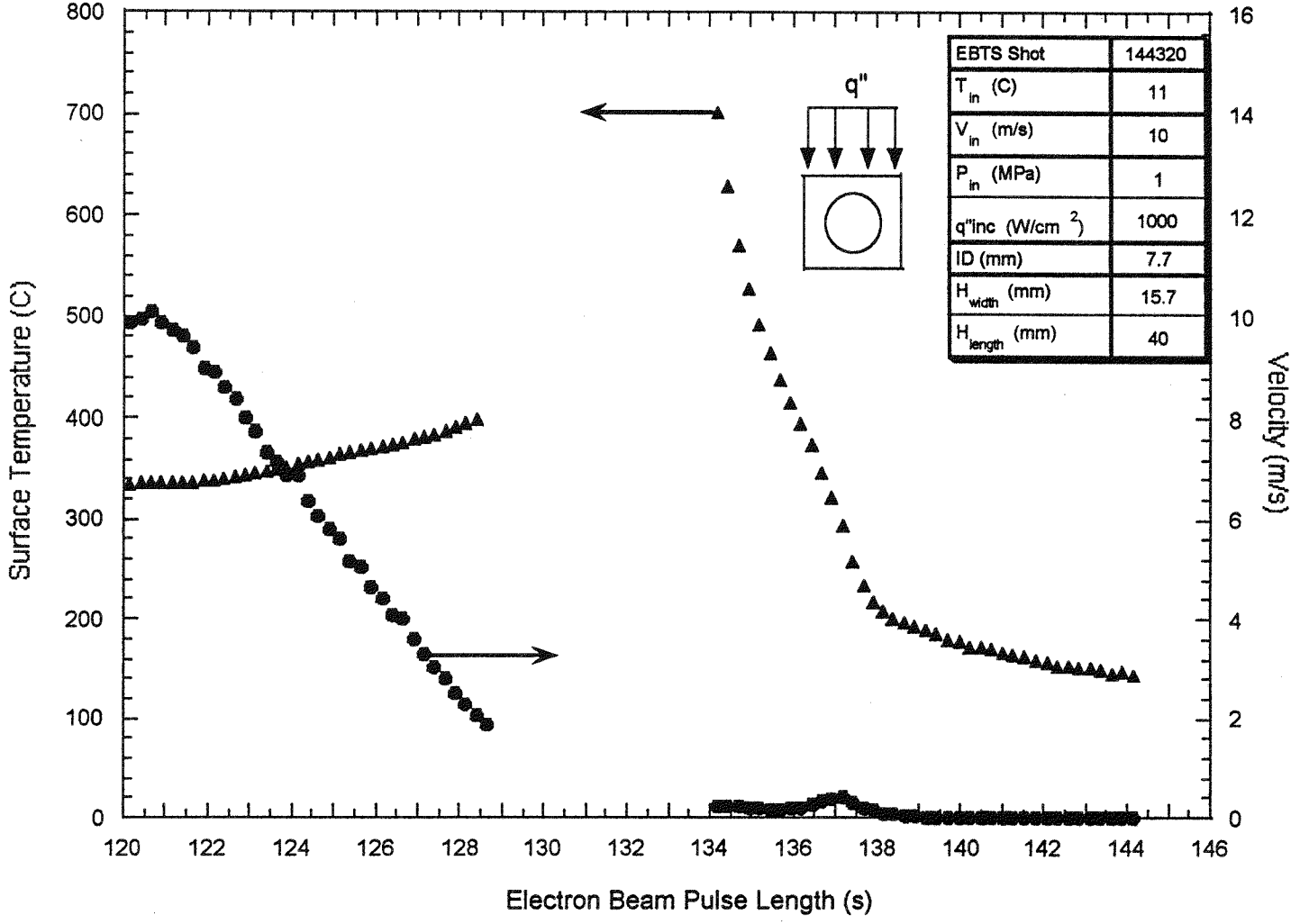

Figure 5-6: Surface (thermocouple) Temperature and Inlet Velocity Responses Used to Calculate TBO for EBTS Shot 144320.

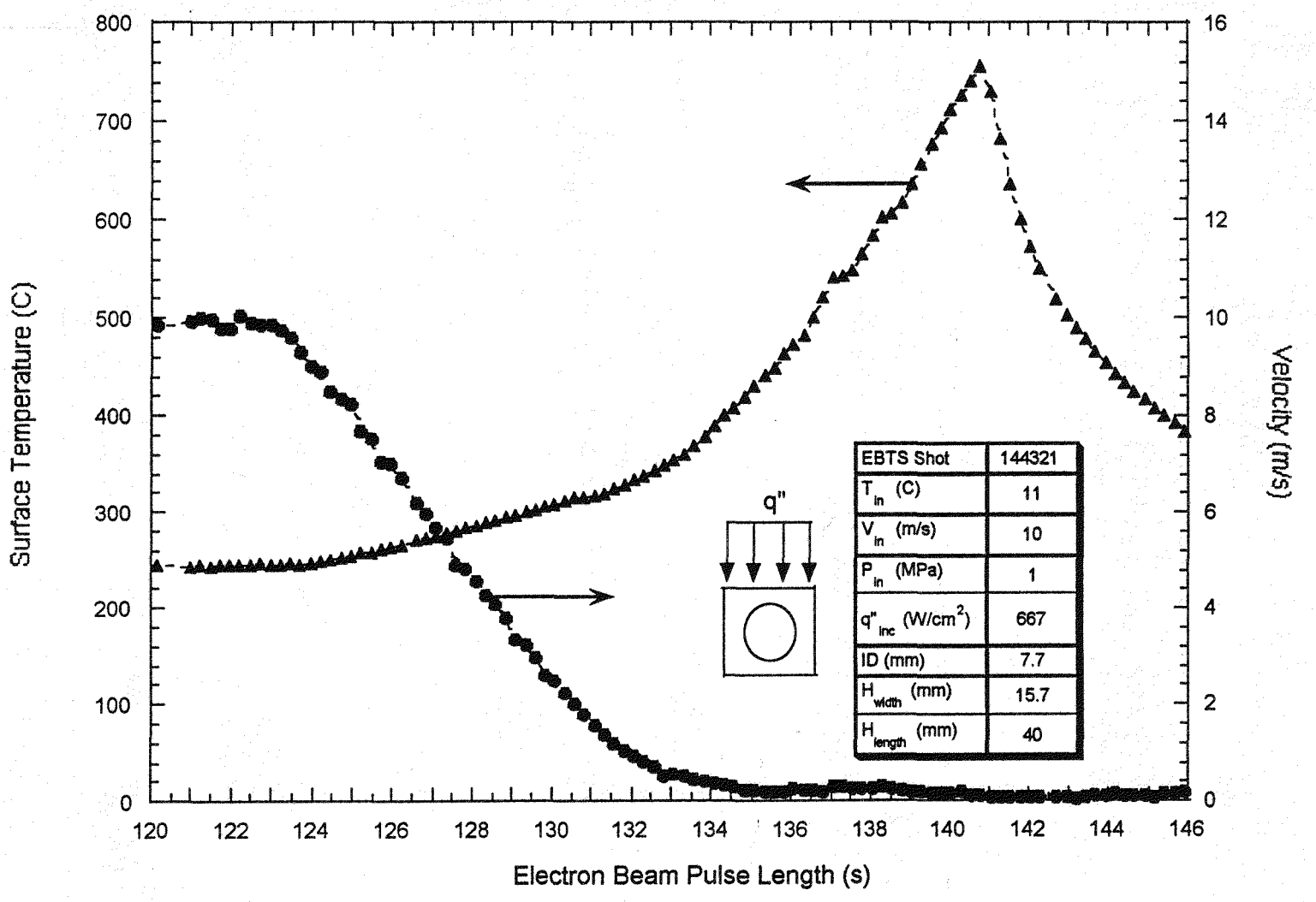

Figure 5-7: Surface (thermocouple) Temperature and Inlet Velocity Responses Used to Calculate TBO for EBTS Shot 144321.

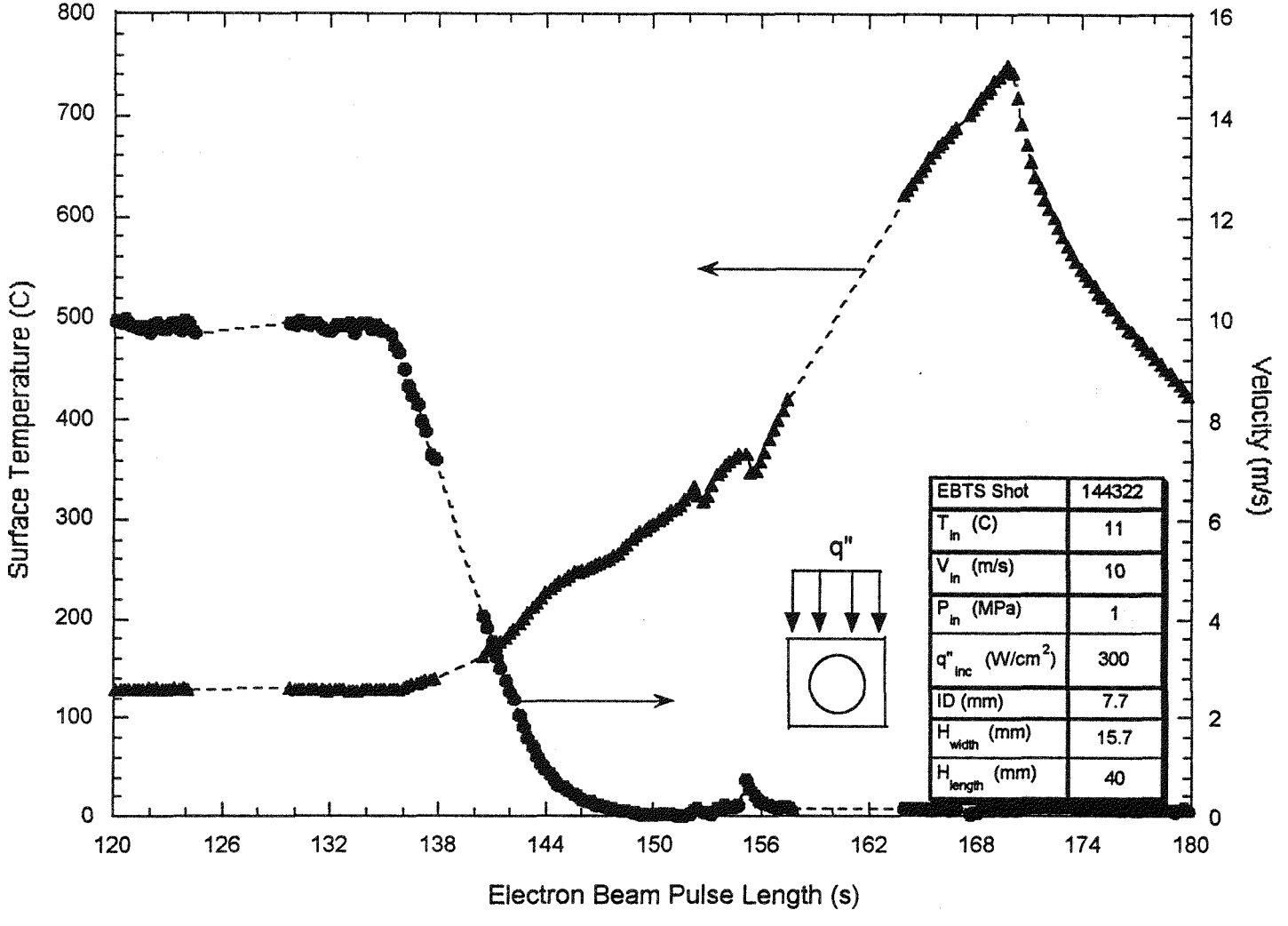

Figure 5-8: Surface (thermocouple) Temperature and Inlet Velocity Responses Used to Calculate TBO for EBTS Shot 144322.

6.0 Modeling Results

6.1 Introduction

This chapter presents the theoretical calculations of thermocouple temperatures, temperature isocontours, critical heat fluxes (CHFs), and wall heat fluxes versus tube wall angle for the experimental cases. The calculations are performed using the ABAQUS finite element analysis code and the Tong-75 CHF correlation.

The methodology and nomenclature of Schlosser and Boscary [25] are consistent with those used in this paper for the discussions on heat fluxes. Schlosser's incident burnout heat flux (IBHF) and wall critical heat flux (WCHF) are equivalent to the and , respectively. This consistency is part of an international effort to standardize thermalhydraulics terminology and thereby promote experimental data exchanges and reproducibility.

6.2 ABAQUS Calculations

6.2.1 Steady State Temperatures

Steady-state temperature profiles for a two-dimensional cross section of the cooling channel are calculated using the finite element analysis code ABAQUS [26]. The mockup was meshed with eight-noded, isoparametric, quadrilateral elements (DC2D8) with 760 nodes and 200 elements, as shown in Figure 6-1. Heat transfer from the mockup to the coolant water via forced convection is calculated by ABAQUS as a second-order equilibrium solution using a user-supplied film subroutine. This subroutine calculates the heat transfer coefficient as a function of wall temperature.

The current version of the film subroutine contains the Sieder-Tate [27] correlation for single-phase heat transfer,

$$q'' = h \cdot (T_{wall} - T_{bulk}) \cdot \left(\frac{\mu_{wall}}{\mu_{bulk}} \right) \qquad (6\text{-}1)$$

where,

h is the heat transfer coefficient, W/cm^2-°C,
T_{wall} is the wall temperature, °C,
T_{bulk} is the bulk temperature, °C,
μ_w is the viscosity at the wall, kg/m-s,
μ_b is the viscosity at the bulk, kg/m-s.

The fully developed nucleate boiling regime of heat transfer is modeled by the film subroutine through the use of the Thom [28] correlation,

$$\Delta T_s = 22.65 \cdot \sqrt[0.5]{q''} \cdot e^{-p/87} \qquad (6\text{-}2)$$

where

ΔT is the wall superheat, °C,
p is the water pressure, bars,
q" is the incident heat flux, MW/m^2.

Table 6-1 has the ABAQUS predicted surface temperatures for the steady-state conditions of each of the 8 experimental cases. The term "steady-state" is used to define the time invariant thermalhydraulic state prior to the coolant pump trip.

6.2.3 Peaking Factors

Figures 6-2 through 6-9 are plots of calculated wall temperature and q_w versus angle around the tube for the experimental cases. Essentially what the figures show is that in progressing around the circumference of the tube wall, from the top of the tube to the bottom, the heat flux and wall temperature simultaneously decrease. Thus, the highest heat flux and temperature will be at the top of the tube wall. Note that Figures 6-2 through 6-9 are for the steady-state heating of the mockup, that is, prior to the pump trip.

As shown in Figures 6-2 through 6-9, a divertor plate with a square cross-section and circular coolant channel will have an incident heat flux, q_i, that differs from the heat flux at the tube wall-to-water interface, q_w. This difference is due to a geometric focusing (or "peaking") effect. Geometrical peaking of the incident heat flux is unavoidable due to the fact that q_i is focused into a smaller heated area (upper region) at the tube wall-to-water interface. This results in q_w being greater than the corresponding q_i by typically 50%.

The heat flux peaking factor can also be calculated through finite element analysis. This peaking factor is termed the finite element peaking factor, FEPF, and is more accurate than the geometric peaking factor since it includes the mechanisms of heat transfer.

Mathematically, the FEPF is defined as:

$$\text{FEPF} \equiv \frac{q''_w}{q''_s} \qquad (6\text{-}3)$$

where,

$q''_{w(\text{peak})}$ is the peak heat flux at the channel wall,
q''_s is the surface heat flux.

As an example, consider electron beam shot number 144198,

$$\text{FEPF} = \frac{760\ \text{MW/m}^2}{580\ \text{MW/m}^2} = 1.3 \tag{6-4}$$

Table 6-2 presents the FEPFs for all of the experimental cases. In reviewing the peaking factors, EBTS shots 144201, 144321, and 144322 have peaking factors less than unity. This is believed to be a consequence of the viscosity ratio term in the Seider-Tate correlation. As the wall temperature of the mockup increases from sustained incident heating, the water viscosity at the wall, μ_w in Equation 6-1, decreases while the water viscosity of the bulk, μ_b in Equation 6-1, remains constant. Accordingly, the ratio of the two viscosities decreases and likewise lowers the heat transfer coefficient, h. In this scenario, h continues to decrease with increasing wall temperature until the wall is hot enough to induce boiling and its inherent high heat transfer capabilities.

6.2.4 Finite Element Analysis Time-to-Burnout

Table 6-3 shows the finite element analysis predicted TBO for the eight experimental cases. For the prediction, the film subroutine within ABAQUS was rewritten to set the heat transfer coefficient equal to zero (adiabatic case) when the analysis beam pulse length equals the experimental beam pulse length at the time of pump trip. It is very unrealistic to set the heat transfer coefficient to zero, but it was done to bound the worst-case scenario rather than to predict the actual thermal performance of the mockup.

The FEA TBO is calculated by subtracting the time when the coolant pump was tripped in the analysis from the time when the thermcouple temperature calcualted by ABAQUS match that of the high-temperature trip set in the experiment. Mathematically, the equation is written as:

$$t_{\text{burnout}} = t_{\text{temperature trip}} - t_{\text{pump trip}} \tag{6-5}$$

Table 6-3 shows the predicted time-to-burnout for the experimental cases.

6.3 Critical Heat Fluxes

For comparison purposes, q_i^{CHF}, is calculated for the experimental cases using the Tong-75 CHF correlation, as programmed in a Sandia internal FORTRAN code. Note that the Tong-75 correlation predicts the CHF at the wall, which according to Equation 6-3, must be divided by the FEPF to get the incident CHF, q_i^{CHF}. Table 6-4 presents the predicted incident CHF, q_i^{CHF}, for the experimental cases.

6.4 Burnout Safety Margin

The burnout safety margin (BSM) is calculated as the ratio of the incident critical heat flux, q_i^{CHF} to the applied surface heat flux, q_i.

$$\text{BSM} = \frac{q_i^{CHF}}{q_i} \tag{6-6}$$

where,

q_i^{CHF} is the incident heat flux at CHF,
q_i is the incident heat flux.

If the BSM is less than one, it is likely that the mockup will fail before the requested incident heat flux is reached. A BSM greater than unity suggests that the requested incident heat flux will not cause high heat flux burnout failure of the mockup. All of the test cases have BSMs greater than unity since it was desired that steady-state heating of the mockup did not cause CHF conditions.

Figures 6-10 through 6-17 show the experimentally measured surface temperature and predicted BSM as a function of beam pulse time. In the figures the unity value of the BSM is approximated by the center of the cross hair. The BSM is determined by calculating the self-consistent CHF (Tong-75 correlation) at the steady-state inlet conditions for each experimental case and dividing this value by the incident heat flux for the case.

During the simulated LOFA, after the coolant pump is tripped, the CHF values change since they are a function of inlet velocity and that velocity is decreasing. Accordingly, CHF values for specific values of the decreasing velocity response are calculated and divided by the uniform incident heat flux being applied after the pump trip. This change in post-pump trip CHF is responsible for the BSM curve decreasing as a function of time in the figures.

It was anticipated that the BSM would decline to 1.0 as the high-temperature setpoint was reached during the experiment; however, the data plots do not show this trend. In EBTS shots 144201, 144205, 144321, and 144322 (Figures 6-11, 6-12, 6-16, and 6-17 respectively), the BSM curves reached their minimum before the high-temperature trips occurred. Currently, it is conjectured that the BSM is able to achieve such low values without mockup failure because of the additional heat conduction paths provided by the relatively thick (3 mm) tube walls.

Table 6-1. ABAQUS Predicted Thermocouple Temperatures

	Water Inlet Conditions			Experimental	Predicted
EBTS Shot	Pressure (MPa)	Velocity (m/s)	Temp. (°C)	$q_{incident}$ (MW/m^2)	Thermocouple Temp. (°C)
144198	1	1	68	6	291
144201	1	10	68	6	234
144205	1	5	68	6	275
144318	1	10	11	16	433
144319	1	10	11	15	384
144320	1	10	11	10	343
144321	1	10	11	7	282
144322	1	10	11	3	137

Table 6-2. Finite Element Peaking Factor Calculated by ABAQUS

	Water Inlet Conditions			Steady State		
EBTS Shot	Pressure (MPa)	Velocity (m/s)	Temp. (°C)	$q_{incident}$ (MW/m^2)	q_{wall} (MW/m^2)	FEPF
144198	1	1	68	580	760	1.3
144201	1	10	68	580	550	0.9
144205	1	5	68	600	690	1.1
144318	1	10	11	1567	2100	1.3
144319	1	10	11	1250	1650	1.3
144320	1	10	11	1000	1300	1.3
144321	1	10	11	667	725	1.1
144322	1	10	11	300	240	0.8

Table 6-3. ABAQUS Predicted Time-to-Burnout with $h_{film} = 0$ at Pump Trip

	Water Inlet Conditions			Predicted
EBTS Shot	Pressure (MPa)	Velocity (m/s)	Temp. (°C)	TBO (s)
144198	1	1	68	3
144201	1	10	68	3.5
144205	1	5	68	3.1
144318	1	10	11	0.6
144319	1	10	11	1
144320	1	10	11	1.5
144321	1	10	11	2.5
144322	1	10	11	8

Table 6-4. Predicted CHF Limits

	Inlet Conditions			CHF: Tong-75	
EBTS Shot	Pressure (MPa)	Velocity (m/s)	Temp. (°C)	Surface (MW/m^2)	Wall (MW/m^2)
144198	1	1	68	4	8
144201	1	10	68	12	24
144205	1	5	68	8.7	17
144318	1	10	11	21.5	43
144319	1	10	11	21.5	43
144320	1	10	11	21.5	43
144321	1	10	11	21.5	43
144322	1	10	11	21.5	43

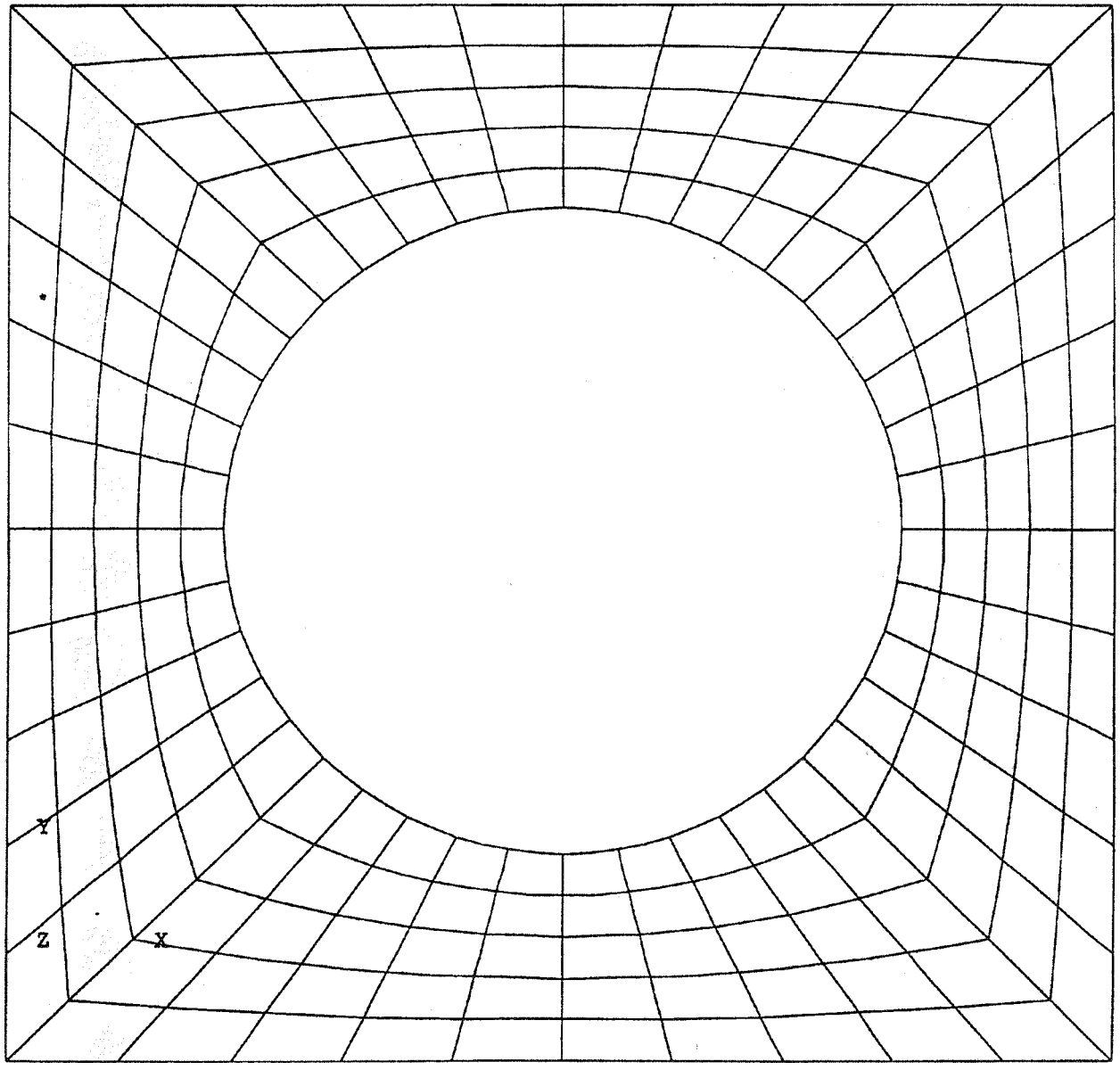

Figure 6-1. PATRAN Finite Element Mesh of Mockup - 200 Elements and 760 Nodes.

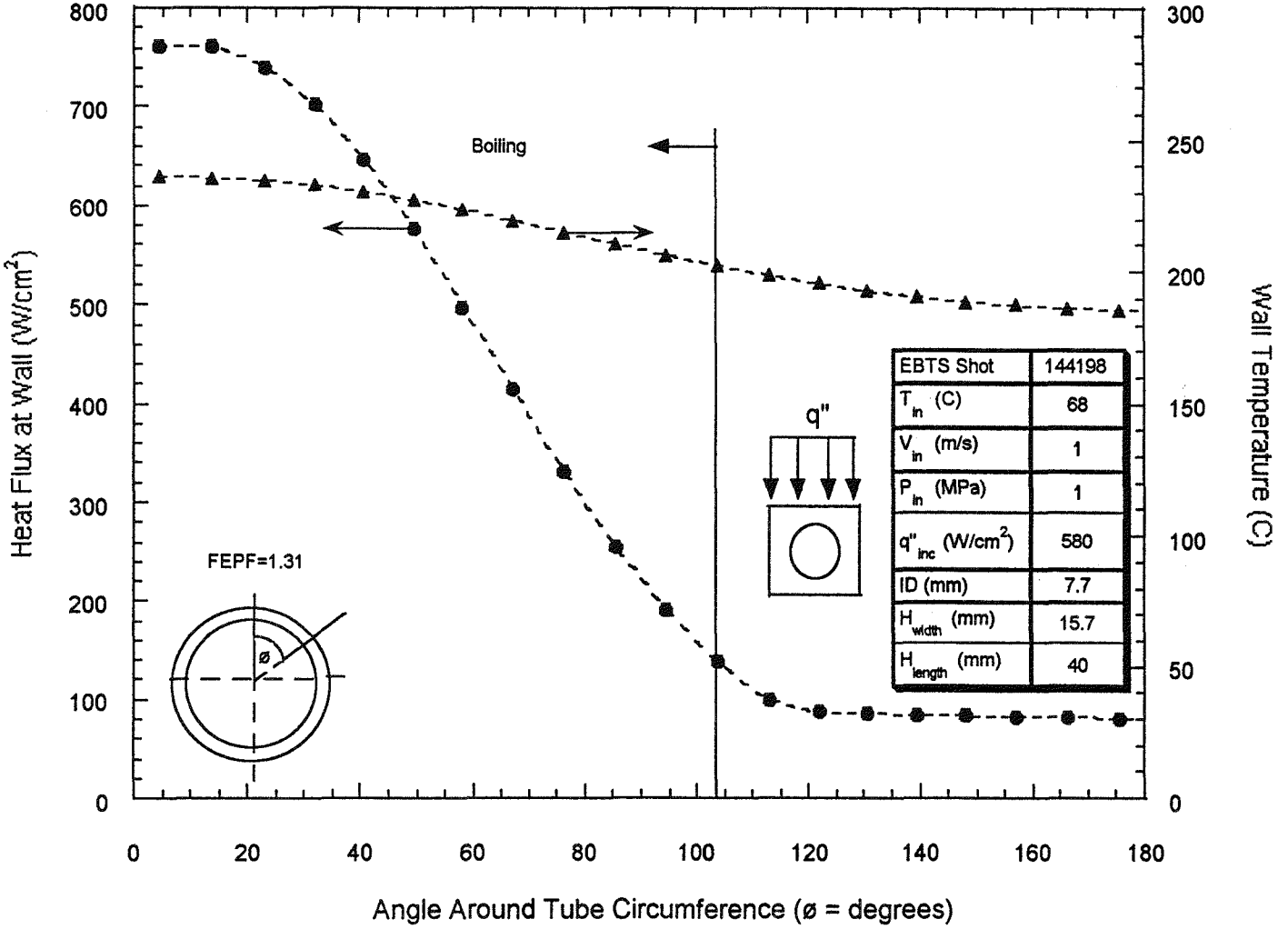

Figure 6-2: Predicted Angular Temperature and Heat Flux Distributions at the Channel Wall for EBTS Shot 144198.

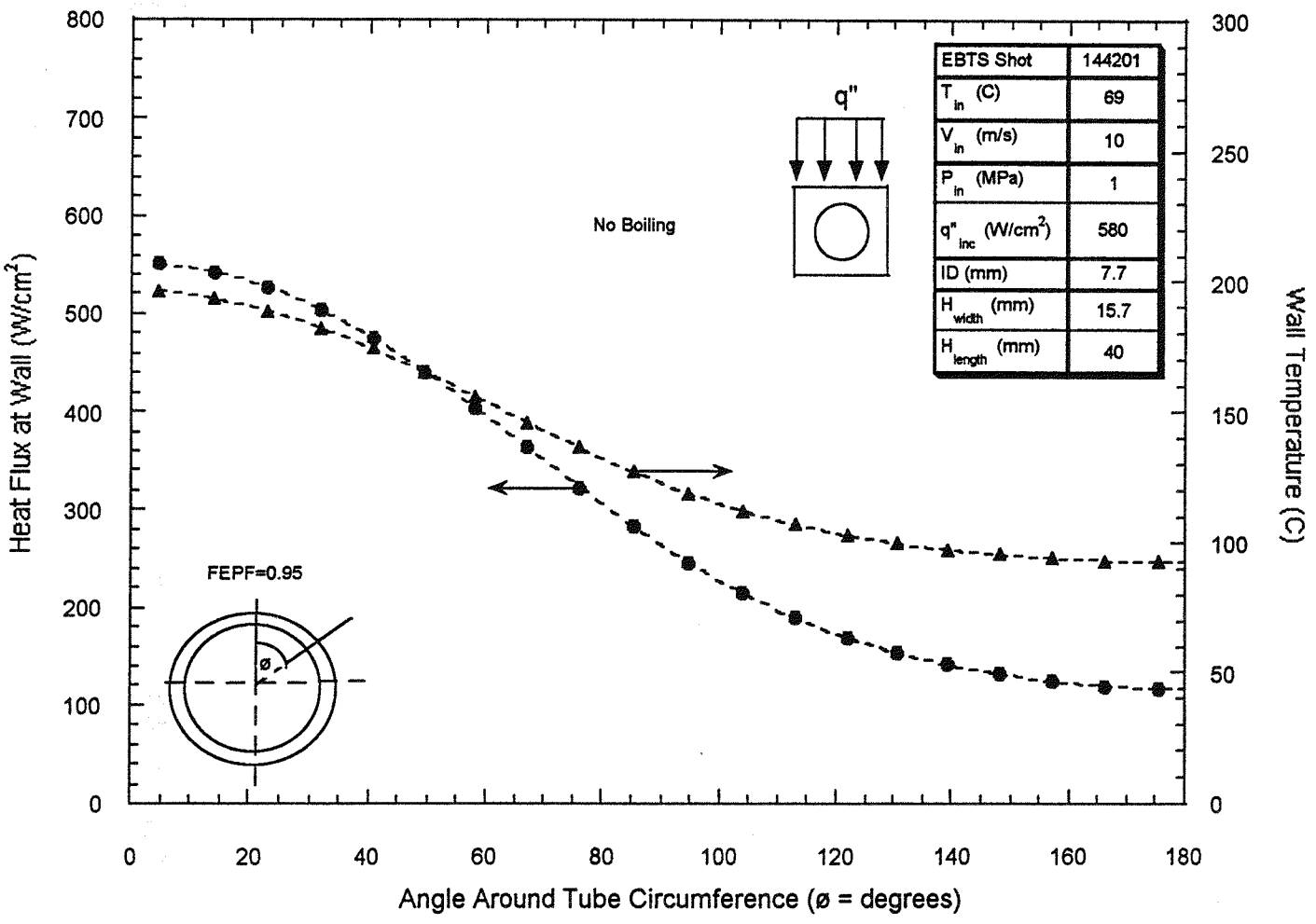

Figure 6-3: Predicted Angular Temperature and Heat Flux Distributions at the Channel Wall for EBTS Shot 144201.

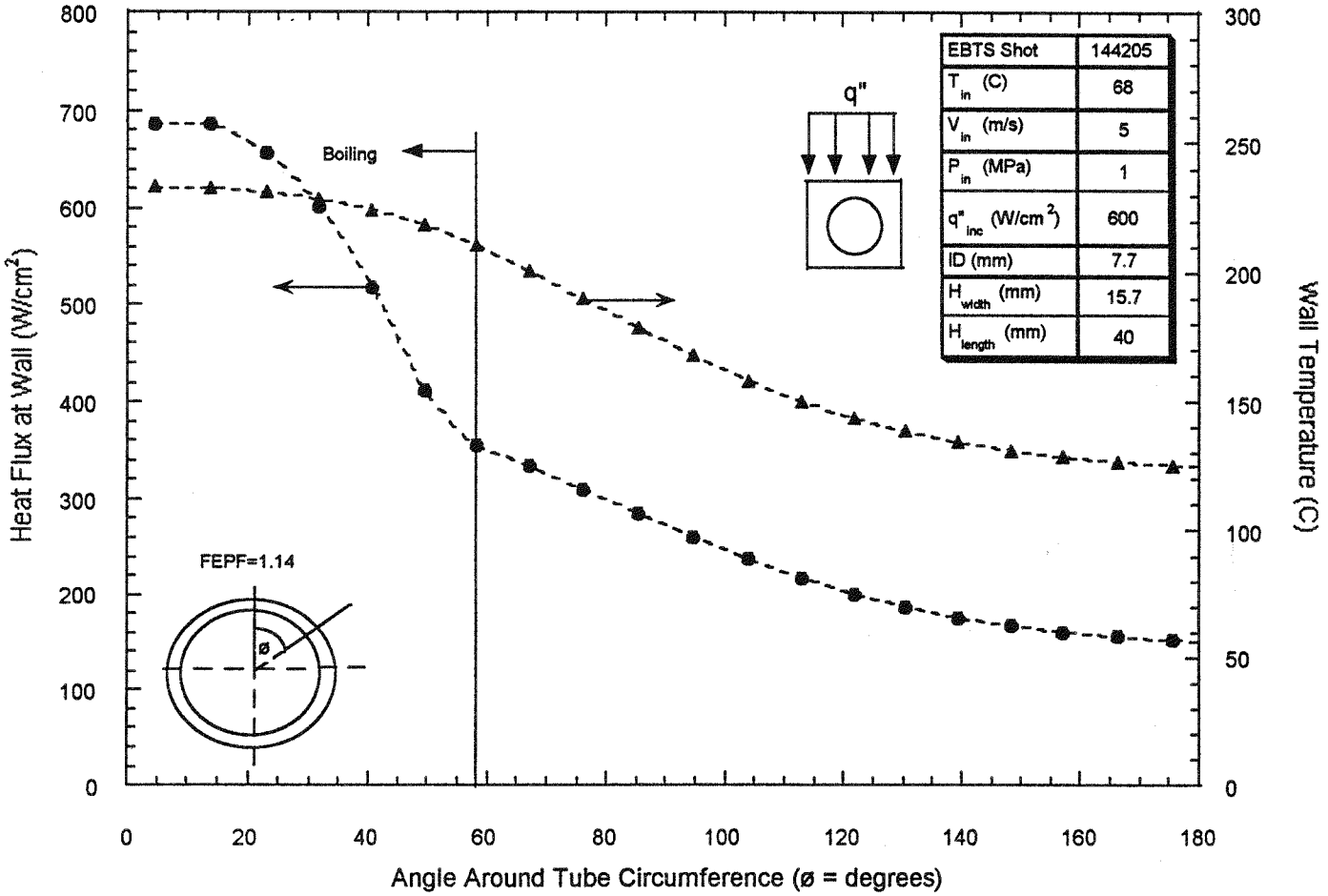

Figure 6-4: Predicted Angular Temperature and Heat Flux Distributions at the Channel Wall for EBTS Shot 144205.

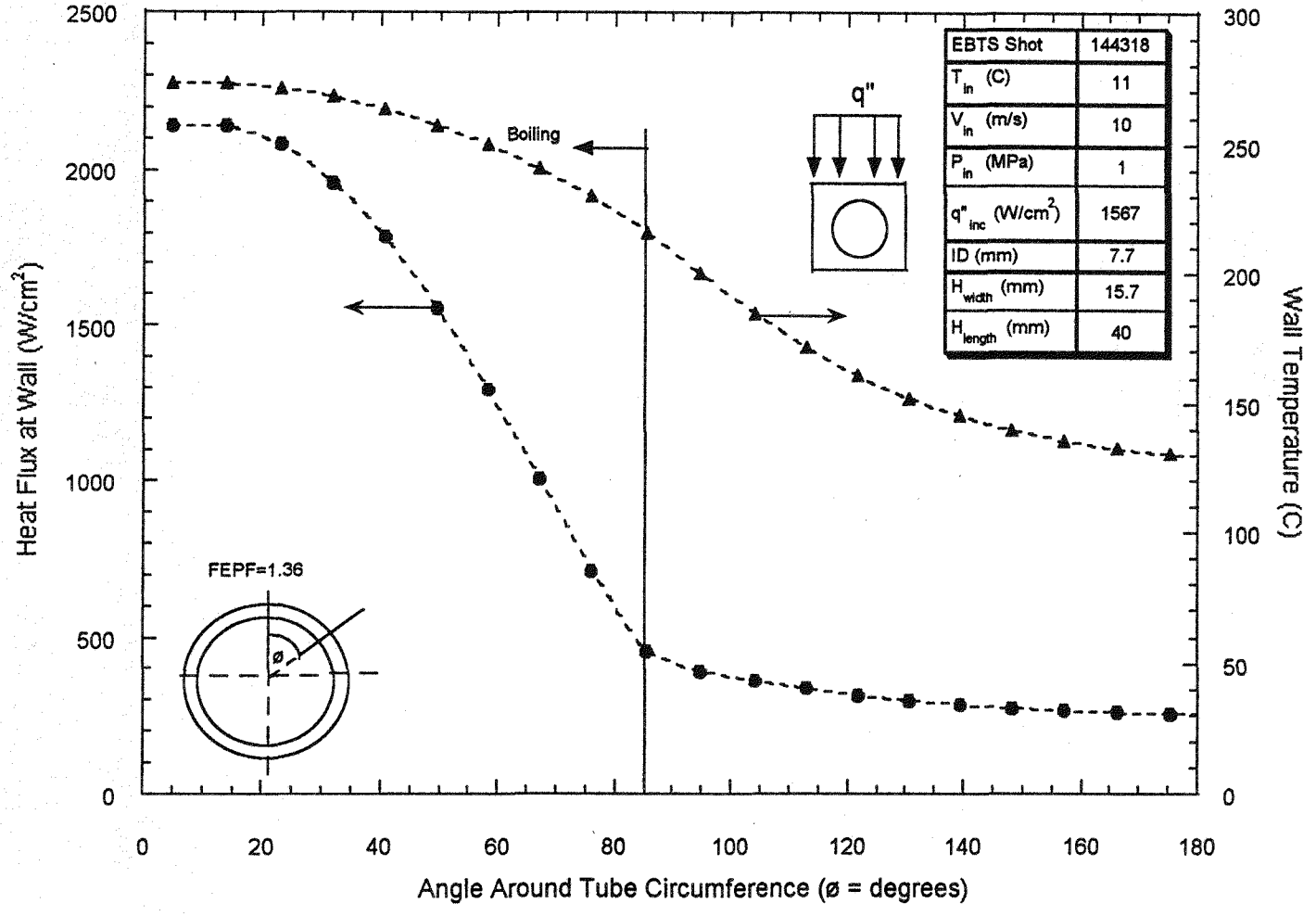

Figure 6-5: Predicted Angular Temperature and Heat Flux Distributions at the Channel Wall for EBTS Shot 144318.

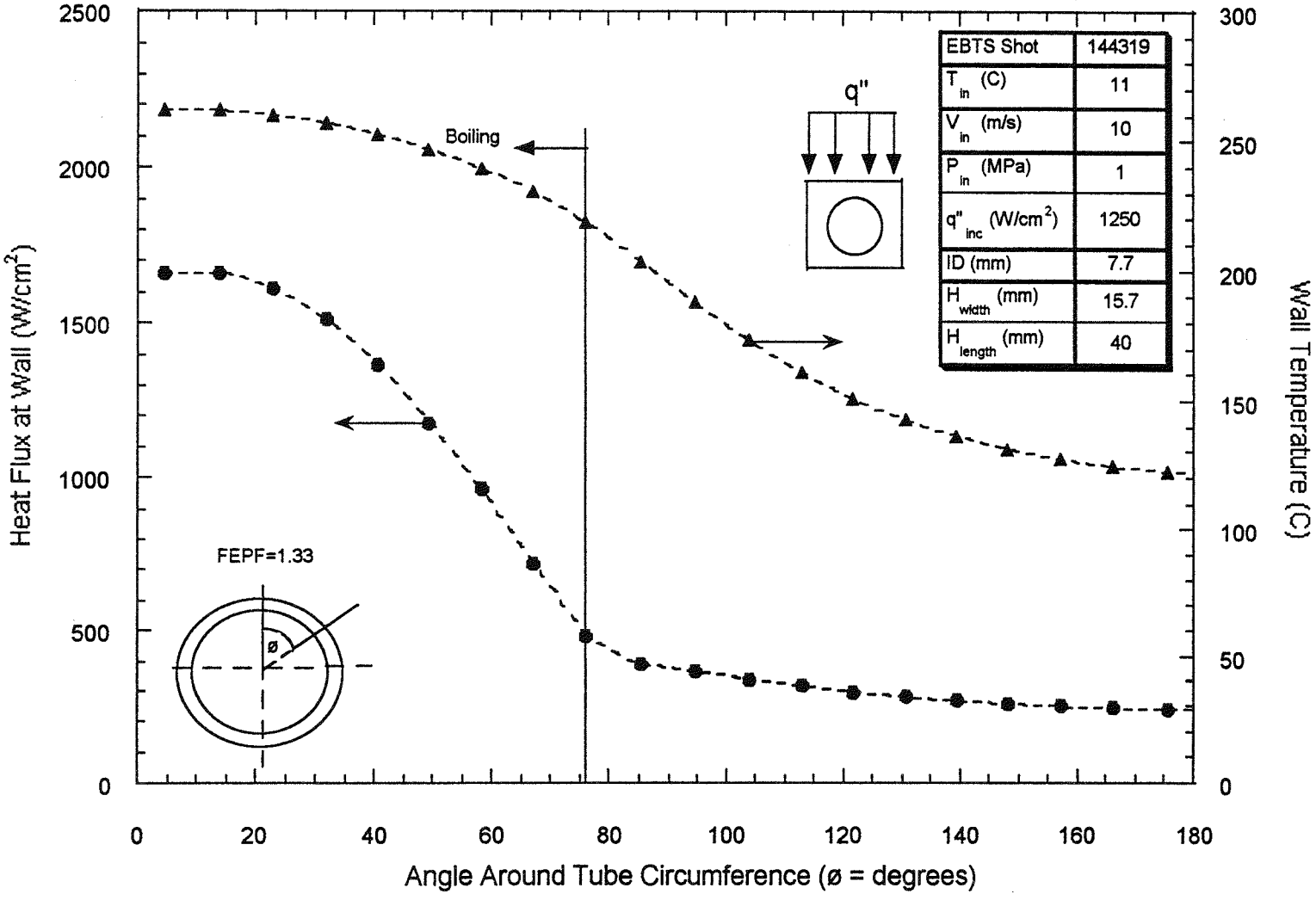

Figure 6-6: Predicted Angular Temperature and Heat Flux Distributions at the Channel Wall for EBTS Shot 144319.

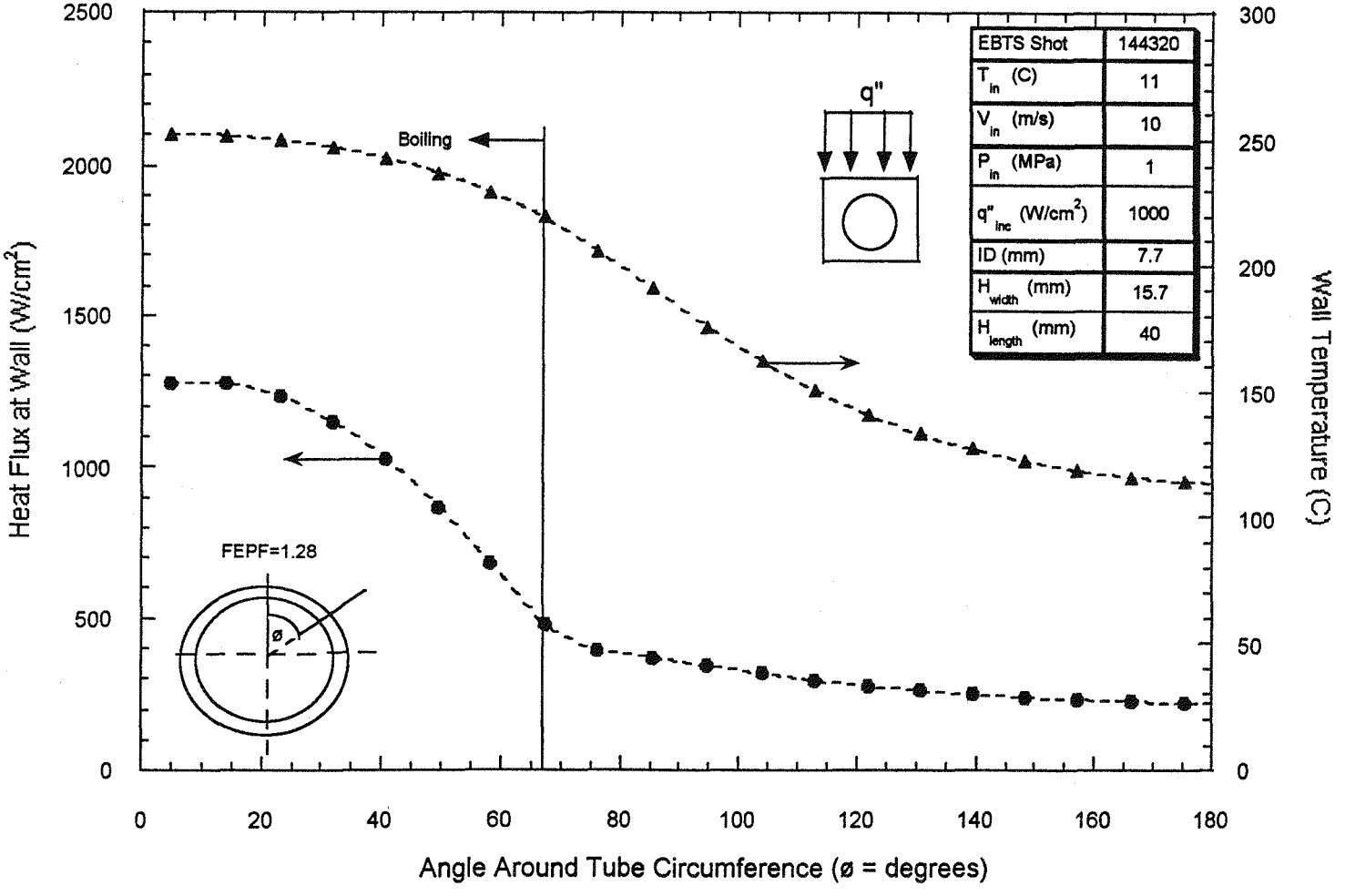

Figure 6-7: Predicted Angular Temperature and Heat Flux Distributions at the Channel Wall for EBTS Shot 144320.

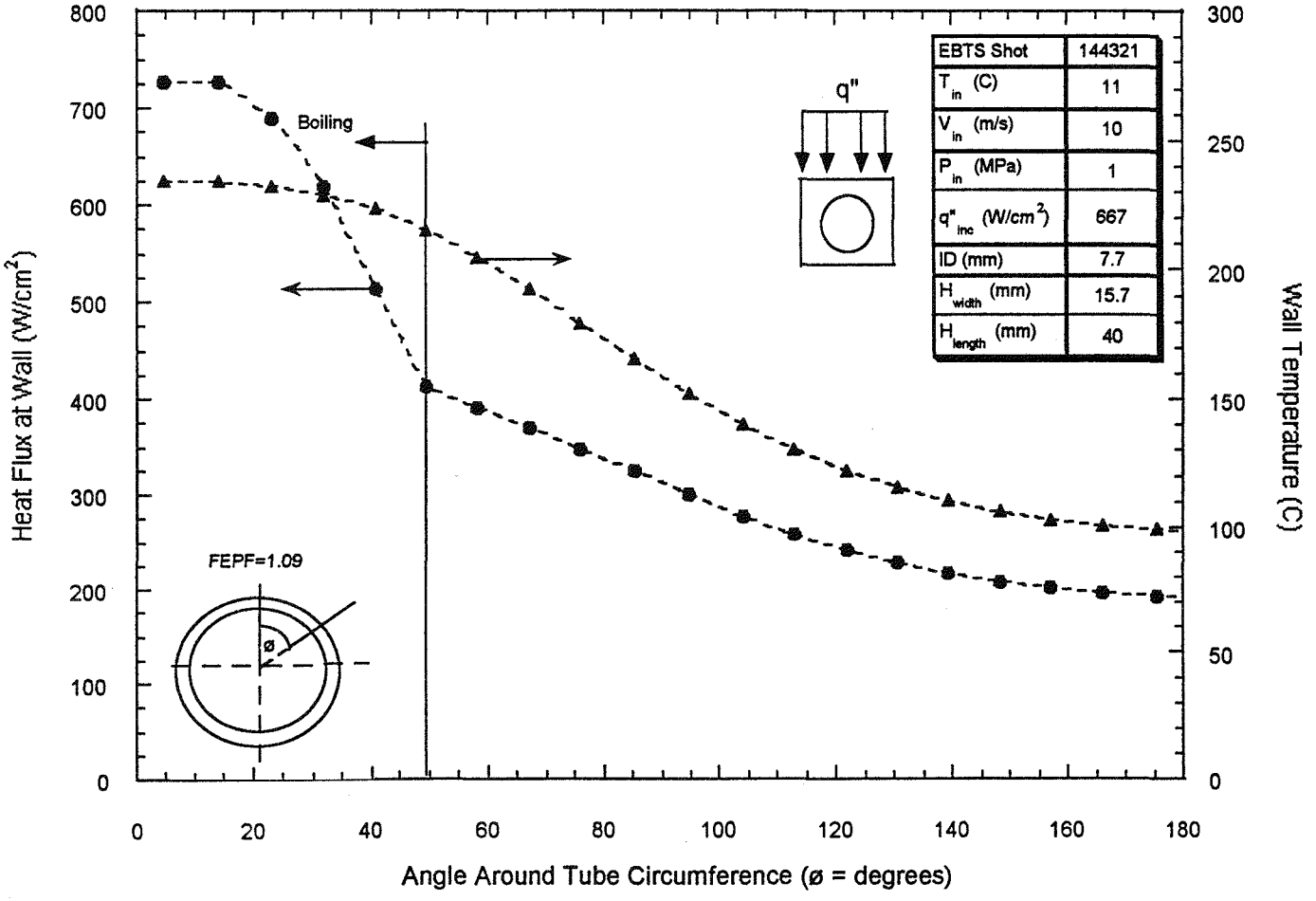

Figure 6-8: Predicted Angular Temperature and Heat Flux Distributions at the Channel Wall for EBTS Shot 144321.

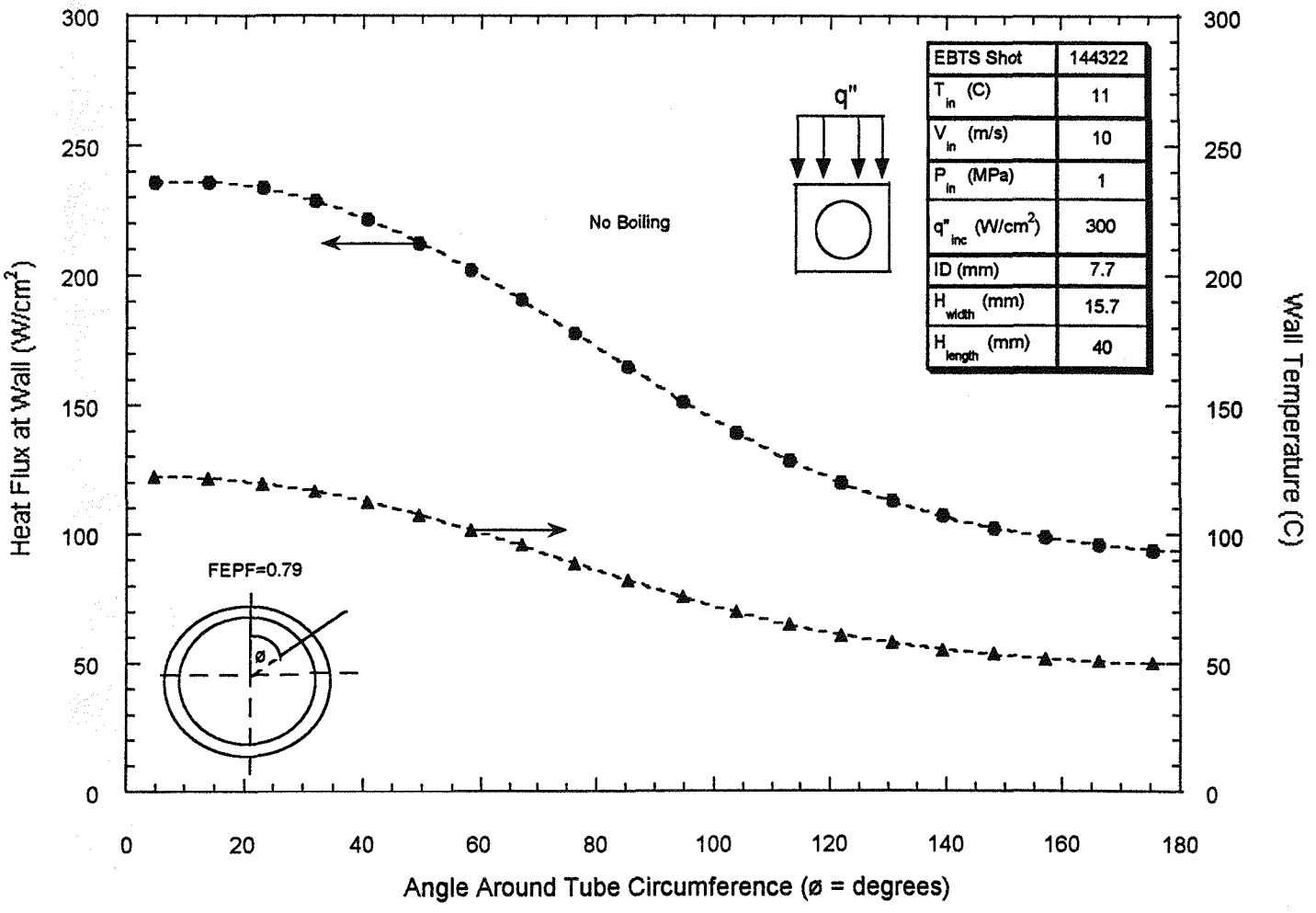

Figure 6-9: Predicted Angular Temperature and Heat Flux Distributions at the Channel Wall for EBTS Shot 144322.

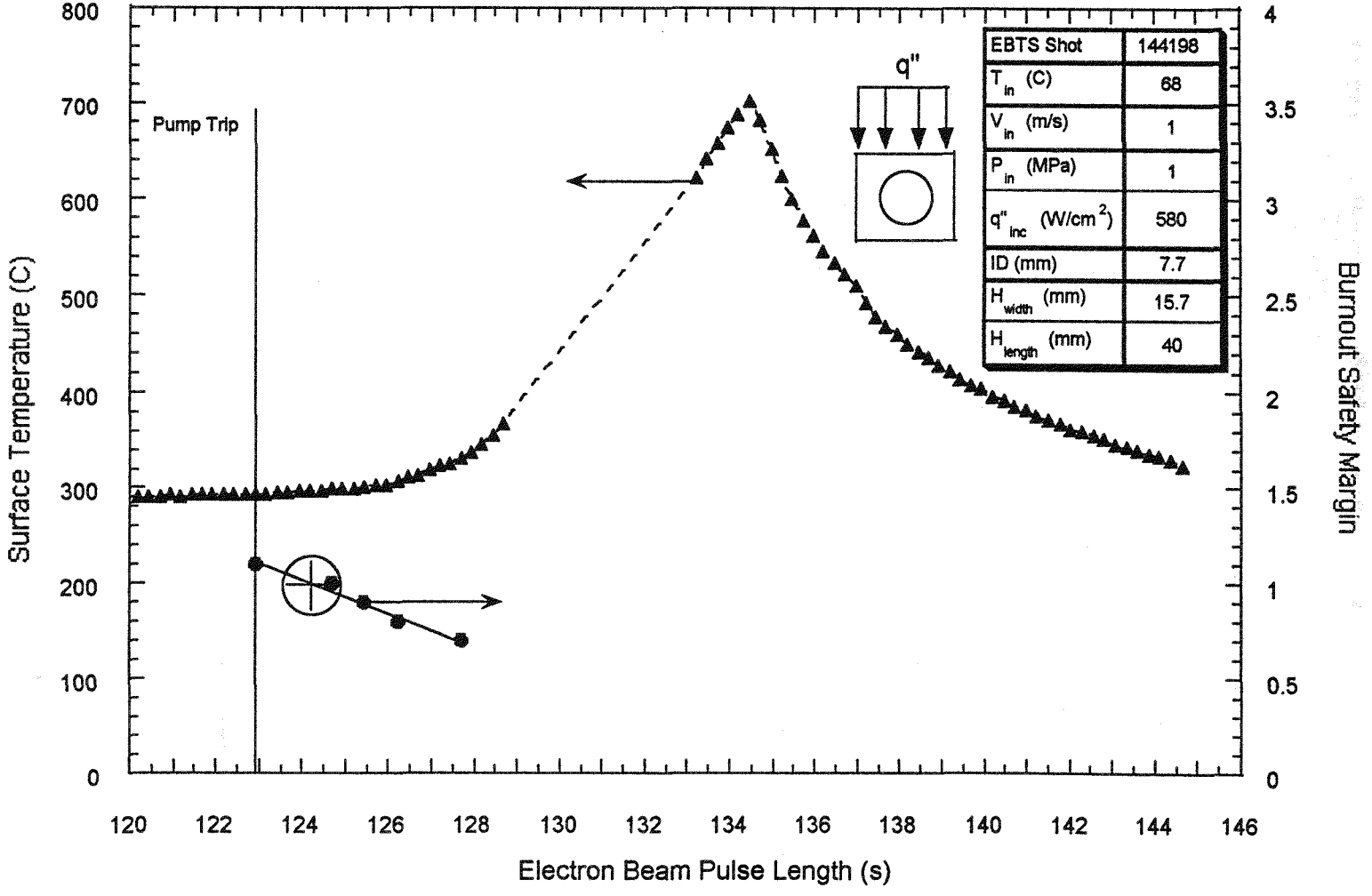

Figure 6-10: Comparison of the Burnout Safety Margin Decline and the Surface Temperature Rise During the Experimental Pump Trip for EBTS Shot 144198.

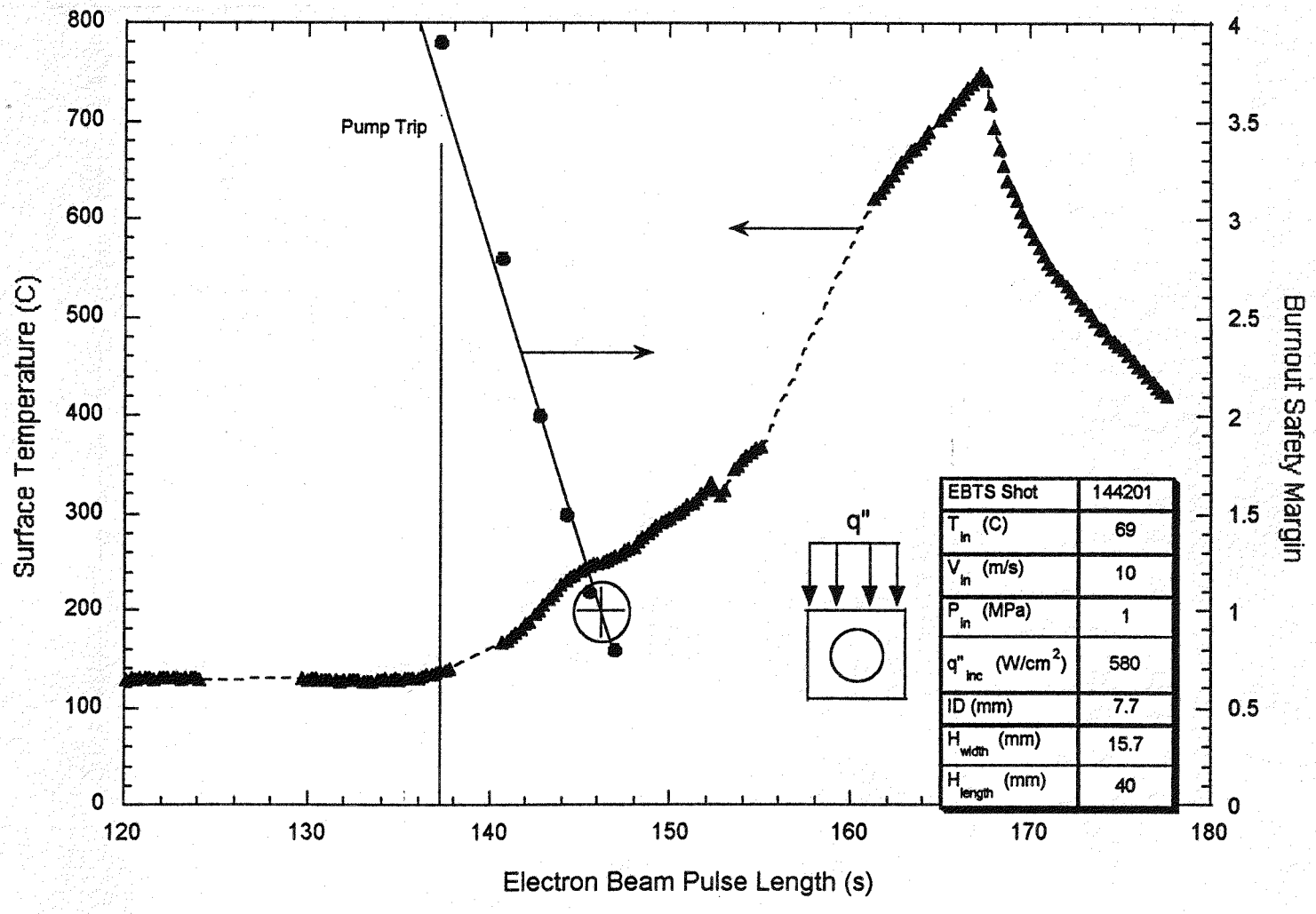

Figure 6-11: Comparison of the Burnout Safety Margin Decline and the Surface Temperature Rise During the Experimental Pump Trip for EBTS Shot 144201.

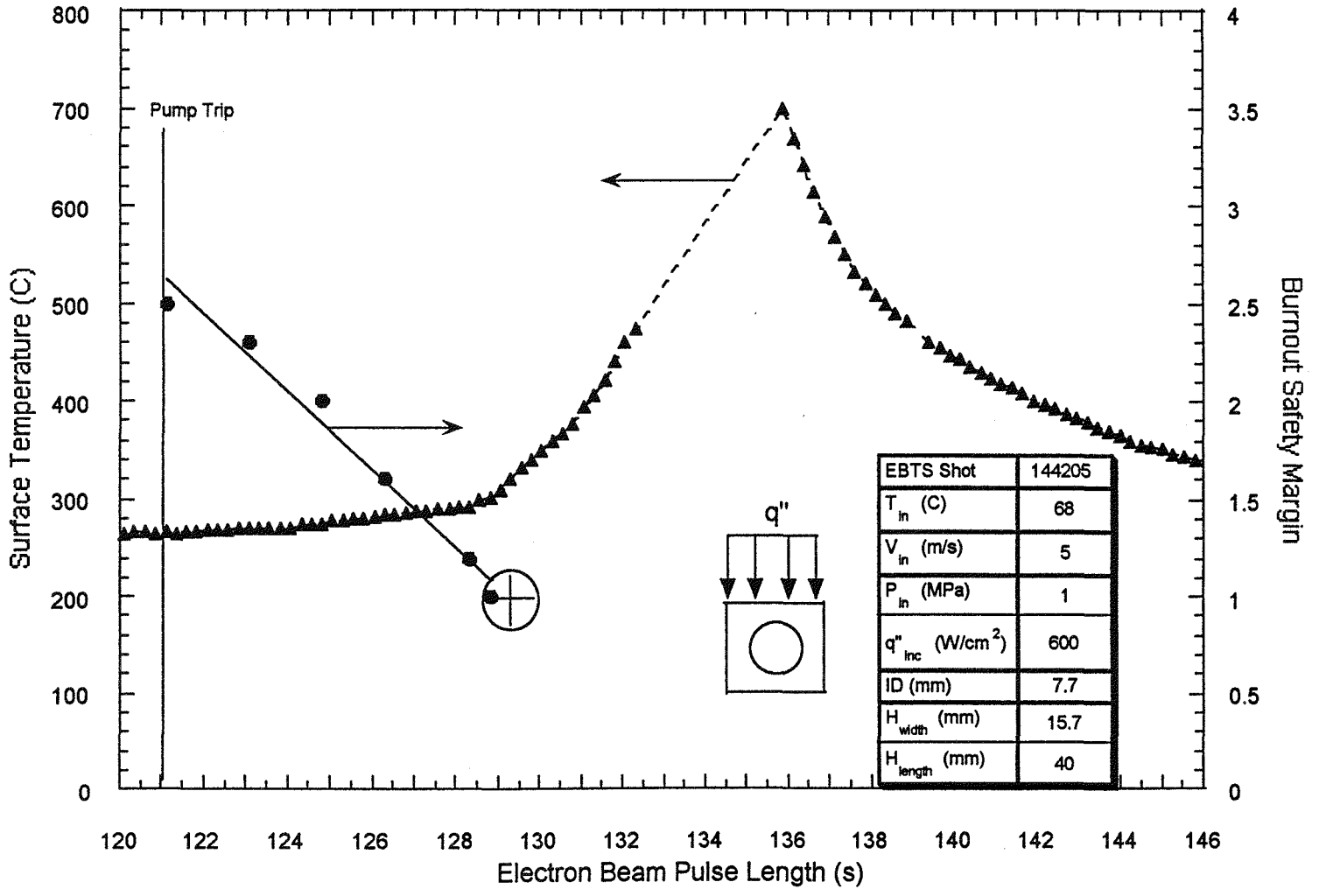

Figure 6-12: Comparison of the Burnout Safety Margin Decline and the Surface Temperature Rise During the Experimental Pump Trip for EBTS Shot 144205.

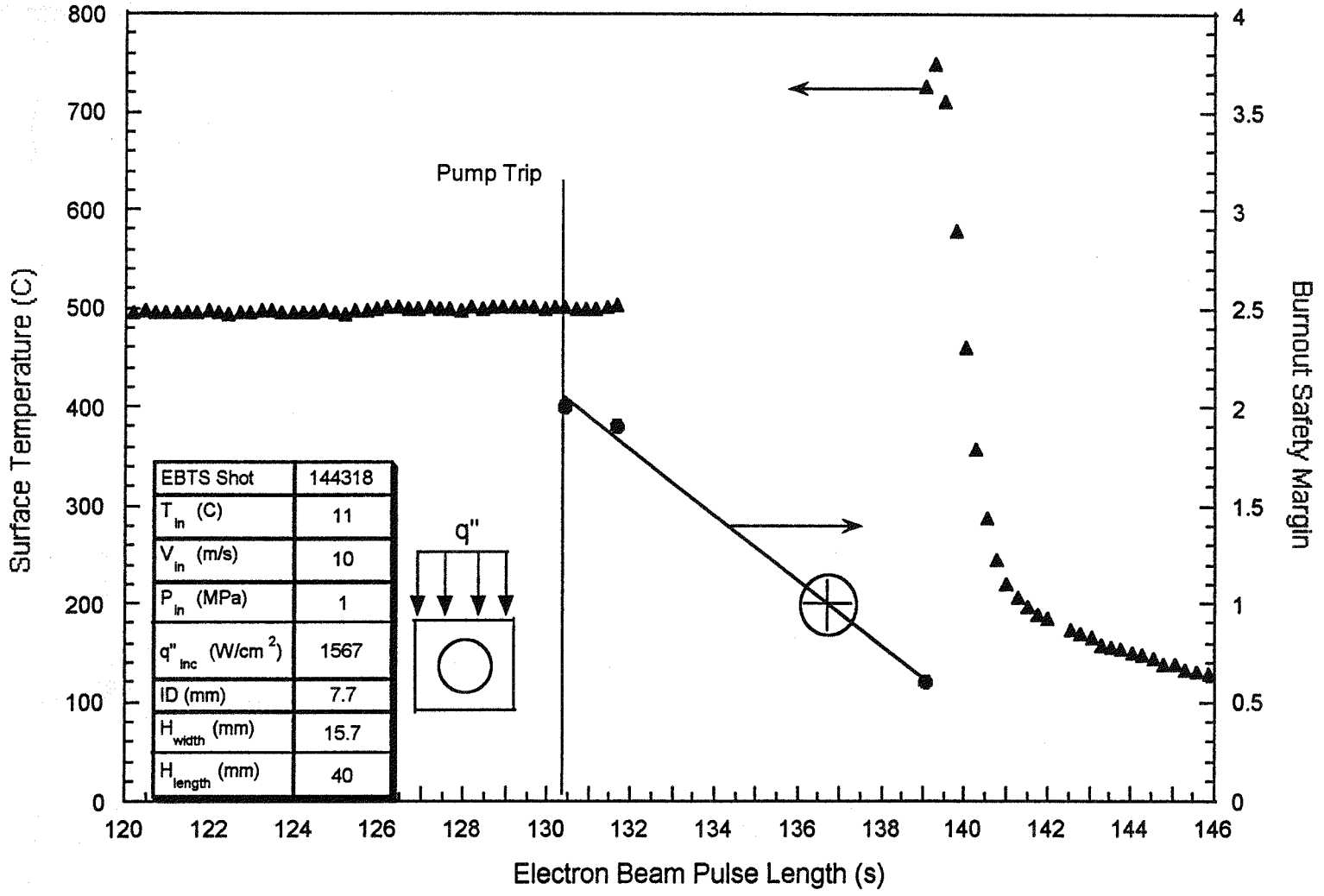

Figure 6-13: Comparison of the Burnout Safety Margin Decline and the Surface Temperature Rise During the Experimental Pump Trip for EBTS Shot 144318.

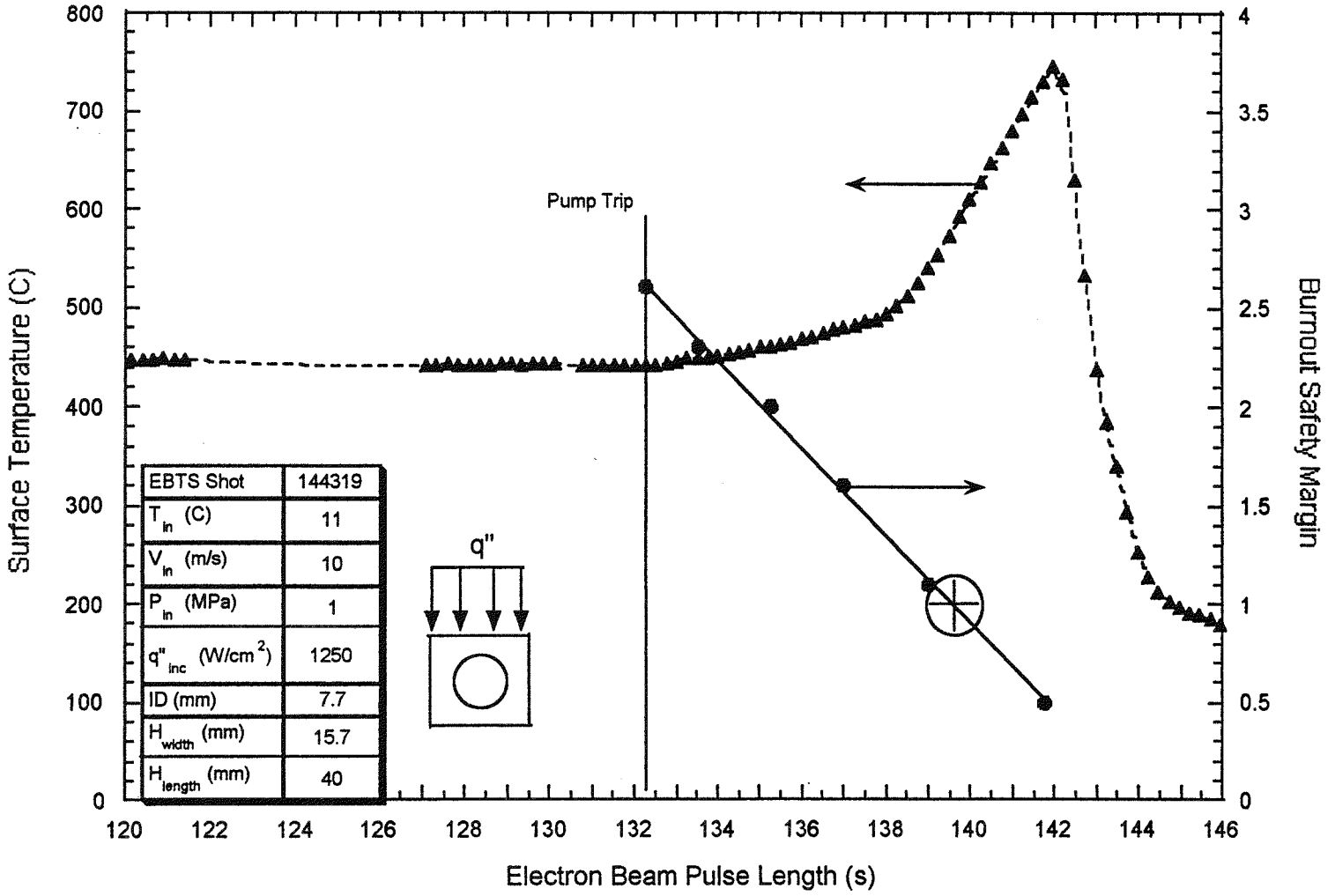

Figure 6-14: Comparison of the Burnout Safety Margin Decline and the Surface Temperature Rise During the Experimental Pump Trip for EBTS Shot 144319.

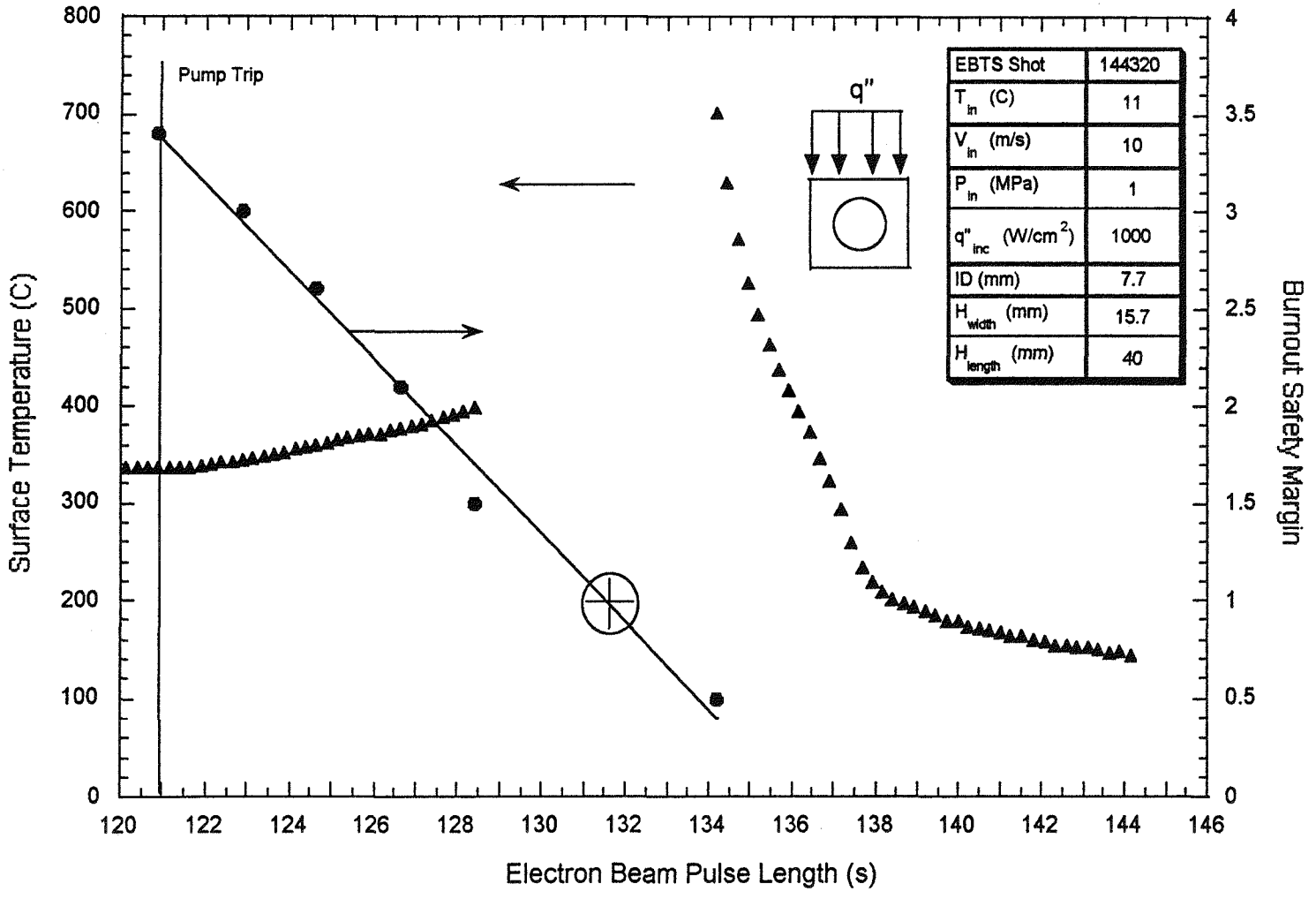

Figure 6-15: Comparison of the Burnout Safety Margin Decline and the Surface Temperature Rise During the Experimental Pump Trip for EBTS Shot 144320.

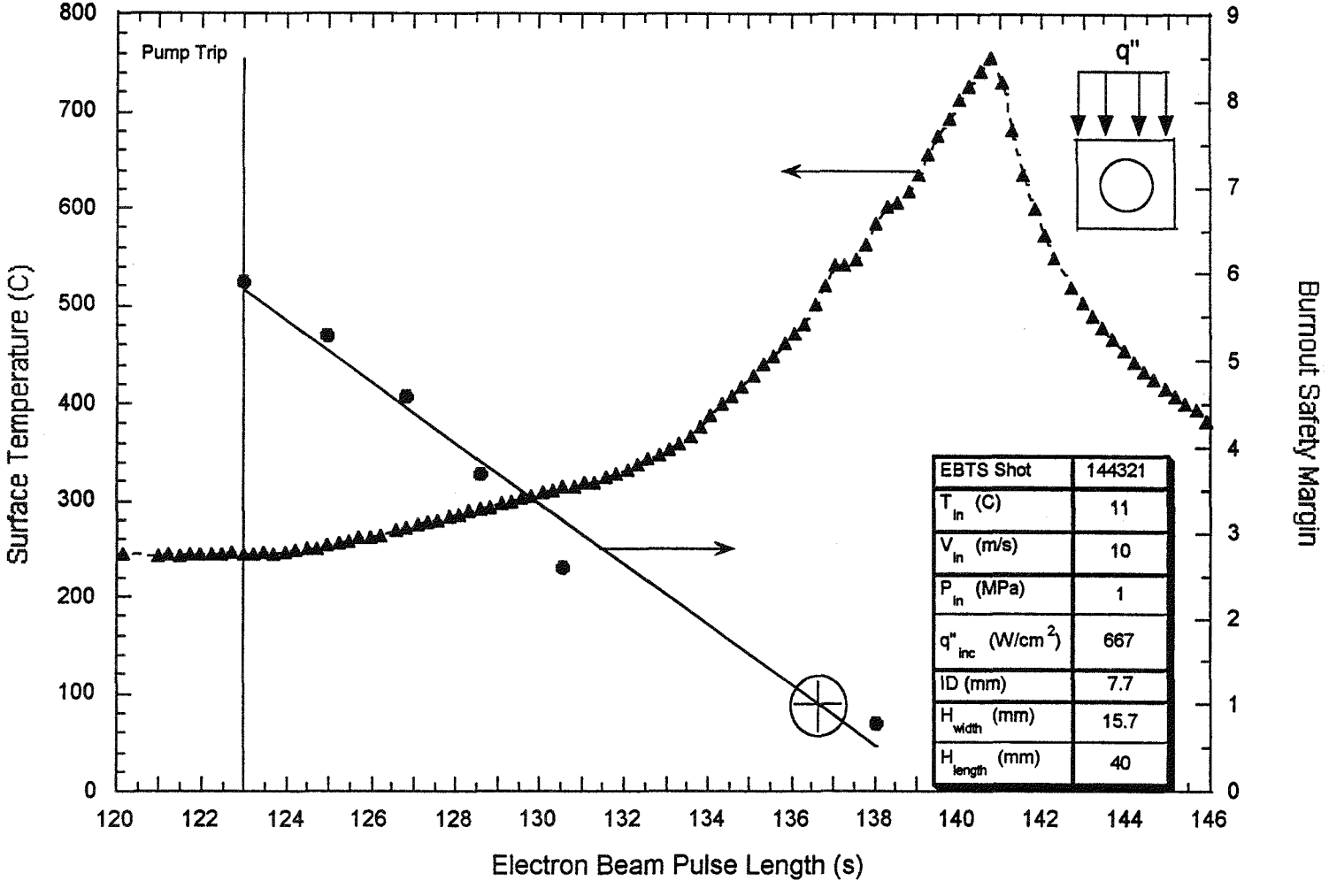

Figure 6-16: Comparison of the Burnout Safety Margin Decline and the Surface Temperature Rise During the Experimental Pump Trip for EBTS Shot 144321.

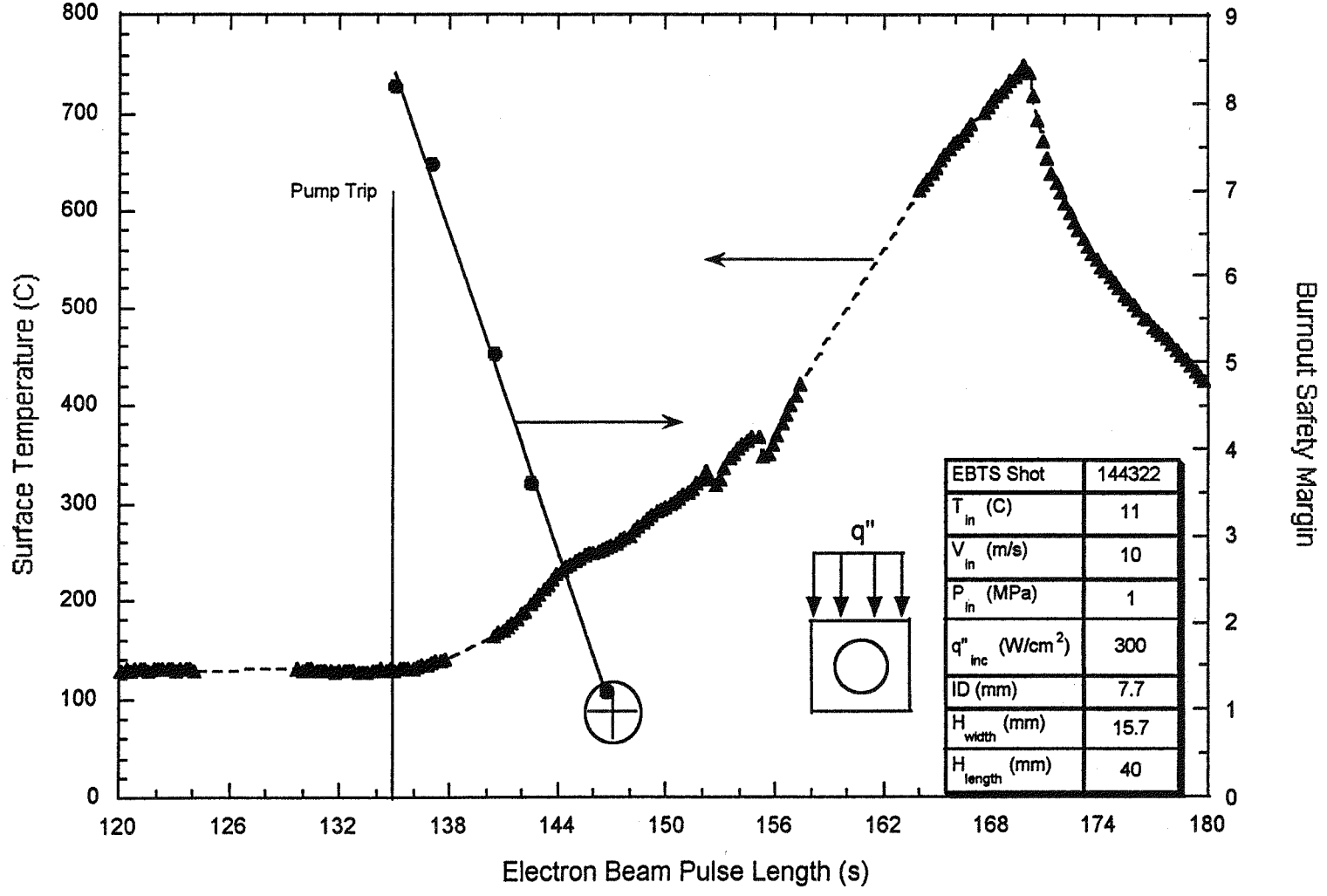

Figure 6-17: Comparison of the Burnout Safety Margin Decline and the Surface Temperature Rise During the Experimental Pump Trip for EBTS Shot 144322.

7.0 Discussion

7.1 Introduction

Since the objective of the experiment was to obtain a variety of LOFA data, the mockup could not be tested to true burnout since this would mean its destruction. Instead, high-temperature trip setpoints were chosen so that burnout could be approached without destroying the mockup. The melting temperature of copper is 1083 °C, but consideration of the potential hoop stresses at 1 MPa resulted in 700 °C being chosen conservatively as the high-temperature trip setpoint. Later during the experiment, the high-temperature trip setpoint was increased to 750 °C in order to closer approach the true burnout temperature. Regardless, it is important to recognize that the TBO reported here is not equivalent to the ultimate failure of the divertor plate mockup.

This chapter is divided into five sections:

- calculation of and discussion on the TBO data from Chapter 6,
- comparison of and discussion on the modeling results and experimental data,
- experimental thermal responses and the BSM,
- error analysis of experimental data,
- thermalhydraulic scaling for applicability to full-size divertor assemblies.

7.2 Time-to-Burnout Data

From the experimental data, Figures 5-1 through 5-8, the TBO is calculated by subtracting the time when the coolant pump was tripped from the time when the high-temperature signal by the embedded thermocouples in the heated area tripped off the electron beam. Mathematically, the equation for the TBO is written as:

$$t_{\text{burnout}} = t_{\text{temperature trip}} - t_{\text{pump trip}} \qquad (6\text{-}7)$$

Table 7-1 shows the inlet conditions for the experimental cases while Table 7-2 presents the time of pump trip, time of high-temperature trip, calculated TBO and high temperature trip setpoint for each of the experimental cases.

Examining the TBO data in Table 7-2 reveals the expected behavior. Using a constant incident heat flux of 6 MW/m^2, holding inlet temperature and pressure at 70 °C and 1 MPa, and varying the inlet velocity from 1, 5, and 10 m/s (electron beam shot numbers 144198, 144201, and 144201), the TBO increases parabolically from 12 to 32 s, as shown in Figure 7-1. If the inlet conditions are held constant at 11 °C, 1 MPa, and 10 m/s, but the incident heat flux is varied from 3, 7, 10, 13, and 16 MW/m^2, then the TBO decreases parabolically from 35 to 9 s, as shown in Figure 7-2.

Using the data in Figure 7-1, we can make the following inference. Assuming normal ITER operations, the divertor plates are being subjected to a constant incident heat flux of 5 MW/m^2 with

water inlet conditions of 1 MPa, 70 °C, and 10 m/s*. At these conditions, the experimental data in this report suggest that the plant engineers and operators will have approximately 32 s to both detect the onset of the LOFA and safely shut down the plasma. While it is possible that the actual response time may be longer since this experiment did not test to ultimate failure of the divertor plate mockup, the additional time is believed to be a maximum of 10 seconds. Even with these additional seconds, it still appears that additional engineering measures are necessary to provide the ITER plant engineers and operators enough time to safely counteract the LOFA initiation.

Figures 7-1 and 7-2 can be used to develop an intuitive feeling for the behavior of a typical ITER divertor plate during a postulated LOFA. What is very interesting to note from the two figures is the implied influence of aggressive cooling. The data shown in Figure 7-1 are for a modest cooling scheme since it has relatively low inlet subcooling and low water velocity. Using the experimental data and the experimental conditions from Figure 7-1, for a LOFA that occurs during normal ITER operations (i.e., 1 MPa, 10 m/s, 70 °C, 5 MW/m^2), plant engineers and operators will have 32 s to detect the LOFA and shut down the plasma. The data shown in Figure 7-2 are representative of a very aggressive cooling scheme (i.e., T_{in} is 11 °C, v_{in} is 10 m/s, and P_{in} equals 1 MPa). However, using the data in Figure 7-2 with the implied inlet conditions during normal ITER operations, plant operators and engineers will have only 20 seconds to detect the LOFA and shut down the plasma. This suggestion that the more aggressive cooling scheme gives less response time than the less aggressive cooling scheme is quite perplexing and further research is necessary.

7.3 LOFA Modeling

With the experimental TBO data as a reference, there is much interest in the predictive ability of ABAQUS to model mockup thermal responses during a simulated LOFA. Using a custom user-supplied film subroutine for ABAQUS, two very different approaches are taken in order to quantify current modeling capabilities. The modeling approaches are:

1. setting the heat transfer coefficient equal to zero at the time of the experimental pump trip,
2. including the experimentally measured velocity coast down response into the film subroutine, having it occur at the time of the experimental pump trip.

In both approaches, uniform heating of the mockup continued after the pump trip.

7.3.1 Finite Element Modeling: Adiabatic Case

As shown in Figures 6-10 through 6-17, the wall temperature around the circumference of the tube varies as a function of angle and consequentially so does the heat transfer distribution at the tube wall. Given the wide range of potential heat transfer coefficients, h's,** during the simulated LOFA,

---

*December 1995 ITER EDA specifications

**Depending upon the temperature at a given angle on the wall, (h << 1 W/cm^2-°C) or (h <= 4 W/cm^2-°C).

it is desirable to have a lower boundary for h. Setting h equal to zero is not truly indicative of the physical process since even in film boiling a finite amount of heat transfer occurs. However, setting the heat transfer coefficient equal to zero does serve as a limiting case, that is, worst case scenario.

ABAQUS cases with inlet conditions identical to the experiment are run with the heat transfer coefficient being assigned a value of zero at the time of the experiment pump trip. ABAQUS is allowed to calculate thermocouple temperatures beyond the pump trip, until the temperatures match those of the experimental high-temperature trip. Equation 7-1 is used with the ABAQUS data to calculate a finite element analysis TBO.

Table 7-3 shows a comparison between the adiabatic TBO and the experimentally measured TBO. Figures 7-3 and 7-4 show plots of the predicted TBO versus the experimental TBO. Figure 7-3 corresponds to the inlet conditions of 1 MPa, 68 °C, 6 MW/m^2, and 1, 5, and 10 m/s. Figure 7-4 is for the cases with inlet conditions of 1 MPa, 11 °C, 10 m/s, and 3, 7, 10, 15, and 16 MW/m^2.

In Figure 7-5, which shows the ratio of the experimental to the predicted TBO it is seen that the predicted TBO differs from the experimental TBO by a minimum factor of 4 and a maximum factor of 9. Just as disturbing is the fact that in Figure 7-3 the predicted TBO response to changes in the steady-state velocity does not follow the response curve for the experimental TBO. This unresponsiveness is due to the ABAQUS predictions being linear solutions to the same equation. That is, without incorporation of the velocity variable in the heat transfer correlation, ABAQUS is solving the same adiabatic equation for each of the three cases.

While Figure 7-6 does show a minimum and maximum difference factor of 4 and 15, respectively, the shape of the response curve in Figure 7-4 for the predicted TBO data follows that of the experimental TBO. The difference in prediction accuracy between Figures 7-3 and 7-4 is that in Figure 7-4 ABAQUS is solving different versions of the two-dimensional heat transfer equation.

Figures 7-7 through 7-14 show a comparison of the ABAQUS-predicted (adiabatic) and the experimentally-measured surface temperature response subsequent to the pump trip. In all cases, the predicted temperature response is linear while the experimentally-measured response is not. In addition, the experimentally-measured temperatures have a small time lag due to sustained heat transfer by the decreasing water velocity. This time lag is not evident in the predicted temperature response. These results imply that the adiabatic model does not accurately predict the physical properties that occur within the cooling channel during the LOFA.

Figure 7-15 shows the effects of initial inlet velocity on the thermocouple rate of temperature increase following the coolant pump trip, for the ABAQUS adiabatic cases. While the figure does show that the post-pump trip thermocouple temperature increases more slowly with higher initial inlet velocity, it also suggests that this is not a strong one-to-one relationship. This is in direct contrast to the experimental data. However, the inaccuracy of the FEA predictions for these cases is understandable since there is no velocity variable in the Thom nucleate boiling correlation.

In Figures 7-16, the incident heat flux is seen to strongly influence the thermocouple rate of temperature increase following the coolant pump trip, for the ABAQUS adiabatic cases. This is encouraging, but with the poor ratio of experimental TBO to predicted TBO, the results are still

inadequate.

Review of the plots presented in this section suggests that setting the heat transfer coefficient equal to zero is not a judicious choice when attempting to model the LOFA. While this suggestion appears to be intuitive, the LOFA experiments in this report provide tangible support for it.

7.3.2 Finite Element Modeling: Velocity Coastdown

As an alternative to the technique of setting the heat transfer coefficient equal to zero, the velocity ramp-down response following the pump trip (refer to Figure 5-1) was incorporated into the user-supplied ABAQUS film subroutine. The hypothesis was that the ramp-down response of the coolant velocity would allow the predicted TBO to better agree with the experimental TBO.

However, this proved not to be the case because the nucleate boiling correlation currently employed by the ABAQUS film subroutine does not include a velocity term. Thus, once nucleate boiling was established at an element in the mockup mesh, a decrease in the inlet velocity had no effect on the heat transfer coefficient for that element. For the mesh elements whose temperatures were in the single-phase heat transfer regime, decreasing the velocity did affect the heat transfer coefficient. Accordingly, the temperatures for these elements were dependent on velocity until nucleate boiling was initiated.

Figure 7-17 shows a plot of the ABAQUS prediction for the LOFA EBTS shot 144319, using the velocity ramp-down equation in the film subroutine. In the figure, there is a slight thermocouple temperature increase following the pump trip and then the thermocouple temperature reaches another steady-state value. The slight temperature increase is due to the backside of the coolant channel experiencing a decrease in heat transfer as the velocity coasts down. The subsequent steady-state temperature results because the backside of the coolant channel eventually reaches nucleate boiling temperatures.

The ABAQUS temperature predictions in Figure 7-17 is disconcerting because for a factor of five difference in incident heat flux it shows the same time period for the temperature transient, approximately 10 seconds. These results imply that the rate of transition from single phase to nucleate boiling is nearly independent of incident heat flux. Physically this is not possible so apparently the velocity ramp-down approach of modeling the LOFA is either overlooking or underestimating some aspect of the thermalhydraulics during the LOFA.

Figure 7-18 summarizes the two LOFA modeling attempts for EBTS shot 144318. The adiabatic method yields a TBO that is several factors small than the experimental TBO and lacks the response curve shape of the experimental data. Similarly, the velocity ramp-down method produces a thermal response curve that bears little resemblance to the experimental thermal response. What is most obvious from the data curves in Figure 7-18 is the fact that we cannot accurately predict the thermal responses of a divertor plate mockup during a LOFA with our current analysis techniques.

It is hypothesized that inclusion of the transition and film boiling regimes, along with the experimental velocity ramp-down, into the ABAQUS film subroutine will enable ABAQUS to better model the behavior of the heat transfer coefficient during the LOFA. This hypothesis is based on the

observation that in the adiabatic calculations, making the heat transfer coefficient equal to zero produced thermal response curves that were similar in shape to the experimental thermal responses. By including the transition and film boiling correlations in the analysis, the heat transfer coefficient will be small at the higher mockup temperature, but not zero, which should produce the more gradual temperature rise seen in the experimental temperature data. Inclusion of the experimental velocity ramp-down is expected to increase the accuracy of the transition and film boiling correlations and also account for the heat transfer provided by the coolant as its velocity coasts to zero.

7.4 Thermal Responses

Comparison of ABAQUS predicted temperatures with previous EBTS experimental data reveals a relatively high degree of accuracy [29]. This is encouragement that with the proper set of equations for the heat transfer coefficient, ABAQUS can accurately model mockup thermal responses during a LOFA. Table 7-4 presents the steady-state*** temperature data for the 8 experimental LOFA cases

Figure 7-19 shows a comparison of the ABAQUS predicted and experimentally measured thermocouple temperatures for the steady-state conditions of EBTS shots 144198, 144201, and 144205. These three cases are for constant heat flux and varying initial inlet velocity. From the figure, ABAQUS does a very good job of predicting the experimentally measured temperatures.

In Figure 7-20, the comparison between predicted and experimental thermocouple data is for EBTS shots 144318 through 144322. Here, the inlet conditions are constant and the incident heat flux is varying. In the figure, the experimental temperature data has a linear response over the entire range of heat fluxes. This is unusual since there should be an inflection in the response curve due to the transition from single phase to nucleate boiling heat transfer. For example, the single phase-to-nucleate boiling inflection is visible in the predicted data, at approximately 6 MW/m^2. The absence of the inflection in the experimental response curve raises many questions and further research is necessary for a better understanding.

7.4 Burnout Safety Margin

In Chapter 6, plots of the BSM as a function of decreasing water velocity following the coolant pump trip are presented. The BSM is mentioned here because of a potential correlation to the TBO.

During the process of plotting the BSM curves shown in Figures 6-9 through 6-16, it was noticed that the rapid temperature excursion indicative of approaching CHF, was seemingly initiated when the BSM equaled a value of one. Although this is the definition of the BSM, it was surprising to note the behavior with the experimental data.

In Figures 6-11, 6-12, 6-13, and 6-15, following the coolant pump trip, there is a rise in the

***Prior to coolant pump trip.

thermocouple temperature. However, until the BSM for the given inlet conditions and incident heat flux equals 1, the temperature slope is small. When the BSM equals one, the thermocouple temperature rate of change becomes very steep.

If a correlation does exist between the BSM and the TBO, it might be possible to calculate the temperature of the mockup when the BSM equaled 1. This temperature could subsequently be used with an experimentally derived equation that included the inlet conditions, material properties, and desired high-temperature trip, to predict the TBO.

Of course, this technique is all conjecture and requires additional experimental TBO data for application and verification.

7.5 Error Analysis

7.5.1 Water Calorimetry

The incident heat flux, q_i, during an electron beam pulse is calculated by dividing the steady-state water calorimetry data from the ΔT blocks by the heated area of the divertor plate. The accuracy of the incident heat flux calculations is determined using the methodology of Moffat [30]. The error in the water calorimetry is calculated as:

$$\frac{\delta Q}{Q} = \pm\sqrt{\left(\frac{\delta \dot{m}}{\dot{m}}\right)^2 + \left(\frac{\delta \Delta T}{\Delta T}\right)^2} \qquad (6\text{-}8)$$

where

Q is power (W),
T is temperature (°C),
$\dot{m}$ is the mass flow rate (kg/s)

For first order approximations, $\dot{m}$ can be replaced by the water velocity, v. Using the measurement accuracy data from Table 2-2 and the experimental inlet conditions, the following values are used with Equation 7-2:

$$\frac{\delta v}{v} = \frac{0.02 \text{ m/s}}{1 \text{ m/s}}$$

$$\frac{\delta \Delta T}{\Delta T} = \frac{0.1 \text{ °C}}{15 \text{ °C}}$$

to yield an error of ± 2 % for the water calorimetry.

7.5.2 Heated Area

The error in the expected heated area measurement is calculated as:

$$\frac{\delta A}{A} = \sqrt{\left(\frac{\delta L_{heated}}{L_{heated}}\right)^2 + \left(\frac{\delta W_{heated}}{W_{heated}}\right)^2} \qquad (6\text{-}11)$$

where,

A is the heated area, m^2,
L is the length of the heated area, m,
H is the width of the heated area, m,

The heated area for each pulse is estimated to be 624 mm^2 (40 mm heated length by 15.6 mm heated width). Graphite marks and scribes in the oxidation layer, both of which glowed brightly on the IR video during an electron beam pulse, were made on the divertor plate to help the EBTS operators set up the requested heated area. Since the electron beam was intentionally spilled beyond the width of the plate, there was very little uncertainty associated with the heated width (i.e., δW_{heated} is equal to zero).

However, determination of the heated length was not as precise. Thus, an uncertainty, δL_{heated}, of ± 4 mm is assumed. Using δW_{heated} equal to 0 mm and δL_{heated} equal to 4 mm in Equation 7-3 yields an error of ± 10% for the expected heated area.

7.5.3 Heated Area

The equation for the error in the calculated heat flux is:

$$\frac{\delta q_i}{q_i} = \sqrt{\left(\frac{\delta Q}{Q}\right)^2 + \left(\frac{\delta A}{A}\right)^2} \qquad (6\text{-}12)$$

where,

q_i is the incident heat flux, W/cm^2

With a calculated accuracy of ± 10% for the expected heated area and ±2 % for the water calorimetry, Equation 7-4 yields an error of ± 10% in the calculated incident heat flux, q_i.

7.6 Thermalhydraulic Scaling

Magnetic fusion experiments have never been copiously funded, and in this case the divertor tests were performed with the life-testing experiment already at hand. There was no detailed consideration of thermal-hydraulic scaling issues prior to the loss of flow testing. The divertor mockup, of course, is a full-sized segment that is representative of the thousands of divertor tiles that will protect the vacuum vessel. A future task will be to assess the distortions in the data that have been collected.

If design provisions in the full-sized ITER divertor cooling system tend to prolong the tubing lifetime during LOFAs, then the results found in this experiment are conservative. Given that assumption, this experiment has already answered important questions for safety researchers; it has experimentally verified that predicted times to tube burnout [31] are on the order of seconds rather than minutes. Another factor affecting this safety work is that the preliminary design of the ITER divertor flow system has not been completed, and may still be changed even in the final design stages. At present it would be difficult to build a scale model of the divertor cooling system and time pressures for including safety in the ITER design dictate that answers to these questions be approximately known quickly to adequately prepare appropriate plasma safety systems.

An important issue to consider in scaling LOFAs, from the divertor mockup to the full-sized ITER design, should be the coolant pump coastdown time. Another is the volume of water in the test system compared with the full-sized system. Other differences, such as the manifolding and other flow friction losses, and elevation changes in the full-sized system, are not considered very consequential at present, although these factors should not be ignored in the scaling analysis. Pump coastdown is thought to be important since most large fission flow systems can experience localized overheating without having the entire bulk coolant temperature increase up to the cladding melting temperature [that is, a slow bulk water thermal response similar to that during the Three Mile Island accident], so the localized overheating is much more sensitive to the pump coastdown time because the pump will drive some cooler water flow past the localized hot areas to remove heat even as the pump impeller is coasting down to a stop.

Therefore, pump coastdown is perhaps the most sensitive issue in thermalhydraulic scaling to predict the times to tube burnout on the full-sized ITER divertor. Accurate models of the pump on the divertor LOFA experiment and the pump expected to be used in the full-sized facility - or at least a pump head to pump flow performance curve - will be important to scaling LOFA times. Currently, several ideas that are being considered for increasing ITER pump coastdown time are to put flywheels on the pump shaft or to use safety-rated, battery-backed "pony motors" that will continue to turn the pump shaft at perhaps 10 to 15% of the normal rated speed to provide for removal of decay heat in the activated materials in the vacuum vessel. These coastdown schemes rely on timely ITER plasma shutdown in a 1 to 10 s time frame.

The flywheel is viewed as a more passive approach to achieve long coastdown times, but it will most likely expend its stored energy in a short time (on the order of a few minutes - certainly much

less than an hour) and cannot be recharged. The flywheel would have to be analyzed for missile generation, while the pony motors would be active components requiring periodic testing and maintenance. Once these trade-offs have been settled and the pump parameters have been set, then these experimental results can be scaled up and applied to the design of the full sized ITER divertor cooling system.

Scaling is an important issue to be approached in the future. With accurate data on the experiment test system and on the times to tube burnout, scaling can be undertaken when the design of the ITER divertor cooling system has been fixed.

Table 7-1. Definition of Inlet Conditions for Experimental Cases

	Inlet Conditions			CHF: Tong-75		Applied	
EBTS Shot	Pressure (MPa)	Velocity (m/s)	Temp. (°C)	Surface (MW/m^2)	Wall (MW/m^2)	Surface (MW/m^2)	BSM
144198	1	1	68	4	8	6	0.7
144201	1	10	68	12	24	6	2.0
144205	1	5	68	8.7	17	6	1.5
144318	1	10	11	21.5	43	16	1.3
144319	1	10	11	21.5	43	15	1.4
144320	1	10	11	21.5	43	10	2.1
144321	1	10	11	21.5	43	7	3.1
144322	1	10	11	21.5	43	3	16.0

Table 7-2. Times of Pump Trip, High Temperature Trip, and Time-to-Burnout Data

	Water Inlet Conditions			Experimental				
EBTS Shot	Pressure (MPa)	Velocity (m/s)	Temp. (°C)	$q_{incident}$ (MW/m^2)	T_{trip} (°C)	$t_{pump\ trip}$ (s)	$t_{ebeam\ trip}$ (s)	TBO
144198	1	1	68	6	700.0	122.8	134.5	11.8
144201	1	10	68	6	750.0	135.0	167.0	32.0
144205	1	5	68	6	700.0	122.0	136.0	14.0
144318	1	10	11	16	750.0	130.5	139.3	8.8
144319	1	10	11	15	750.0	132.0	142.0	10.0
144320	1	10	11	10	700.0	121.0	134.3	13.3
144321	1	10	11	7	750.0	123.0	140.8	17.8
144322	1	10	11	3	750.0	135.0	170.0	35.0

Table 7-3. ABAQUS Predicted TBO with $h_{film} = 0$ at Pump Trip vs. Experimental TBO

	Water Inlet Conditions				Predicted	Actual	f_{TBO}
EBTS Shot	Pressure (MPa)	Velocity (m/s)	Temp. (°C)	$q_{incident}$ (MW/m^2)	TBO (s)	TBO (s)	Actual/ Predicted
144198	1	1	68	6	3.0	11.8	3.9
144201	1	10	68	6	3.5	32.0	9.1
144205	1	5	68	6	3.1	14.0	4.5
144318	1	10	11	16	0.6	8.8	14.6
144319	1	10	11	15	1.0	10.0	10.0
144320	1	10	11	10	1.5	13.3	8.8
144321	1	10	11	7	2.5	17.8	7.1
144322	1	10	11	3	8.0	35.0	4.4

Table 7-4. Comparison of Predicted and Actual Thermocouple Temperatures

	Water Inlet Conditions				Predicted	Actual
EBTS Shot	Pressure (MPa)	Velocity (m/s)	Temp. (°C)	$q_{incident}$ (MW/m^2)	T_{TC} (°C)	T_{TC} (°C)
144198	1	1	68	6	291.0	290.0
144201	1	10	68	6	234.0	235.0
144205	1	5	68	6	275.0	270.0
144318	1	10	11	16	433.0	500.0
144319	1	10	11	15	384.0	450.0
144320	1	10	11	10	343.0	340.0
144321	1	10	11	7	282.0	245.0
144322	1	10	11	3	137.0	130.0

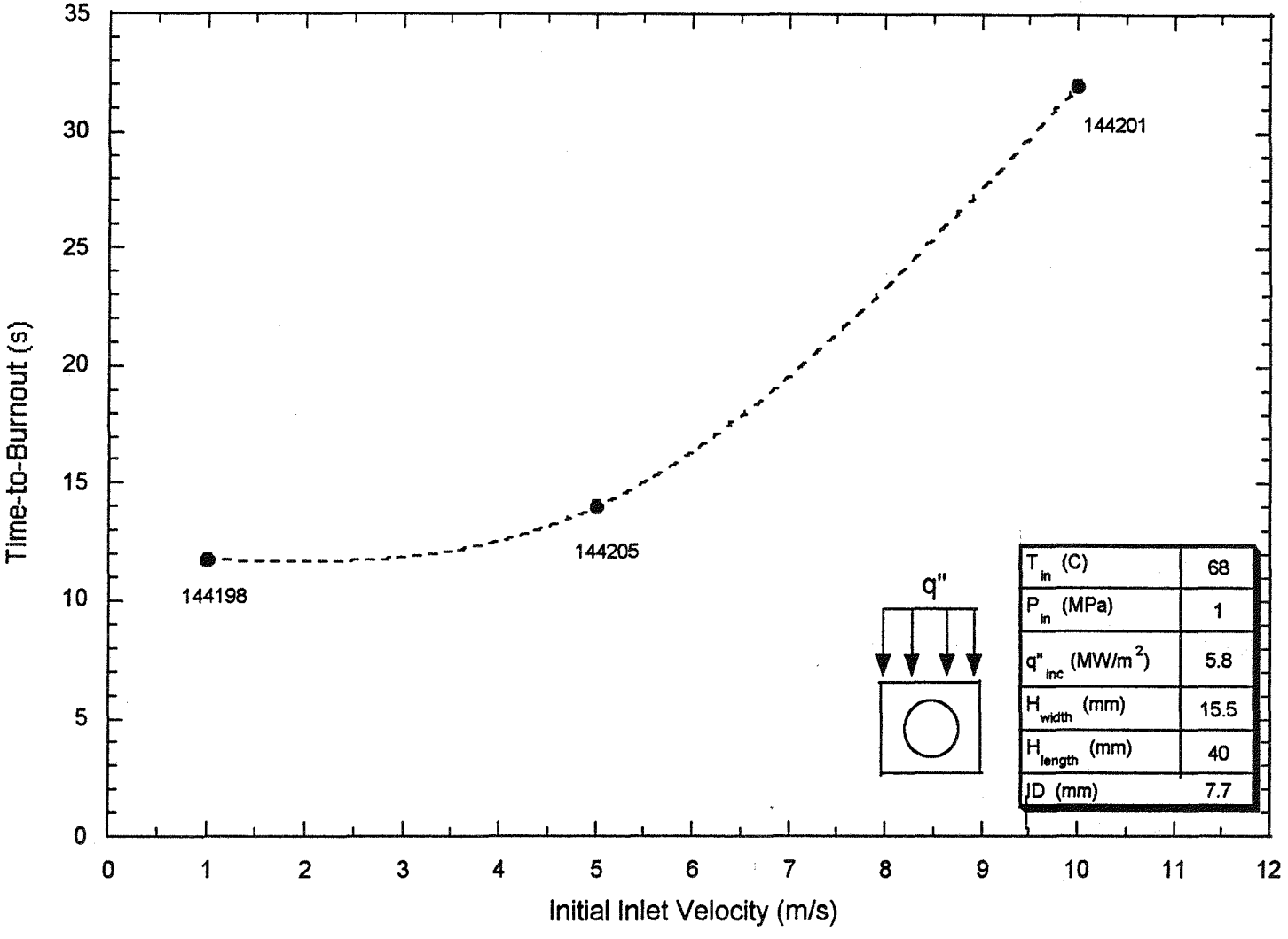

Figure 7-1: Influence of Initial Inlet Velocity on the Experimental Time-to-Burnout Data

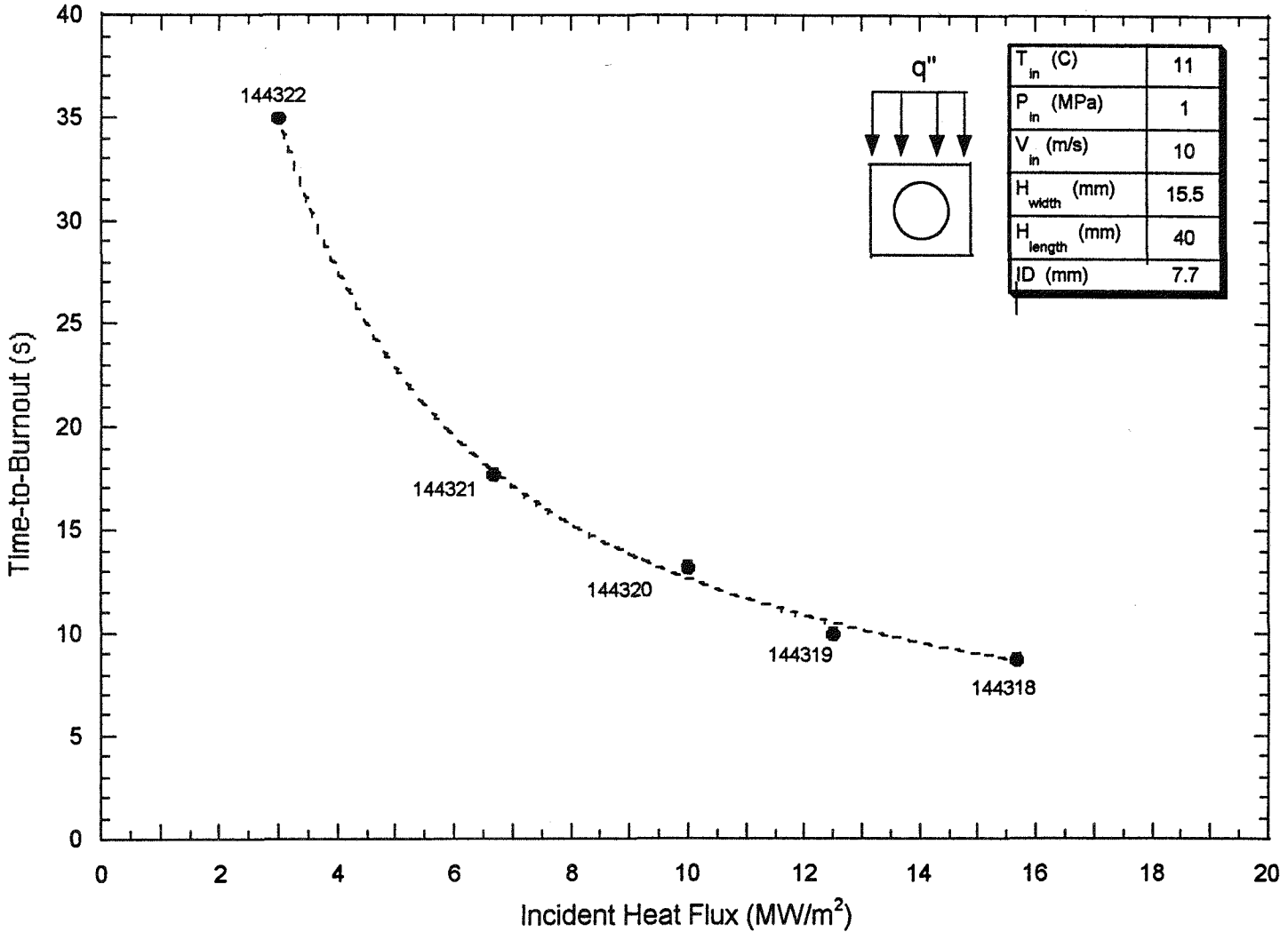

Figure 7-2: Influence of Incident Heat Flux on the Experimental Time-to-Burnout Data.

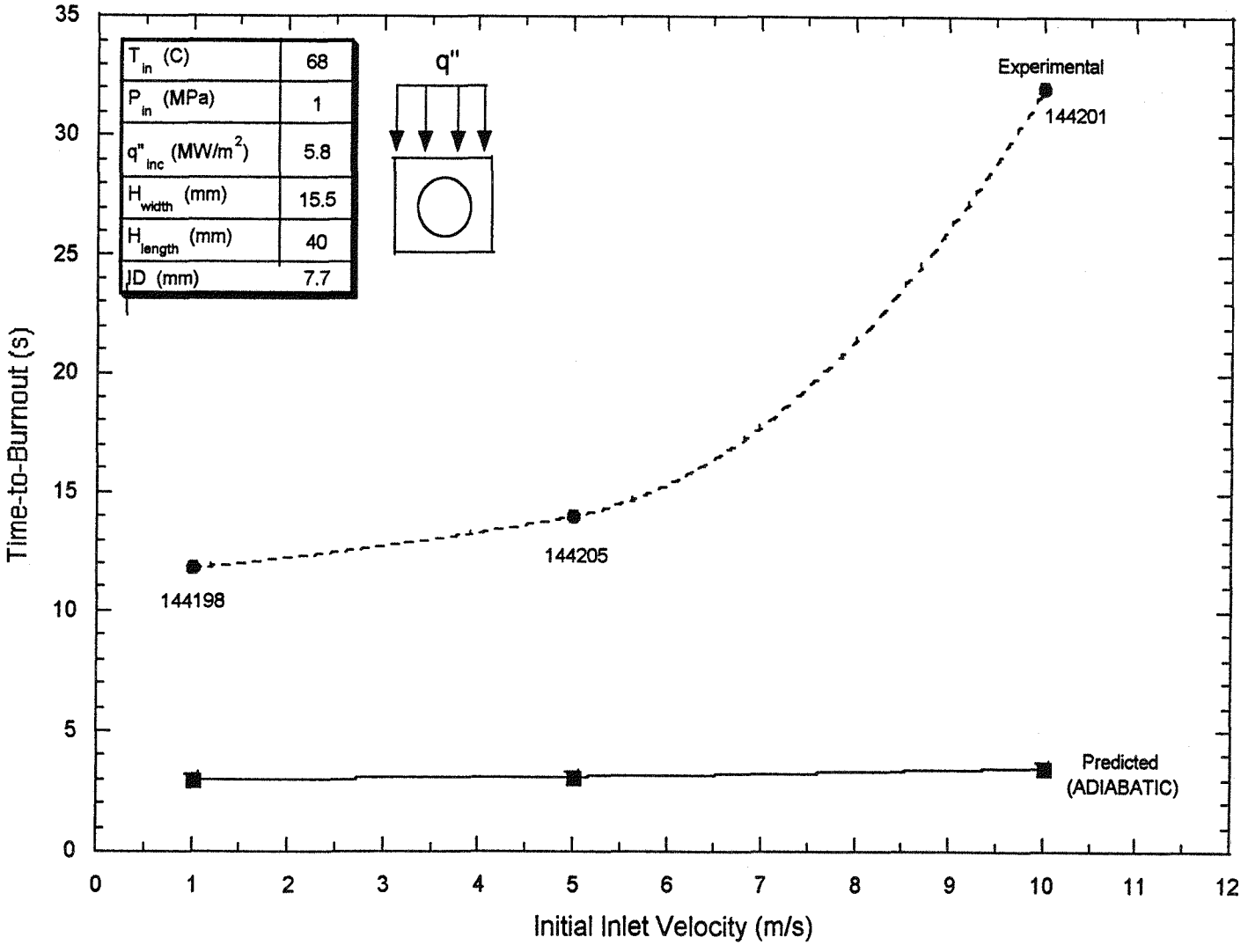

Figure 7-3: FEA Predicted vs. Experimental Time-to-Burnout as a Function of Initial Inlet Velocity.

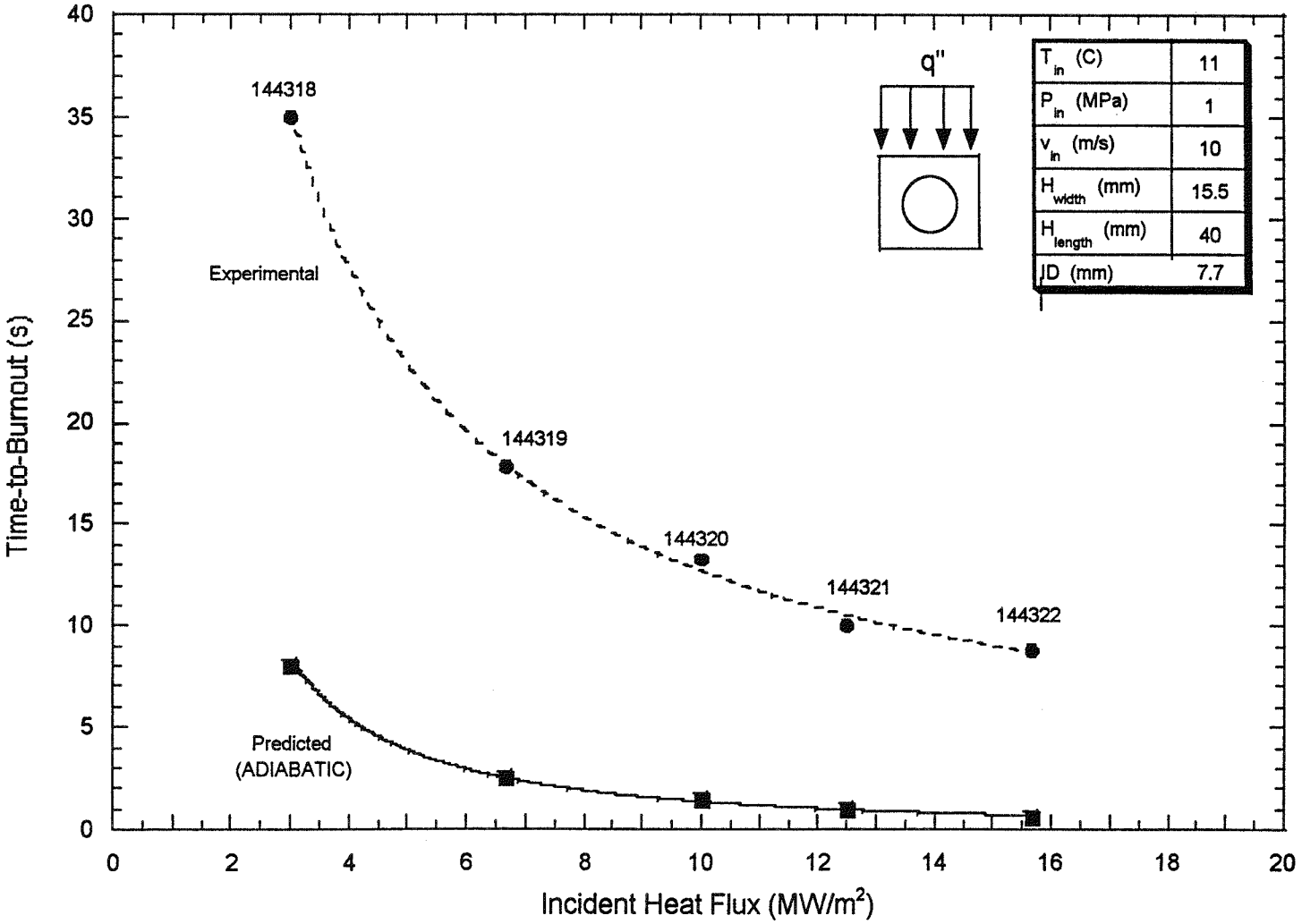

Figure 7-4: FEA Predicted vs. Experimental Time-to-Burnout as a Function of Incident Heat Flux.

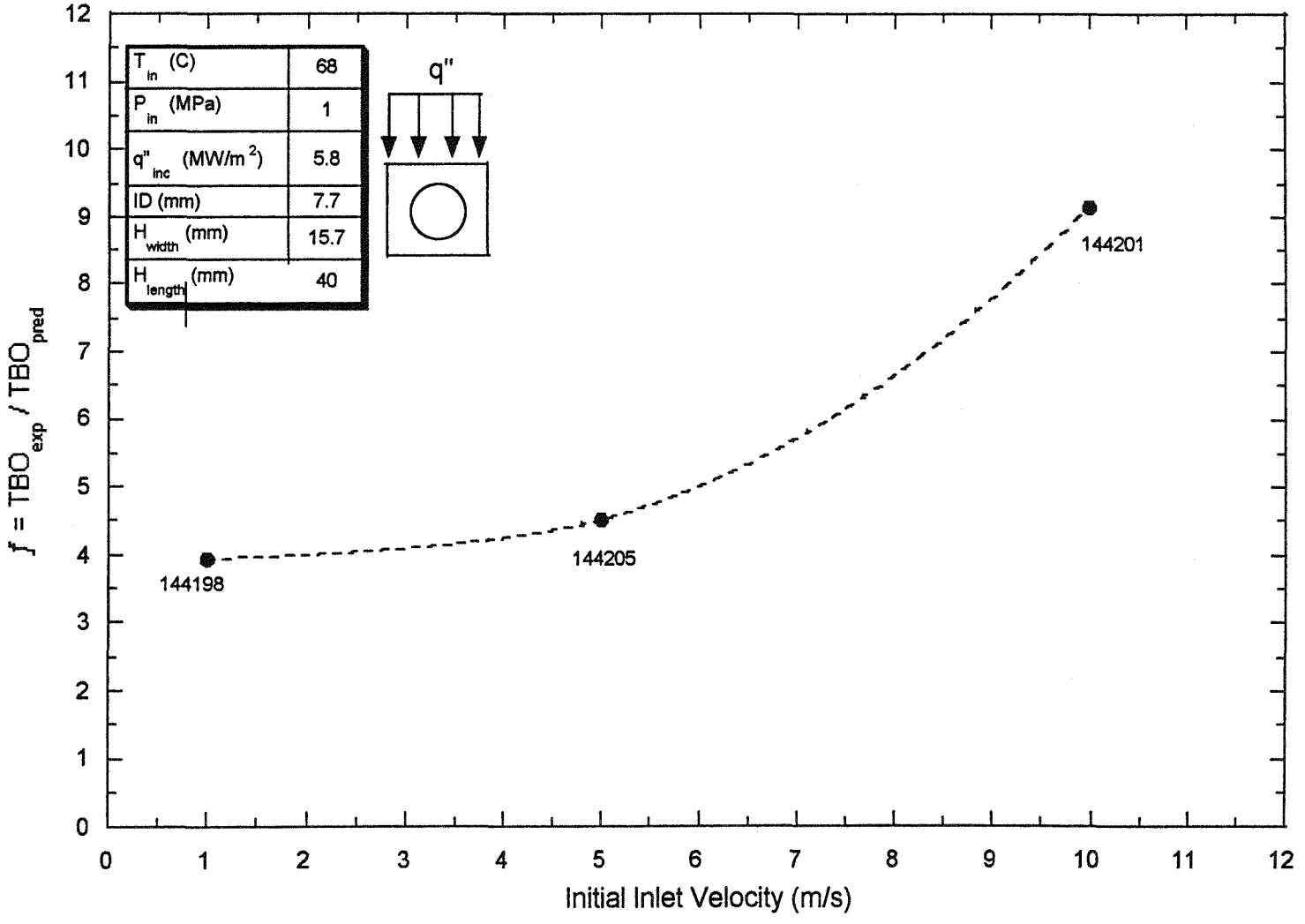

Figure 7-5: Ratio of the Experimental to FEA Predicted Time-to-Burnout as a Function of Initial Inlet Velocity.

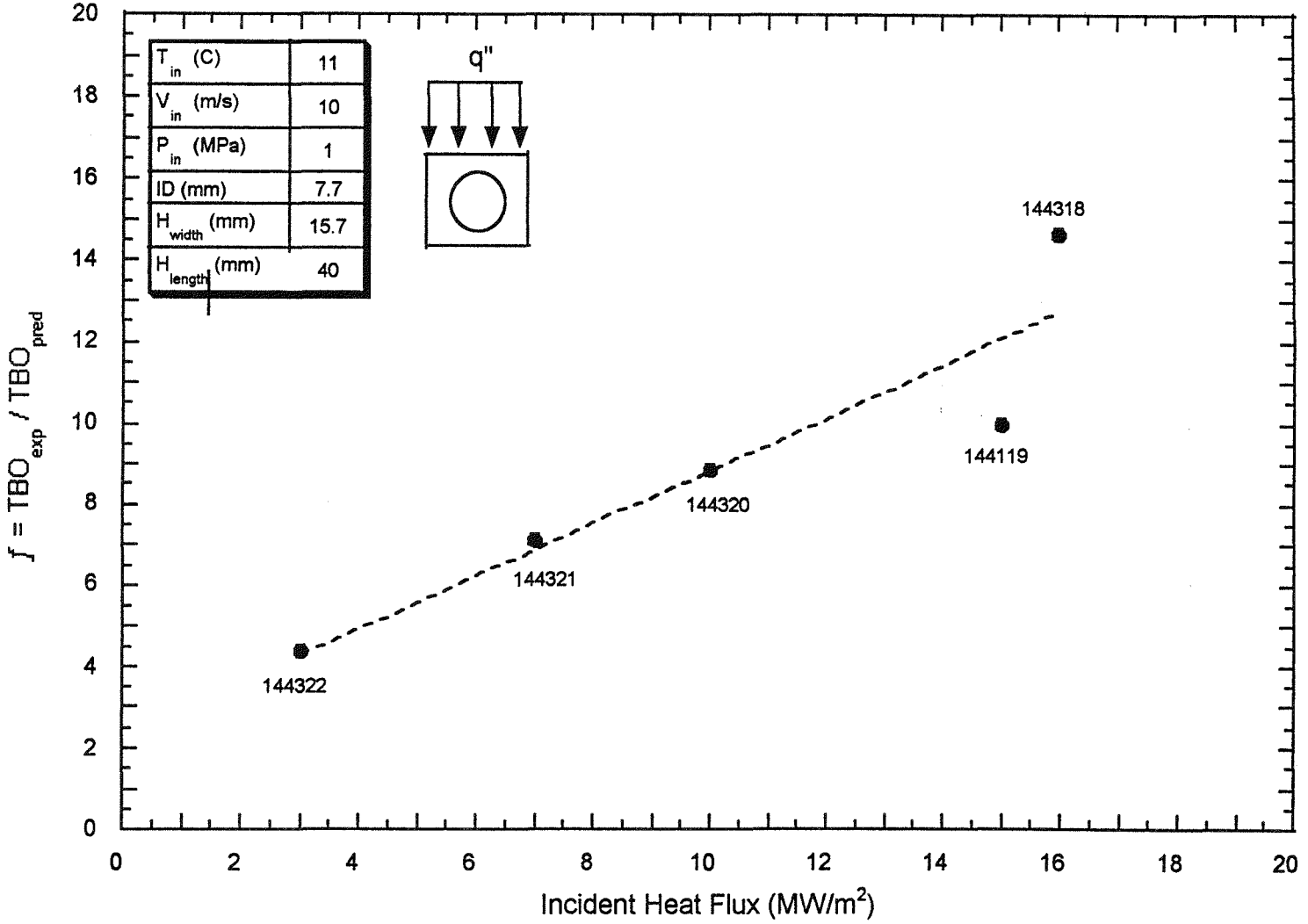

Figure 7-6: Ratio of the Experimental to FEA Predicted Time-to-Burnout as a Function of Incident Heat Flux.

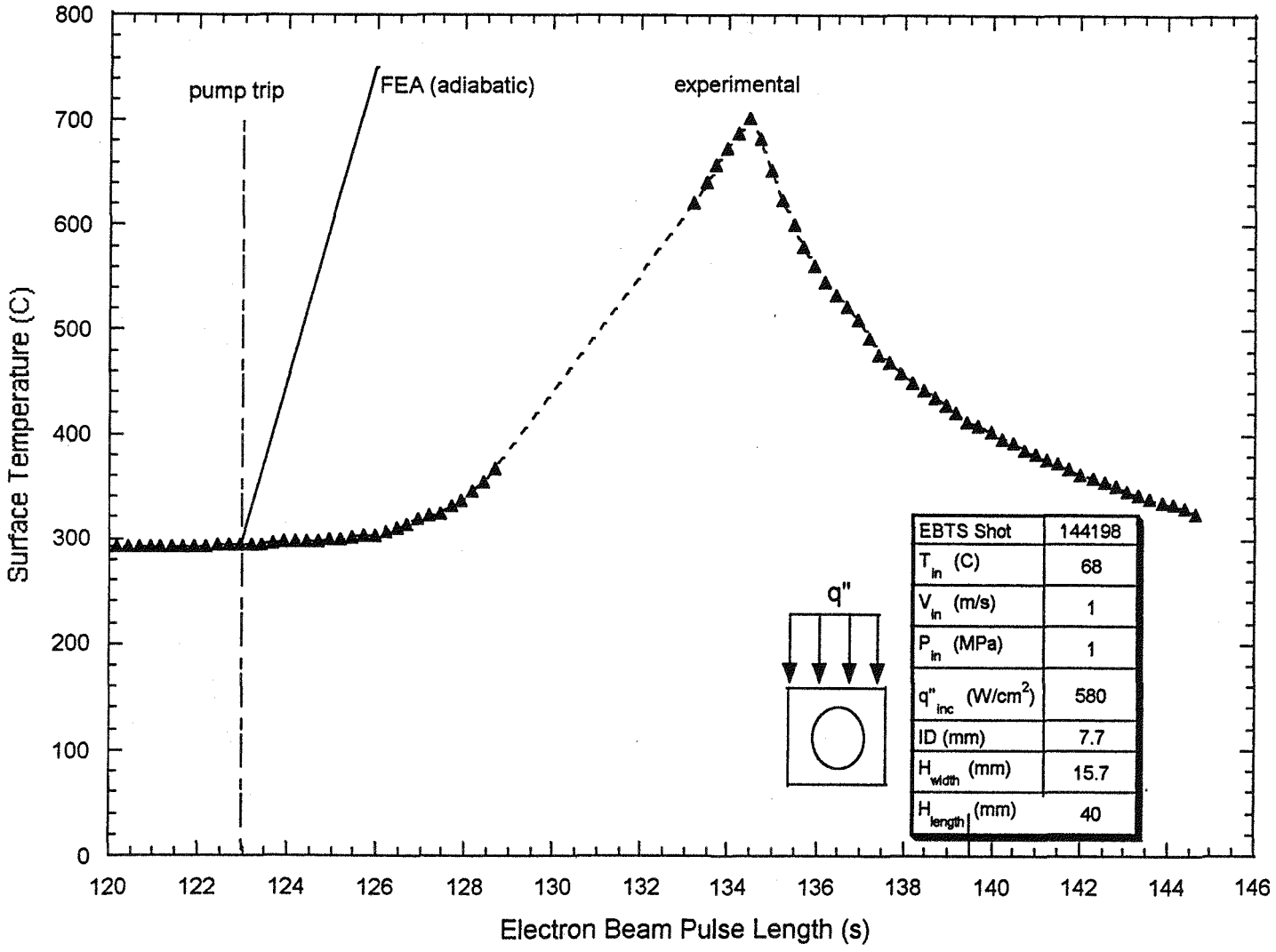

Figure 7-7: FEA (adiabatic) Predicted vs. Surface (thermocouple) Temperatures after Pump Trip for EBTS Shot 144198.

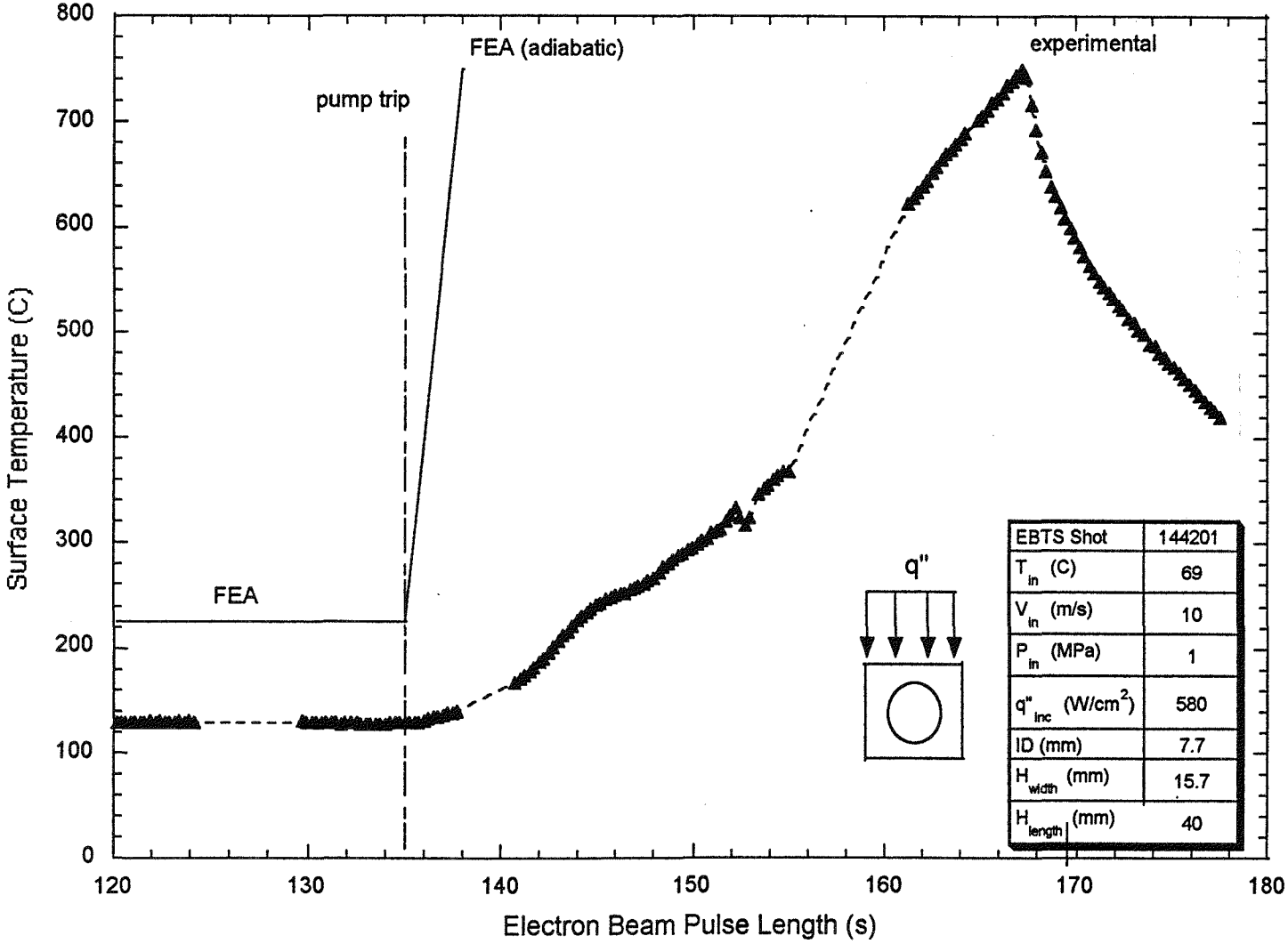

Figure 7-8: FEA (adiabatic) Predicted vs. Surface (thermocouple) Temperatures after Pump Trip for EBTS Shot 144201.

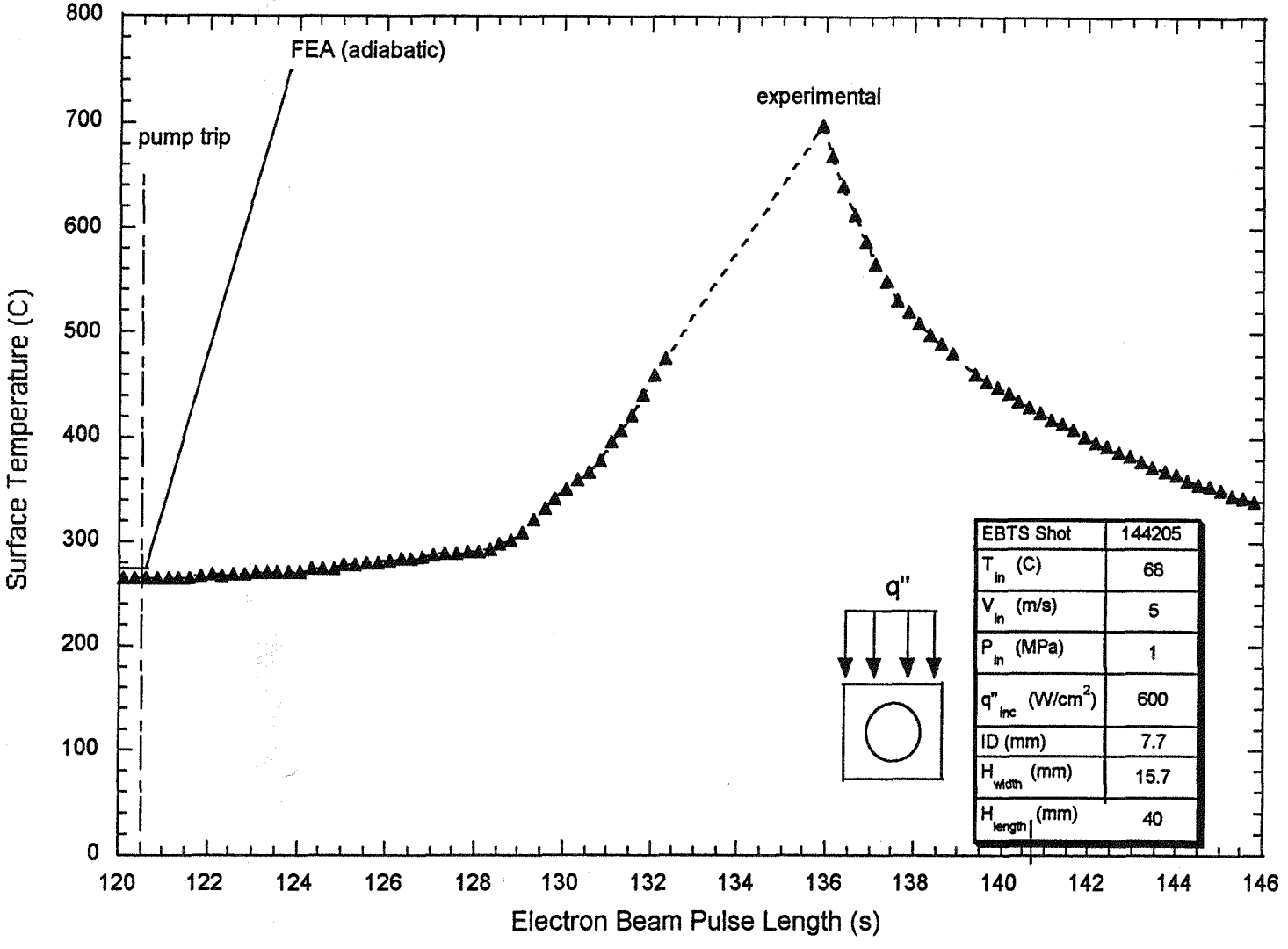

Figure 7-9: FEA (adiabatic) Predicted vs. Surface (thermocouple) Temperatures after Pump Trip for EBTS Shot 144205.

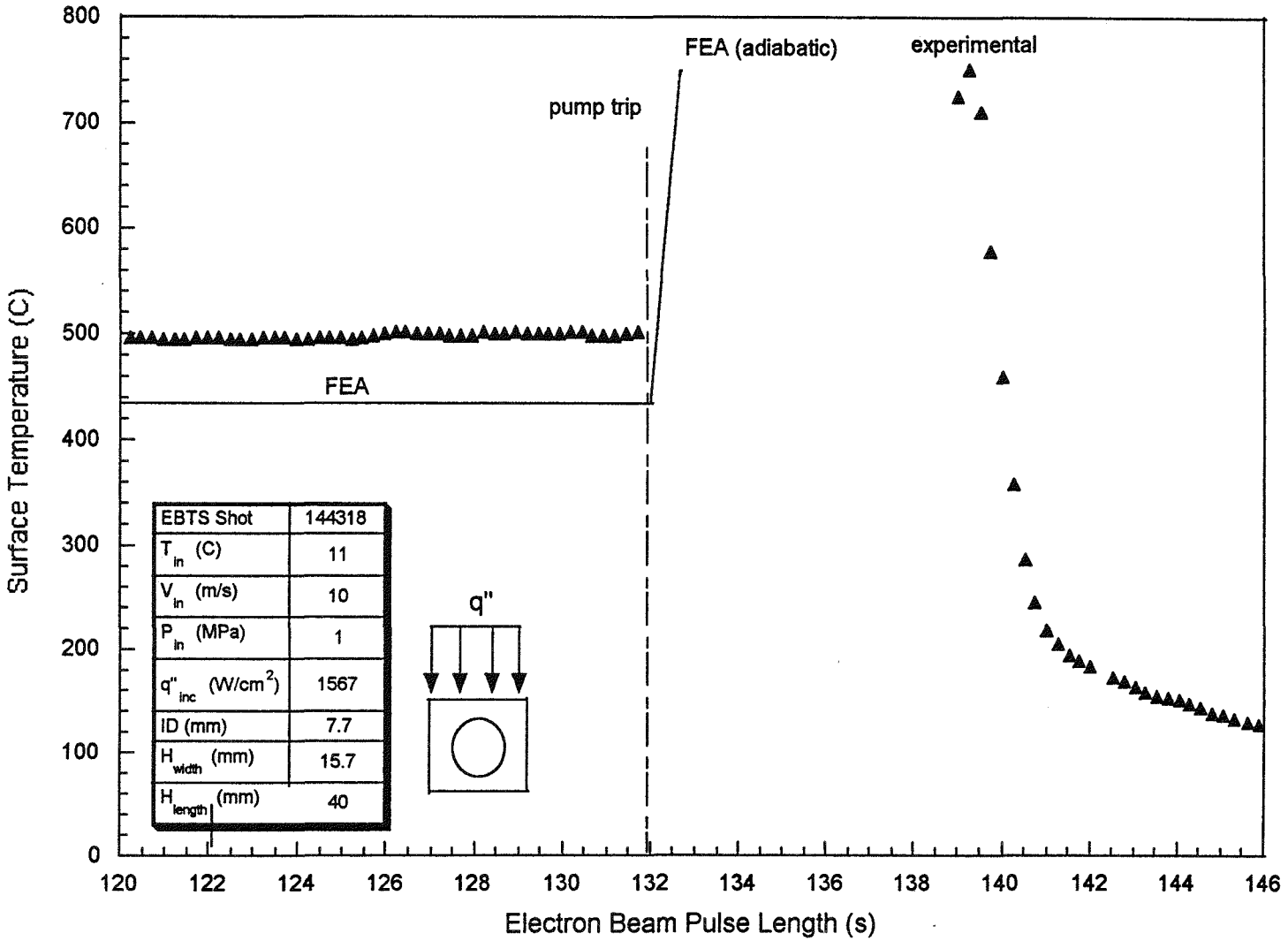

Figure 7-10: FEA (adiabatic) Predicted vs. Surface (thermocouple) Temperatures after Pump Trip for EBTS Shot 144318.

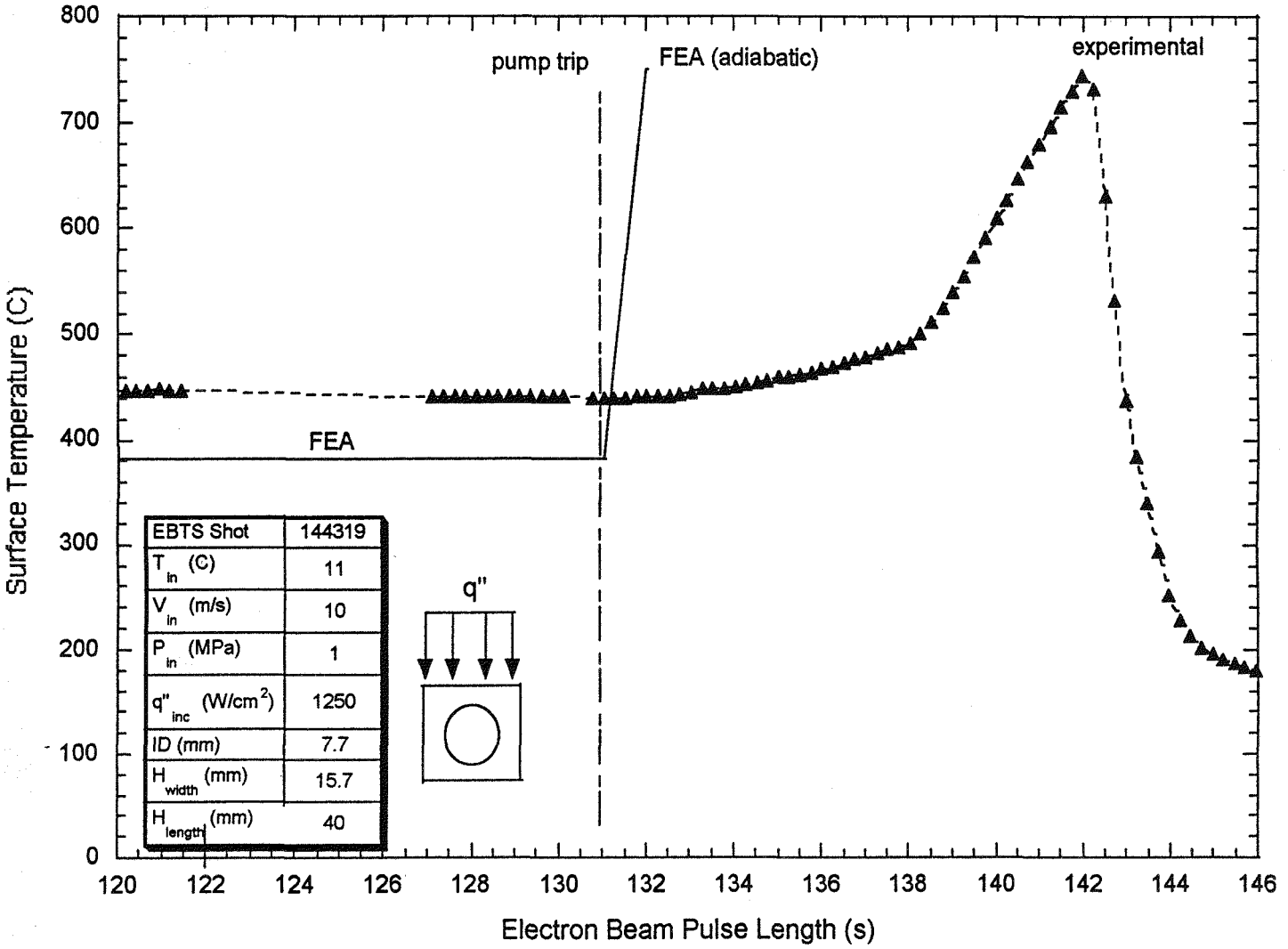

Figure 7-11: FEA (adiabatic) Predicted vs. Surface (thermocouple) Temperatures after Pump Trip for EBTS Shot 144319

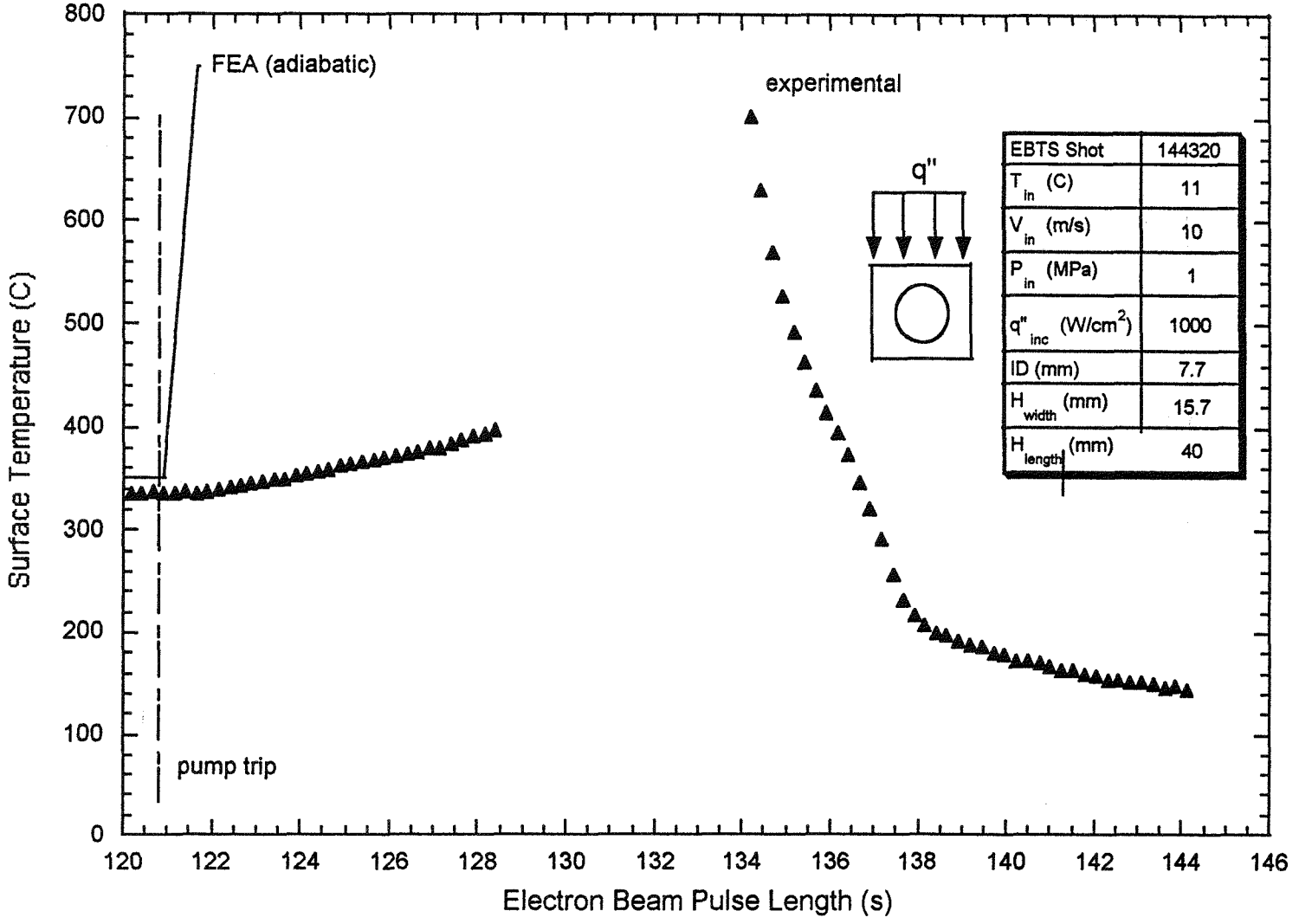

Figure 7-12: FEA (adiabatic) Predicted vs. Surface (thermocouple) Temperatures after Pump Trip for EBTS Shot 144320.

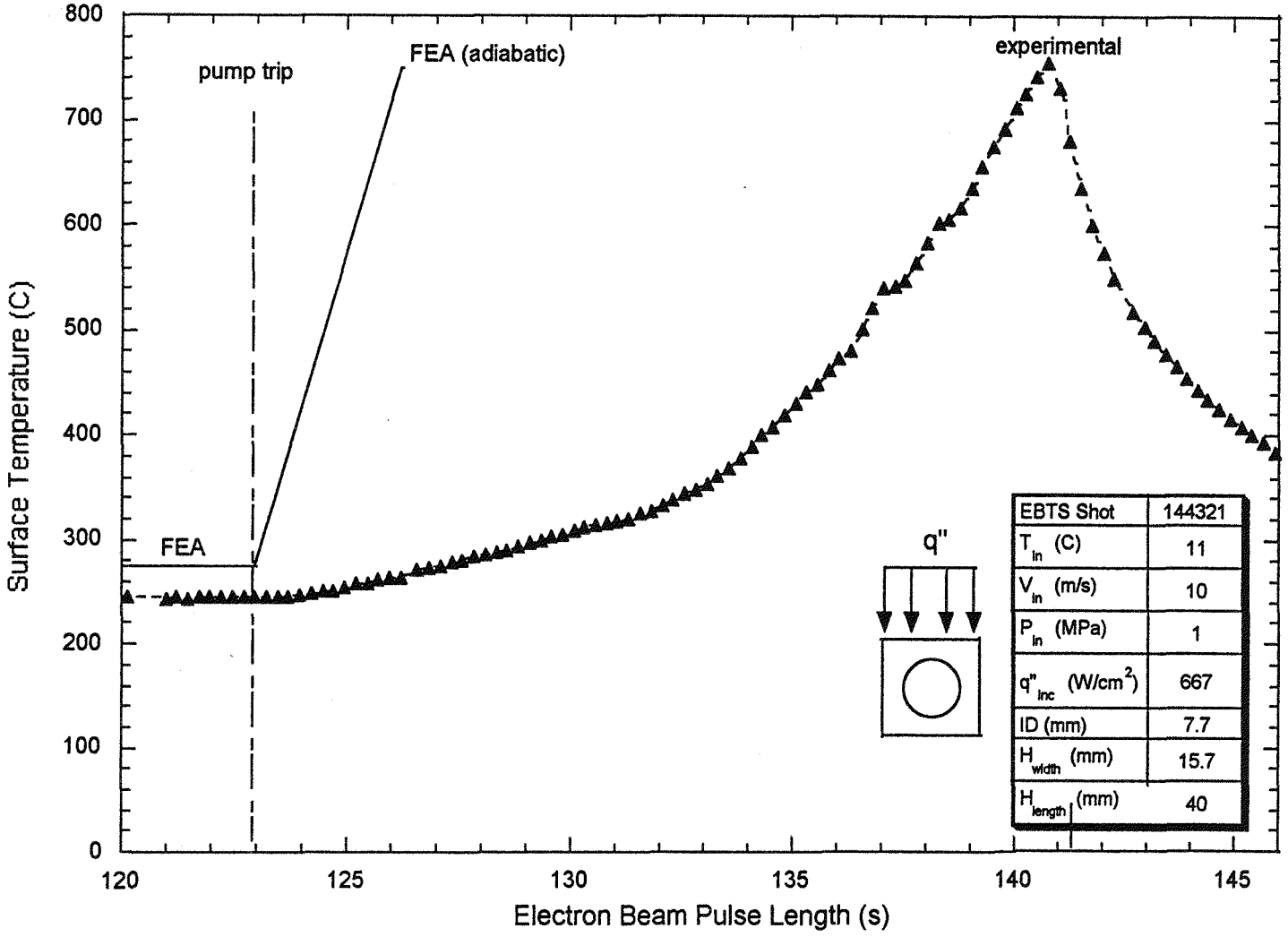

Figure 7-13: FEA (adiabatic) Predicted vs. Surface (thermocouple) Temperatures after Pump Trip for Shot 144321.

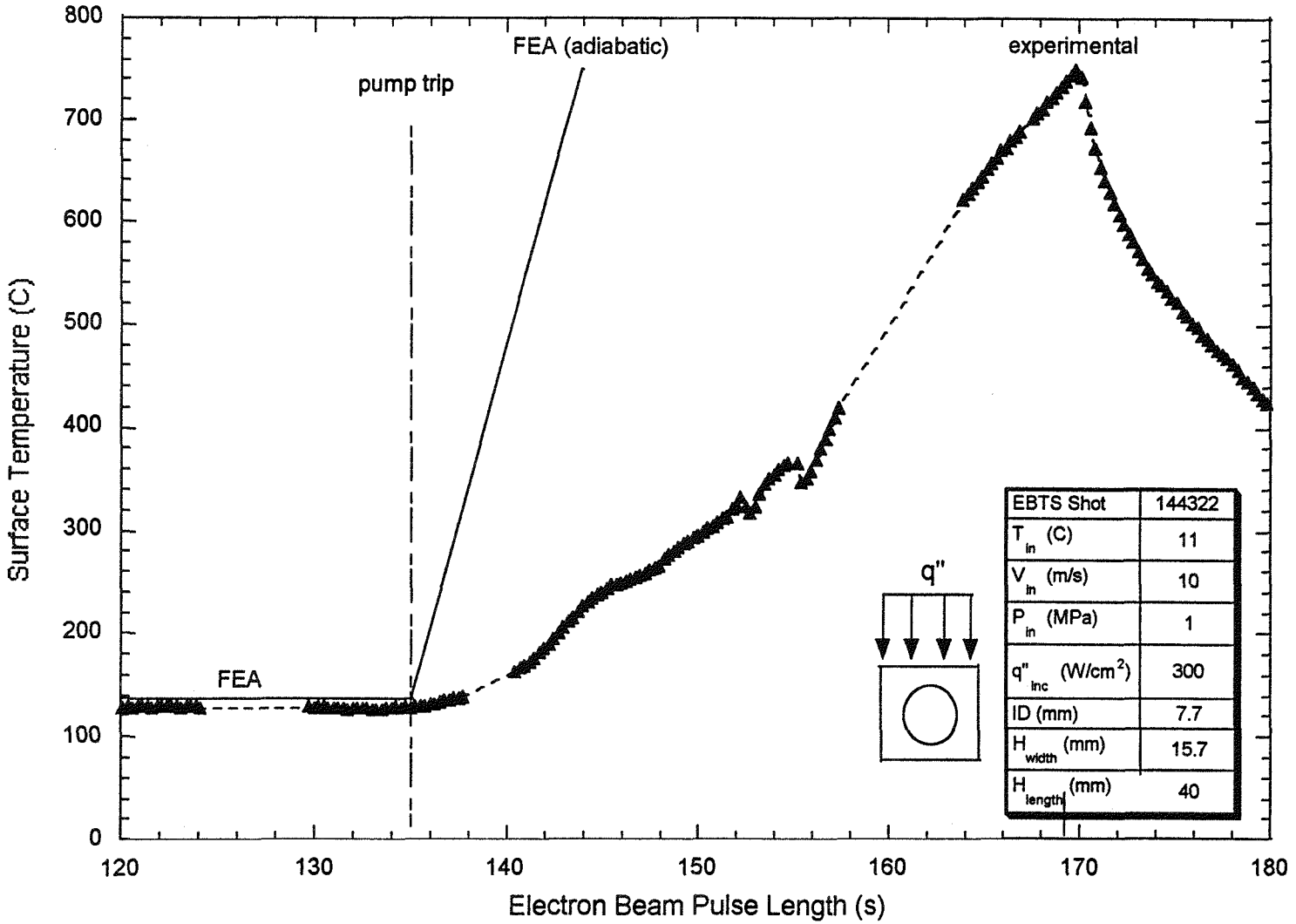

Figure 7-14: FEA (adiabatic) Predicted vs. Surface (thermocouple) Temperatures after Pump Trip for EBTS Shot 144322.

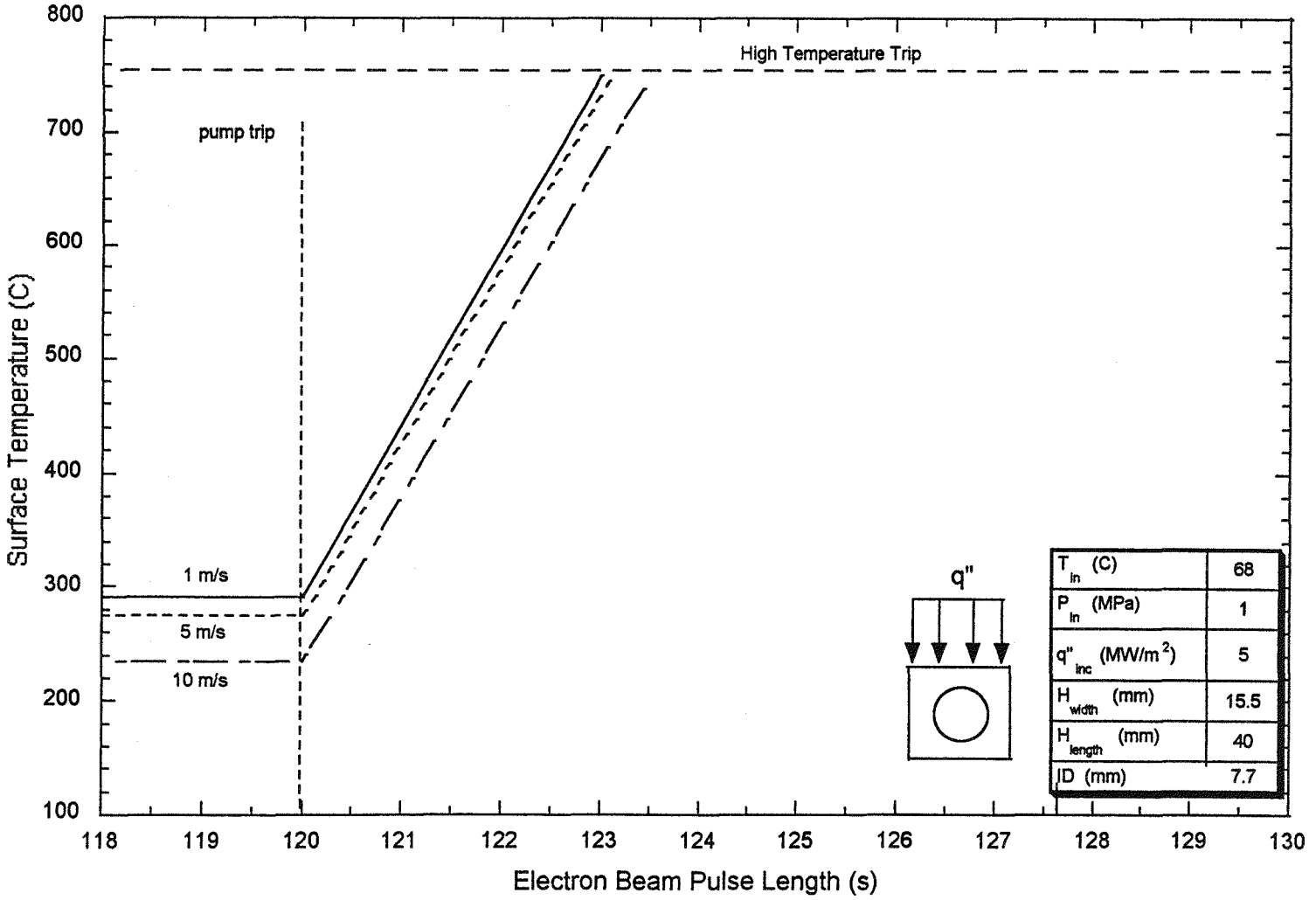

Figure 7-15: Influence of Initial Inlet Velocity on the Surface (thermocouple) Temperature Rate of Increase Following the Coolant Pump Trip.

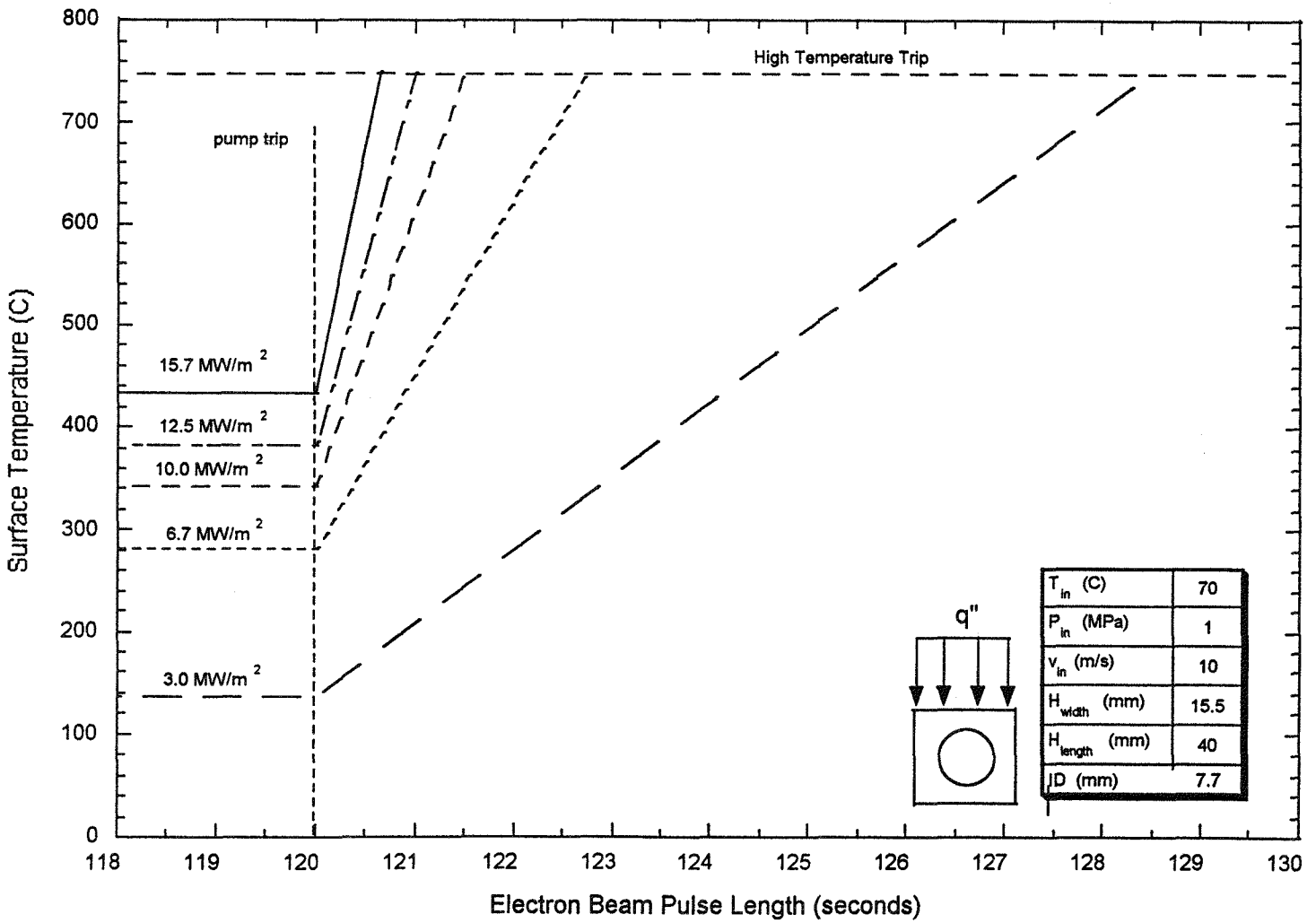

Figure 7-16: Influence of Incident Heat Flux on the Surface (thermocouple) Temperature Rate of Increase Following the Coolant Pump Trip.

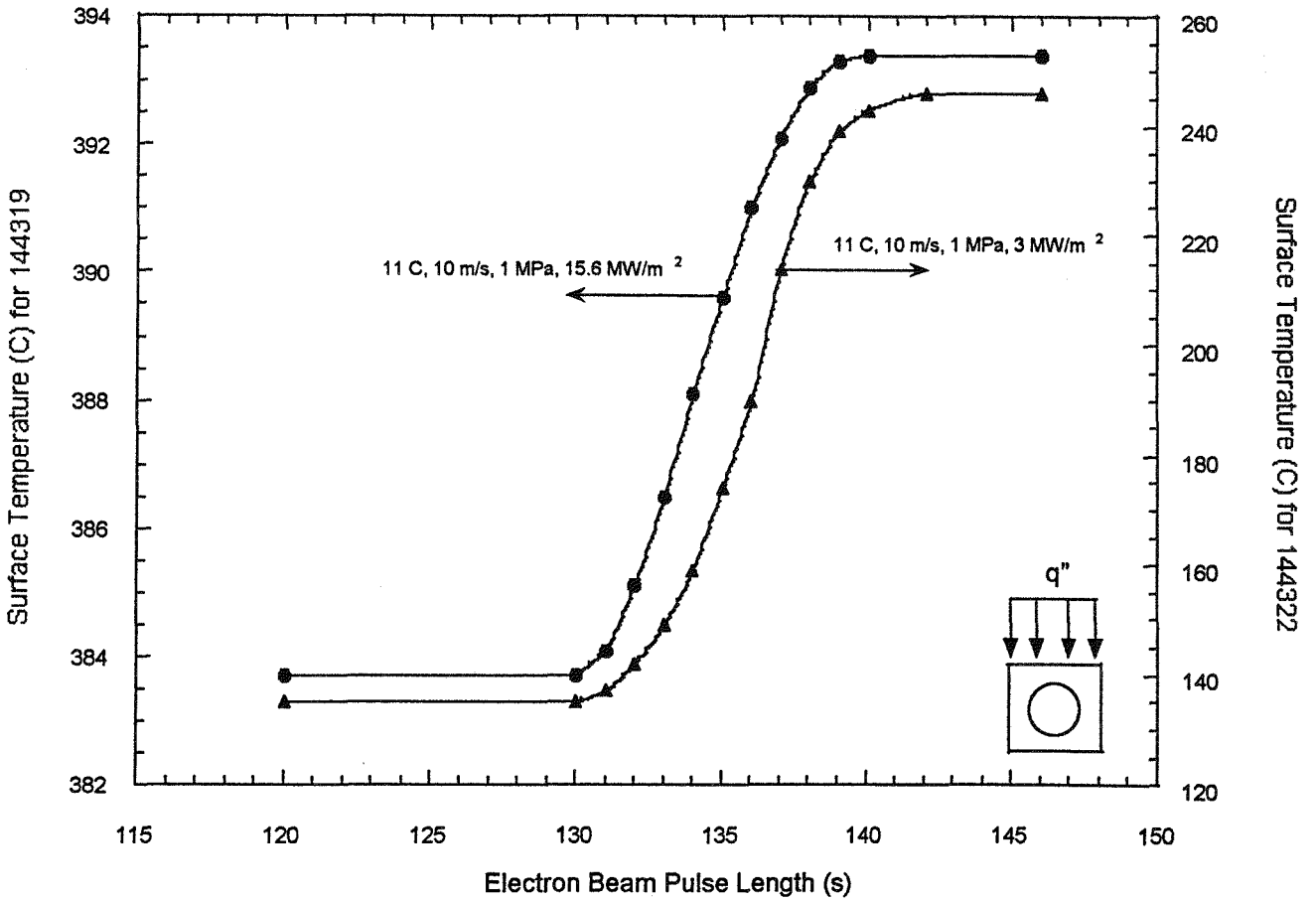

Figure 7-17: Surface (thermocouple) Temperature Response During FEA Simulated LOFA with Experimental Velocity Coast down.

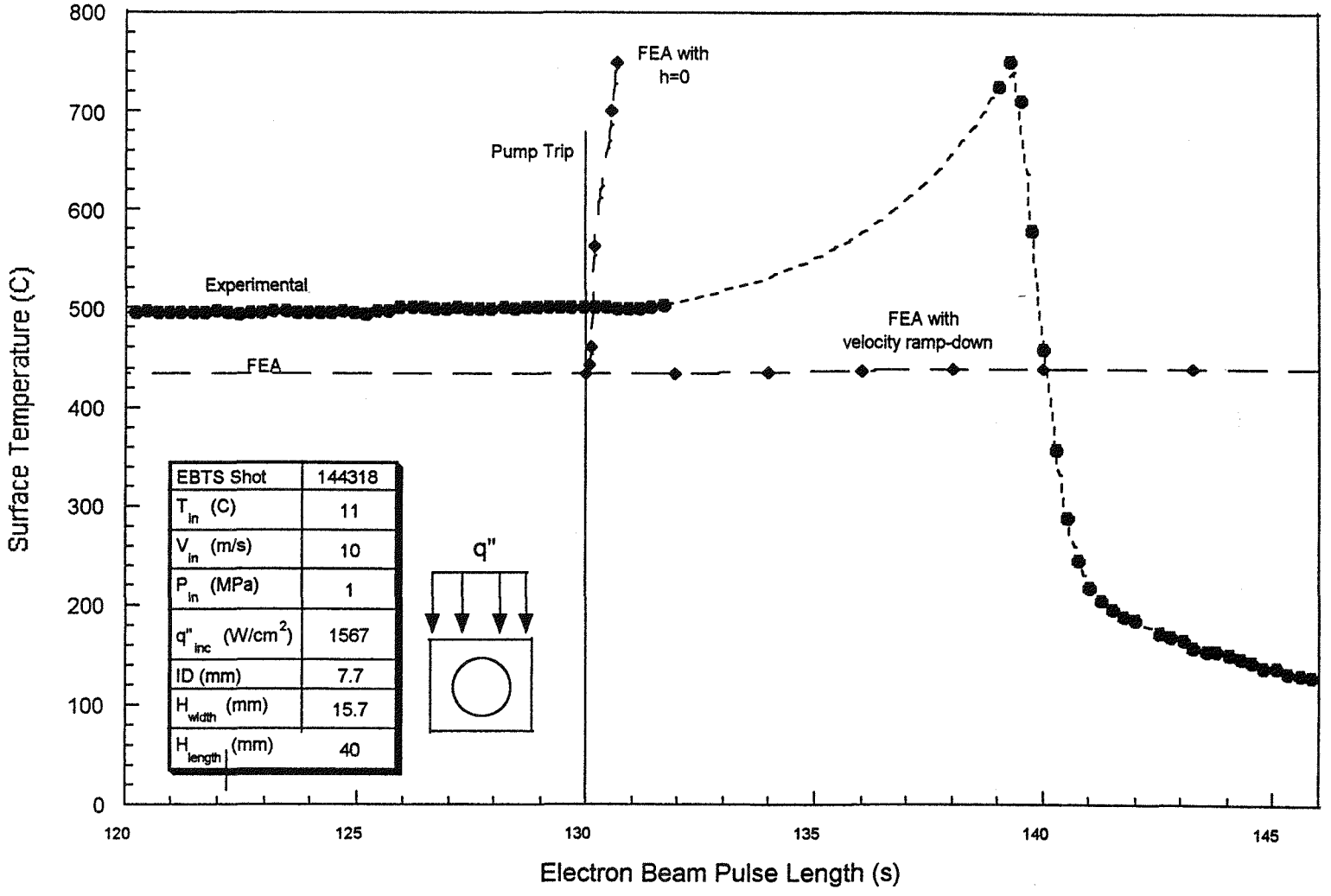

Figure 7-18: Results of FEA Modeling of Simulated LOFA using the Adiabatic and Experimental Velocity Coast Down Techniques.

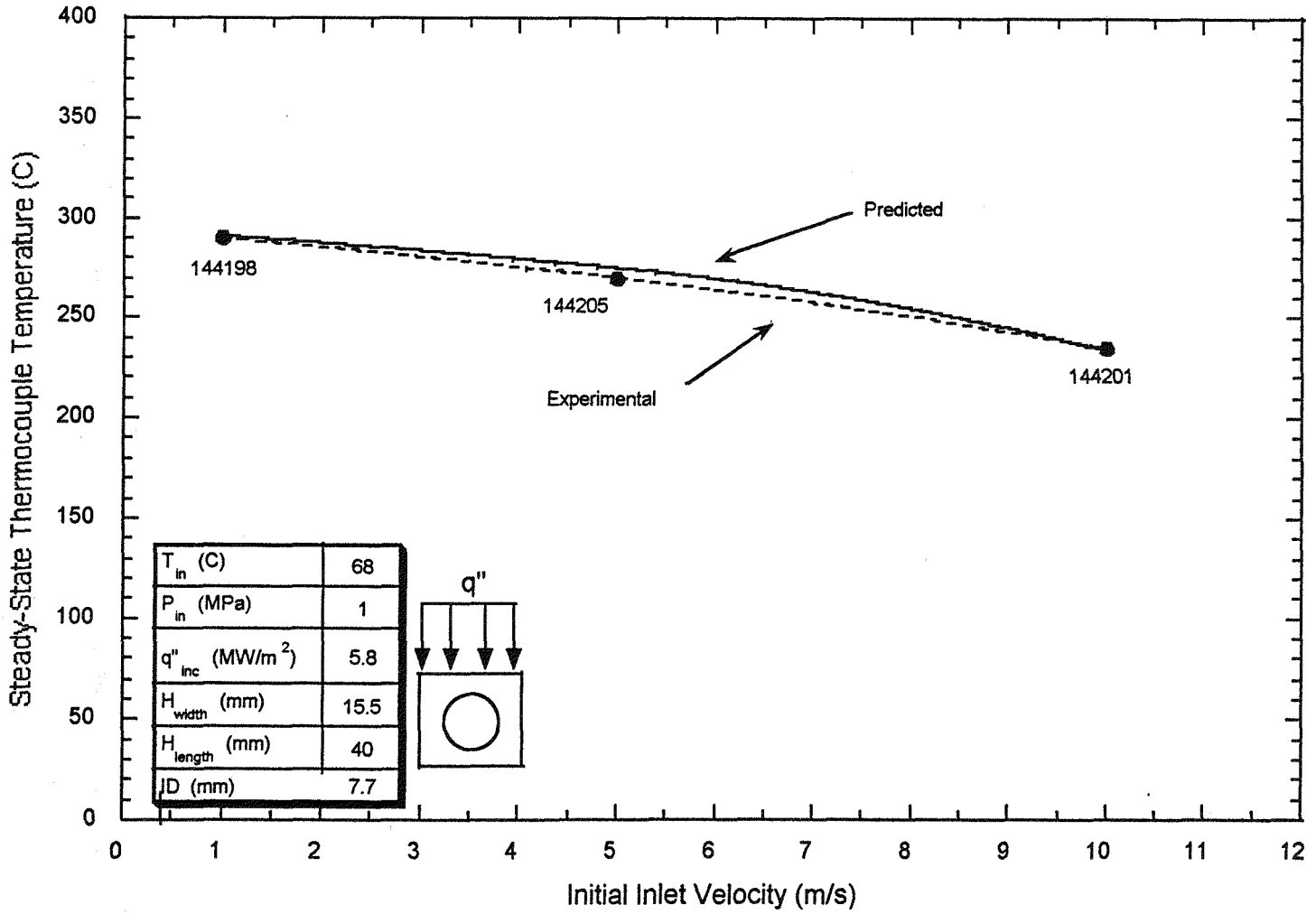

Figure 7-19: Comparison of Predicted and Experimental Thermocouple Temperature as a Function of Initial Inlet Velocity.

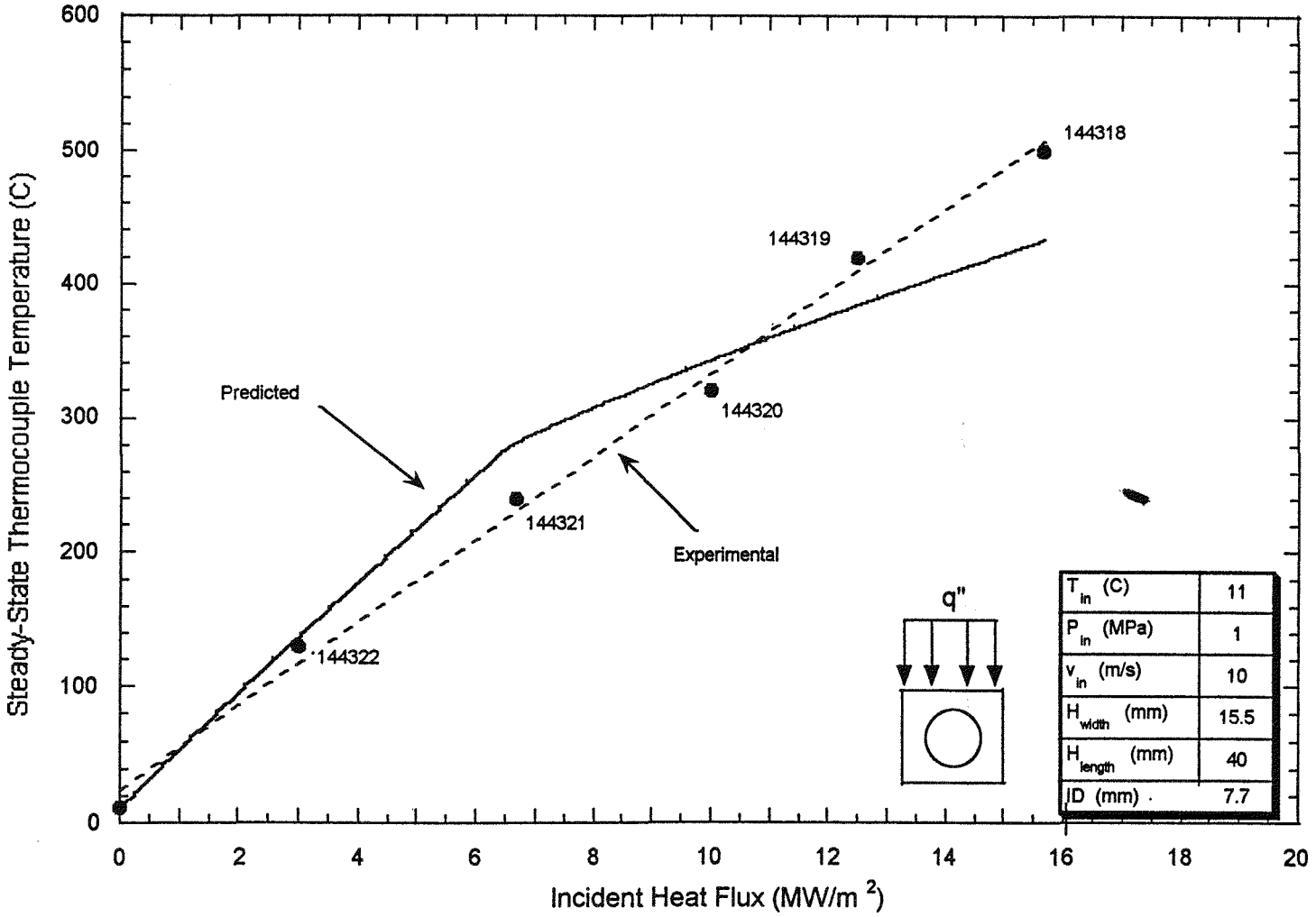

Figure 7-20: Comparison of Predicted and Experimental Thermocouple Temperature as a Function of Incident Heat Flux.

8.0 Conclusions

8.1 Time-to-Burnout Data

Eight experimental cases were run to generate TBO data for a prototypical ITER divertor plate during a simulated LOFA. The eight cases were devised to examine the behavior of the TBO for two scenarios:

1. constant inlet pressure, temperature, incident heat flux, and varying inlet velocity,
2. constant inlet pressure, temperature, velocity; and varying incident heat flux.

The TBO data behave as expected in both scenarios: increasing parabolically in Scenario 1 and decreasing parabolically in Scenario 2. The experimental TBO data further show that the TBO response is a strong function of initial inlet water velocity and incident heat flux.

The objective of the LOFA test was to generate experimental TBO data for a simulated LOFA. These data are intended to give fusion designers an approximate idea of the response time ITER plant engineers and operators will have to successfully detect the onset of a LOFA and safely shut down the plasma. This information is crucial to ensure that the typical ITER divertor plate can safely handle the thermal challenges of a LOFA.

Under normal ITER-like conditions, EBTS Shot 144201 has a TBO of 32 s. This suggests that if plant engineers and operators require more than 32 s for a response, then additional active circulation devices, such as standby emergency pumps, or other measures are necessary to ensure that the typical ITER divertor plate will not fail and dump water into the vacuum vessel. Further tests are required to verify this 32 s time for the given inlet conditions.

The LOFA data indicate that the strongest influence upon the TBO of a divertor plate design is the initial inlet water velocity. As one might imagine, if some sort of flow, even in a reduced state, continues through the divertor plate during the LOFA, the TBO could be increased. This means that flow continuation devices such as inertial flywheels on the pump shafts or fast-acting backup pumps for the primary coolant pump can be used to safely extend the TBO for a given divertor plate design.

The eight experimental cases presented in this report are far from being a statistically robust database upon which one can logically develop a correlation for the behavior of the heat transfer coefficient during a LOFA. Rather, more experiments are necessary and at differing inlet conditions and incident heat fluxes to accurately model the heat transfer coefficient relevant to a LOFA.

8.2 Heat Transfer Coefficient

Finite element analyses of the divertor plate under experimental conditions are performed to determine the accuracy of current finite element modelling of the plate's thermal response during a simulated LOFA. Two different techniques are used to model the LOFA: the adiabatic method and the velocity coast down method.

As a first attempt at modelling the loss of coolant velocity during a simulated LOFA, the heat transfer coefficient was set to a value of zero at the time of pump trip. Although this is not physically possible, the case was run as a conservative boundary calculation. Comparison of the predicted TBOs with the experimental TBOs showed that this technique was very inaccurate. On average, the predicted TBOs for the experimental cases were at least a factor of four lower than the experimental TBOs.

In an attempt to better model the divertor plate's thermalhydraulics during a simulated LOFA, the experimentally measured water velocity coast down was programmed into the ABAQUS film subroutine. This coast down was triggered when the calculation time equaled that of the experimental trip time for the coolant pump. The results showed a modest increase in surface temperature as the temperatures in the back regions of the wetted perimeter increased to initiate the more efficient heat transfer associated with boiling. Once the small temperature excursion occurred, steady-state temperatures were predicted by ABAQUS. This resulted because the film subroutine used by ABAQUS currently does not have any heat transfer coefficient correlations beyond that of nucleate boiling.

The failure of these methodologies for modelling the LOFA-induced thermal response of a prototypical divertor plate suggests that further research into the LOFA phenomenon is definitely necessary. It is postulated that the inclusion of the transition and film-boiling regimes, along with the experimentally measured water velocity coast down, into the ABAQUS film subroutine will improve the ability of ABAQUS to model the heat transfer coefficient behavior during a LOFA. It is further surmised that information about the TBO might be contained in the BSM for given inlet conditions. The pursuit of these hypotheses is necessary for understanding and preventing damage to PFCs due to a LOFA event.

References

[1] "Experience Gained During the First Tritium Experiment with Relevance to the Full D-T Phase of JET," the JET Team, Fusion Engineering and Design, 22, 77-84, 1993.

[2] M. M. Menon et al., "Particle Exhaust Scheme Using an In-Vessel Cryocondensation Pump in the Advanced Divertor Configuration of the DIII-D Tokamak," Fusion Technology, 22, 356-370, 1992.

[3] "Steady-State Heat and Particle Removal with the Actively Cooled Phase III Outboard Pump Limiter in Tore Supra," paper presented at the 11th International Conference on Plasma Surface Interactions, Mito, Japan, 1994.

[4] J. D. Hosea et al., "Deuterium-Tritium Experiments on the Tokamak Fusion Test Reactor," Fusion Technology, 26, 389-398, 1994.

[5] PRA Repository: Surry and Sequoyah, Vol 3, Electric Power Research Institute, Palo Alto, CA, NSAC-152, 1991.

[6] Severe Accident Risk, Final Summary Report, NUREG-1150, U.S. Nuclear Regulatory Commission, 1990.

[7] Reactor Safety Study, Appendix II, WASH-1400, U.S. Nuclear Regulatory Commission, 1975.

[8] T. J. Boucher et al., Scaling Analysis for a Savannah River Reactor Scaled Model Integral System, EGG-EAST-9382, EG&G Idaho, Inc., 1990.

[9] J. R. Welty et al., Fundamentals of Momentum, Heat, and Mass Transfer, 2nd ed.,Chapter 10, Wiley, 1976.

[10] R. B. Byrd et al., Transport Phenomena, Wiley, Chapters 6 & 10, 1960.

[11] T. K. Larson et al., Scaling Criteria and An Assessment of Semiscale MOD-3 Scaling for Small Break Loss-of-Coolant Accidents, EGG-M-21082, EG&G Idaho, Inc., 1982.

[12] K. G. Condie et al., Evaluation of Integral Continuing Experimental Capability (CEC) Concepts for Light Water Reactor Research - PWR Scaling Concepts, NUREG/CR-4824, US Nuclear Regulatory Commission, 1987.

[13] T. D. Marshall and L. C. Cadwallader, In-Vessel ITER Tubing Failure Rates for Selected Materials and Coolants, EGG-FSP-10928, EG&G Idaho, Inc., 1-1 to 1-2, 1994.

[14] J. Schlosser, "Tests of NET Divertor Thermal Hydraulics Mockup Water-Cooled by Circular Swirl Tubes," presented at Divertor Thermal-hydraulics Workshop, Rome, Italy, 1992.

[15] M. Araki, M. Akiba, and M. Suzuki, "Recent Activity of Developing Plasma Facing Components at JAERI," presented at Second Specialists' Workshop on High Heat Flux Components Thermalhydraulics, Rome, Italy, 1992.

[16] G. P. Celata, M. Cumo, and A. Mariani, "Burnout in Highly Subcooled Water Flow Boiling in Small-Diameter Tubes," Transactions of the American Nuclear Society, 64, 1991.

[17] R. D. Watson, ed., "ITER Divertor Engineering Design, Summary of Joint Working Session," Garching, Germany, Max Planck Institute for Plasma Physics, October 1989.

[18] K. J. Dietz et al., "Experience with High Heat Flux Components in Large Tokamaks," Fusion Engineering and Design, 16, 229-251, 1991.

[19] T. D. Marshall and L. C. Cadwallader, In-Vessel ITER Tubing Failure Rates for Selected Materials and Coolants, EGG-FSP-10928, EG&G Idaho Inc., A-9, 1994.

[20] R. D. Boyd, "Critical Heat Flux and Heat Transfer Transition for Subcooled Flow Boiling," J. Heat Transfer, 113, 264, 1991.

[21] J. A. Koski, et al., "Experimental Verification of Subcooled Flow Boiling for Tokamak Pump Limiter Designs,"American Society of Mechanical Engineers, 87-HT-45, 1987.

[22] R. Moffat, "Describing the Uncertainties in Experimental Results," Experimental Thermal and Fluid Science, 1, 3-17, 1988.

[23] M. Araki, R. D. Watson, T. D. Marshall, P. D. Rockett, and M. Akiba, "Effect of Subcooling on the Critical Heat Flux Under One-Sided Heating Conditions," in Proceedings of the 18th Symposium on Fusion Technology, Karlsruhe, Germany, 1994.

[24] J. Schlosser and J. Boscary, "Thermal Hydraulic Tests at NET/ITER Relevant Conditions on Divertor Targets Using Swirl Tubes," Proceedings of the 6th International Conference on Nuclear Reactor Thermalhydraulics, Grenoble, France, pp. 815-824, 1993.

[25] J. Schlosser and J. Boscary, "Thermal Hydraulic Tests at NET/ITER Relevant Conditions on Divertor Targets Using Swirl Tubes," Proceedings of the 6th International Conference on Nuclear Reactor Thermalhydraulics, Grenoble, France, pp. 815-824, 1993.

[26] Hibbitt, Karlsson, and Sorensen Company, Version 4-8 Finite Element Analysis Code, Pawtucket, RI, 1992.

[27] M. Ozisik, Heat Transfer - A Basic Approach, McGraw-Hill, New York, pp. 300-340, 1985.

[28] R. Thom, W. Walker, W. Fallon, and G. Resing, "Boiling in Subcooled Water During Flow Up Heated Tubes in Annuli," Symposium on Boiling Heat Transfer in Steam Generating Units and Heat Exchangers, Institute of Mechanical Engineers Paper No. 6., Manchester, London, 1965.

[29] T. D. Marshall, R. D. Watson, J. M. McDonald, D. L. Youchison, "An Experimental Investigation of the Post-CHF Enhancement Factor a Prototypical ITER Divertor Plate with Water Coolant," Proceeding of the 16th IEEE/NPSS Symposium on Fusion Engineering, Champaign, IL, 1995.

[30] Moffat, R. "Describing the Uncertainties in Experimental Results," Experimental Thermal and Fluid Science, 1, 3-17, 1988.

[31] S. K. Ho et al., "Assessment of Emergency Plasma Shutdown Schemes for ITER," Fusion Technology, 19, 1322-1326, 1991.

[PAGE INTENTIONALLY LEFT BLANK]

Appendix A: Experimental Data

SANDIA NATIONAL LABORATORIES
Fusion Technology
Shot 144322

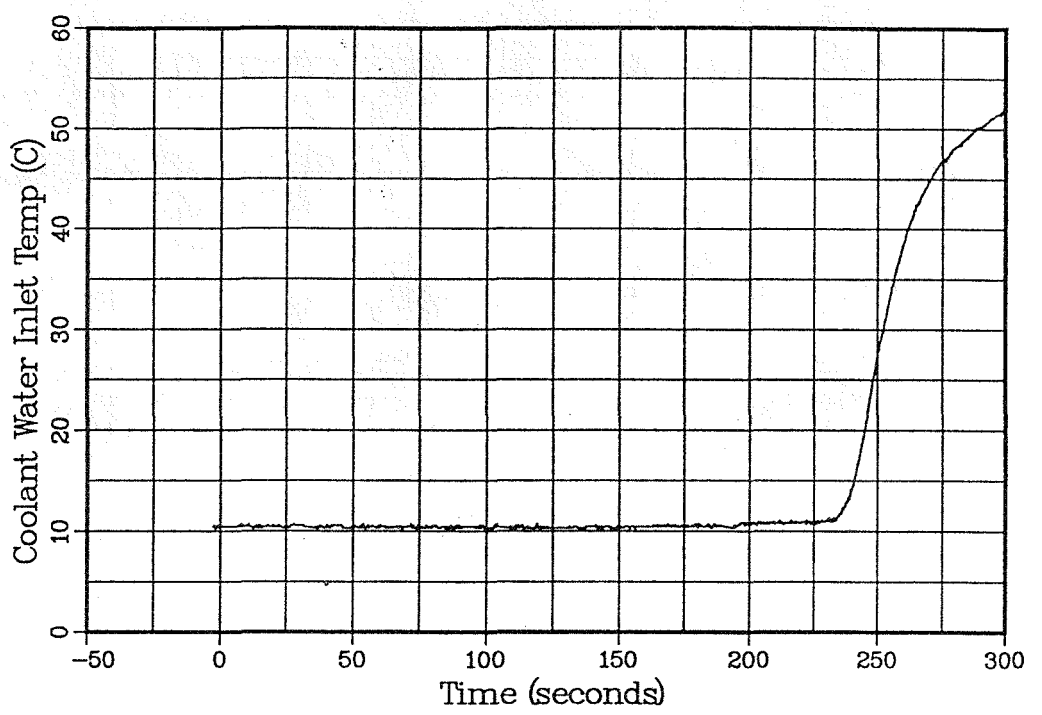

SANDIA NATIONAL LABORATORIES
Fusion Technology
Shot 144322

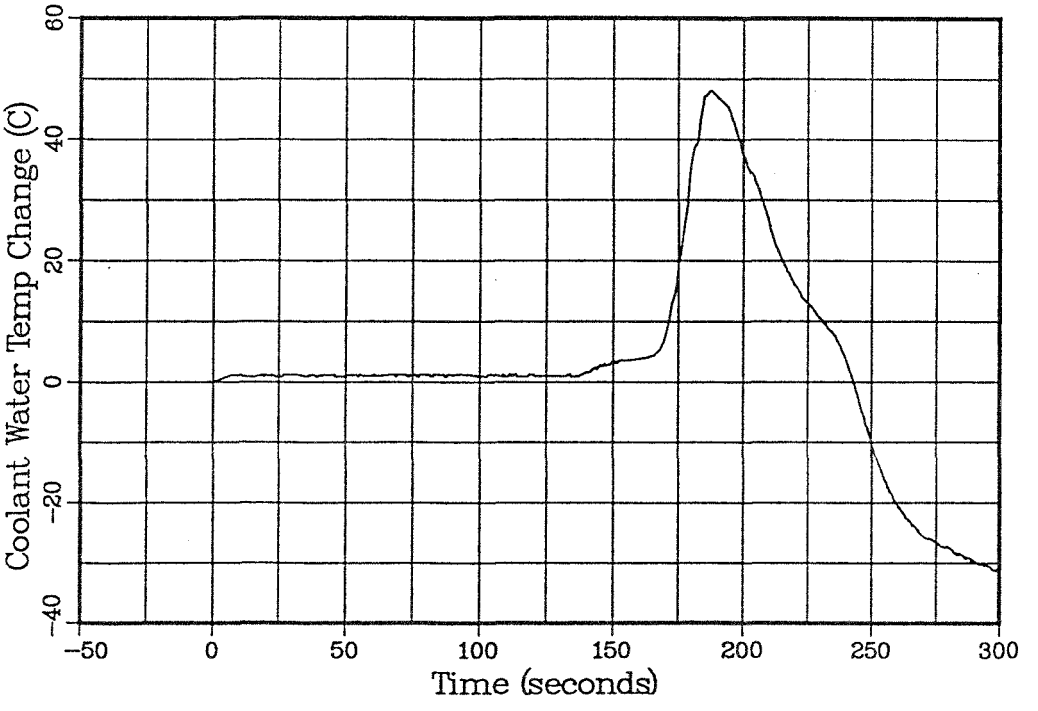

SANDIA NATIONAL LABORATORIES
Fusion Technology
Shot 144322

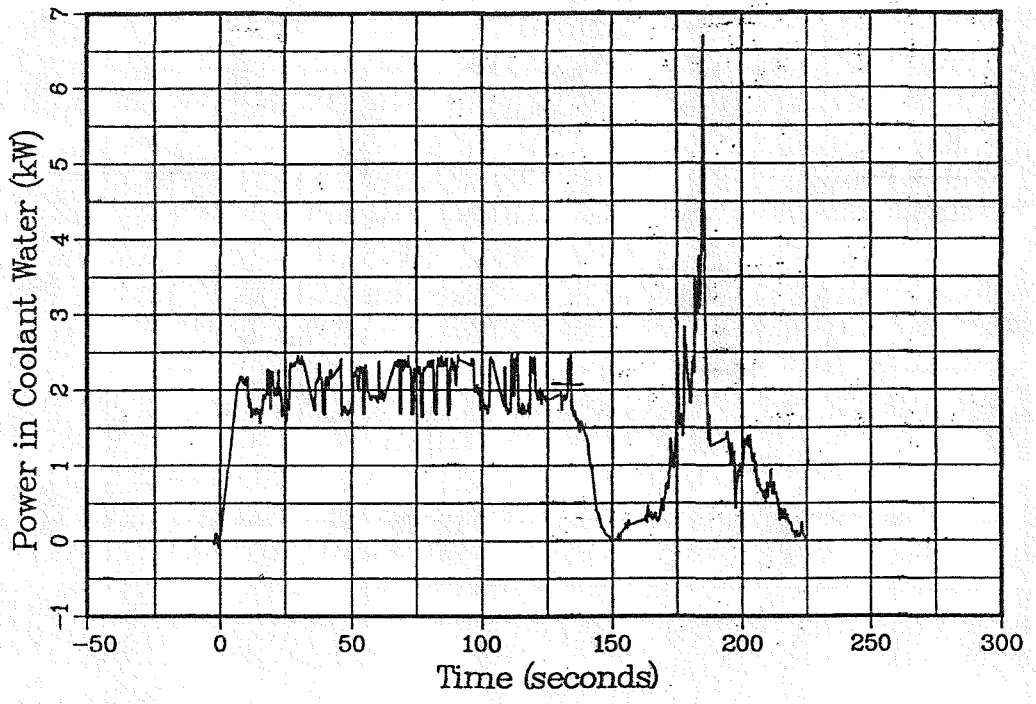

SANDIA NATIONAL LABORATORIES
Fusion Technology
Shot 144322

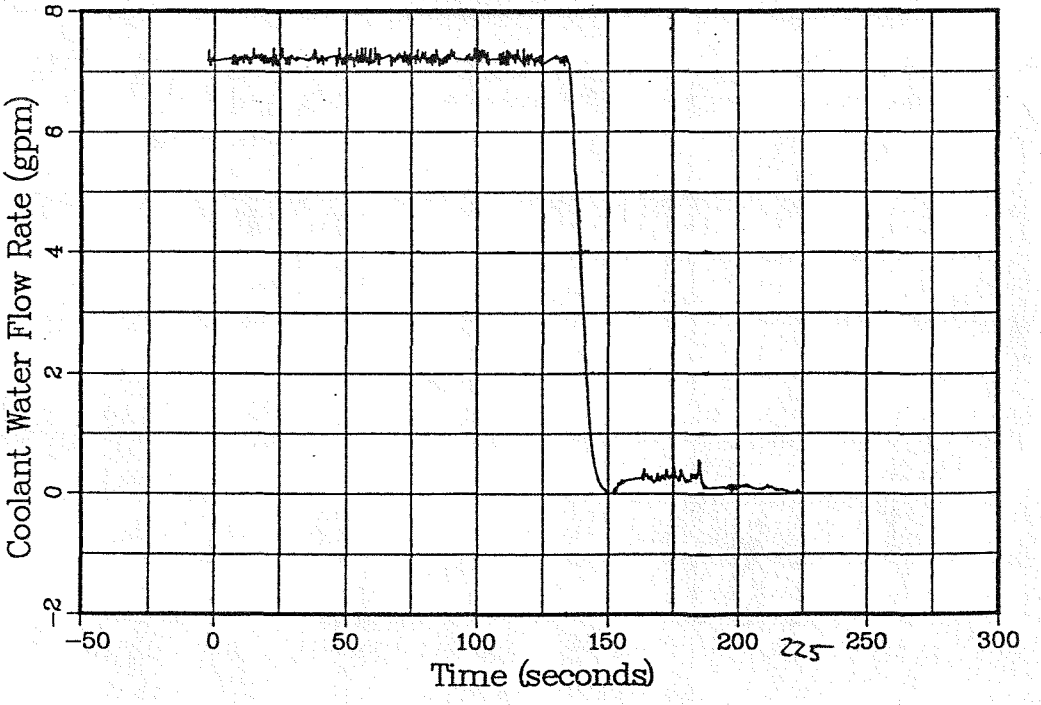

SANDIA NATIONAL LABORATORIES
Fusion Technology
Shot 144322

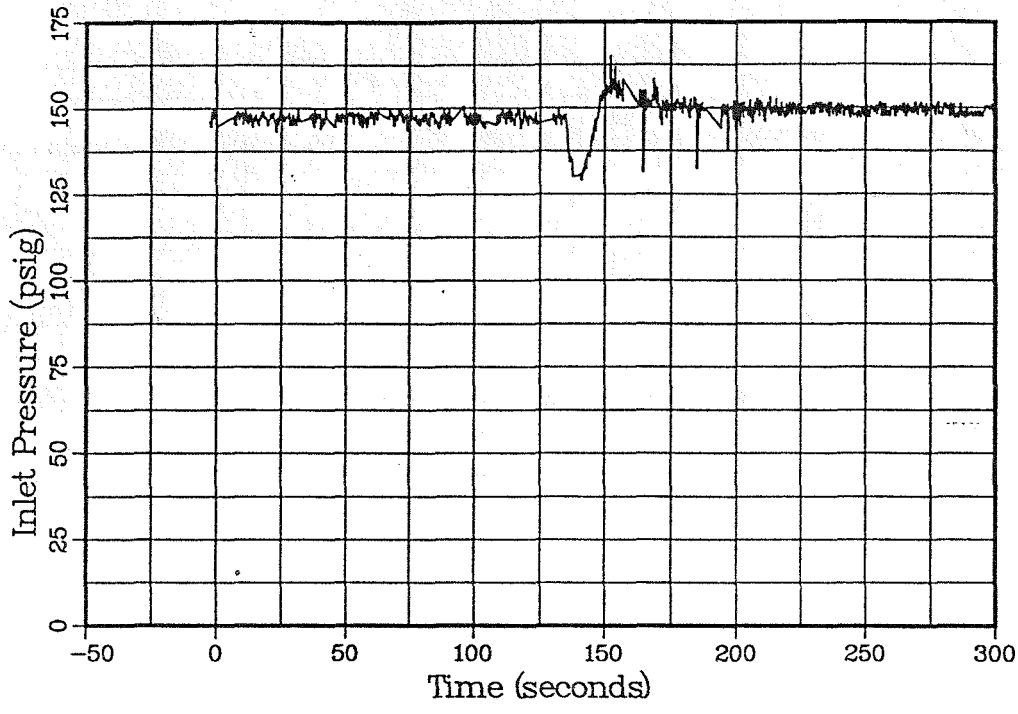

SANDIA NATIONAL LABORATORIES
Fusion Technology
Shot 144322

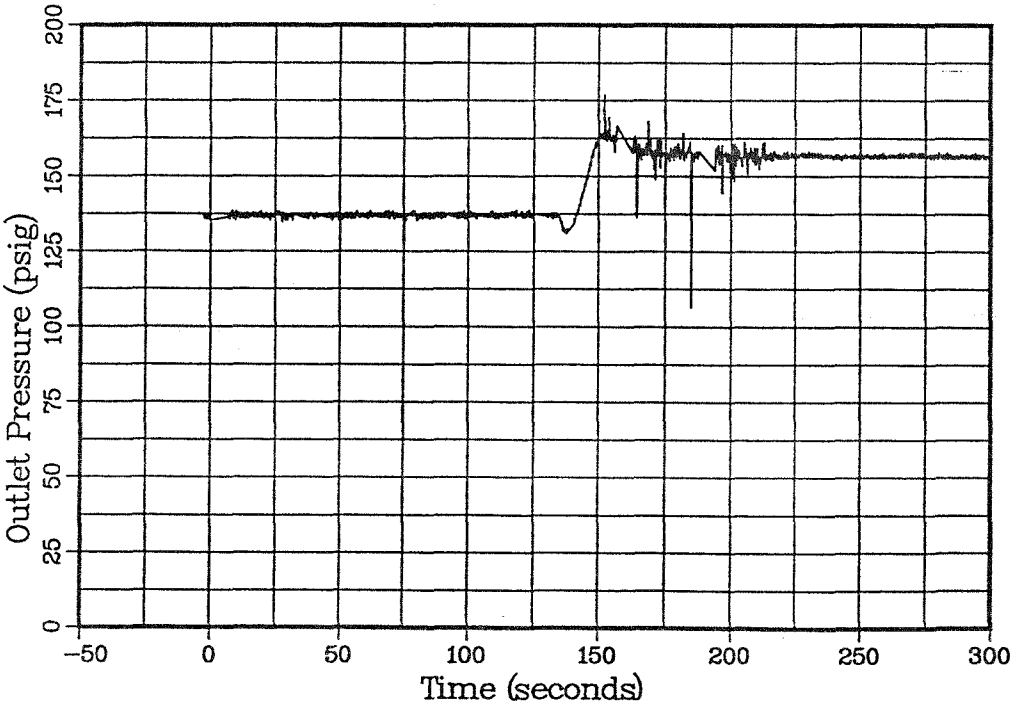

SANDIA NATIONAL LABORATORIES
Fusion Technology
Shot 144322

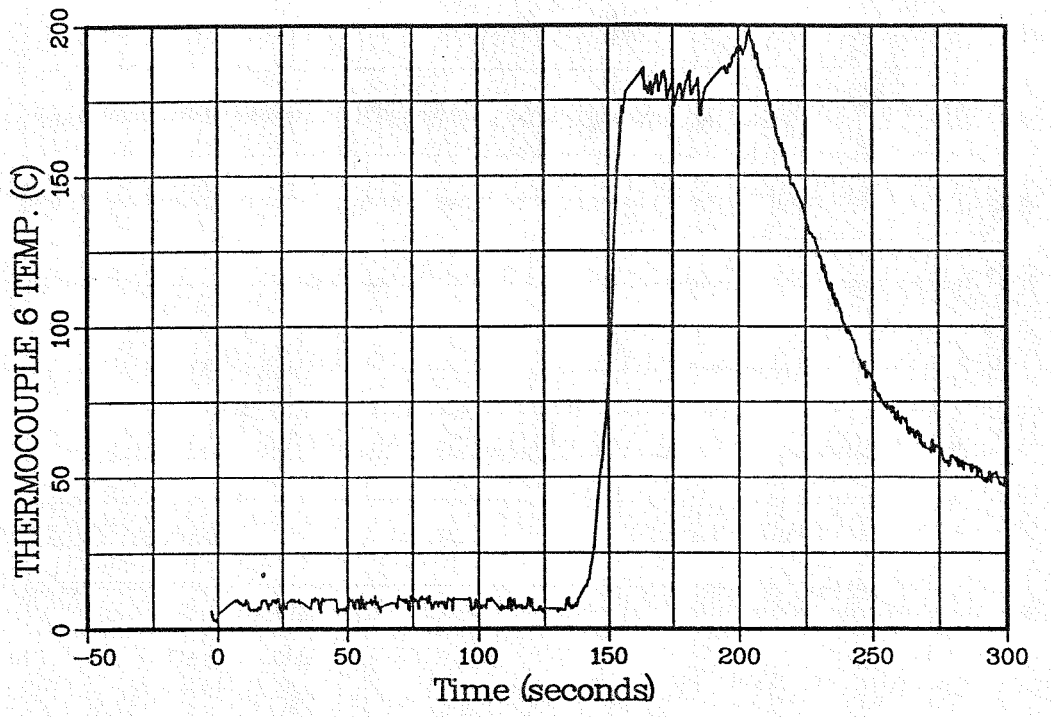

SANDIA NATIONAL LABORATORIES
Fusion Technology
Shot 144322

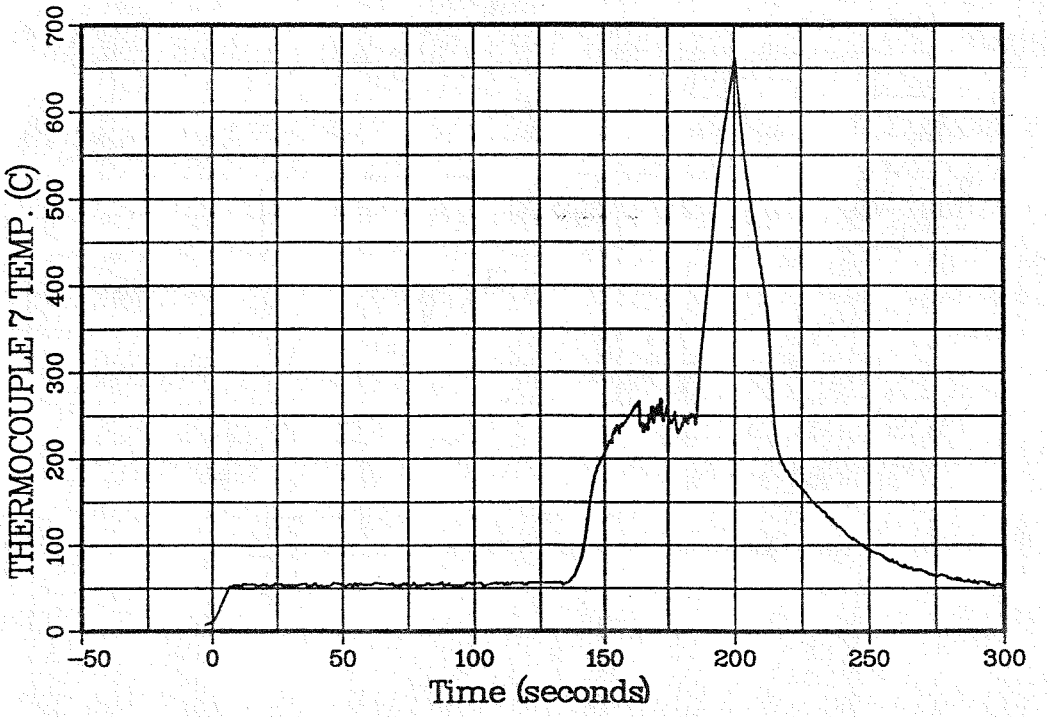

SANDIA NATIONAL LABORATORIES
Fusion Technology
Shot 144322

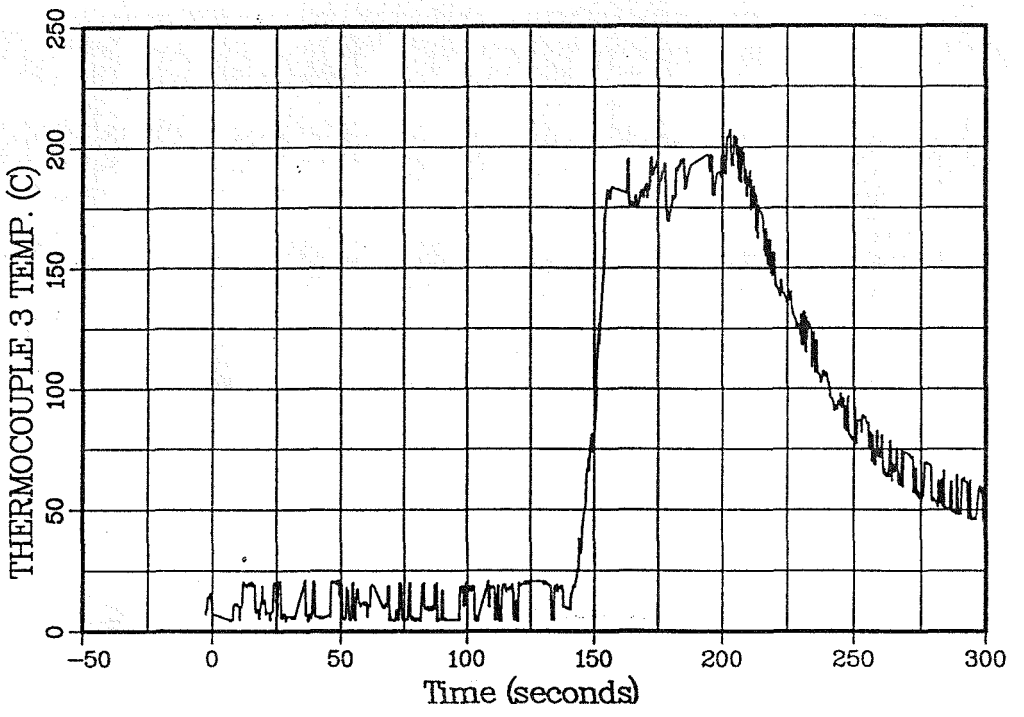

SANDIA NATIONAL LABORATORIES
Fusion Technology
Shot 144322

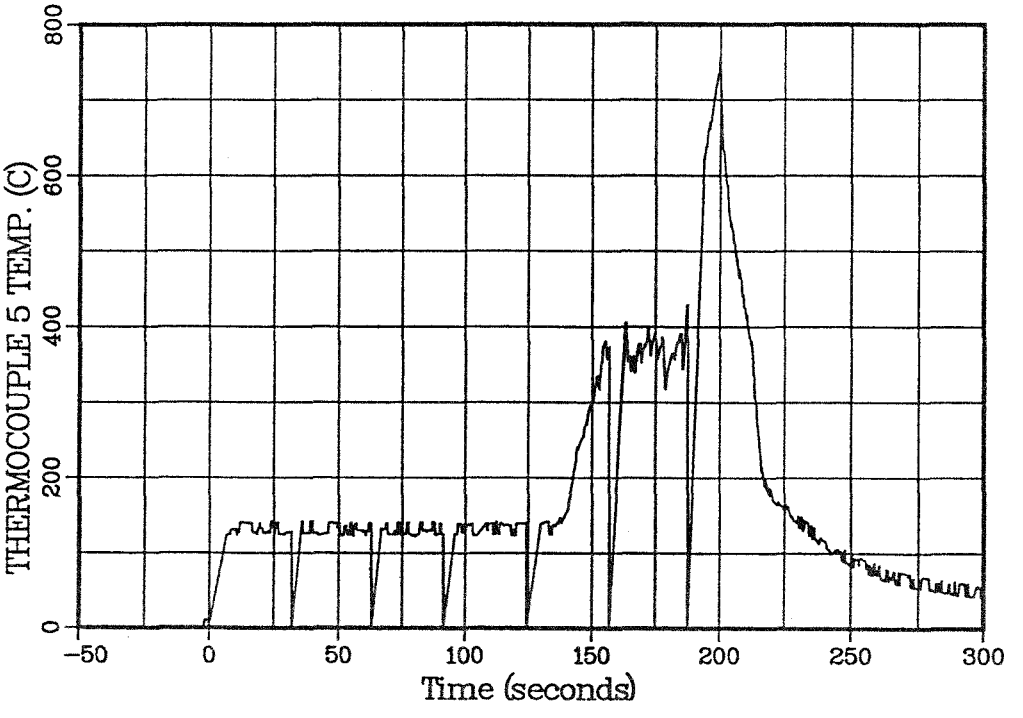

SANDIA NATIONAL LABORATORIES
Fusion Technology
Shot 144322

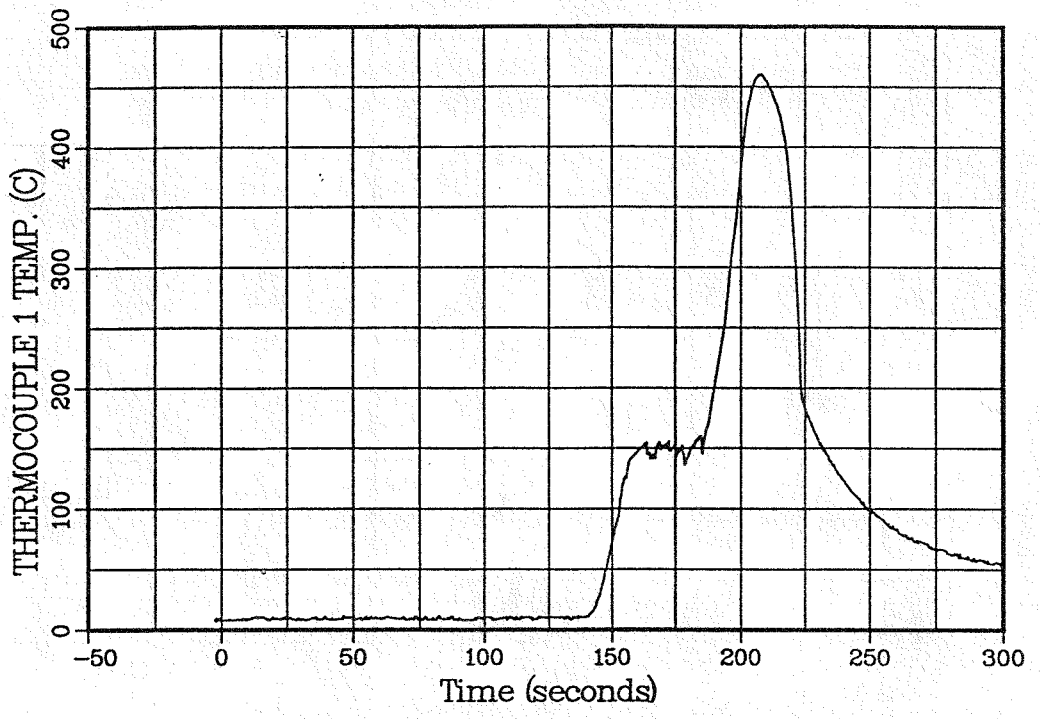

SANDIA NATIONAL LABORATORIES
Fusion Technology
Shot 144322

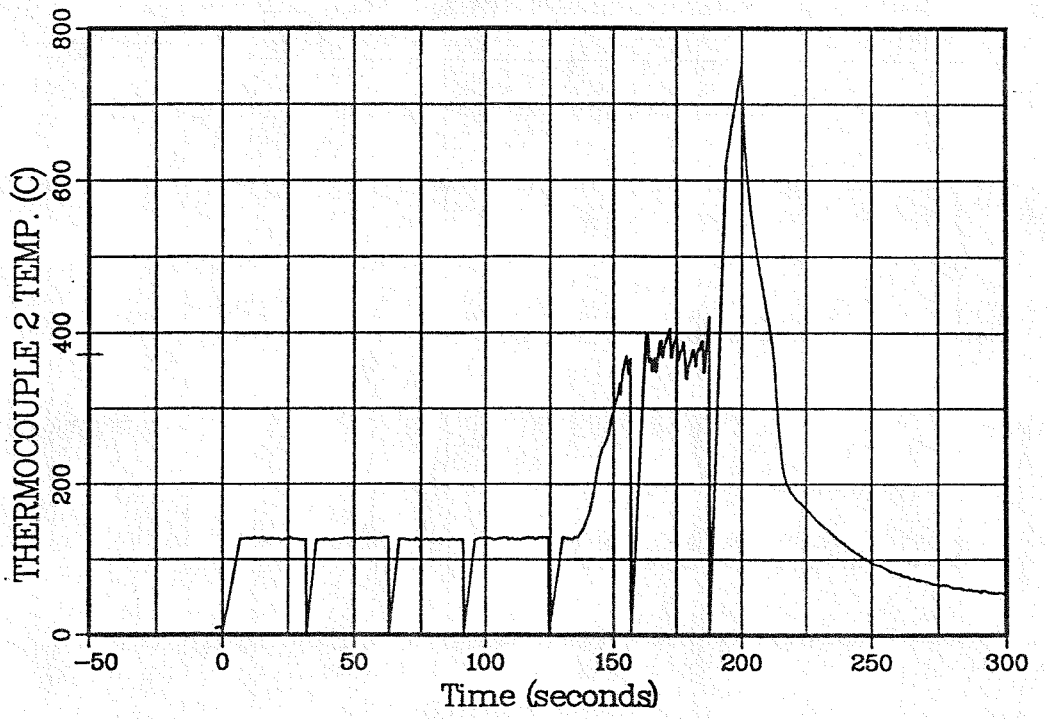

SANDIA NATIONAL LABORATORIES
Fusion Technology
Shot 144322

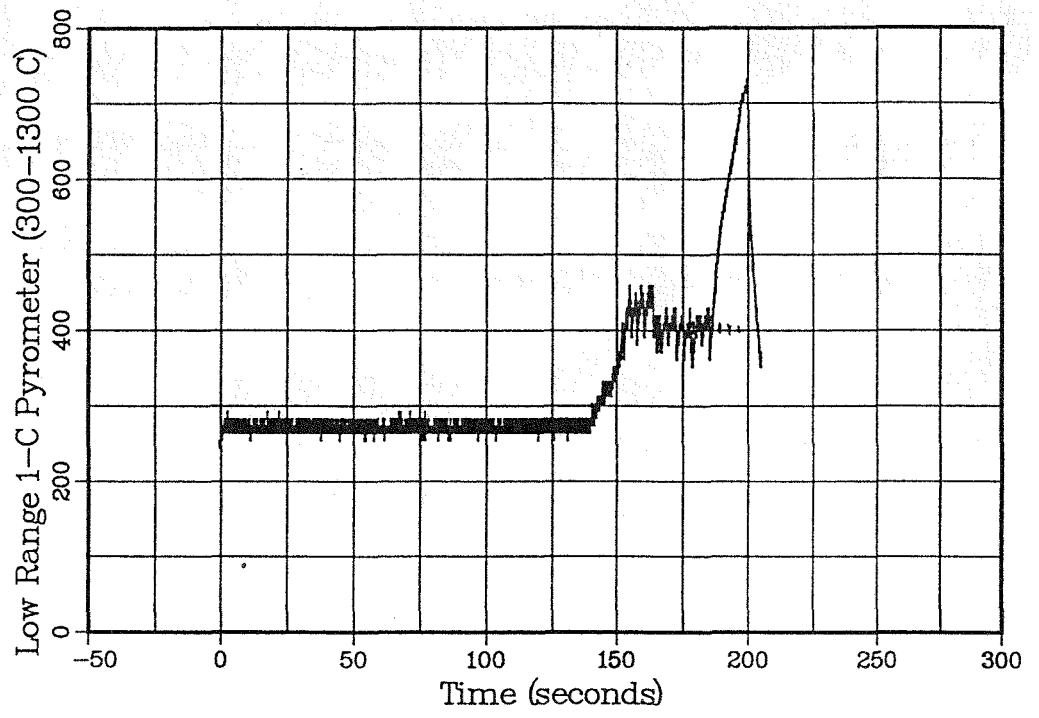

SANDIA NATIONAL LABORATORIES
Fusion Technology
Shot 144322

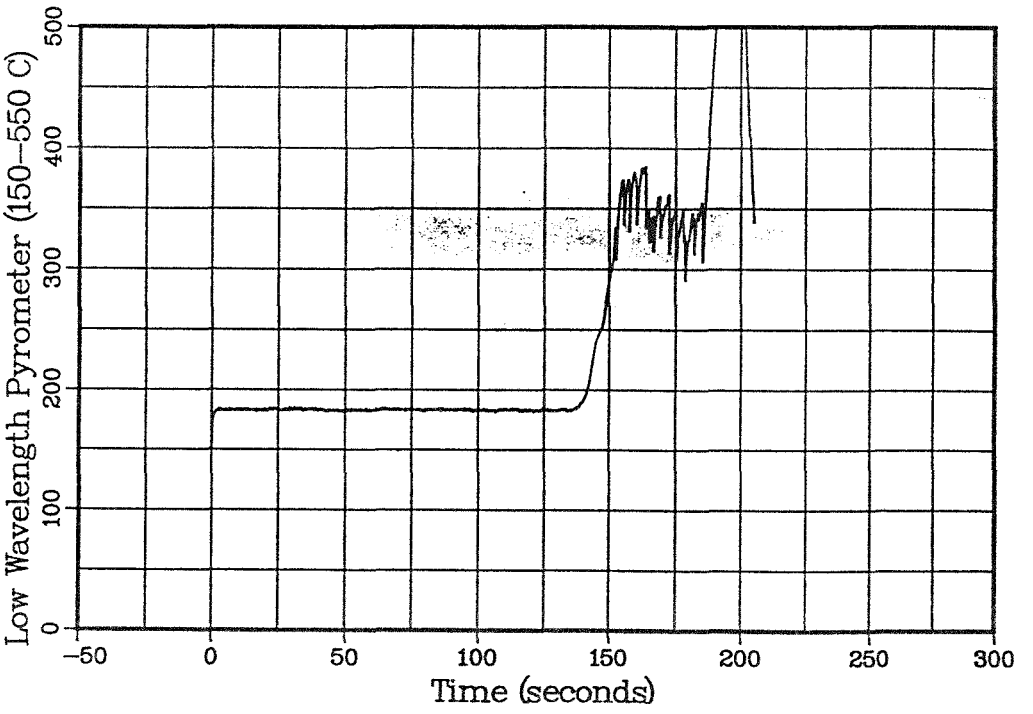

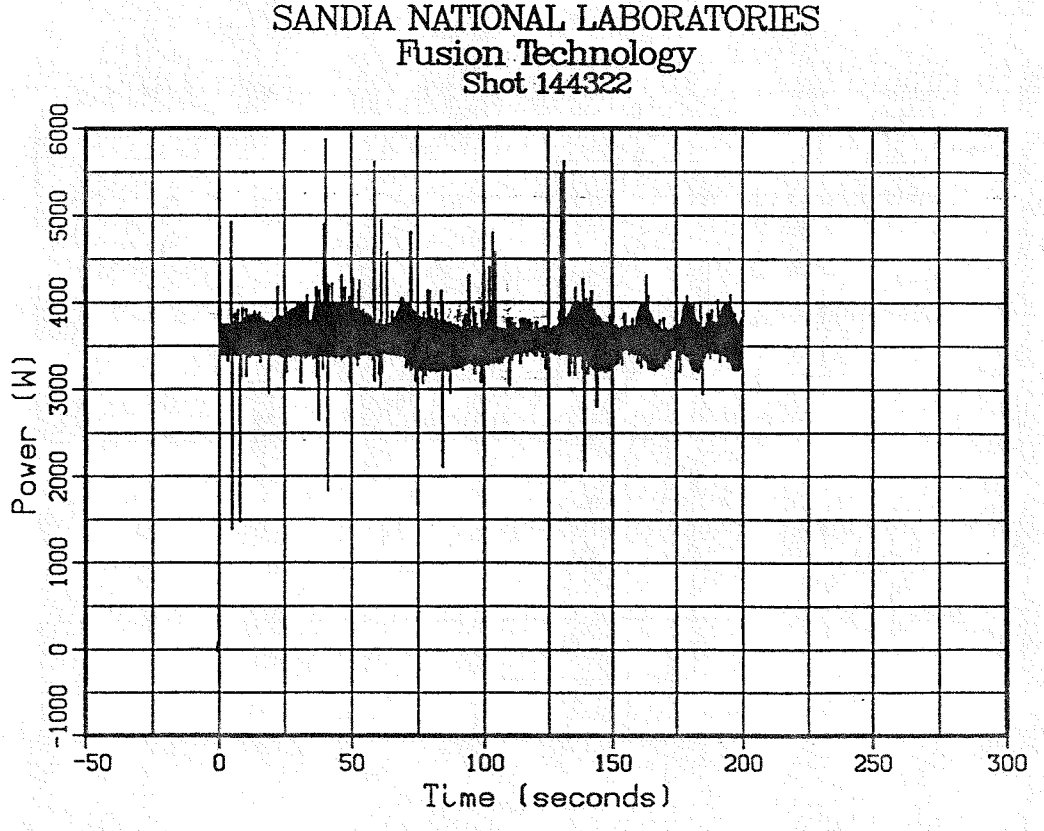
SANDIA NATIONAL LABORATORIES
Fusion Technology
Shot 144322
Power (W)
6000
5000
4000
3000
2000
1000
0
-1000
-50
0
50
100
150
200
250
300
Time (seconds)

SANDIA NATIONAL LABORATORIES
Fusion Technology
Shot 144321

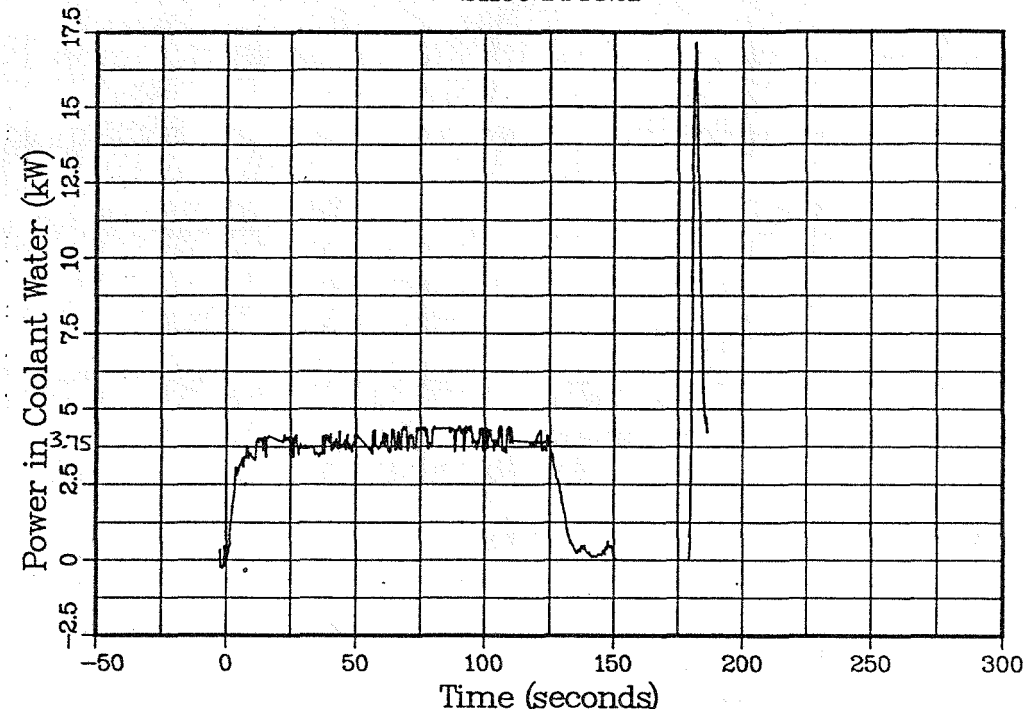

SANDIA NATIONAL LABORATORIES
Fusion Technology
Shot 144321

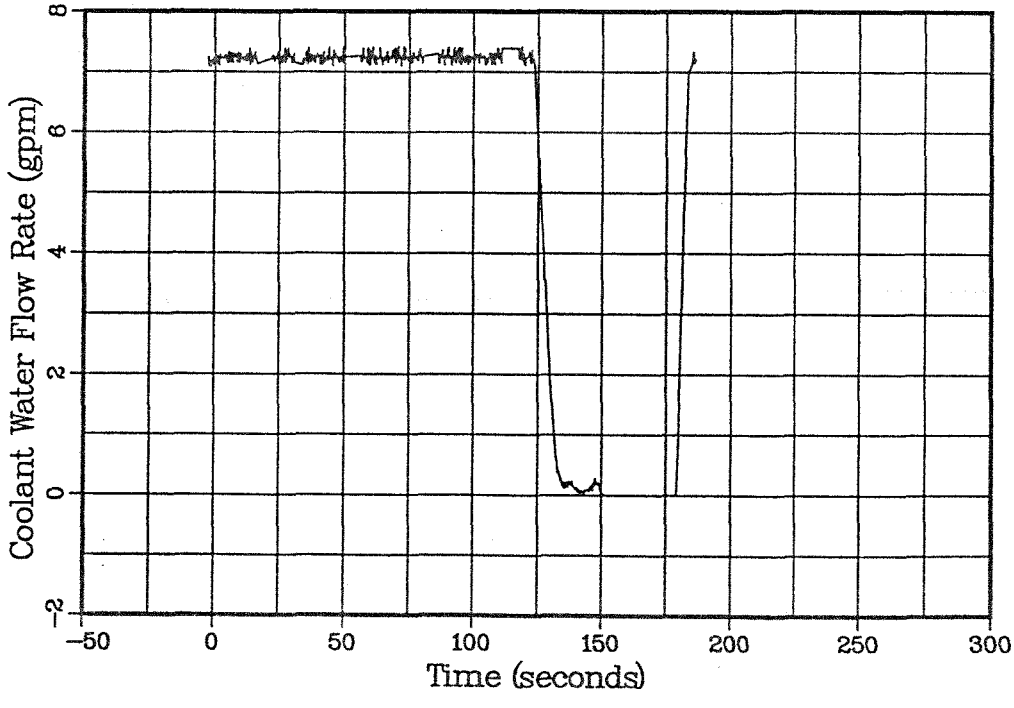

SANDIA NATIONAL LABORATORIES
Fusion Technology
Shot 144321

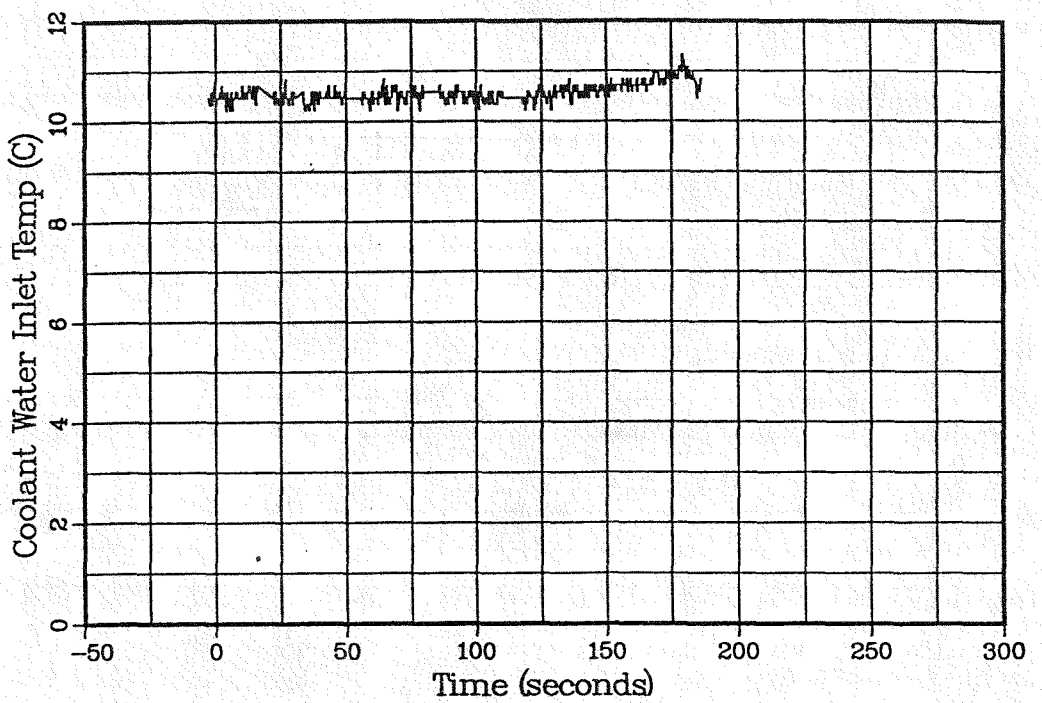

SANDIA NATIONAL LABORATORIES
Fusion Technology
Shot 144321

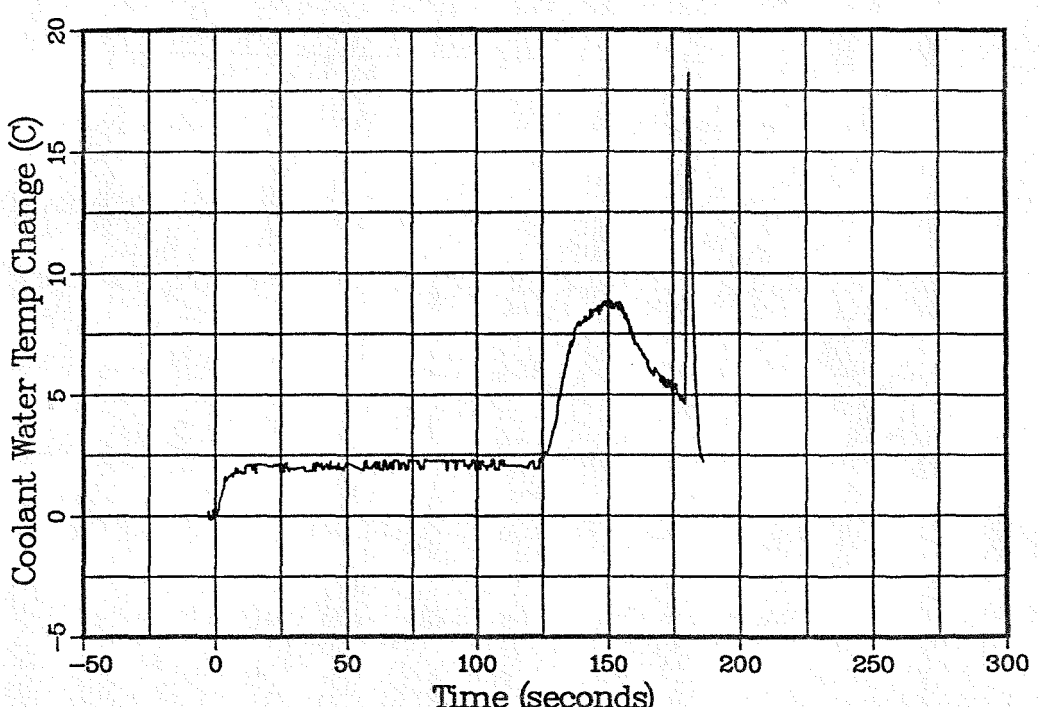

SANDIA NATIONAL LABORATORIES
Fusion Technology
Shot 144321

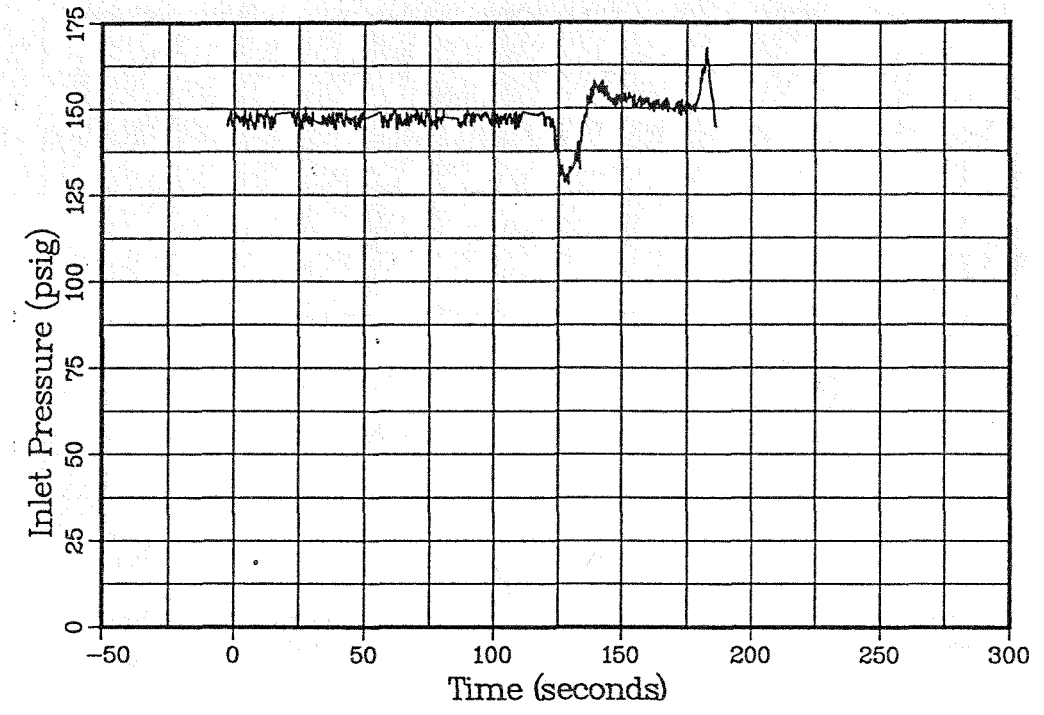

SANDIA NATIONAL LABORATORIES
Fusion Technology
Shot 144321

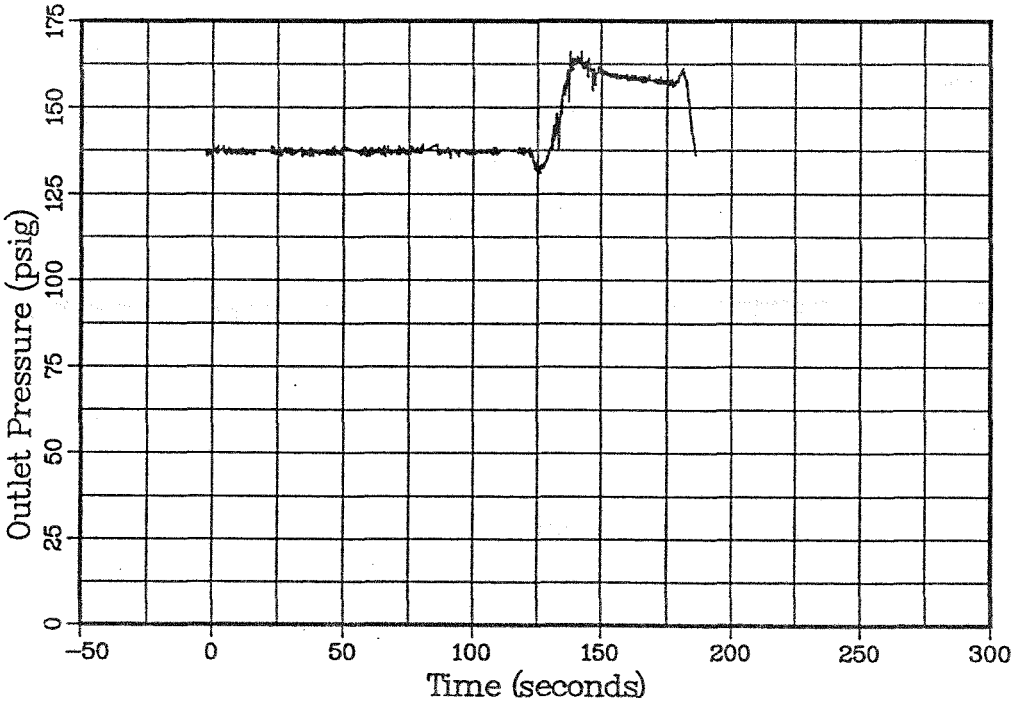

SANDIA NATIONAL LABORATORIES
Fusion Technology
Shot 144321

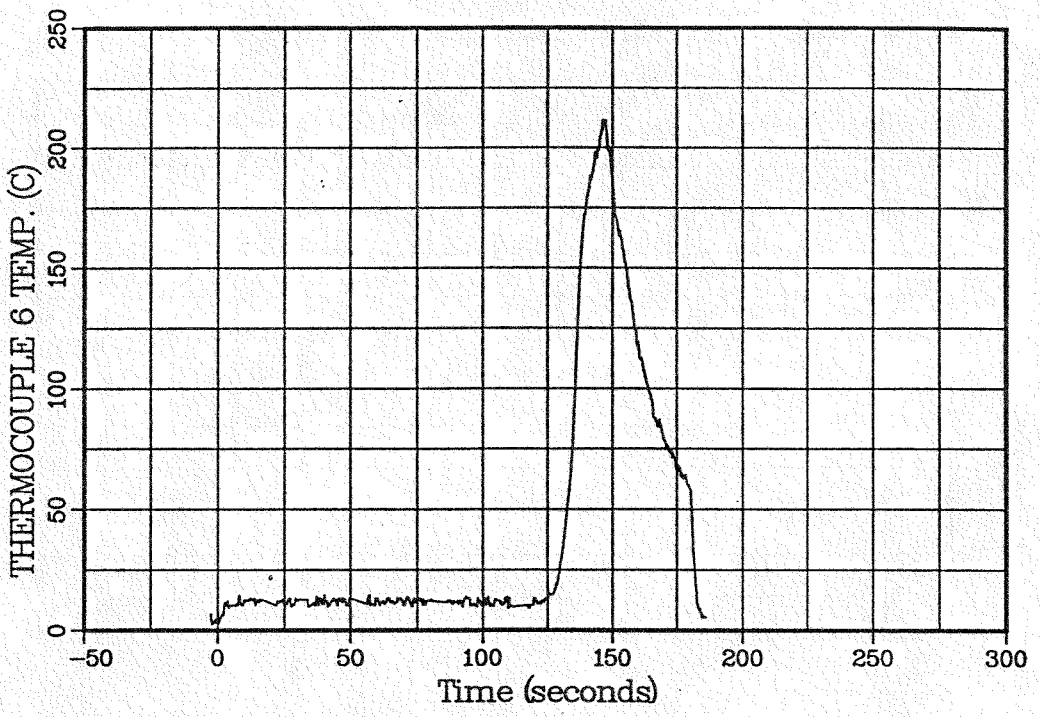

SANDIA NATIONAL LABORATORIES
Fusion Technology
Shot 144321

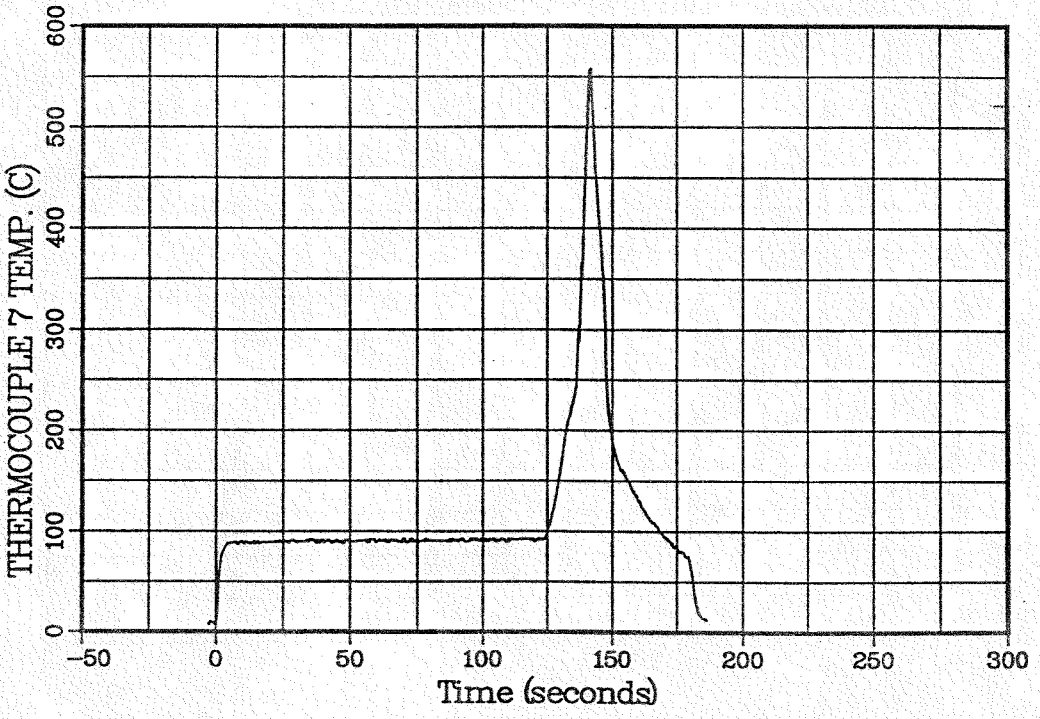

SANDIA NATIONAL LABORATORIES
Fusion Technology
Shot 144321

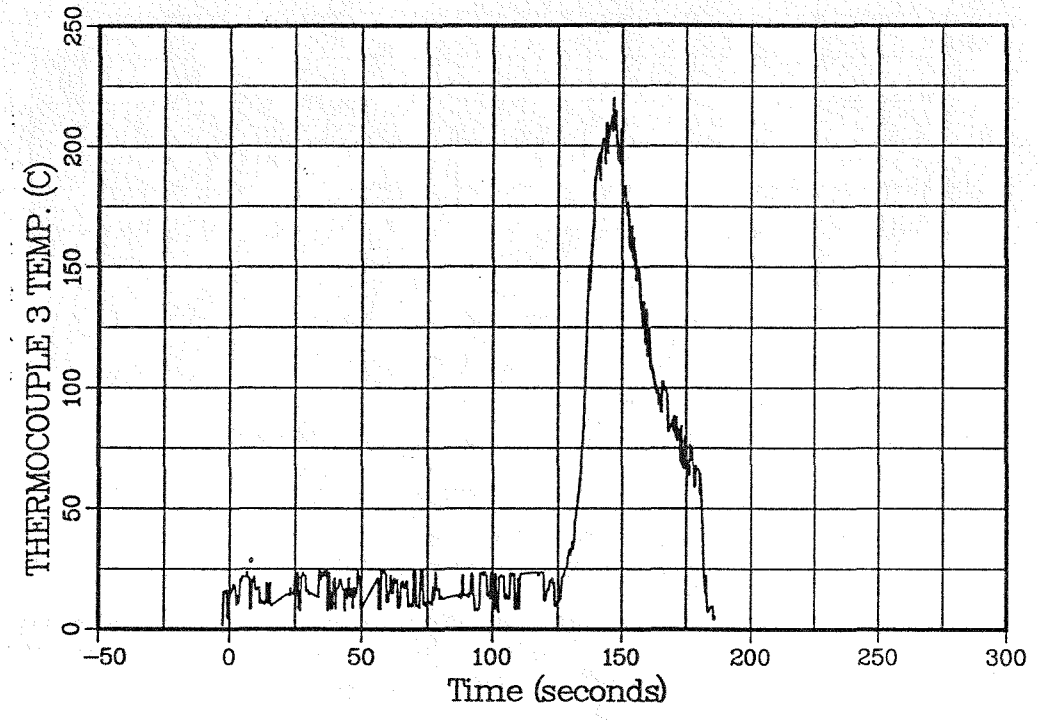

SANDIA NATIONAL LABORATORIES
Fusion Technology
Shot 144321

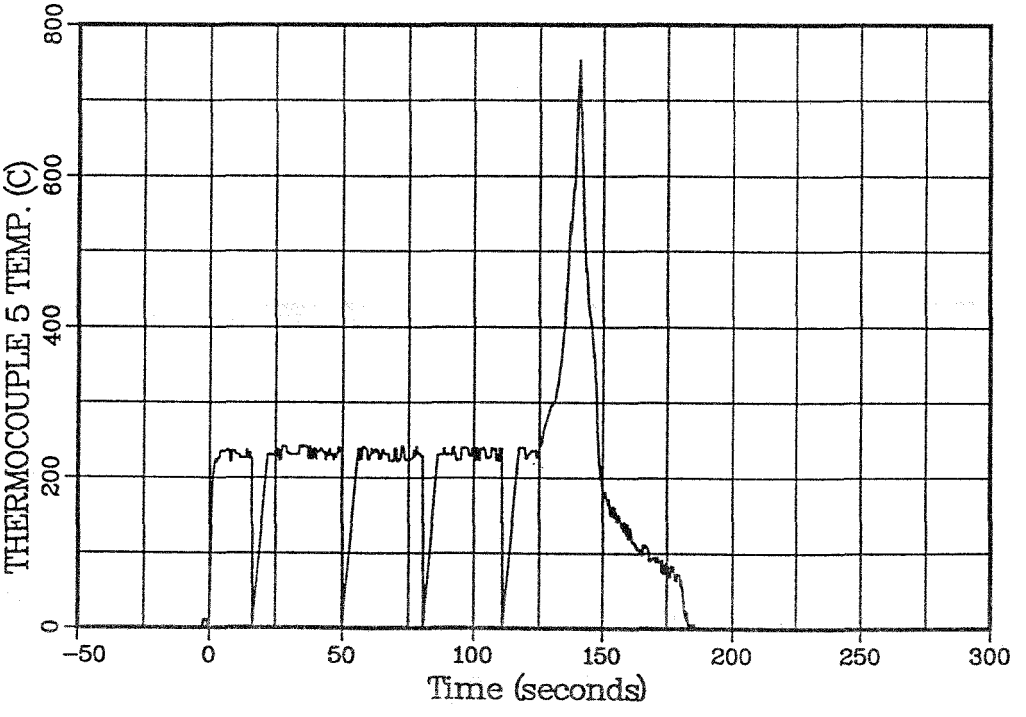

SANDIA NATIONAL LABORATORIES
Fusion Technology
Shot 144321

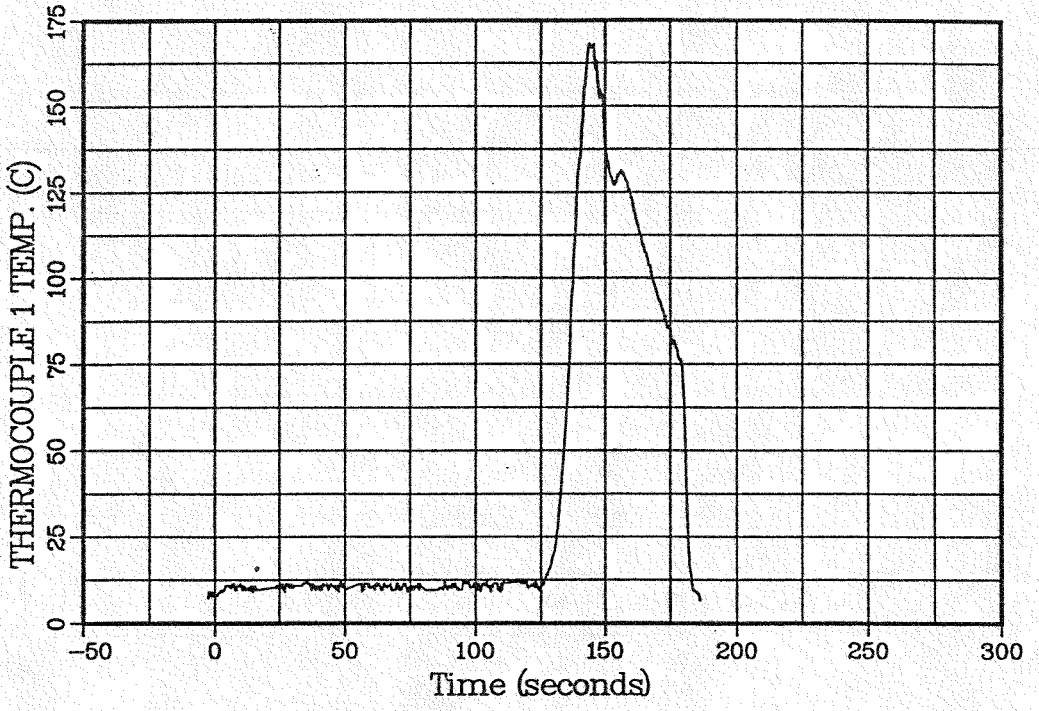

SANDIA NATIONAL LABORATORIES
Fusion Technology
Shot 144321

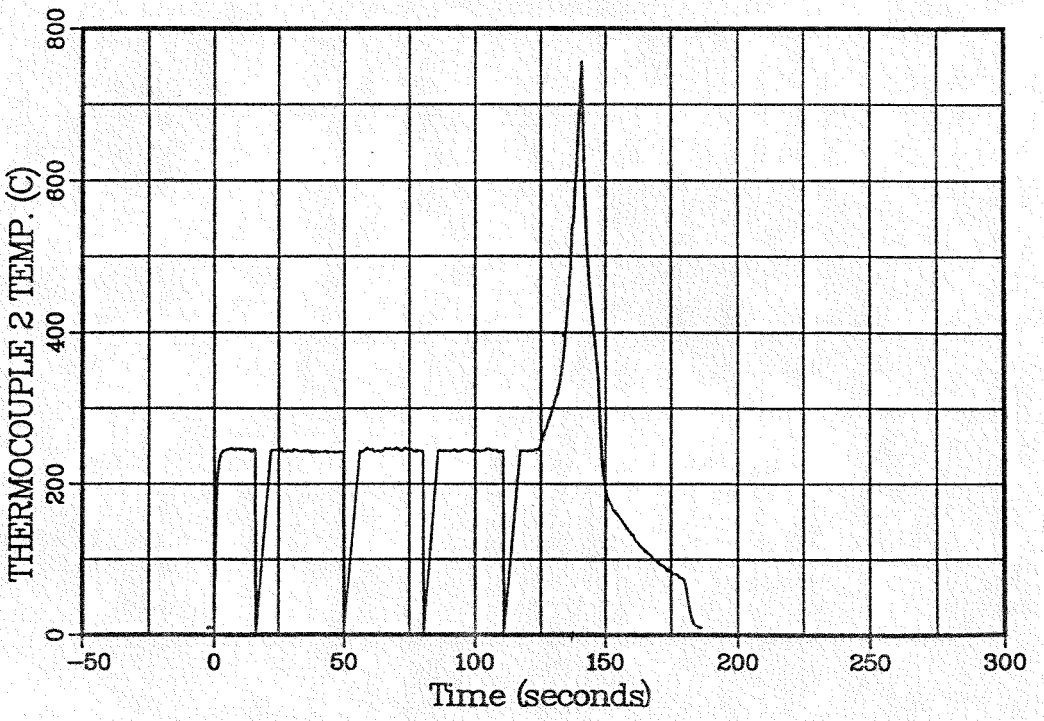

SANDIA NATIONAL LABORATORIES
Fusion Technology
Shot 144321

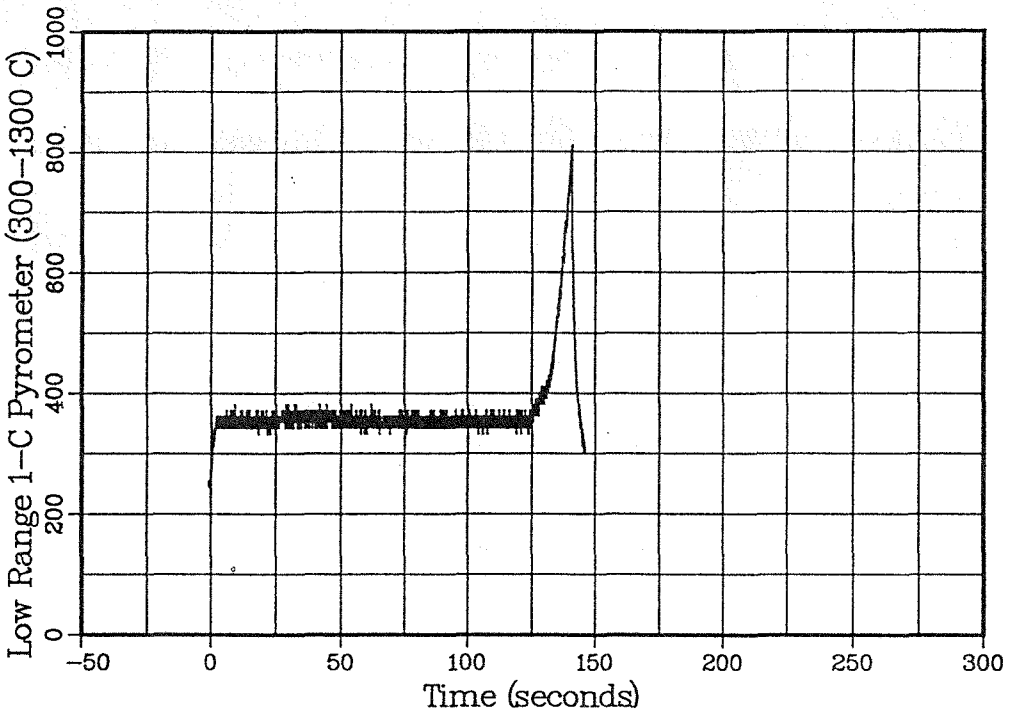

SANDIA NATIONAL LABORATORIES
Fusion Technology
Shot 144321

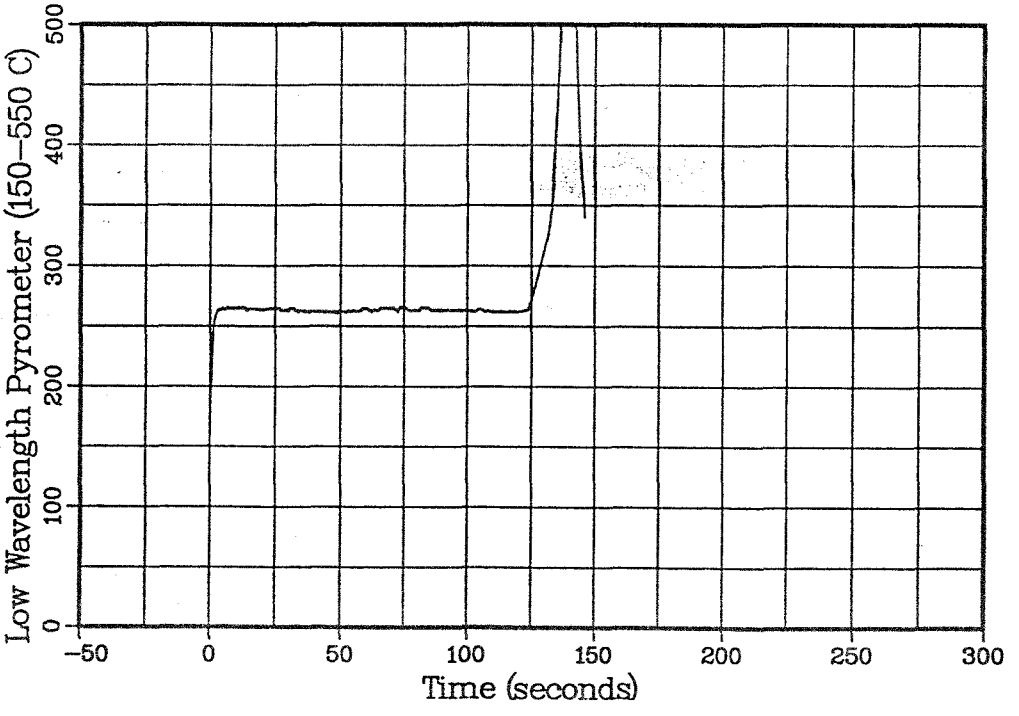

SANDIA NATIONAL LABORATORIES
Fusion Technology
Shot 144321

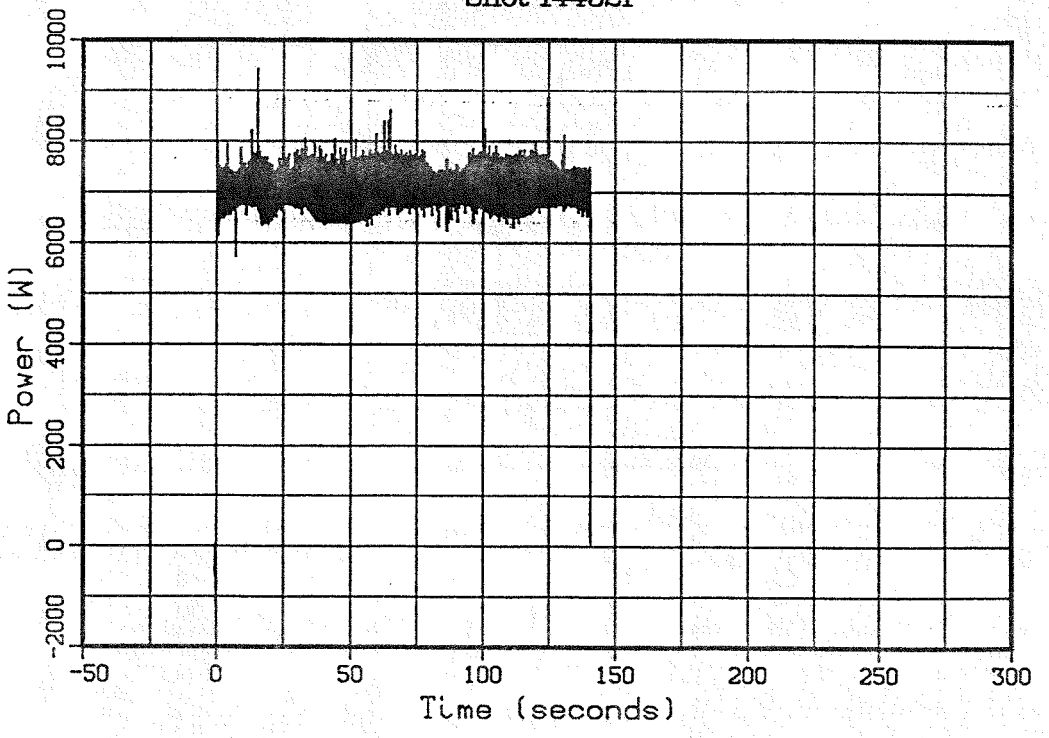

SANDIA NATIONAL LABORATORIES
Fusion Technology
Shot 144320

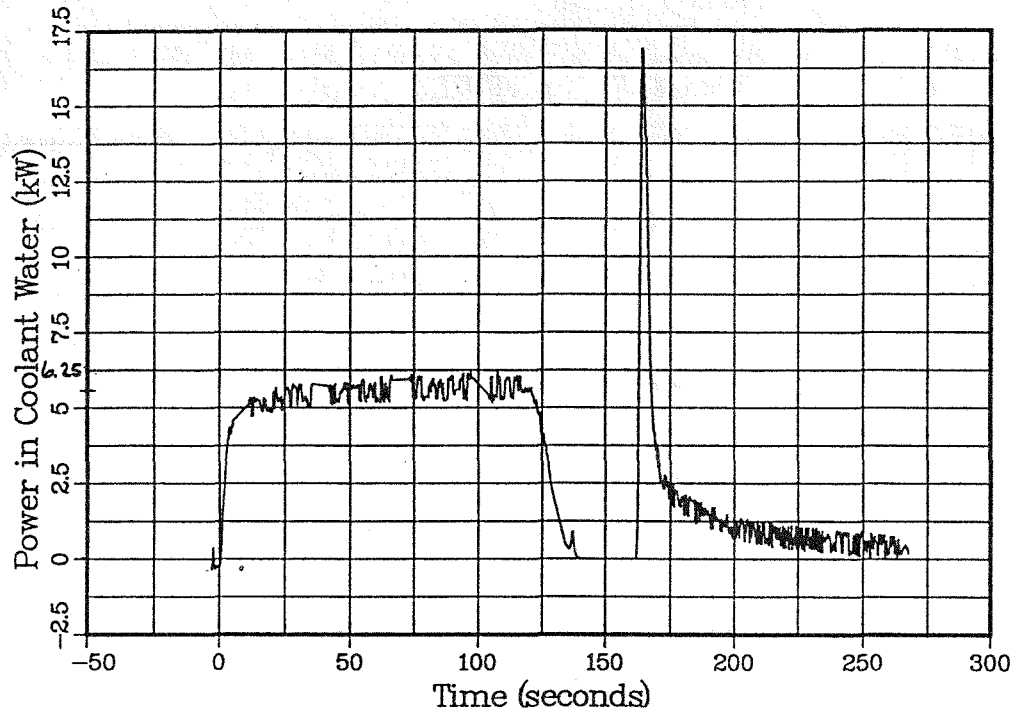

SANDIA NATIONAL LABORATORIES
Fusion Technology
Shot 144320

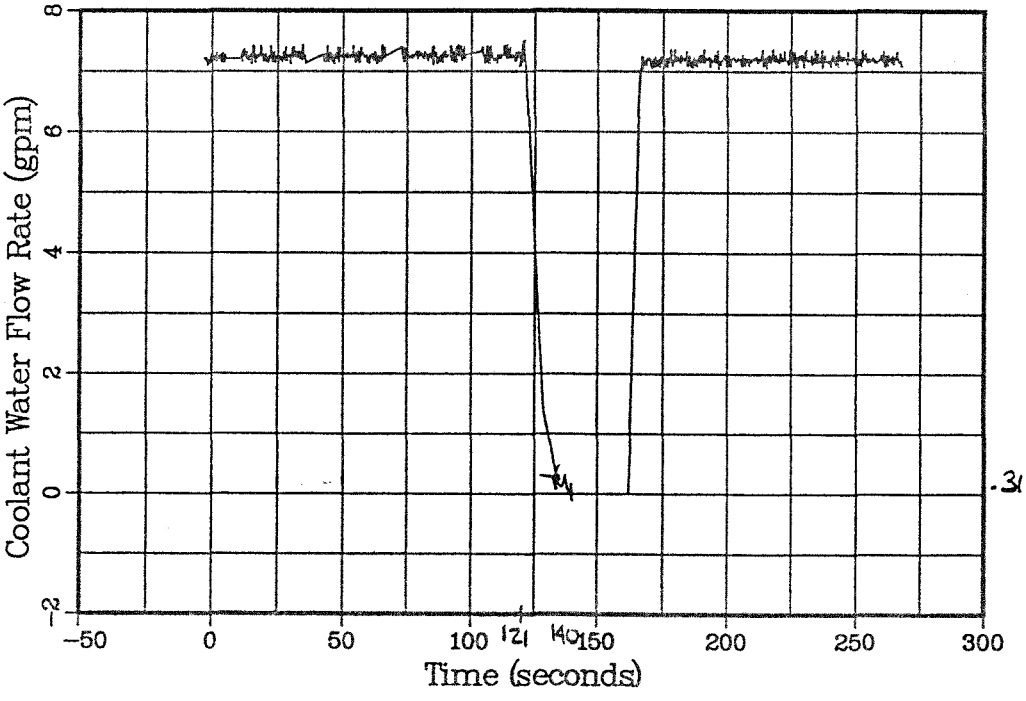

SANDIA NATIONAL LABORATORIES
Fusion Technology
Shot 144320

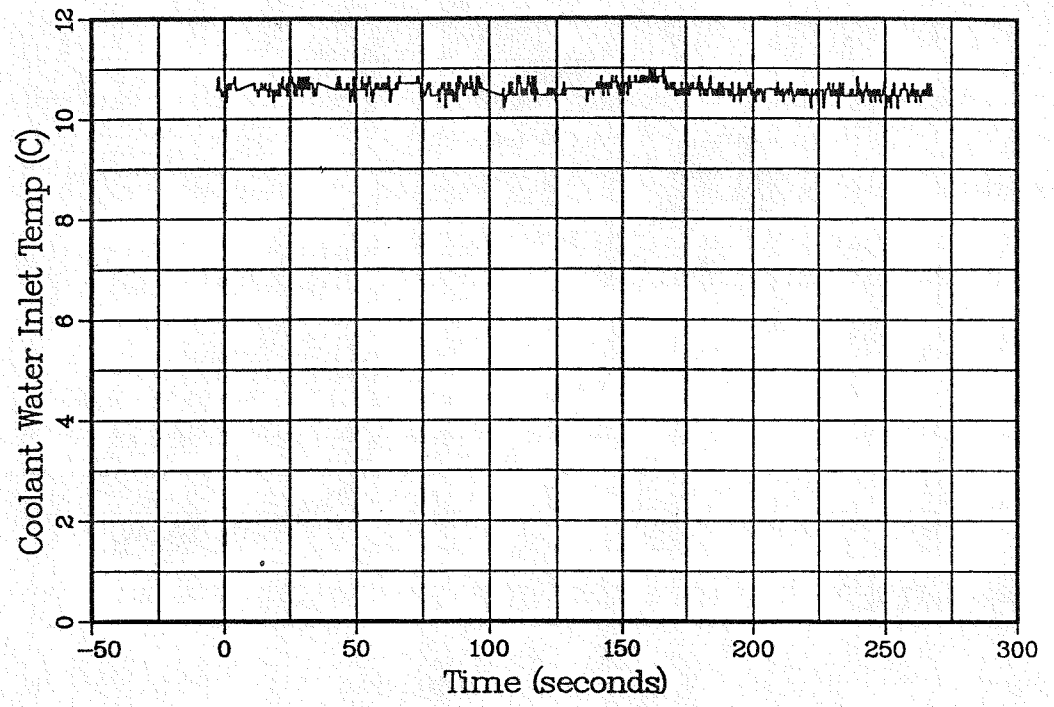

SANDIA NATIONAL LABORATORIES
Fusion Technology
Shot 144320

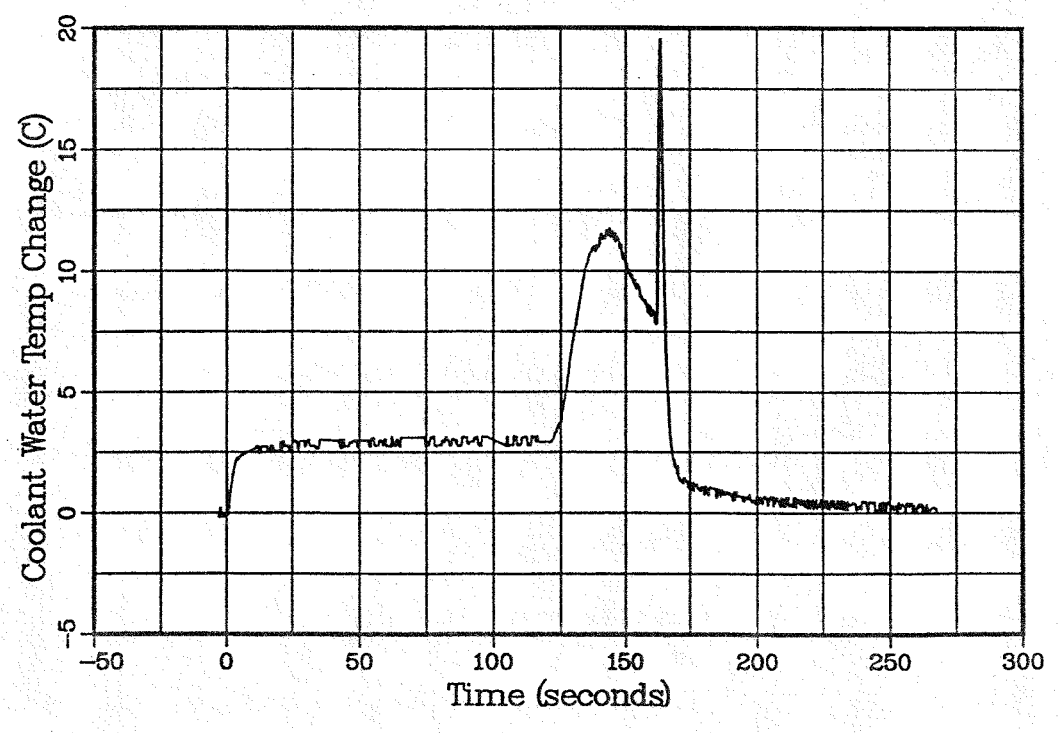

SANDIA NATIONAL LABORATORIES
Fusion Technology
Shot 144320

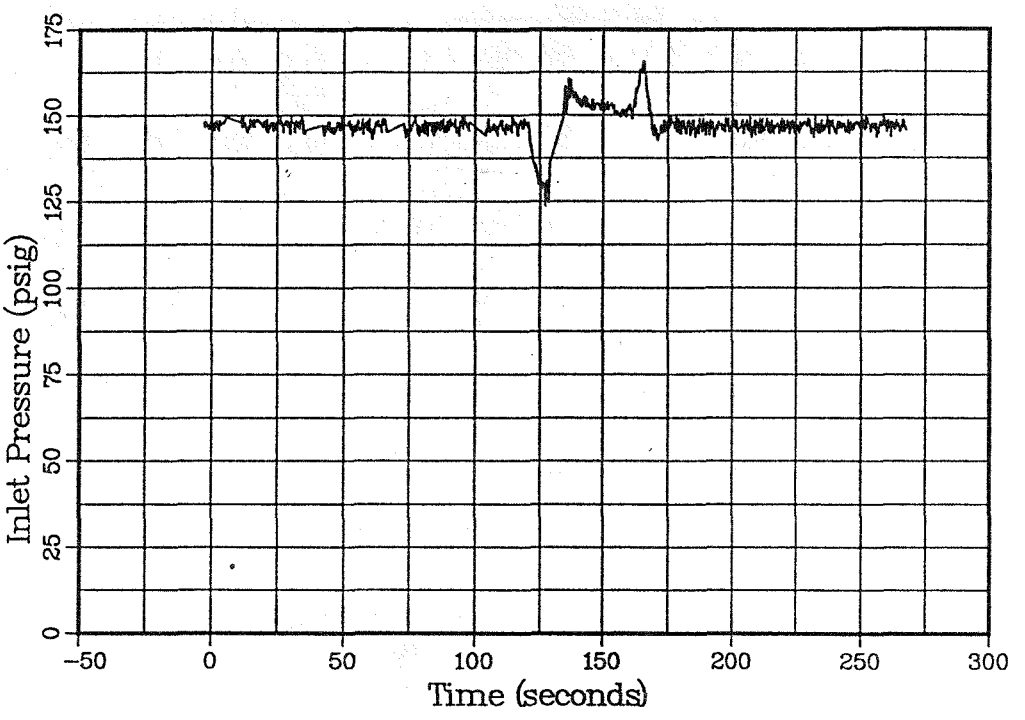

SANDIA NATIONAL LABORATORIES
Fusion Technology
Shot 144320

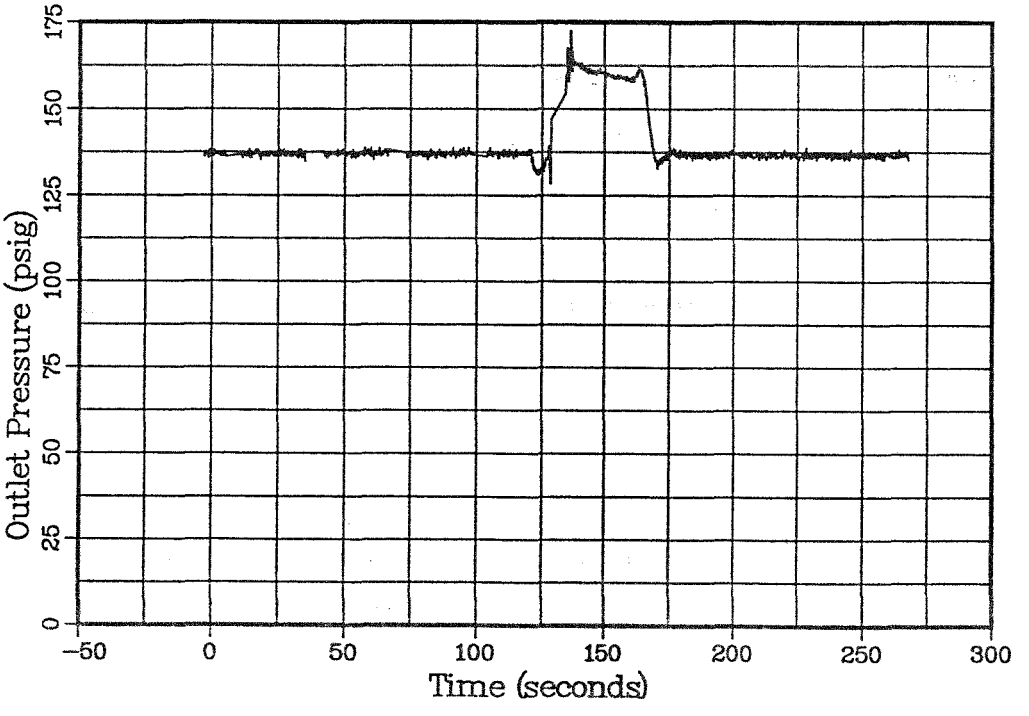

SANDIA NATIONAL LABORATORIES
Fusion Technology
Shot 144320

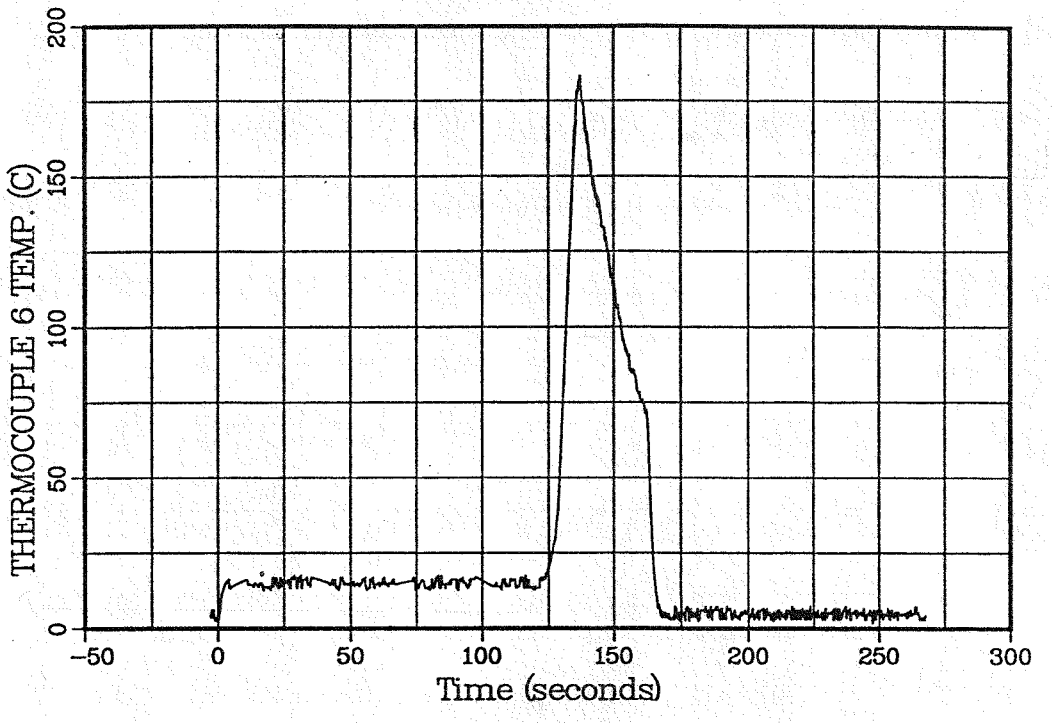

SANDIA NATIONAL LABORATORIES
Fusion Technology
Shot 144320

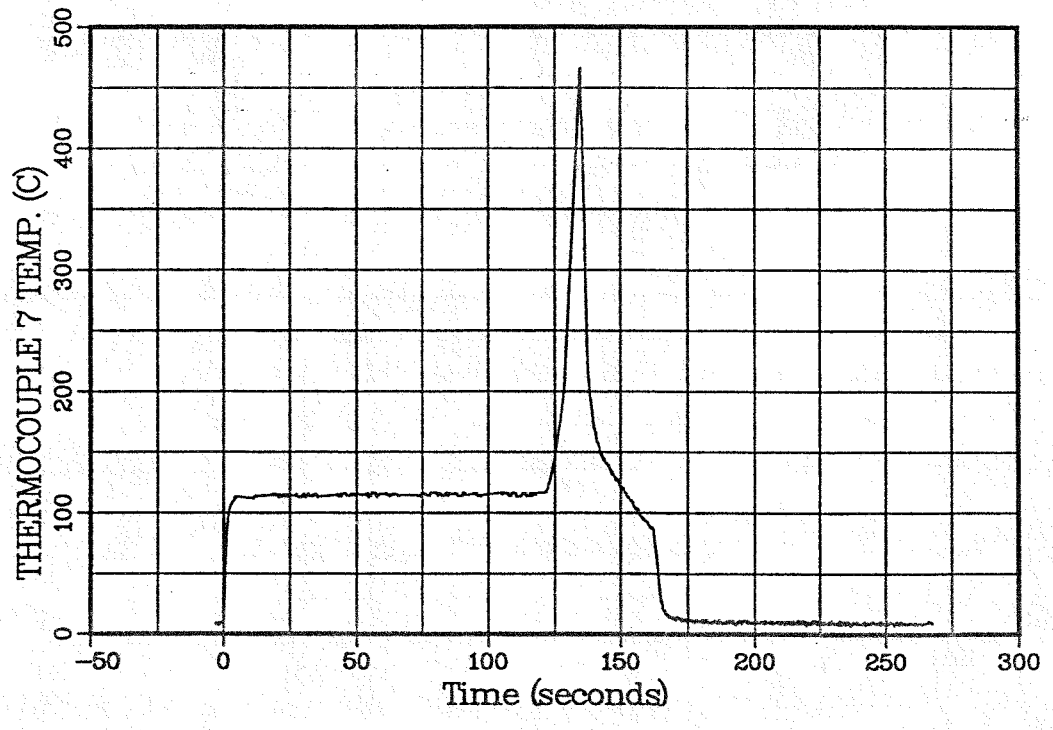

SANDIA NATIONAL LABORATORIES
Fusion Technology
Shot 144320

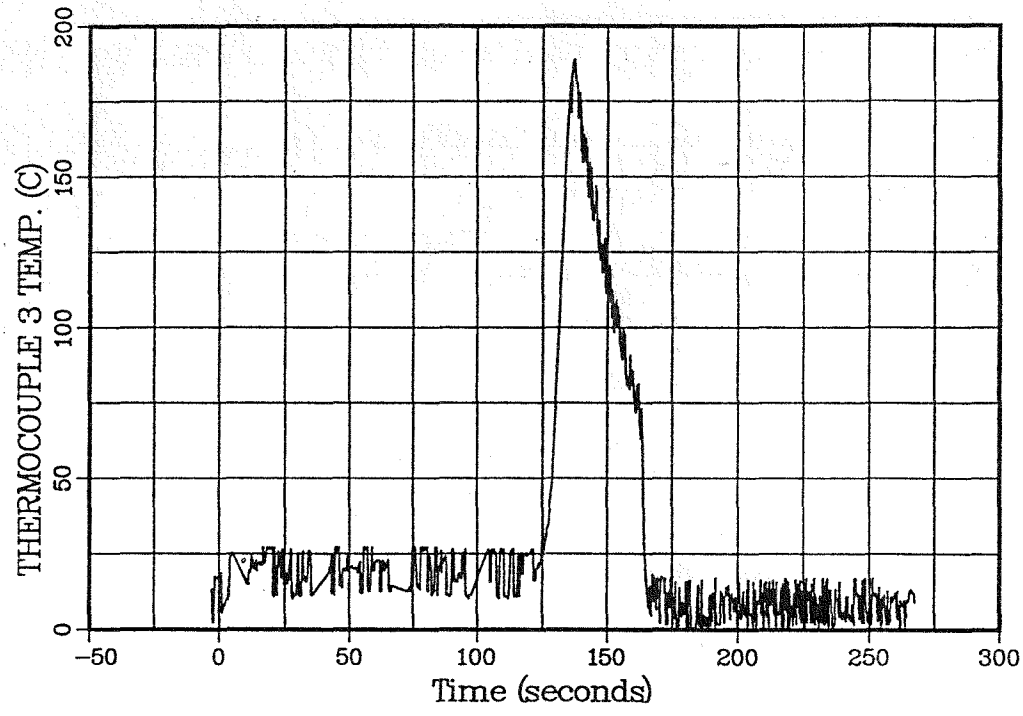

SANDIA NATIONAL LABORATORIES
Fusion Technology
Shot 144320

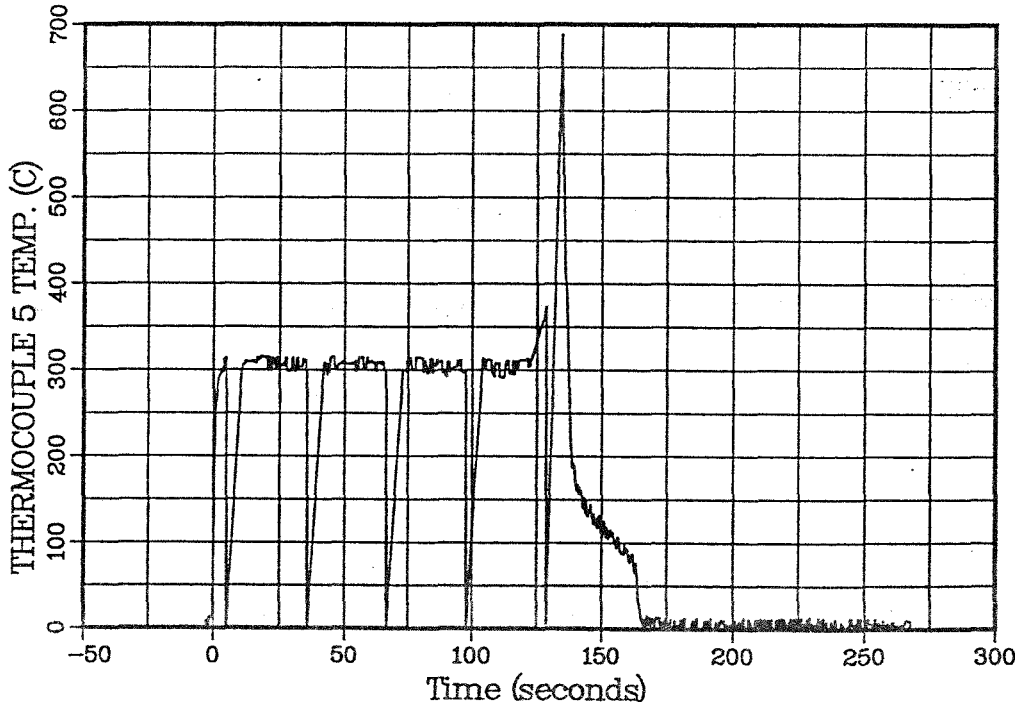

SANDIA NATIONAL LABORATORIES
Fusion Technology
Shot 144320

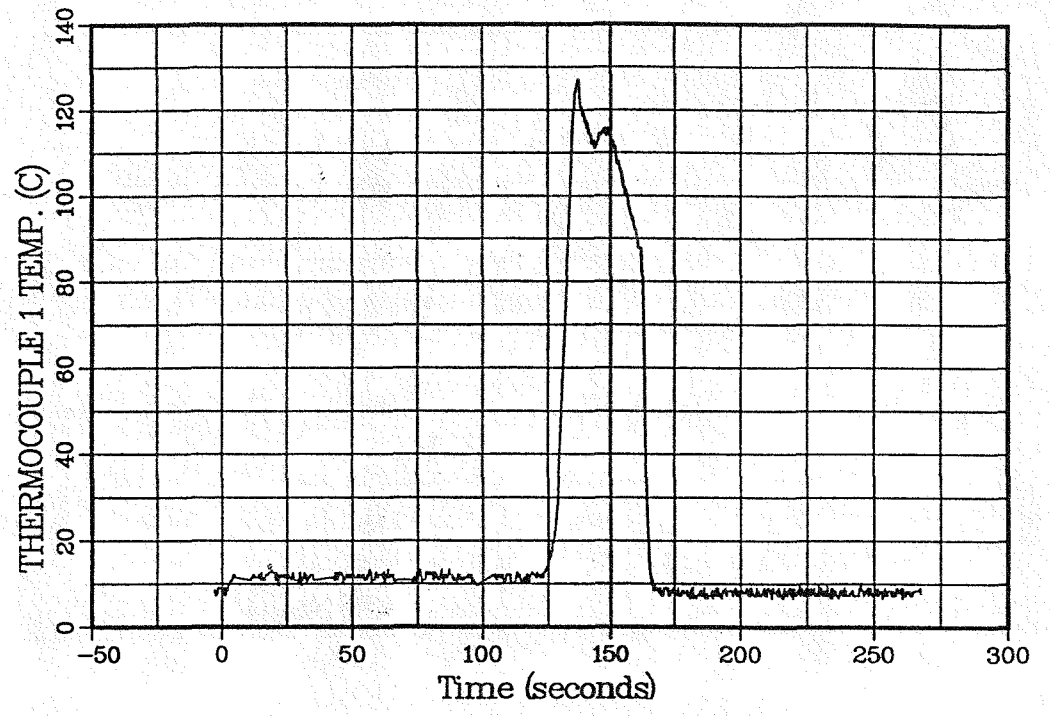

SANDIA NATIONAL LABORATORIES
Fusion Technology
Shot 144320

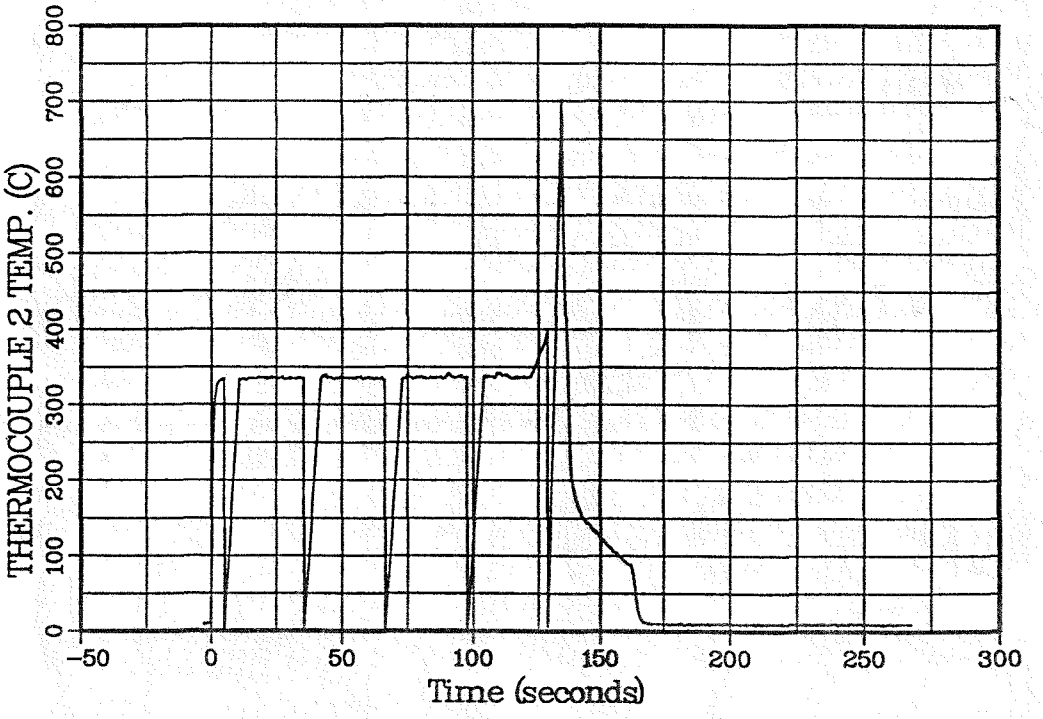

SANDIA NATIONAL LABORATORIES
Fusion Technology
Shot 144320

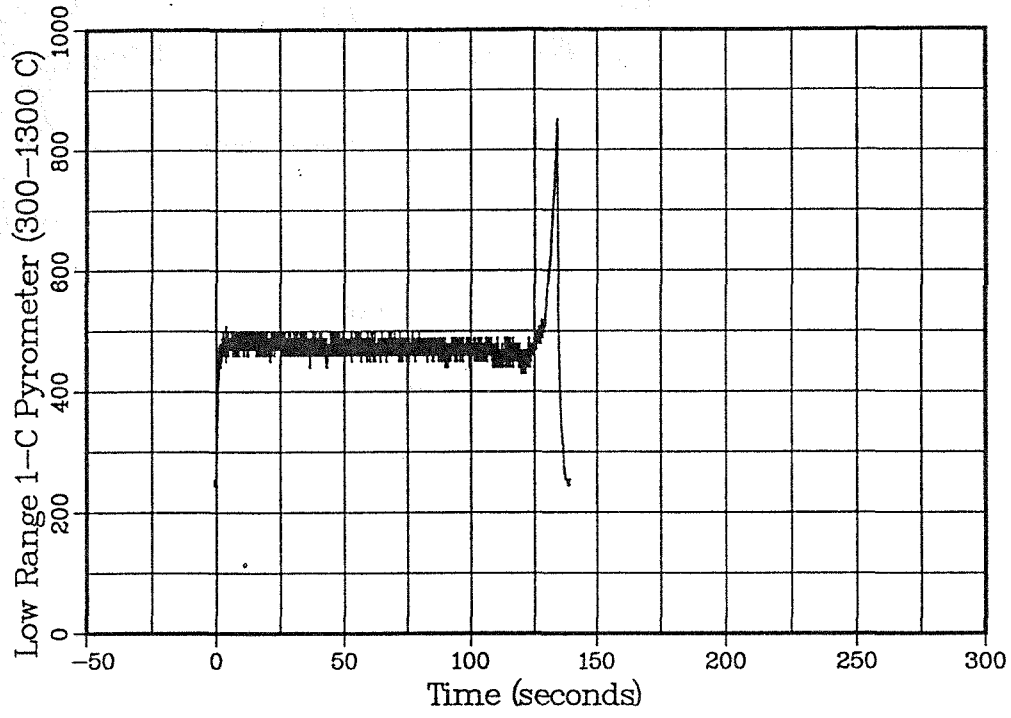

SANDIA NATIONAL LABORATORIES
Fusion Technology
Shot 144320

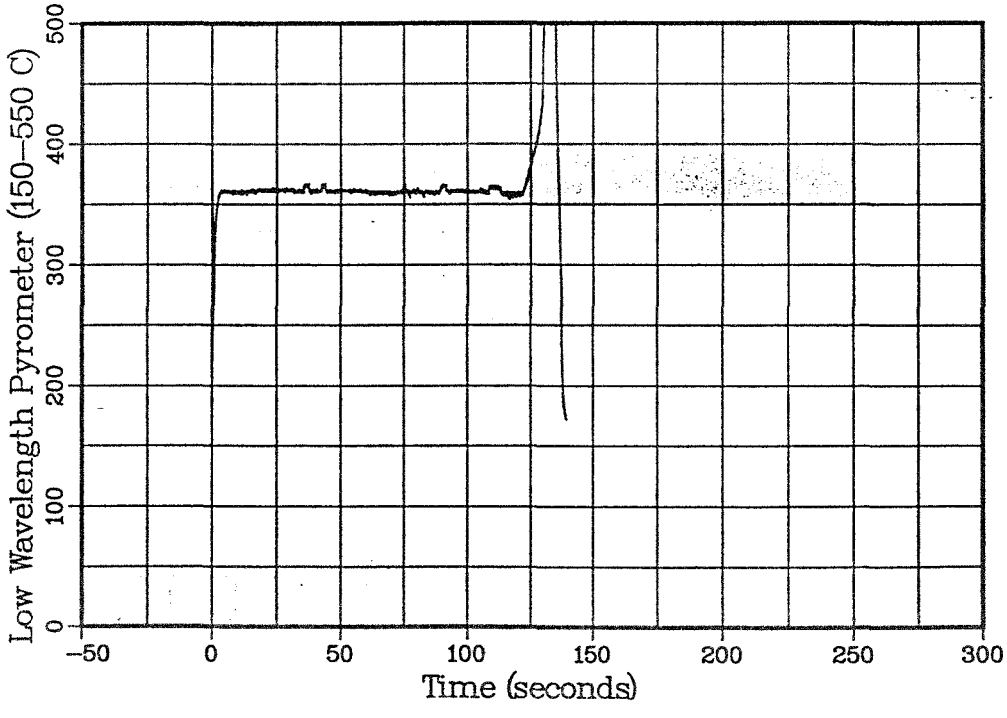

SANDIA NATIONAL LABORATORIES
Fusion Technology
Shot 144320

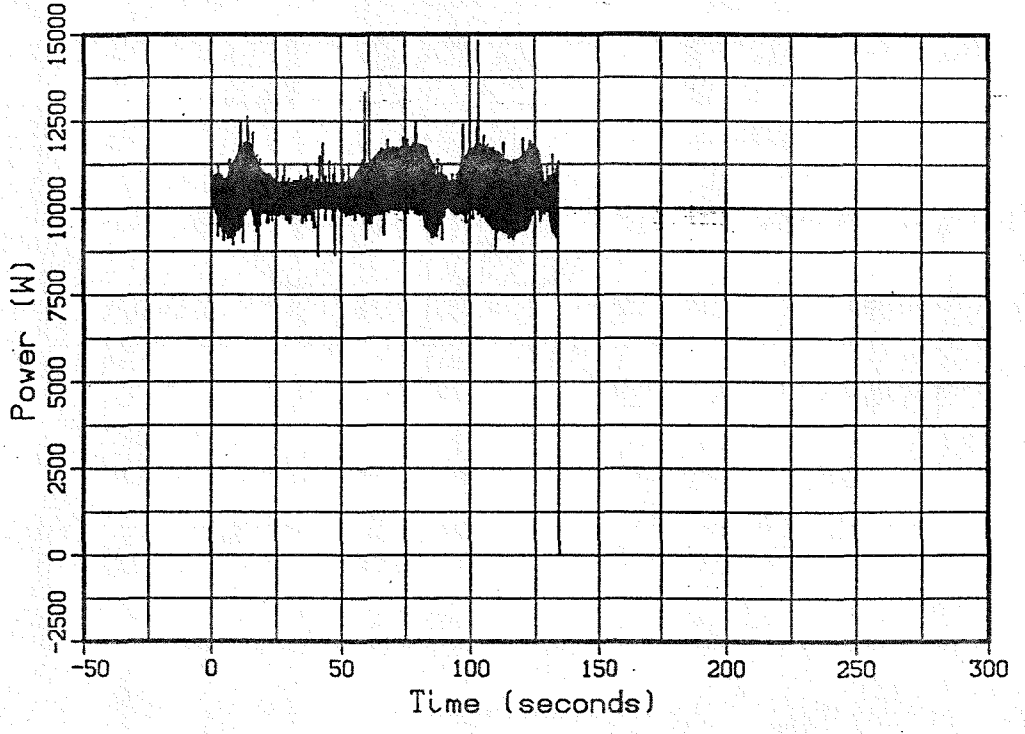

SANDIA NATIONAL LABORATORIES
Fusion Technology
Shot 144319

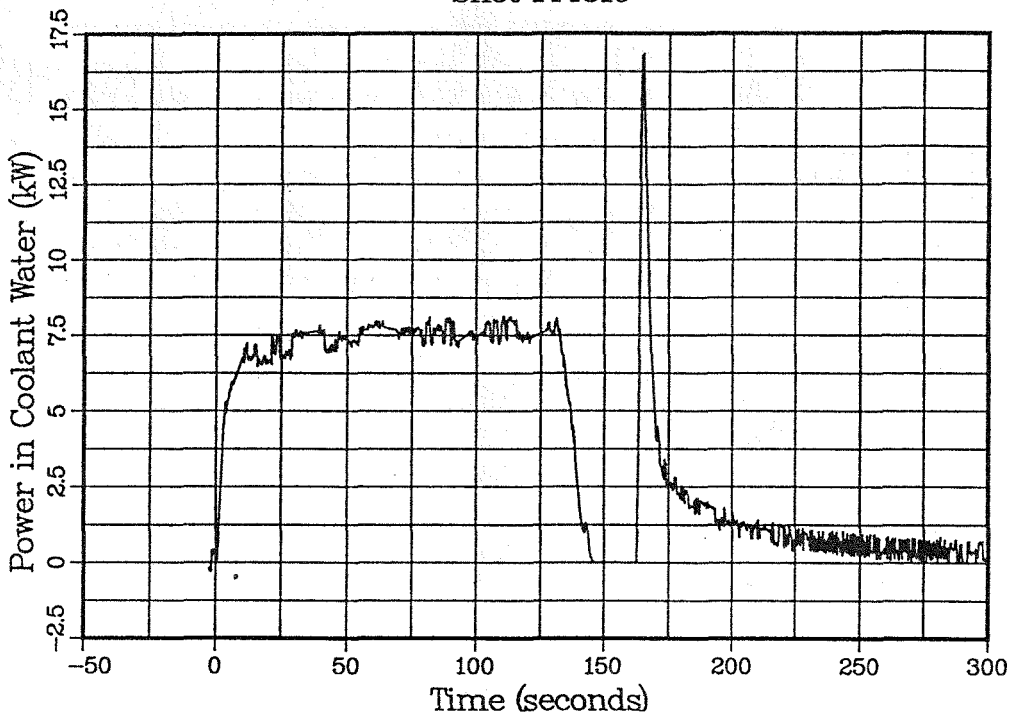

SANDIA NATIONAL LABORATORIES
Fusion Technology
Shot 144319

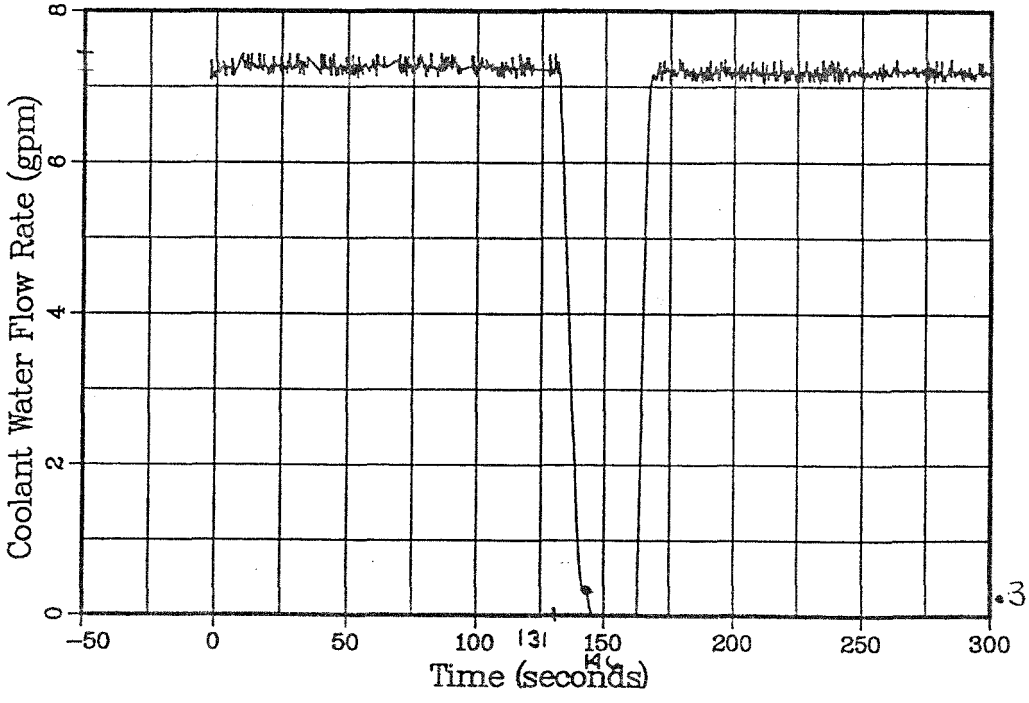

.35 gpm

SANDIA NATIONAL LABORATORIES
Fusion Technology
Shot 144319

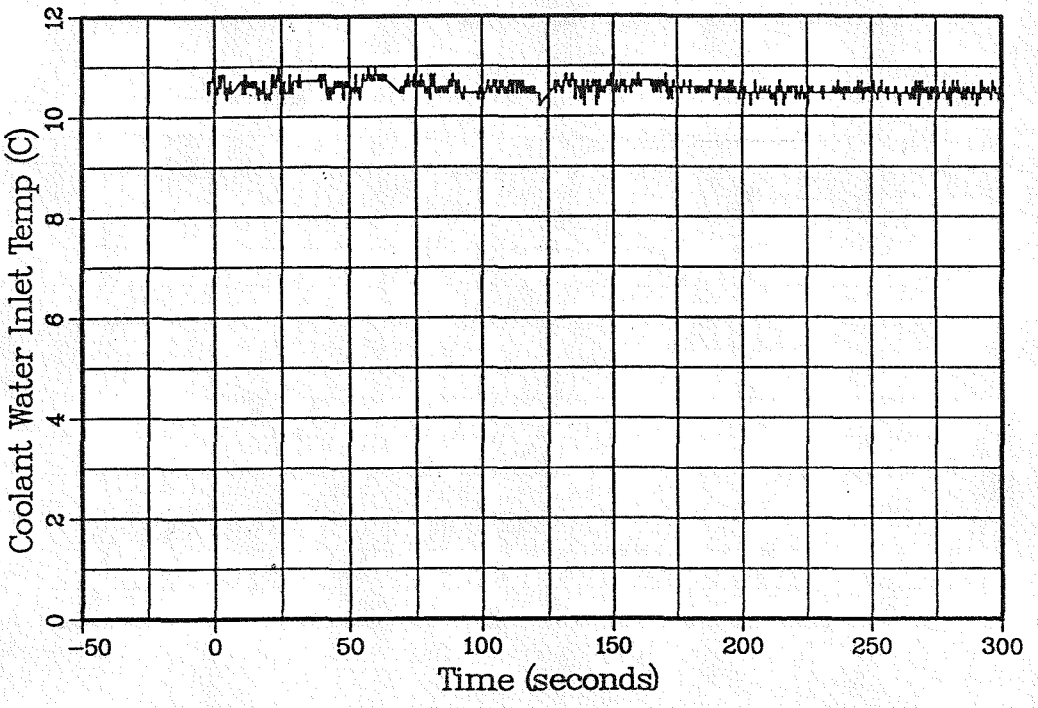

SANDIA NATIONAL LABORATORIES
Fusion Technology
Shot 144319

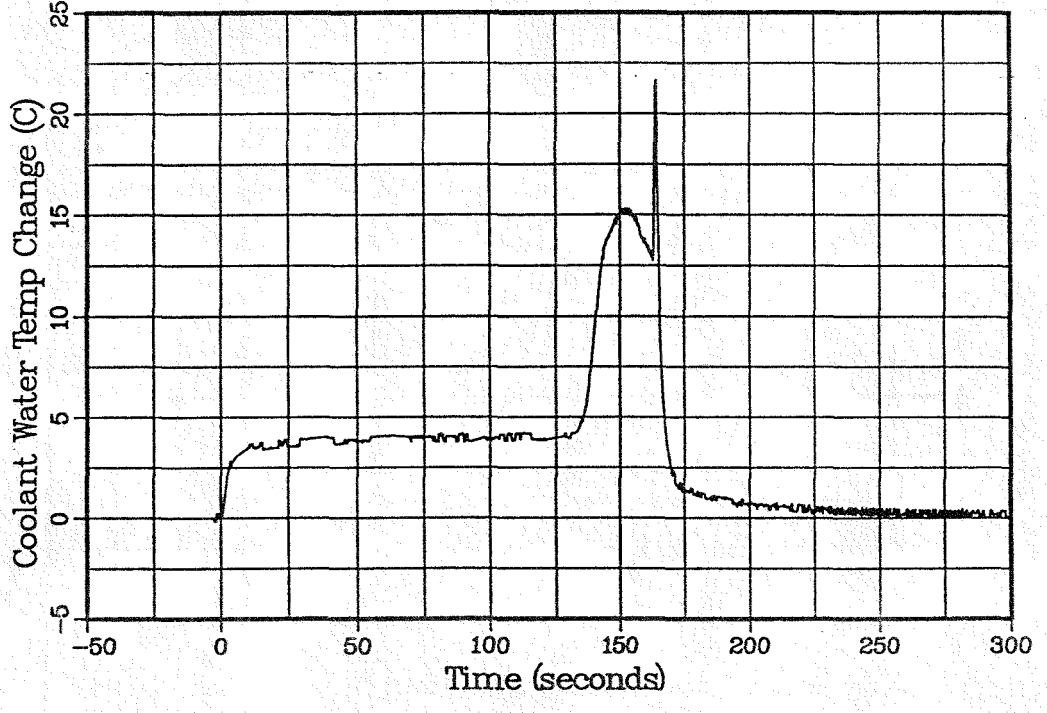

SANDIA NATIONAL LABORATORIES
Fusion Technology
Shot 144319

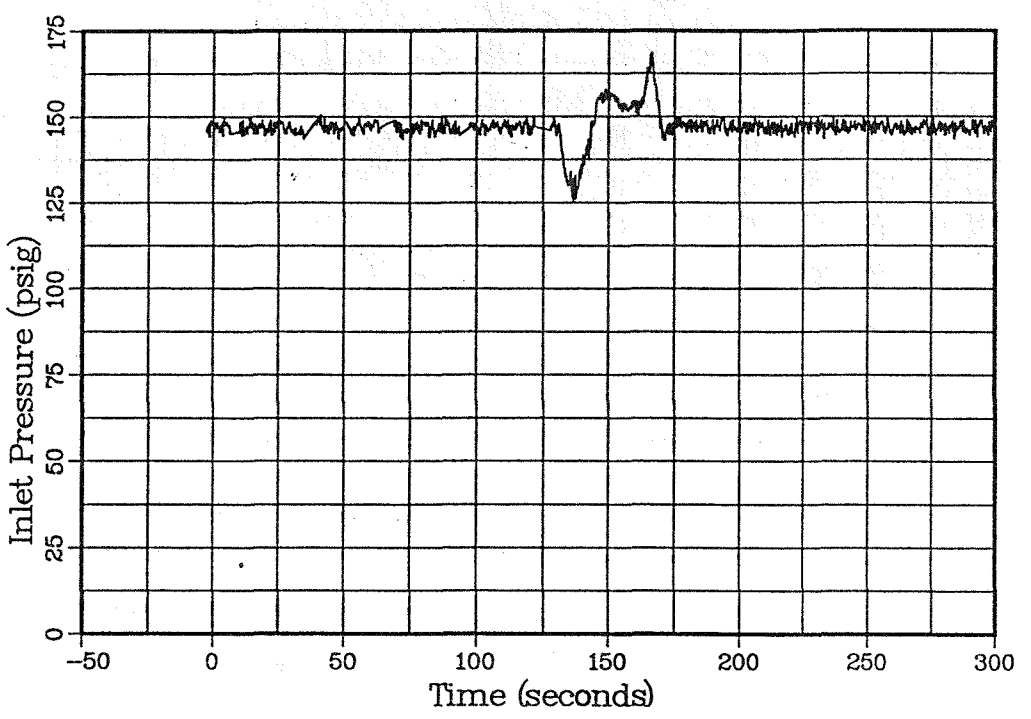

SANDIA NATIONAL LABORATORIES
Fusion Technology
Shot 144319

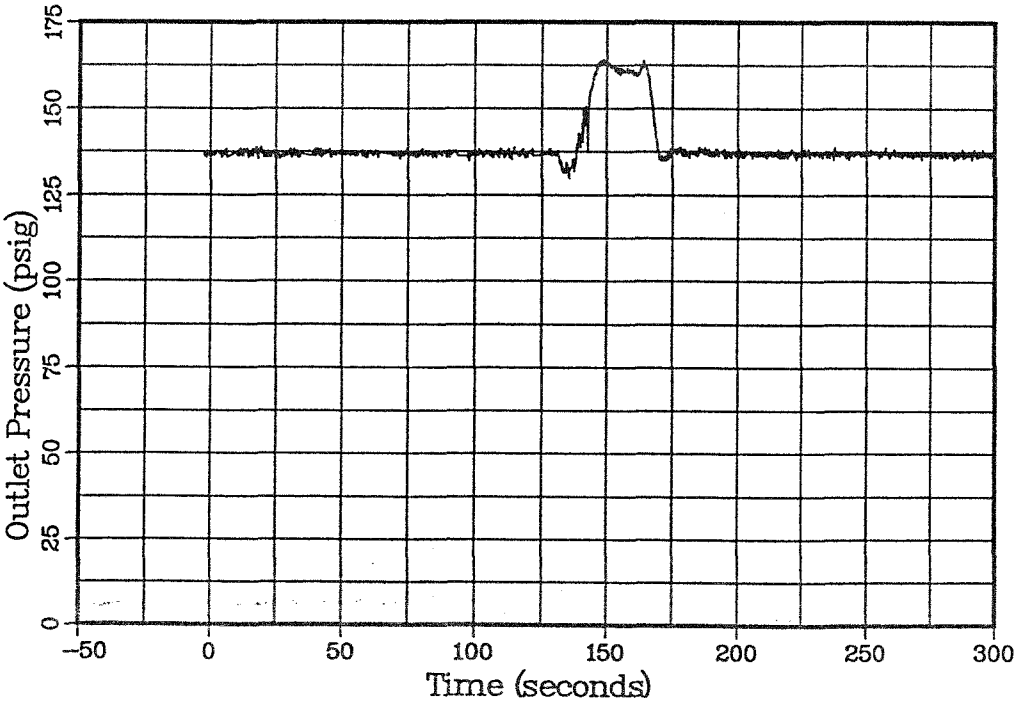

SANDIA NATIONAL LABORATORIES
Fusion Technology
Shot 144319

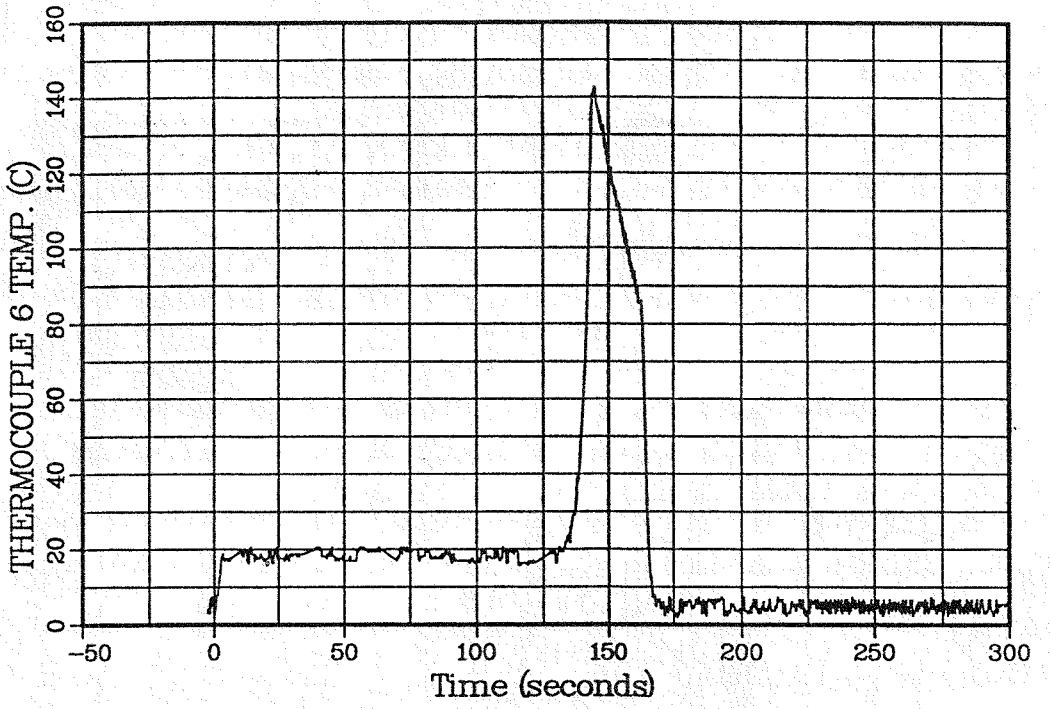

SANDIA NATIONAL LABORATORIES
Fusion Technology
Shot 144319

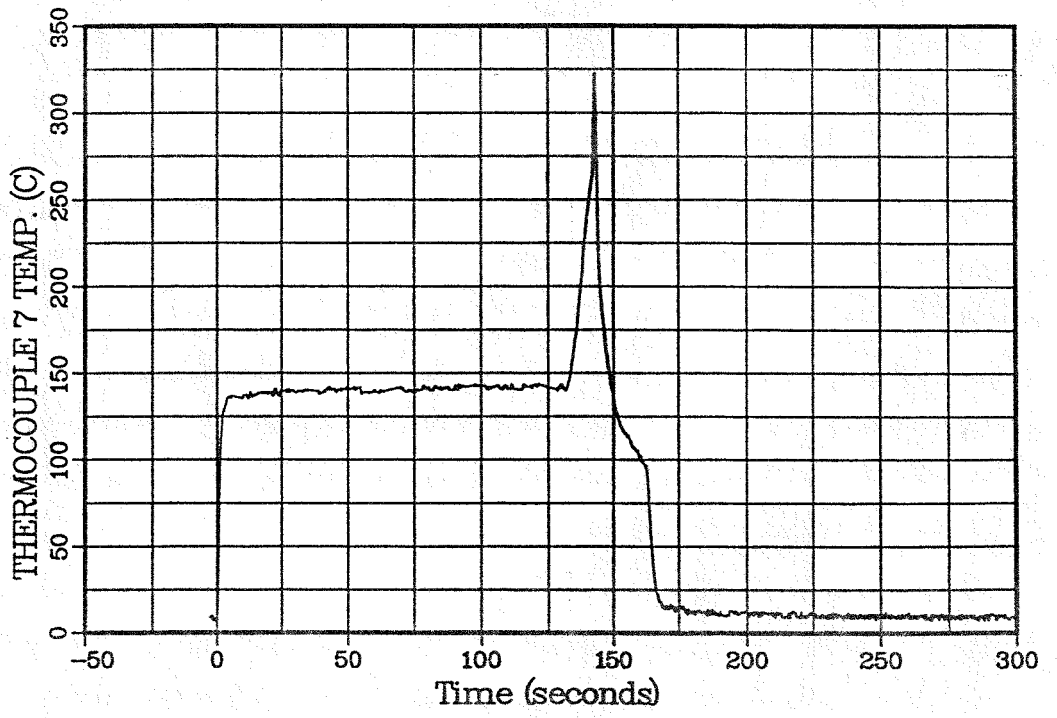

SANDIA NATIONAL LABORATORIES
Fusion Technology
Shot 144319

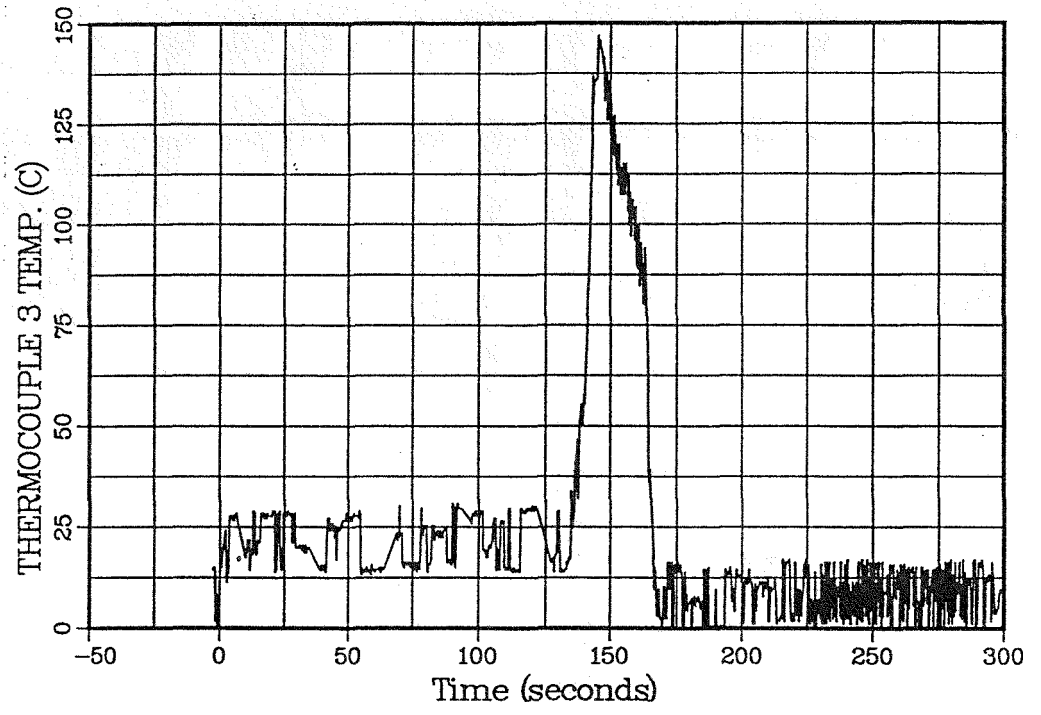

SANDIA NATIONAL LABORATORIES
Fusion Technology
Shot 144319

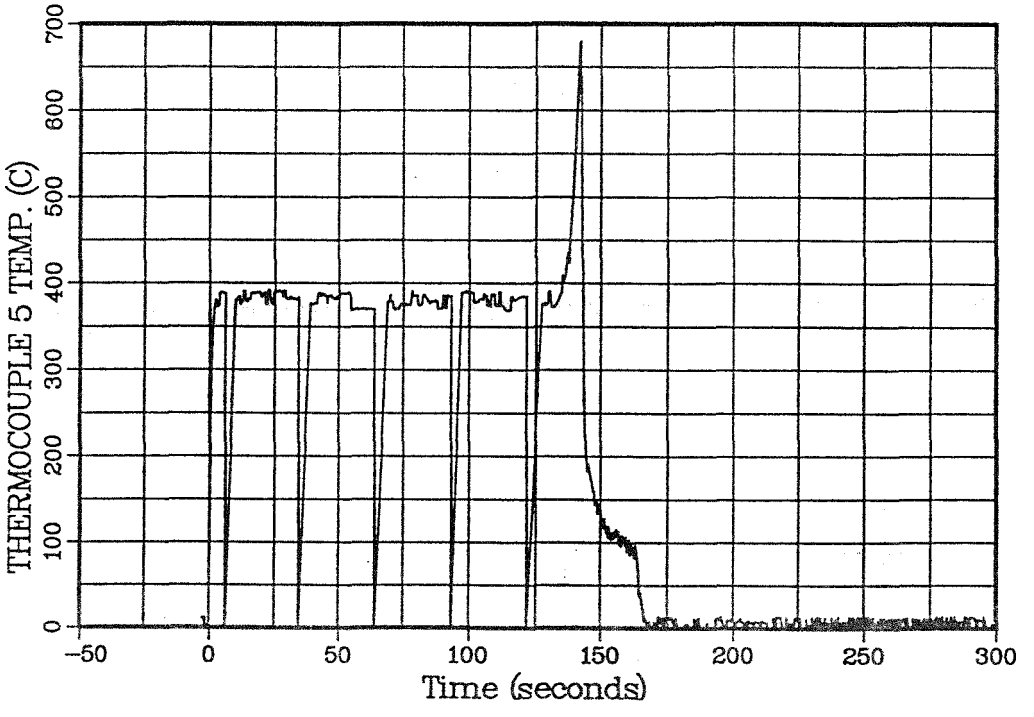

SANDIA NATIONAL LABORATORIES
Fusion Technology
Shot 144319

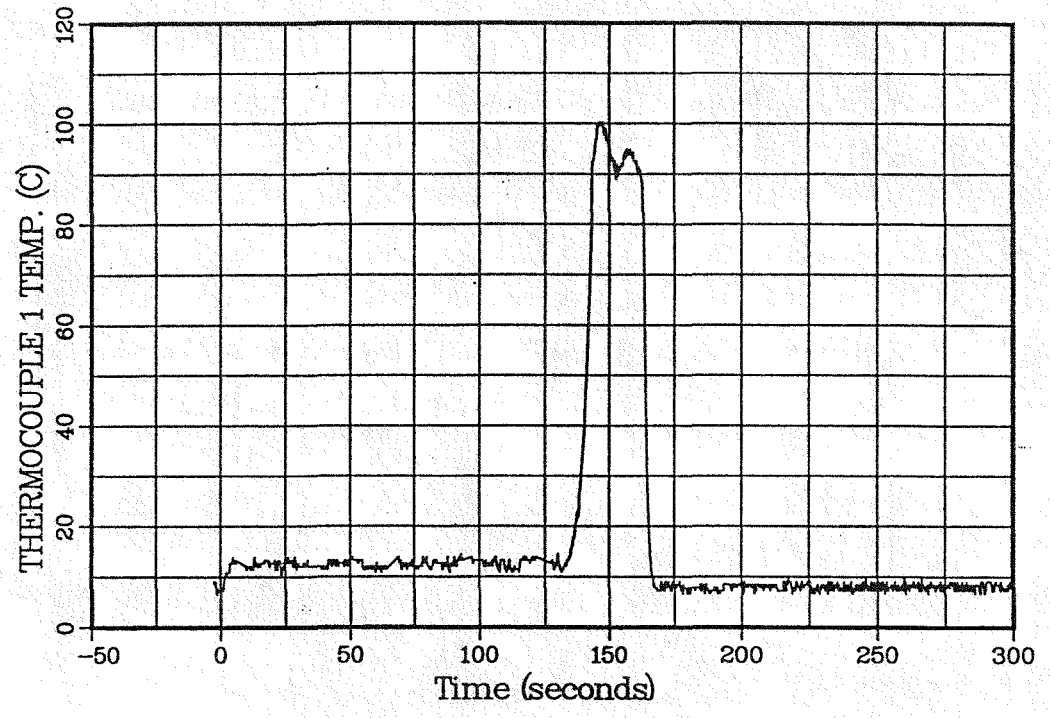

SANDIA NATIONAL LABORATORIES
Fusion Technology
Shot 144319

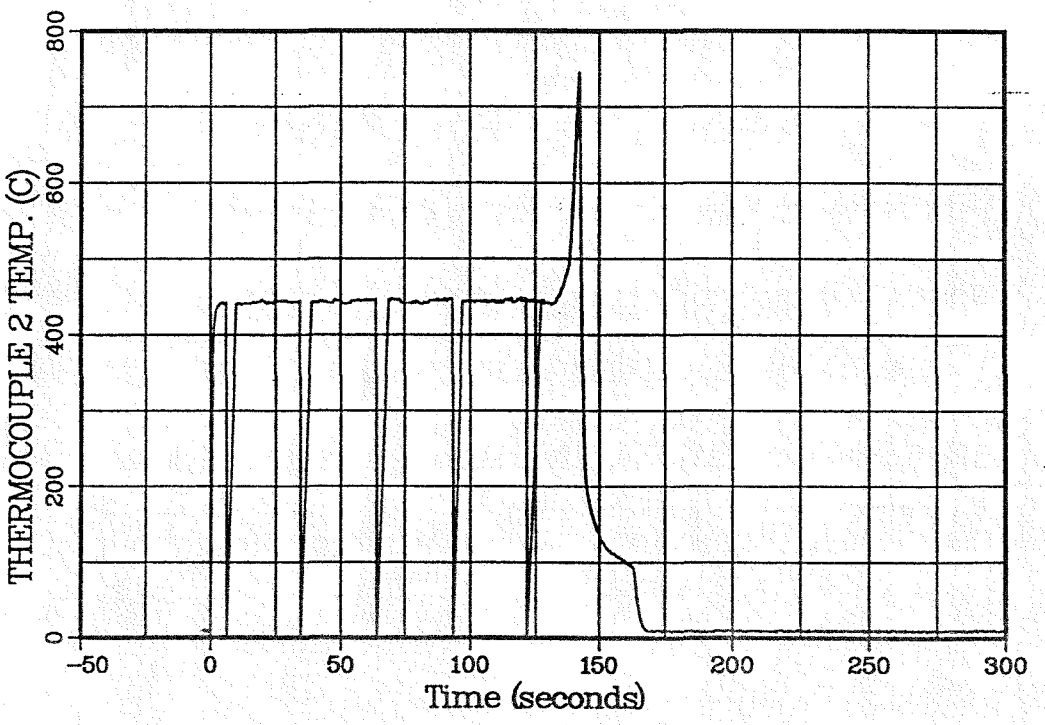

SANDIA NATIONAL LABORATORIES
Fusion Technology
Shot 144319

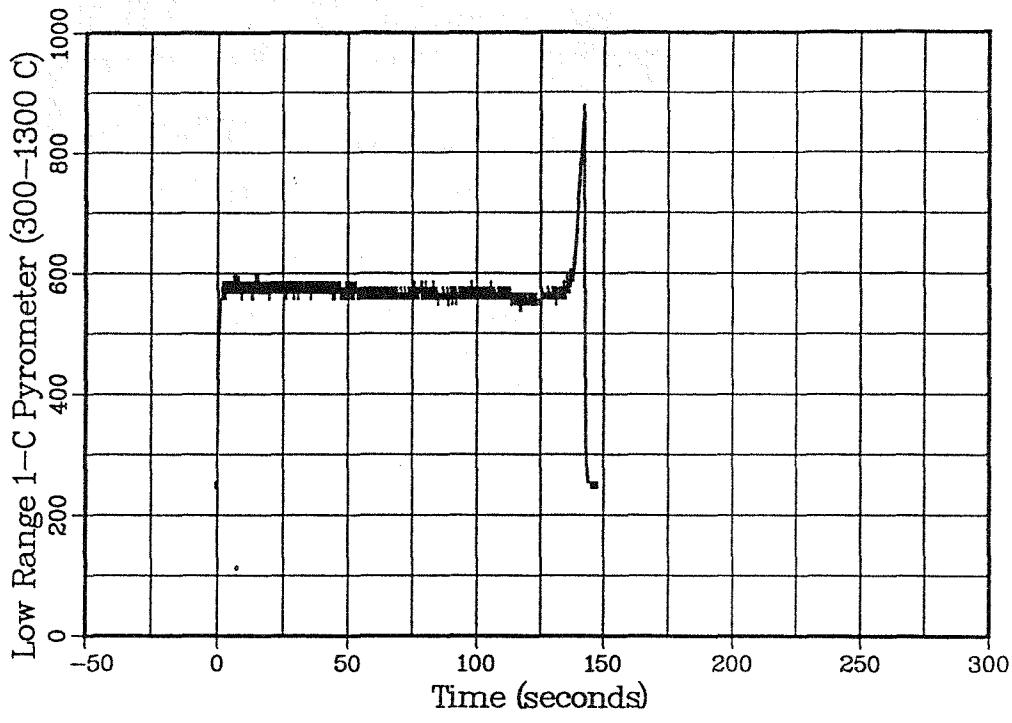

SANDIA NATIONAL LABORATORIES
Fusion Technology
Shot 144319

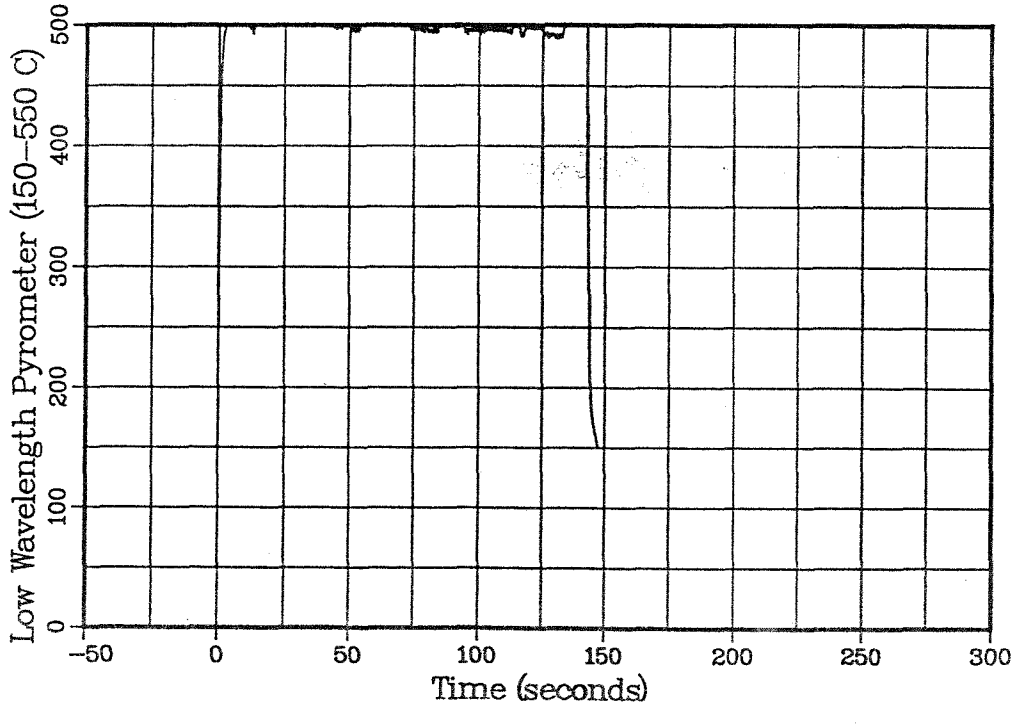

SANDIA NATIONAL LABORATORIES
Fusion Technology
Shot 144319

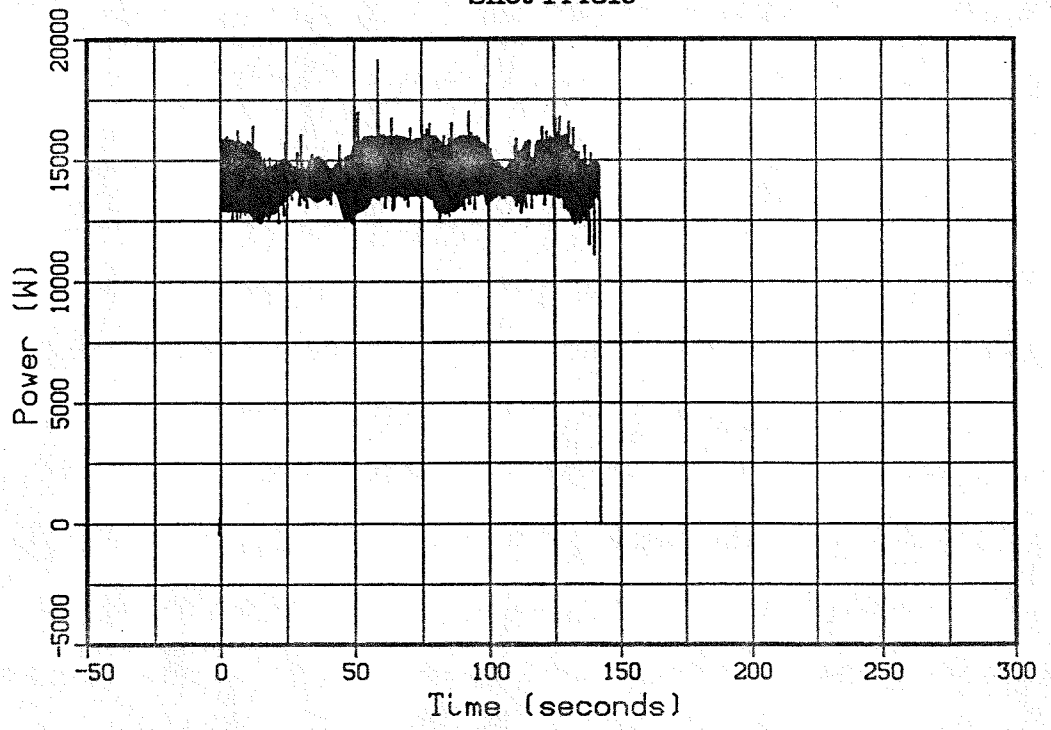

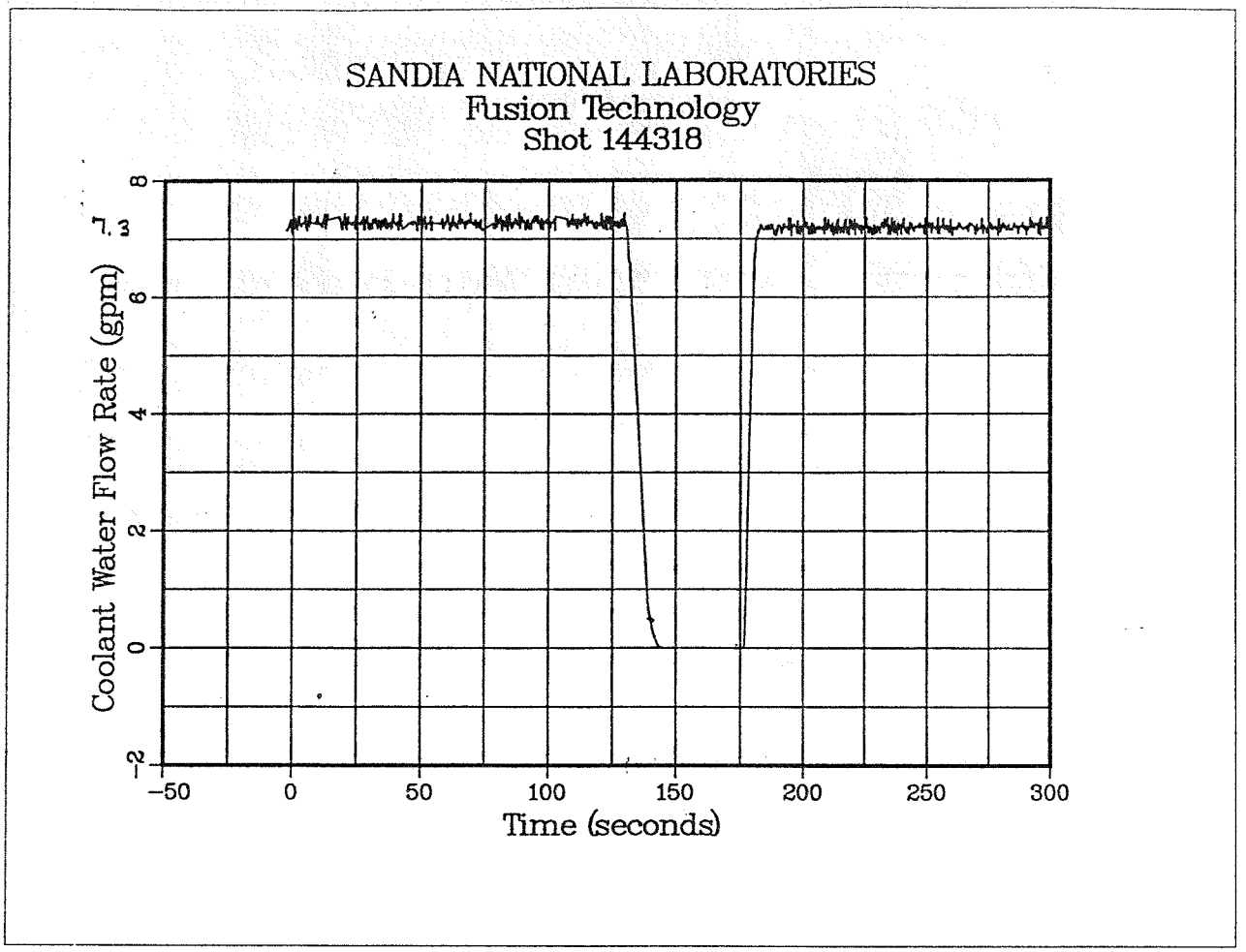
SANDIA NATIONAL LABORATORIES
Fusion Technology
Shot 144318
Coolant Water Flow Rate (gpm)
7.3
8
6
4
2
0
-2
-50
0
50
100
150
200
250
300
Time (seconds)

SANDIA NATIONAL LABORATORIES
Fusion Technology
Shot 144318

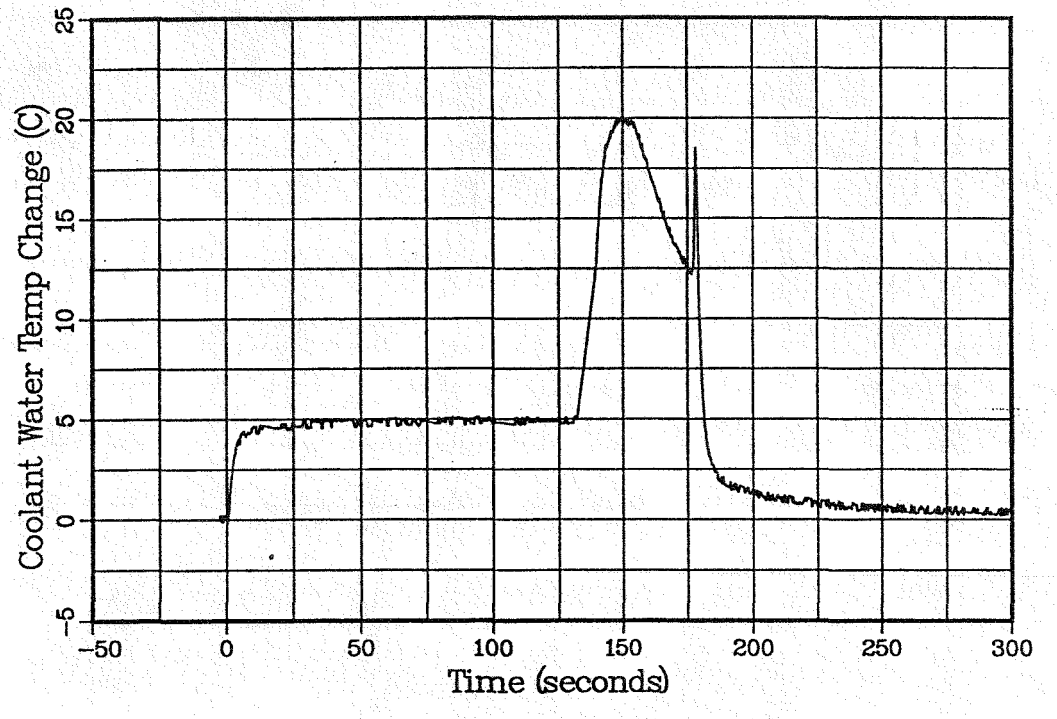

SANDIA NATIONAL LABORATORIES
Fusion Technology
Shot 144318

9.4

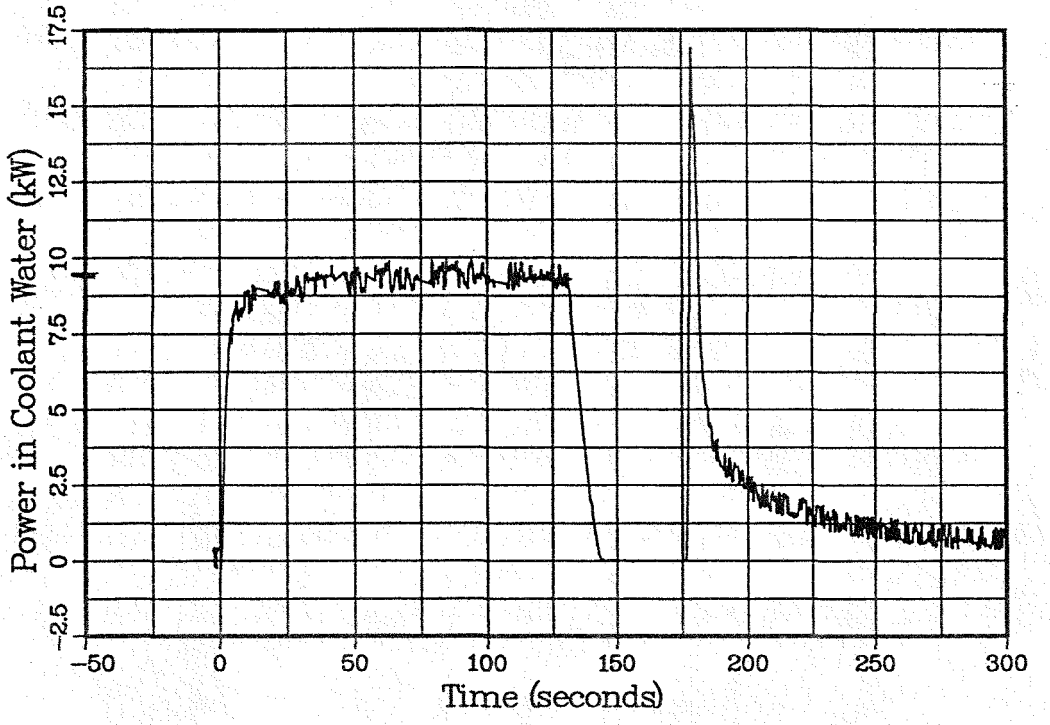

SANDIA NATIONAL LABORATORIES
Fusion Technology
Shot 144318

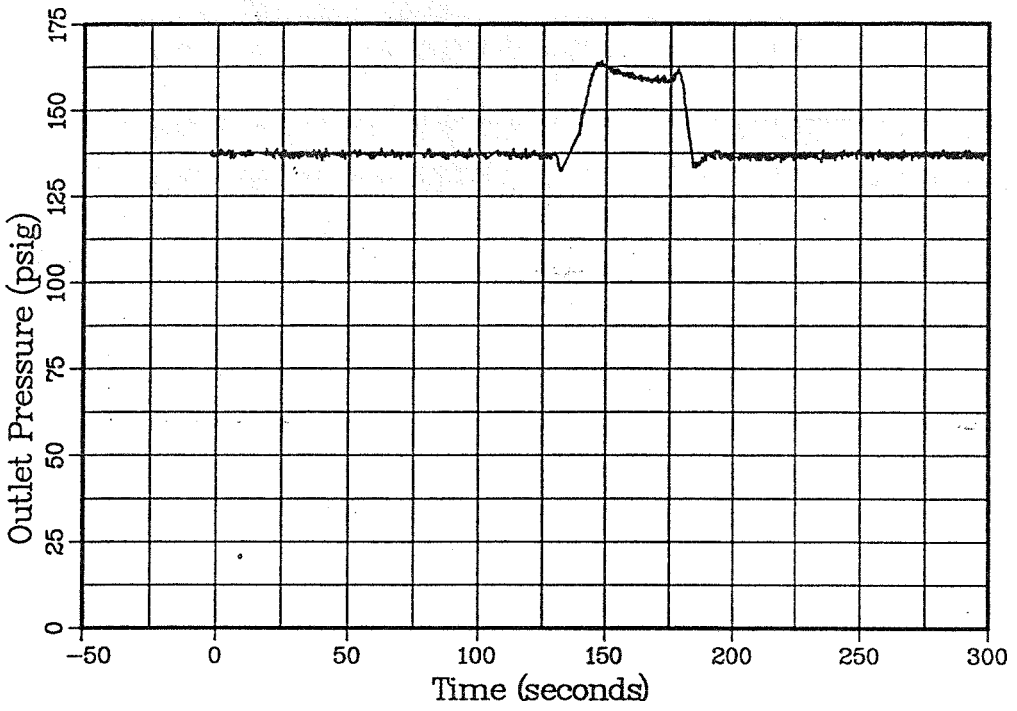

SANDIA NATIONAL LABORATORIES
Fusion Technology
Shot 144318

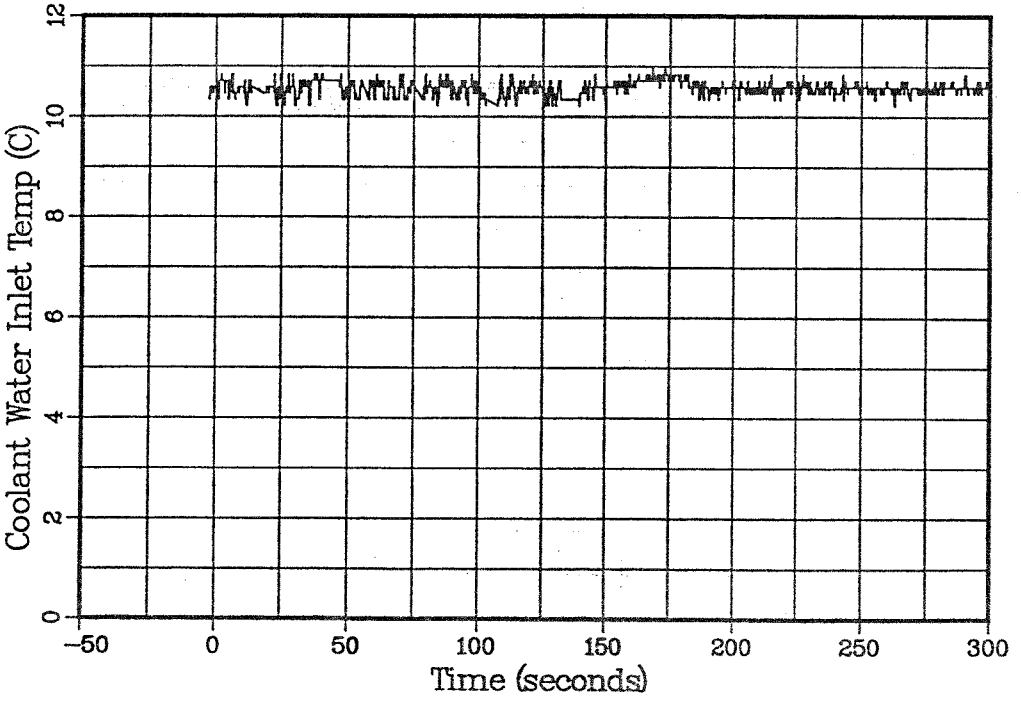

SANDIA NATIONAL LABORATORIES
Fusion Technology
Shot 144318

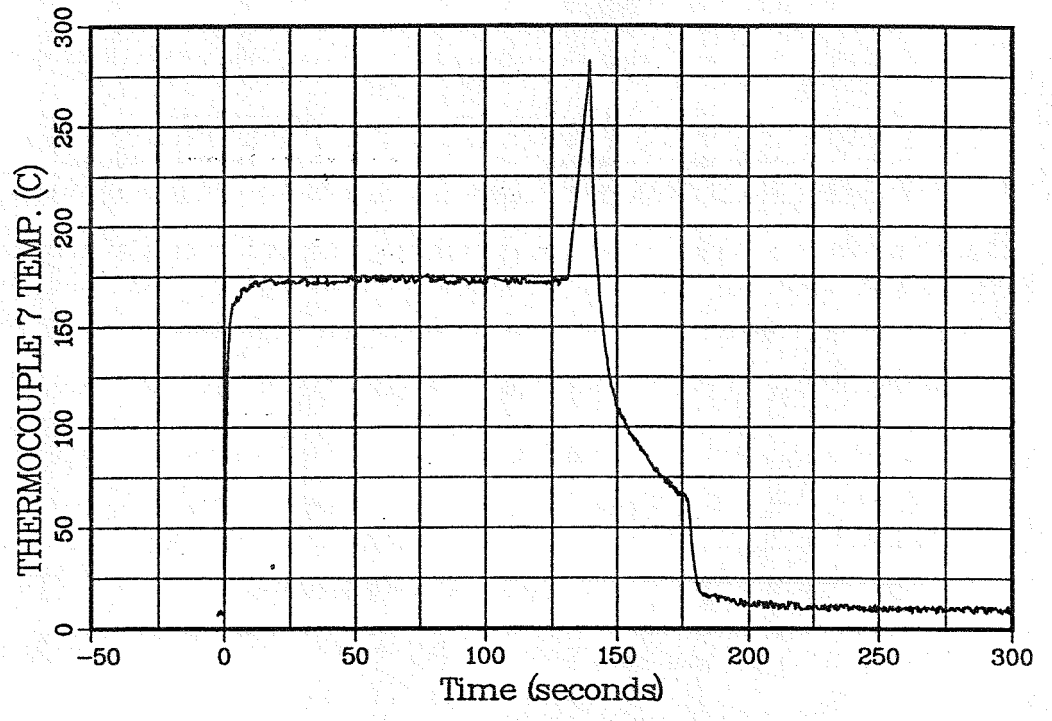

SANDIA NATIONAL LABORATORIES
Fusion Technology
Shot 144318

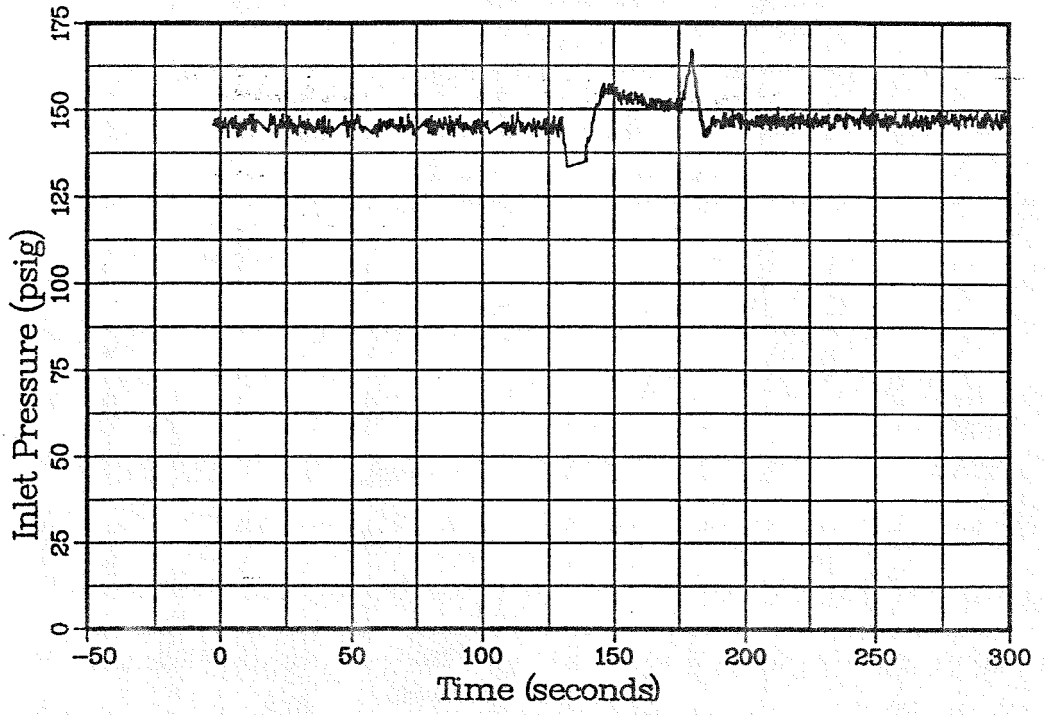

SANDIA NATIONAL LABORATORIES
Fusion Technology
Shot 144318

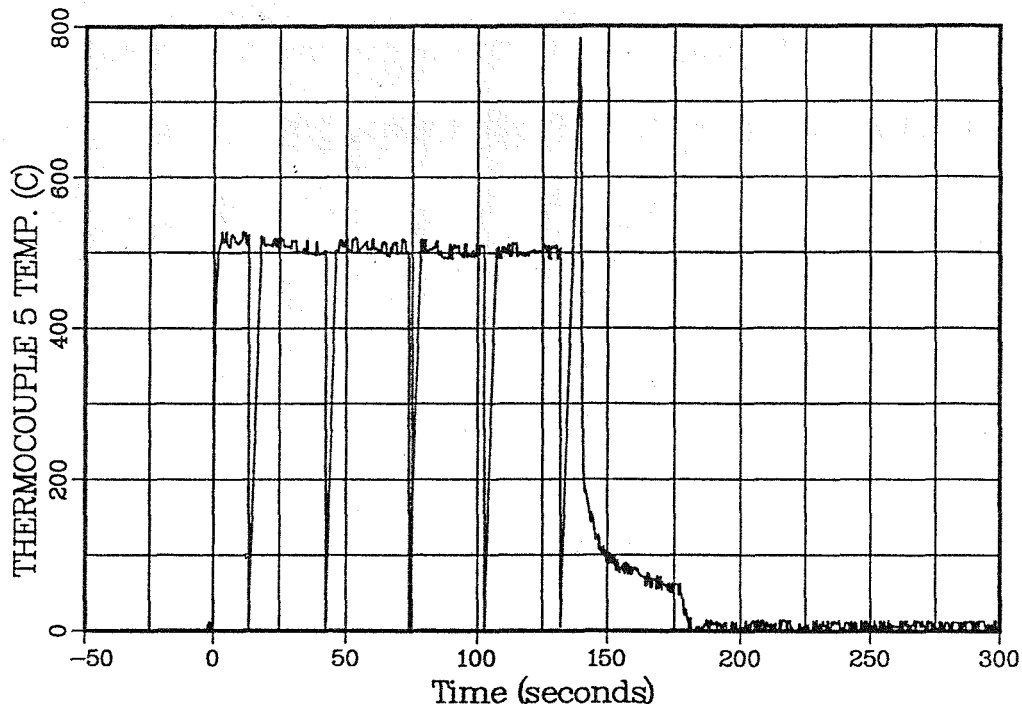

SANDIA NATIONAL LABORATORIES
Fusion Technology
Shot 144318

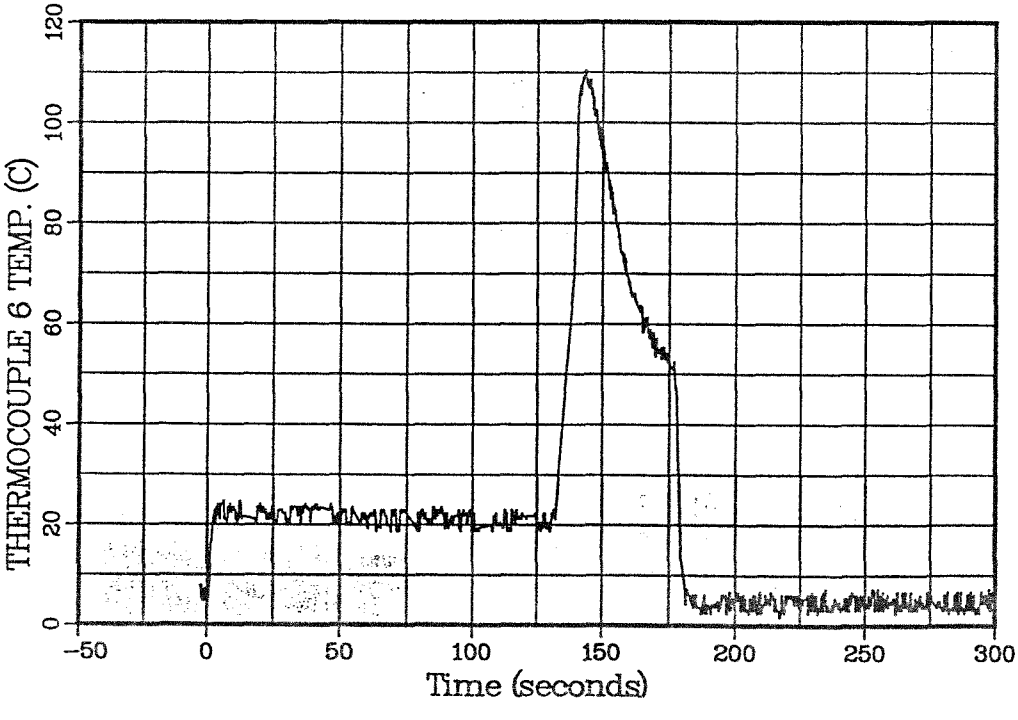

SANDIA NATIONAL LABORATORIES
Fusion Technology
Shot 144318

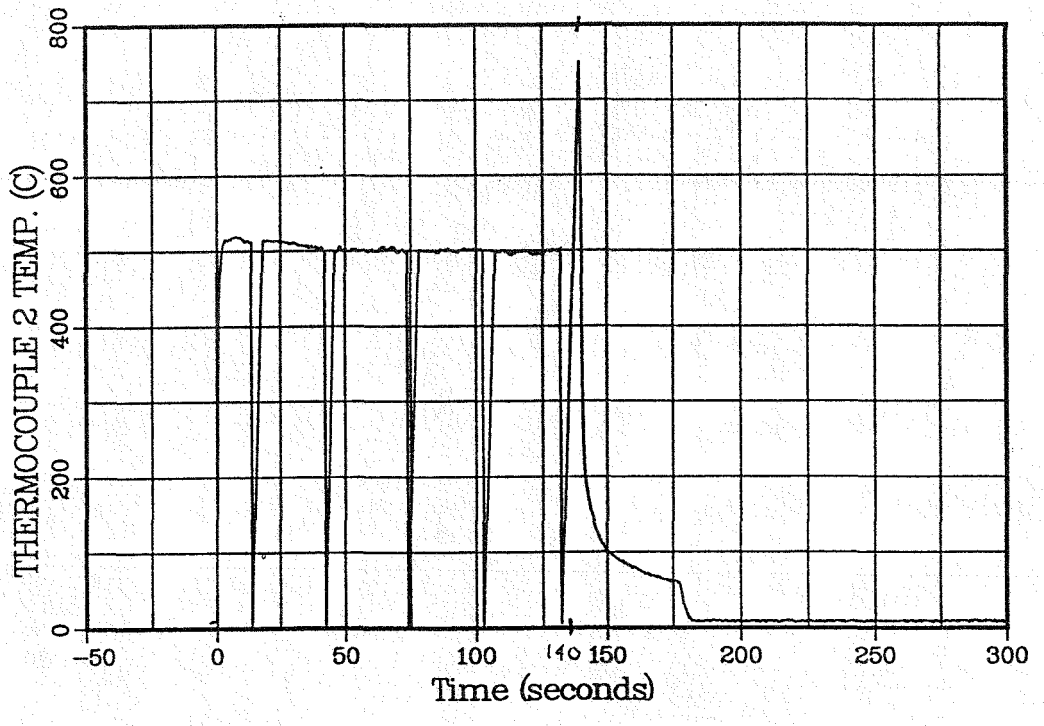

SANDIA NATIONAL LABORATORIES
Fusion Technology
Shot 144318

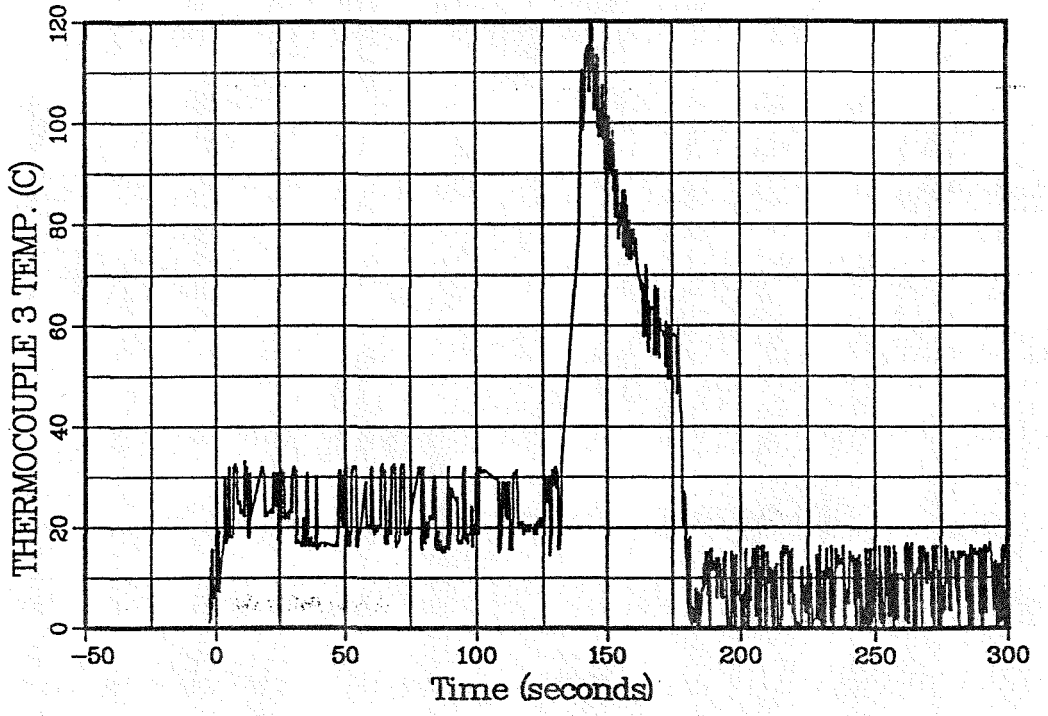

SANDIA NATIONAL LABORATORIES
Fusion Technology
Shot 144318

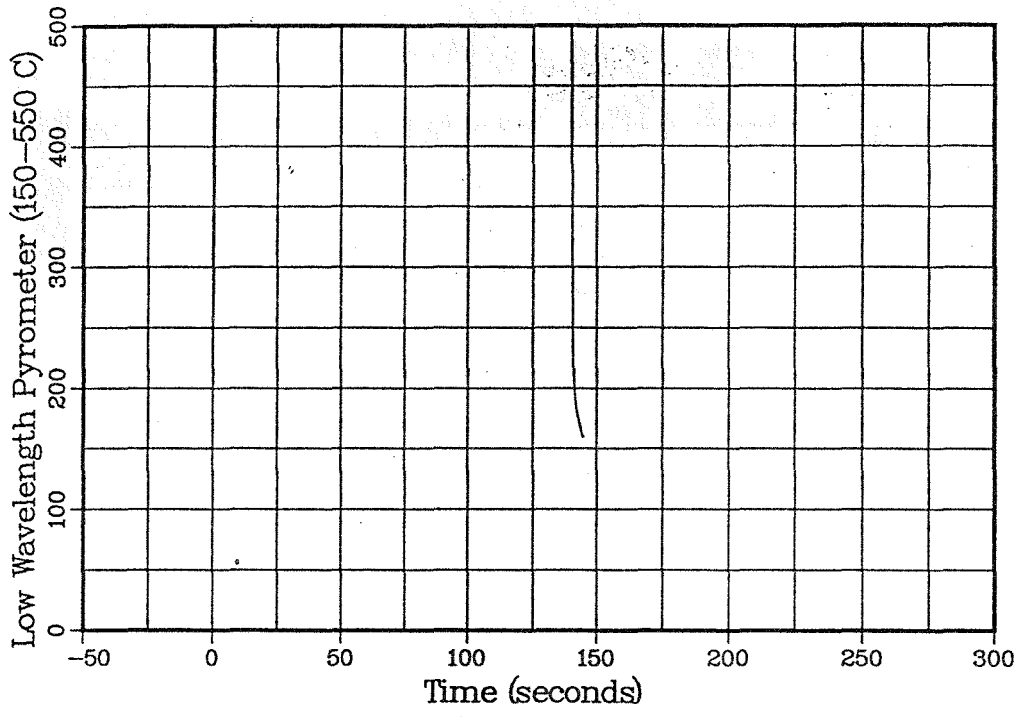

SANDIA NATIONAL LABORATORIES
Fusion Technology
Shot 144318

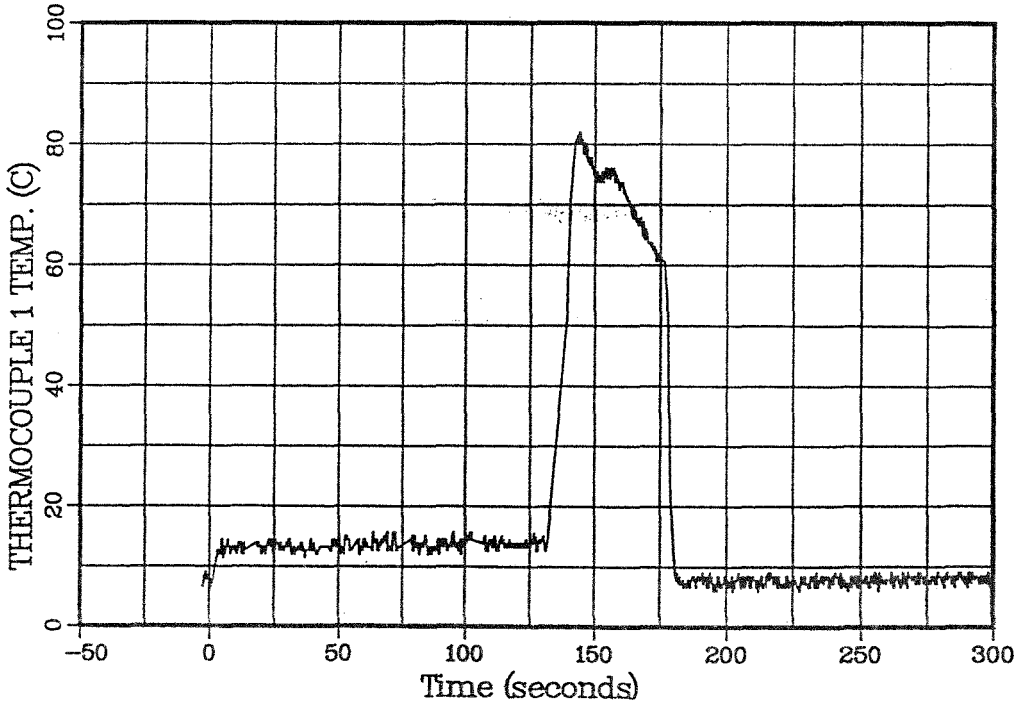

SANDIA NATIONAL LABORATORIES
Fusion Technology
Shot 144318

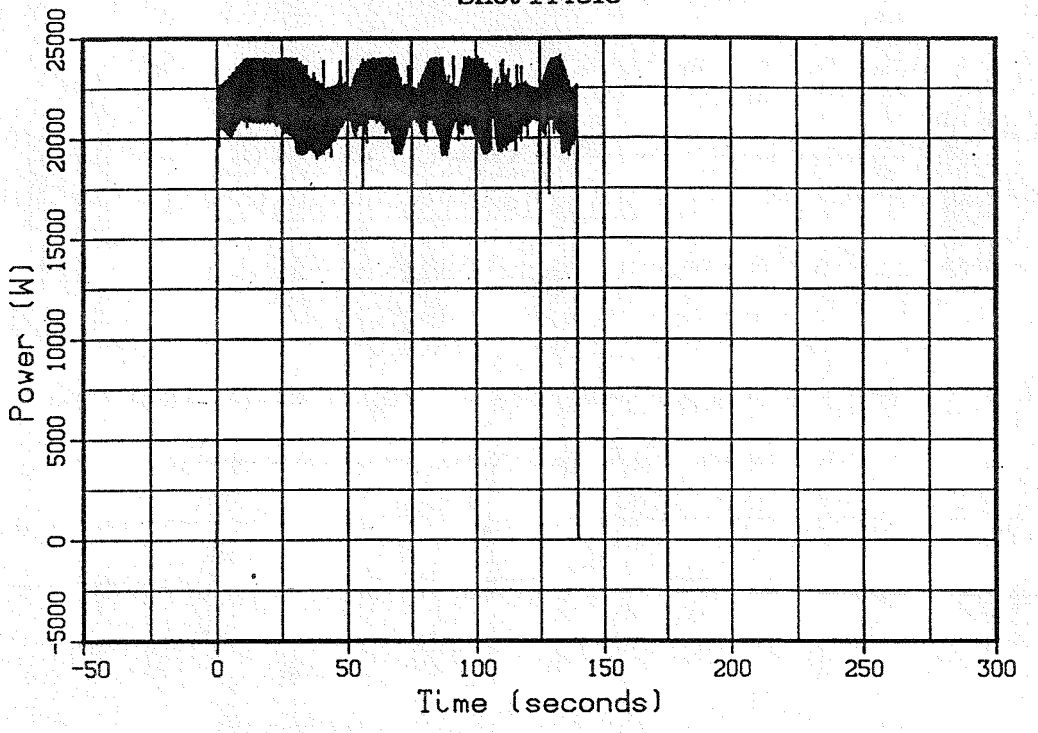

SANDIA NATIONAL LABORATORIES
Fusion Technology
Shot 144318

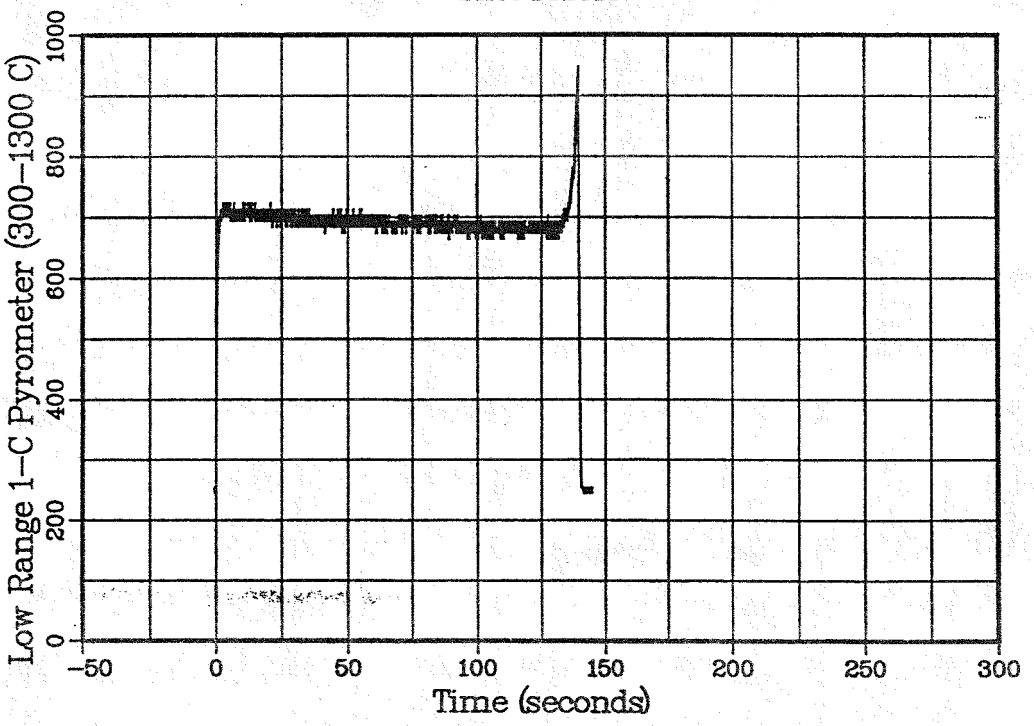

SANDIA NATIONAL LABORATORIES
Fusion Technology
Shot 144205

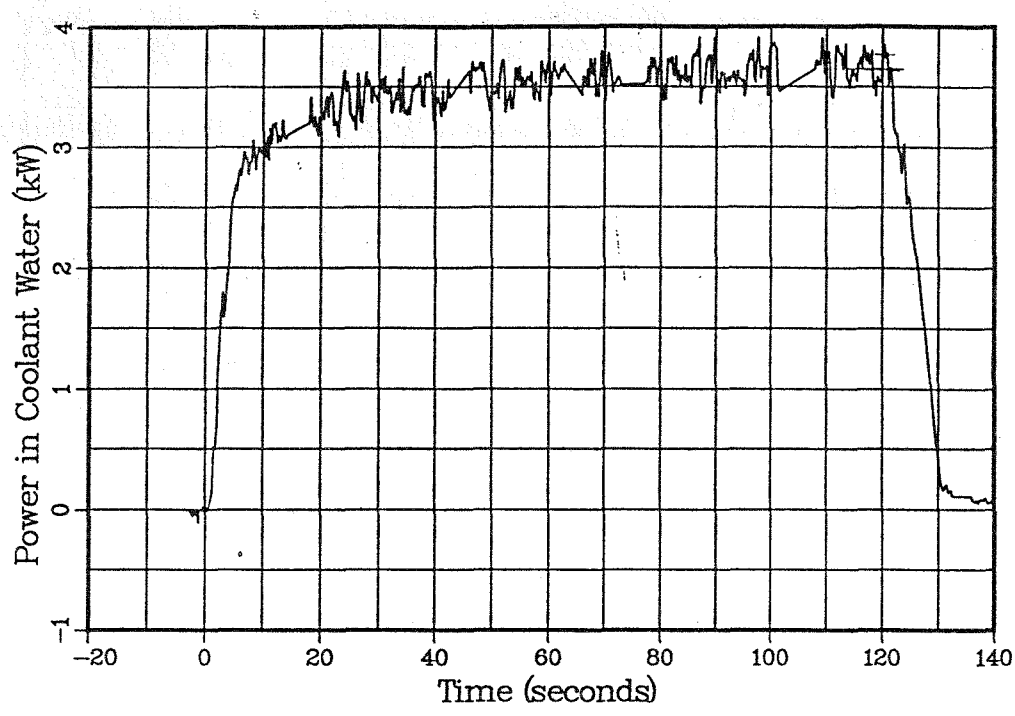

SANDIA NATIONAL LABORATORIES
Fusion Technology
Shot 144205

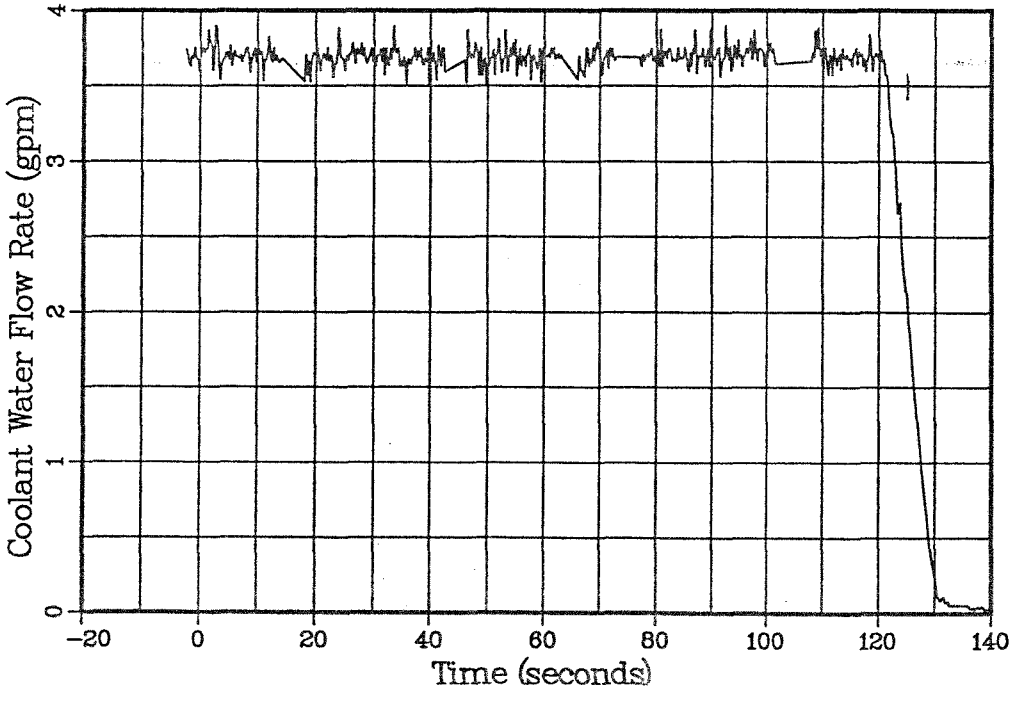

SANDIA NATIONAL LABORATORIES
Fusion Technology
Shot 144205

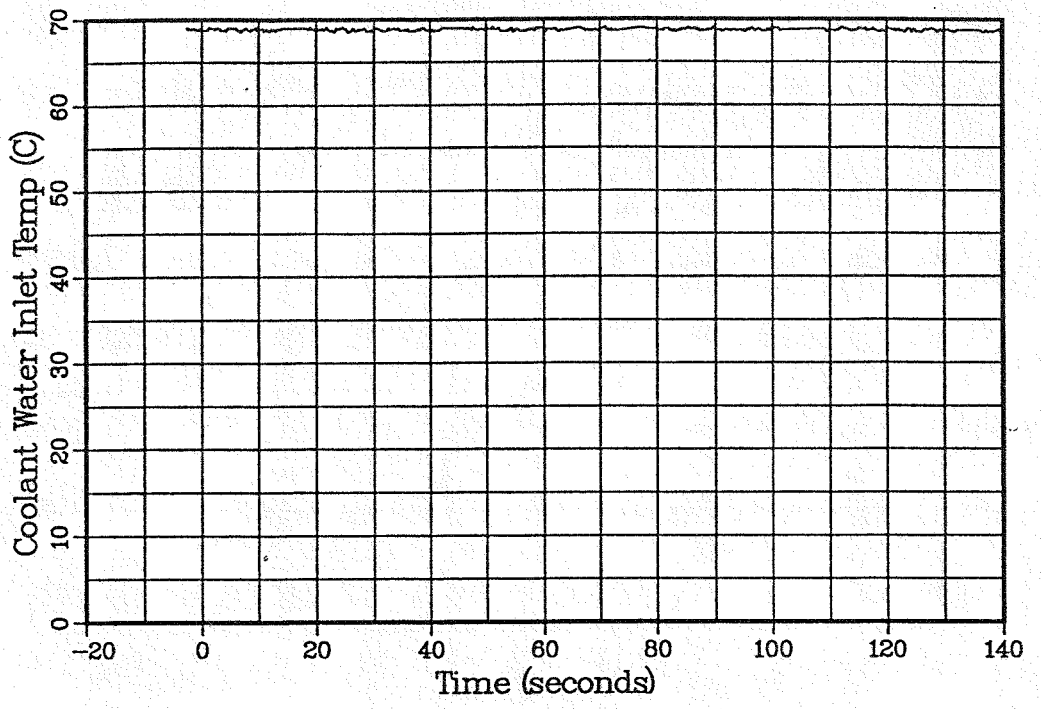

SANDIA NATIONAL LABORATORIES
Fusion Technology
Shot 144205

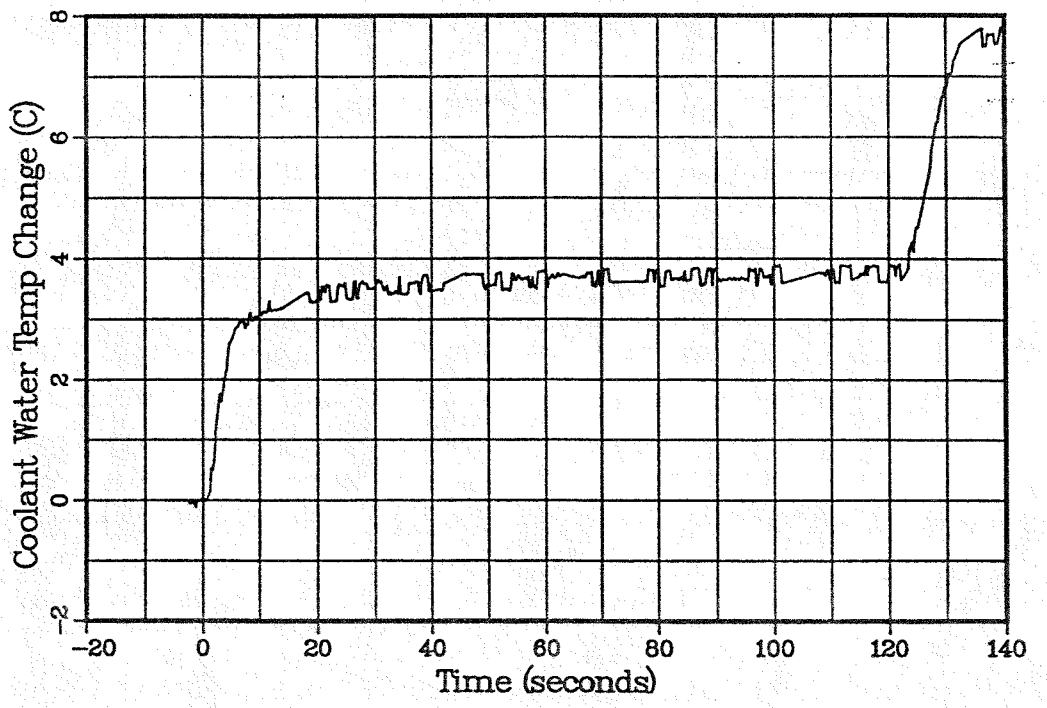

SANDIA NATIONAL LABORATORIES
Fusion Technology
Shot 144205

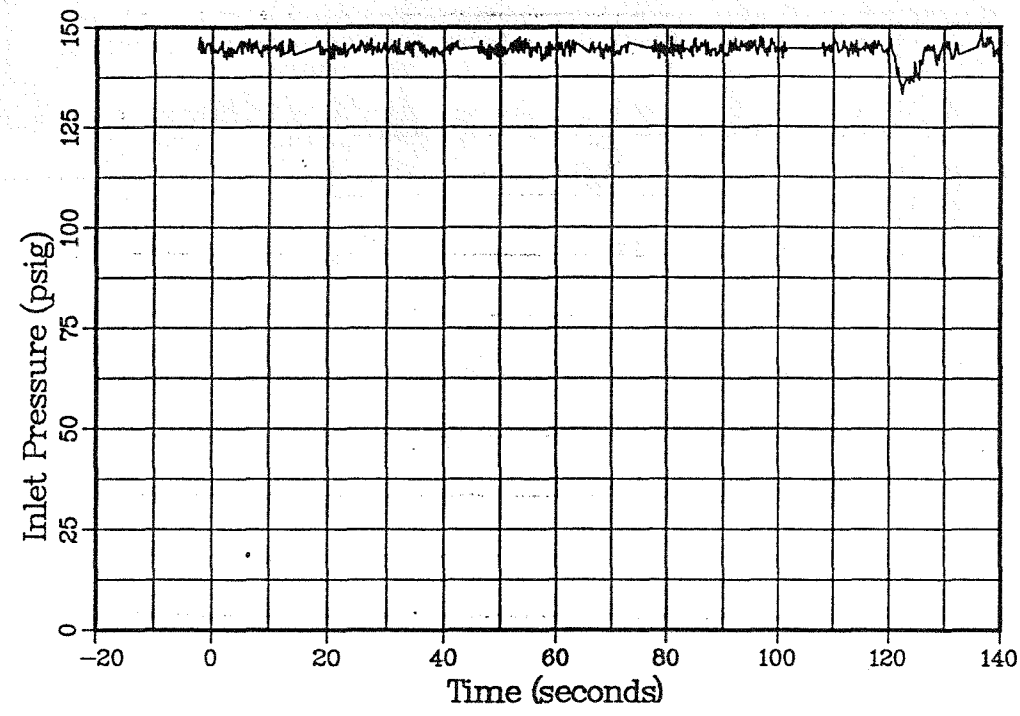

SANDIA NATIONAL LABORATORIES
Fusion Technology
Shot 144205

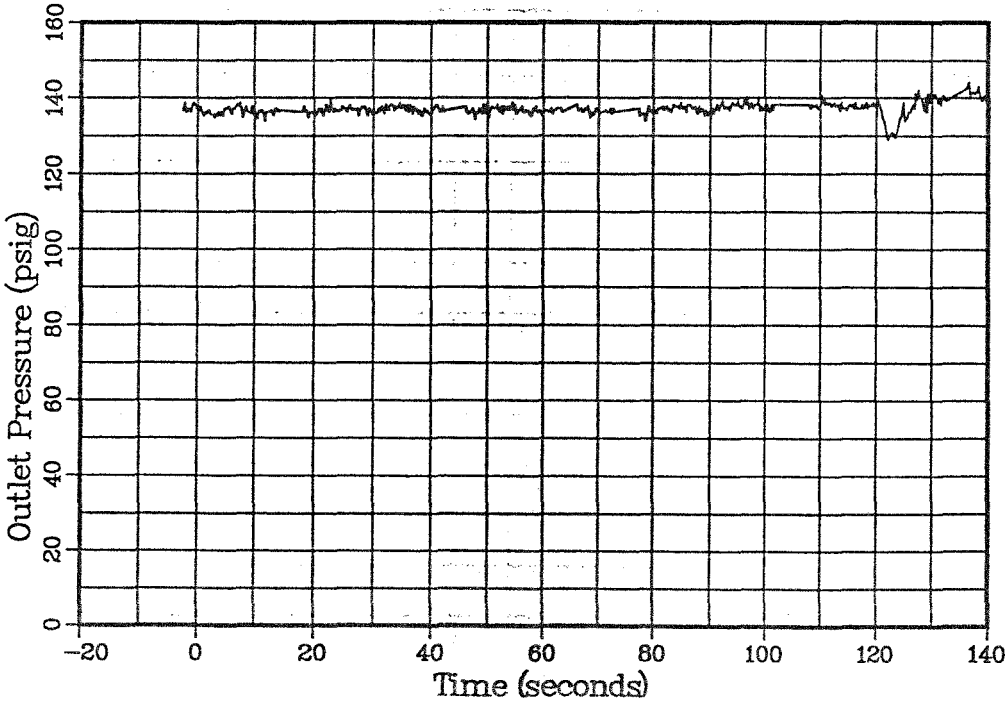

SANDIA NATIONAL LABORATORIES
Fusion Technology
Shot 144205

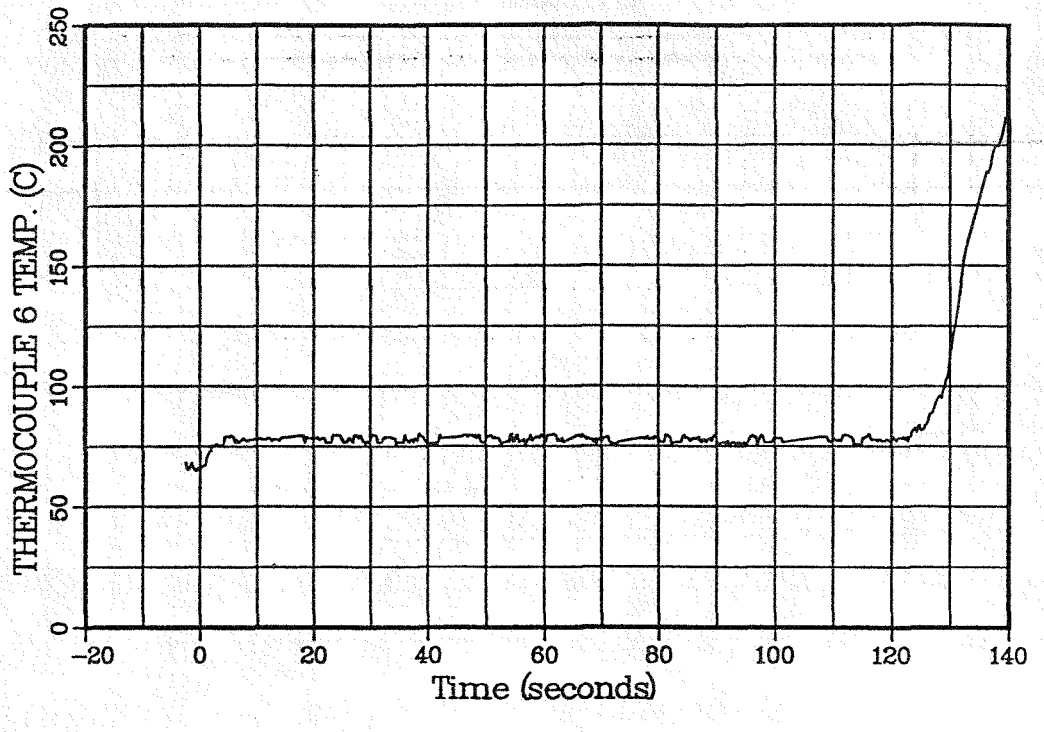

SANDIA NATIONAL LABORATORIES
Fusion Technology
Shot 144205

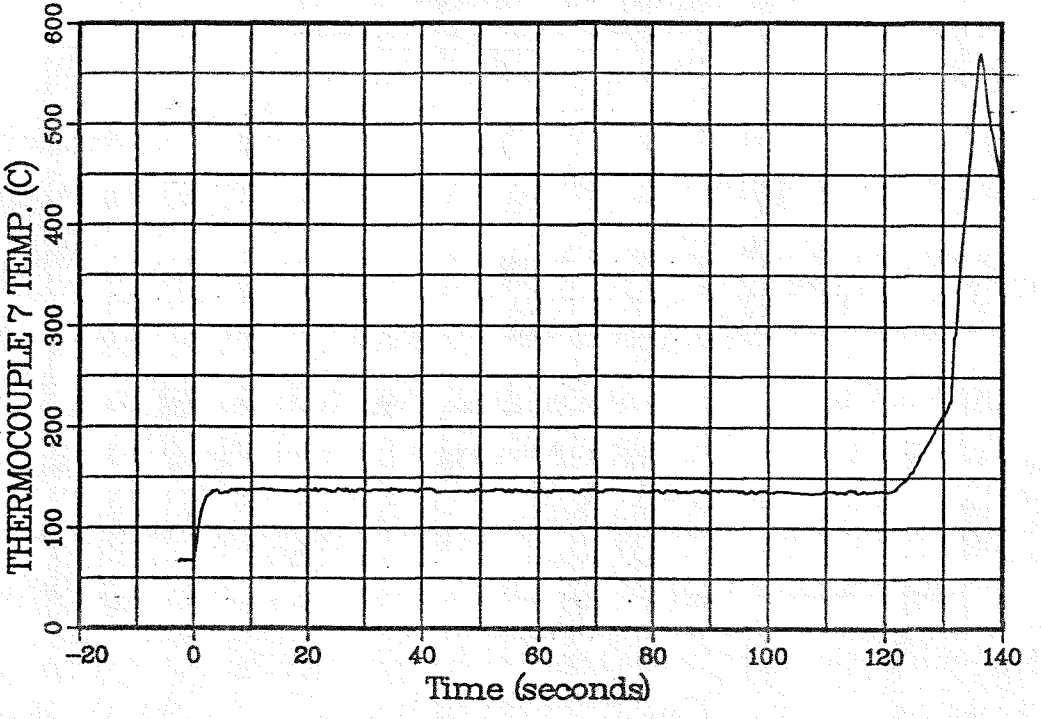

SANDIA NATIONAL LABORATORIES
Fusion Technology
Shot 144205

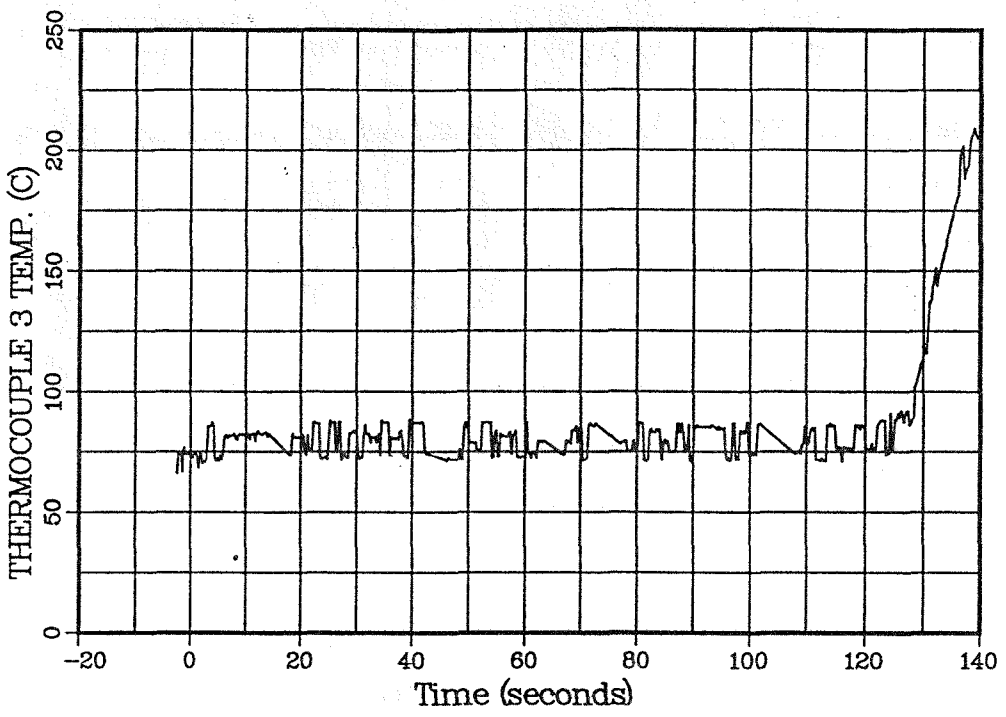

SANDIA NATIONAL LABORATORIES
Fusion Technology
Shot 144205

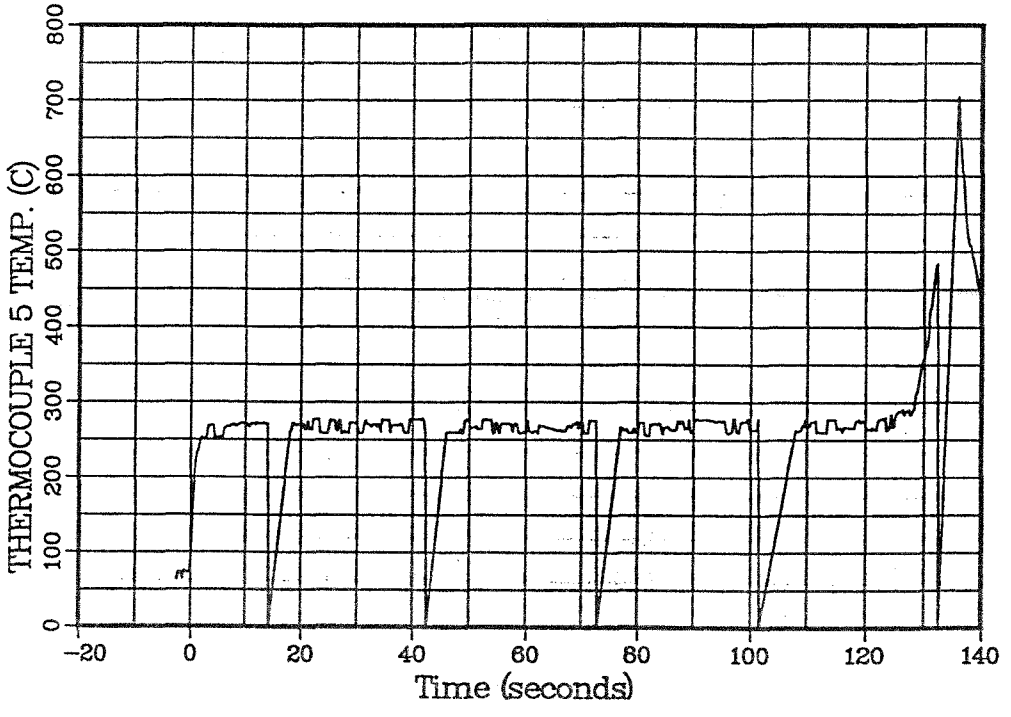

SANDIA NATIONAL LABORATORIES
Fusion Technology
Shot 144205

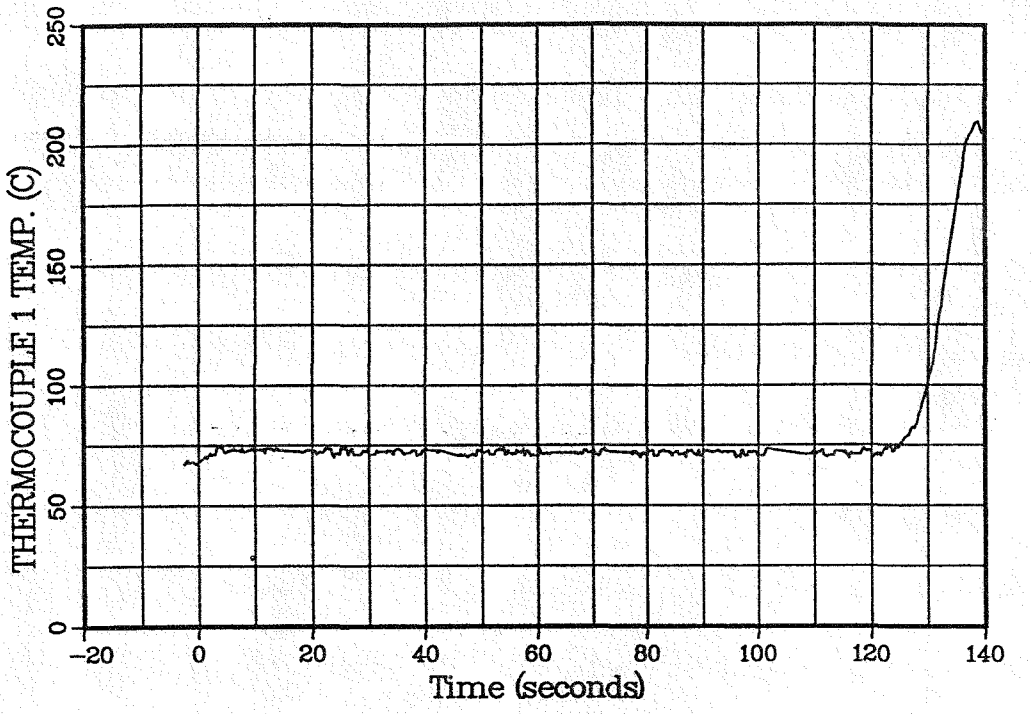

SANDIA NATIONAL LABORATORIES
Fusion Technology
Shot 144205

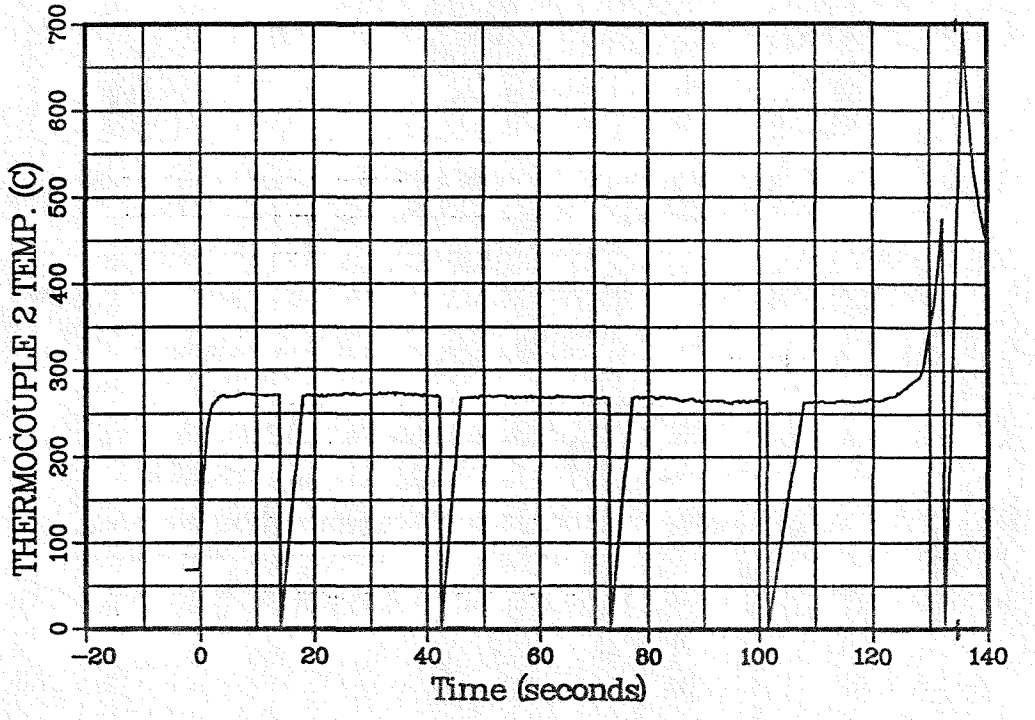

SANDIA NATIONAL LABORATORIES
Fusion Technology
Shot 144205

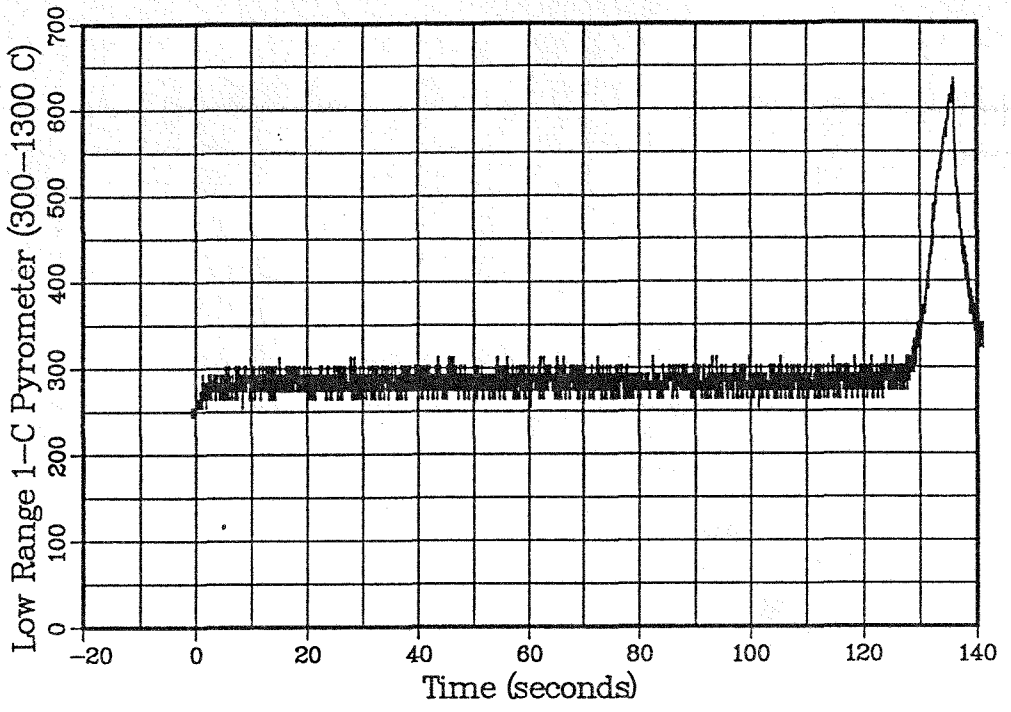

SANDIA NATIONAL LABORATORIES
Fusion Technology
Shot 144205

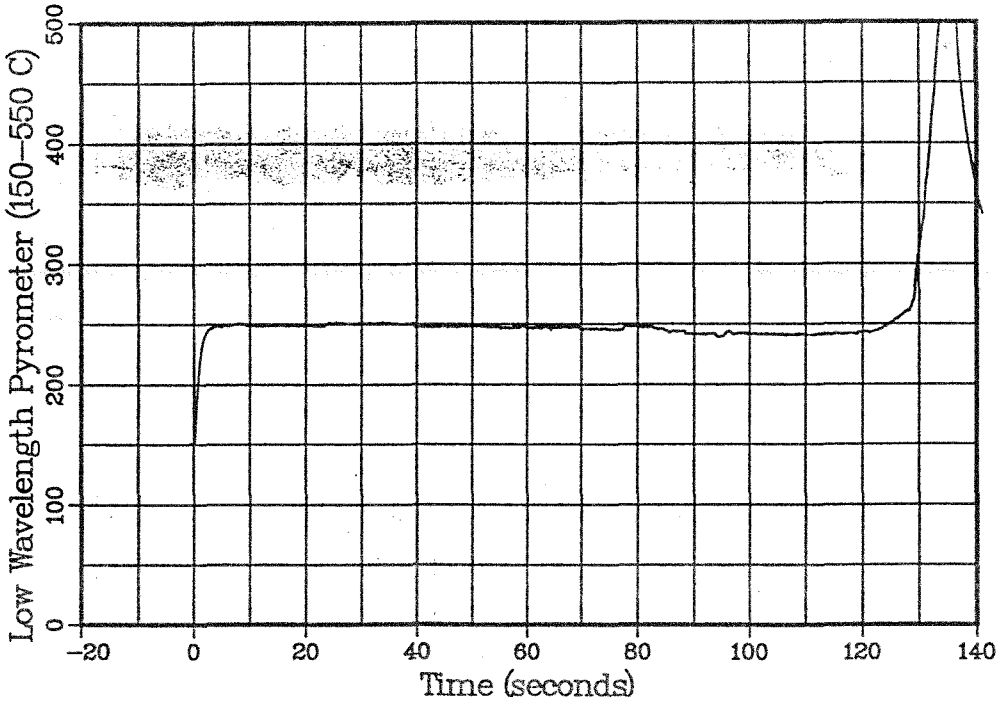

SANDIA NATIONAL LABORATORIES
Fusion Technology
Shot 144205

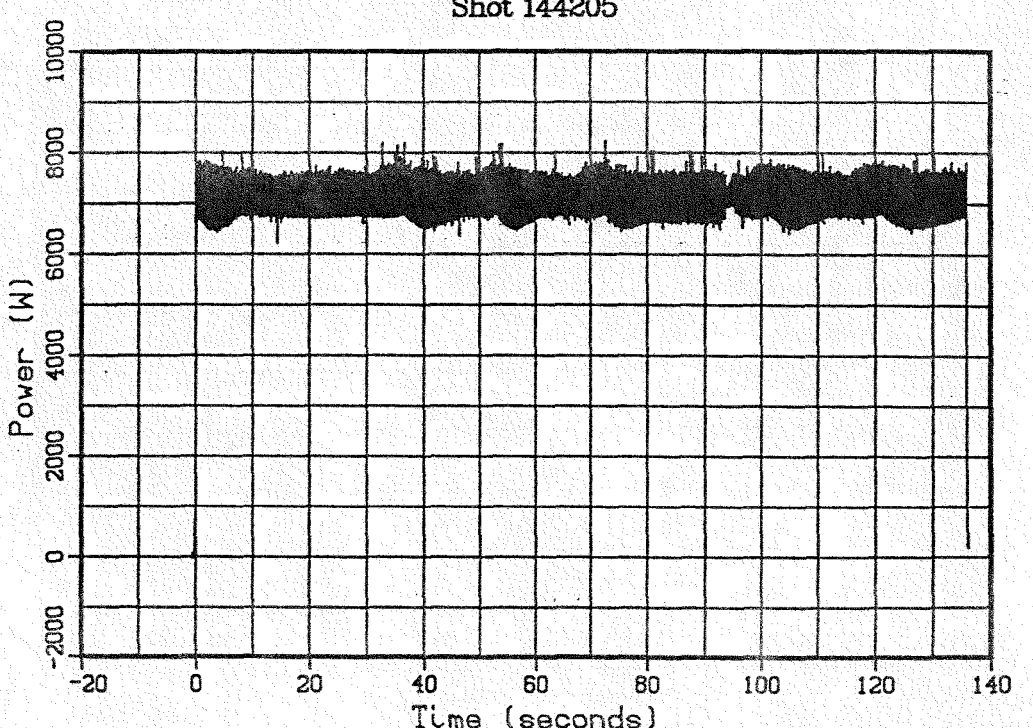

SANDIA NATIONAL LABORATORIES
Fusion Technology
Shot 144201

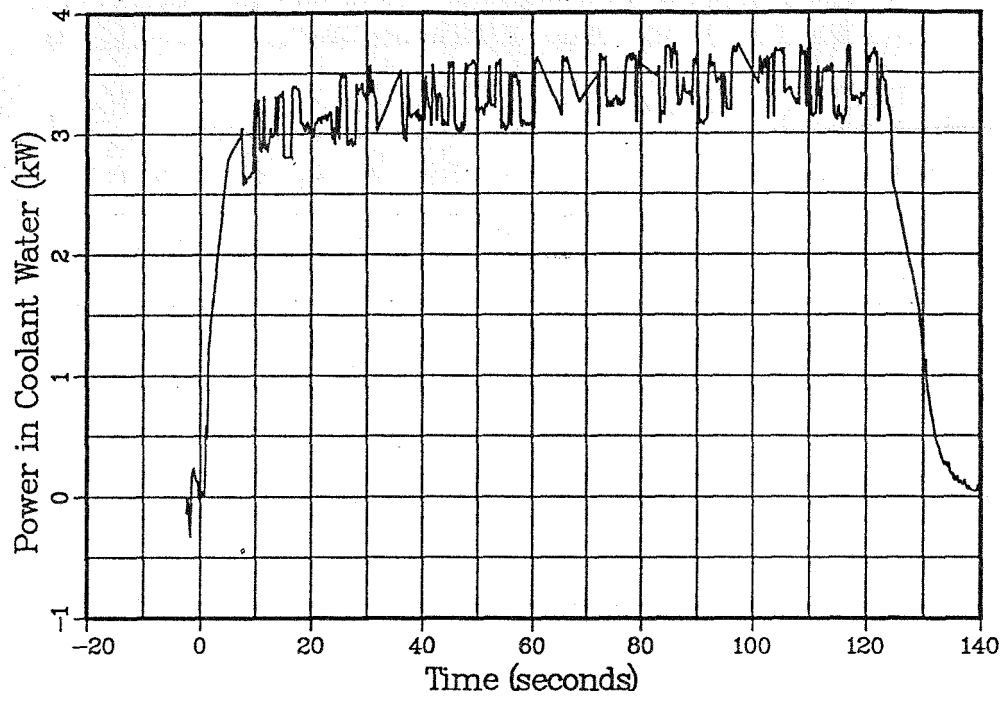

SANDIA NATIONAL LABORATORIES
Fusion Technology
Shot 144201

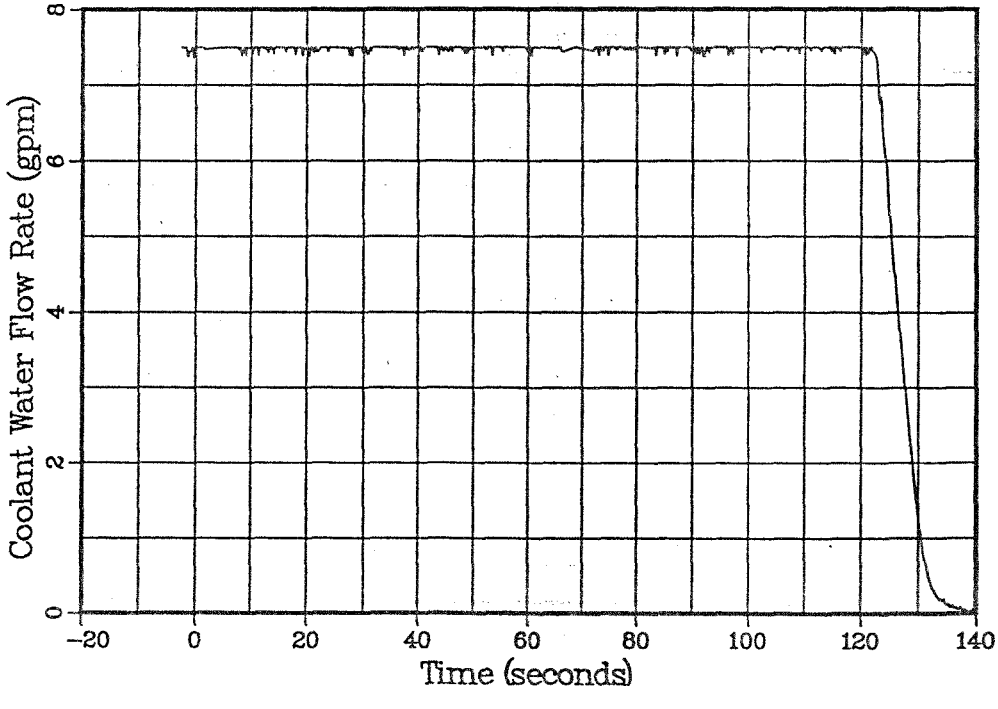

SANDIA NATIONAL LABORATORIES
Fusion Technology
Shot 144201

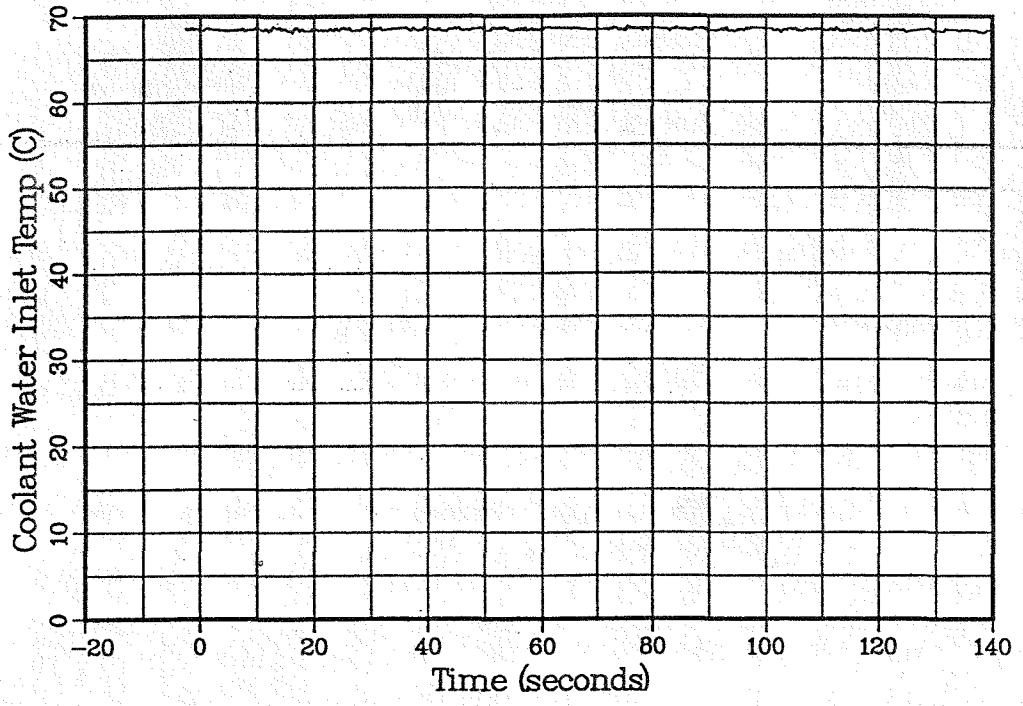

SANDIA NATIONAL LABORATORIES
Fusion Technology
Shot 144201

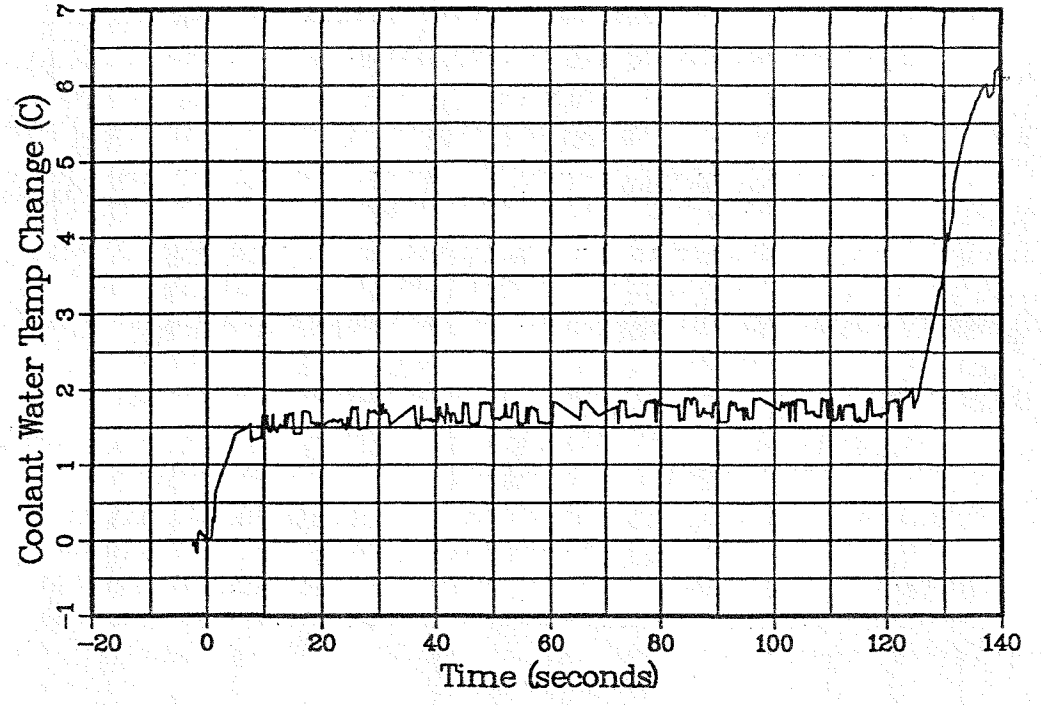

SANDIA NATIONAL LABORATORIES
Fusion Technology
Shot 144201

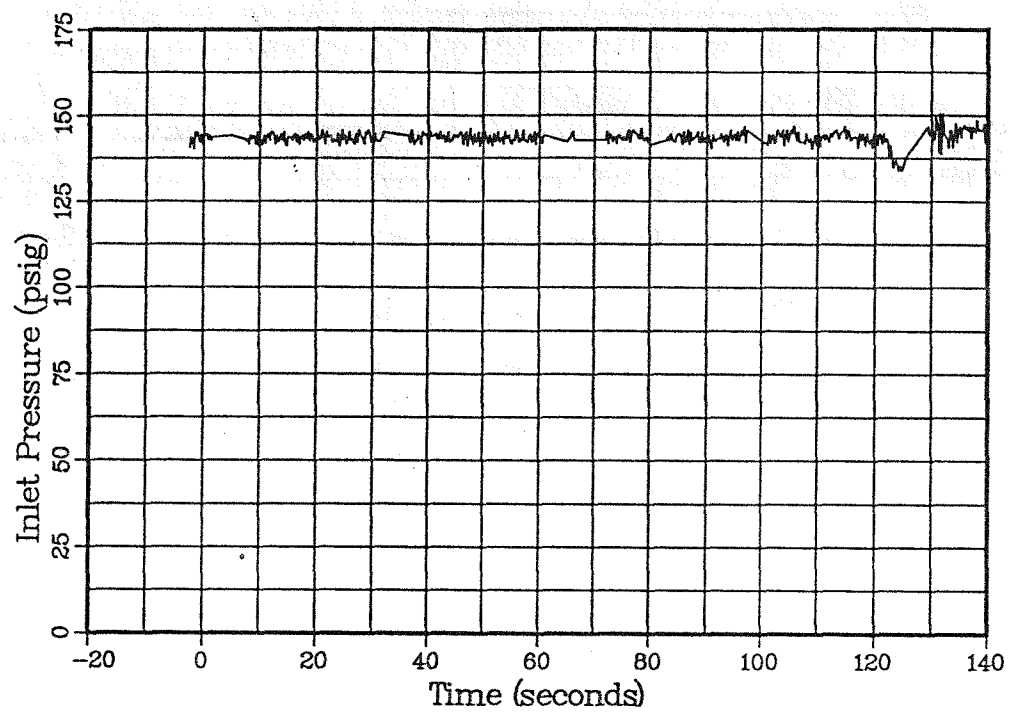

SANDIA NATIONAL LABORATORIES
Fusion Technology
Shot 144201

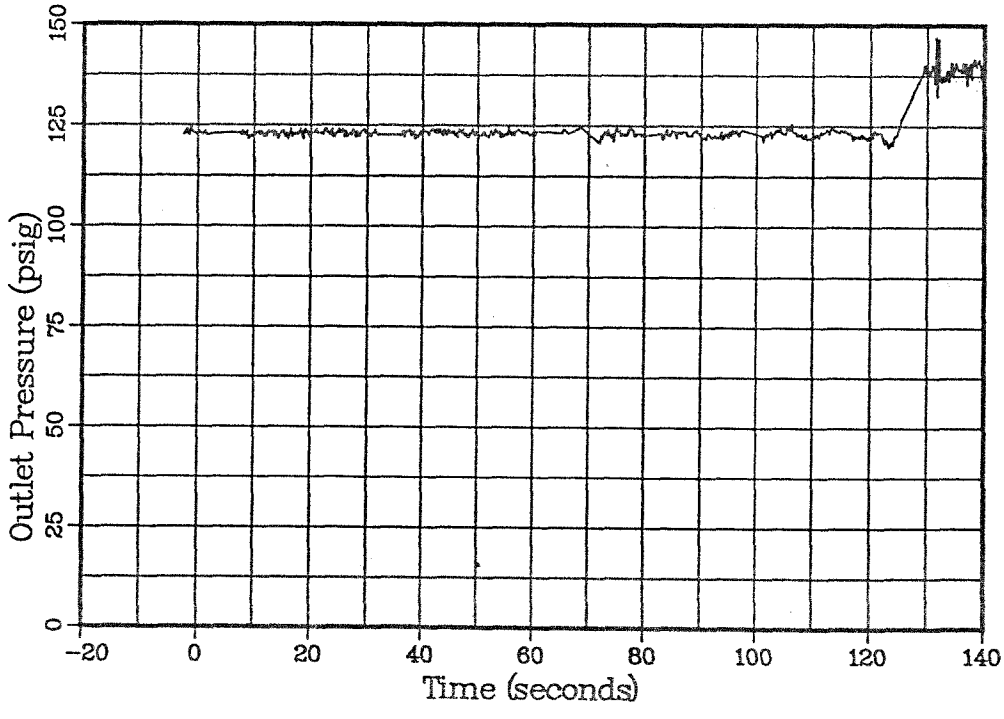

SANDIA NATIONAL LABORATORIES
Fusion Technology
Shot 144201

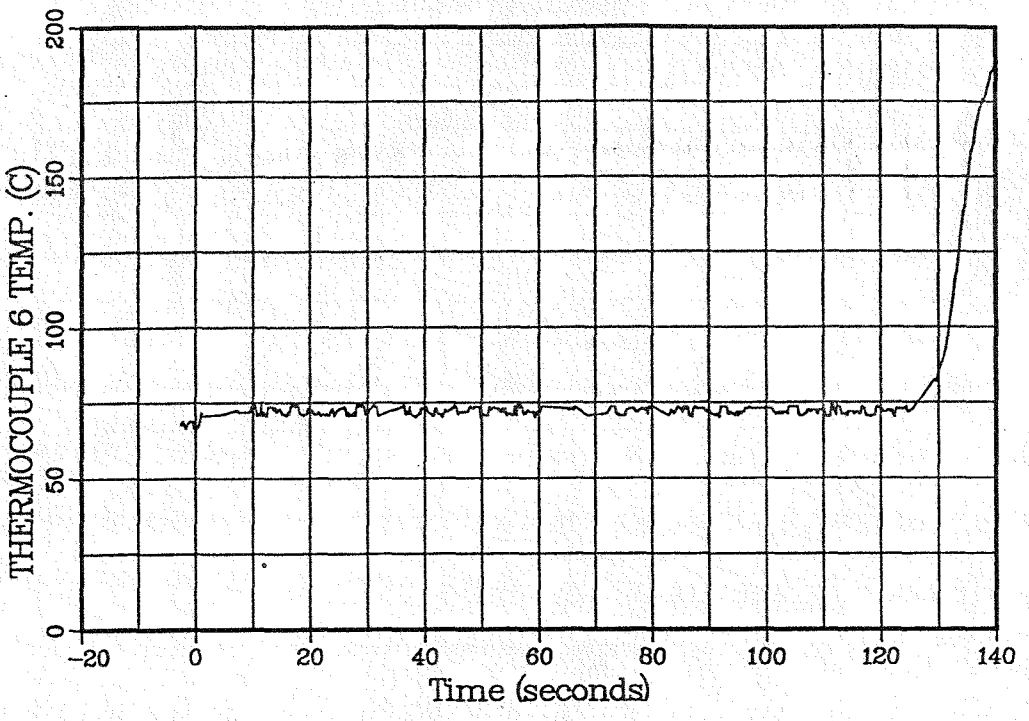

SANDIA NATIONAL LABORATORIES
Fusion Technology
Shot 144201

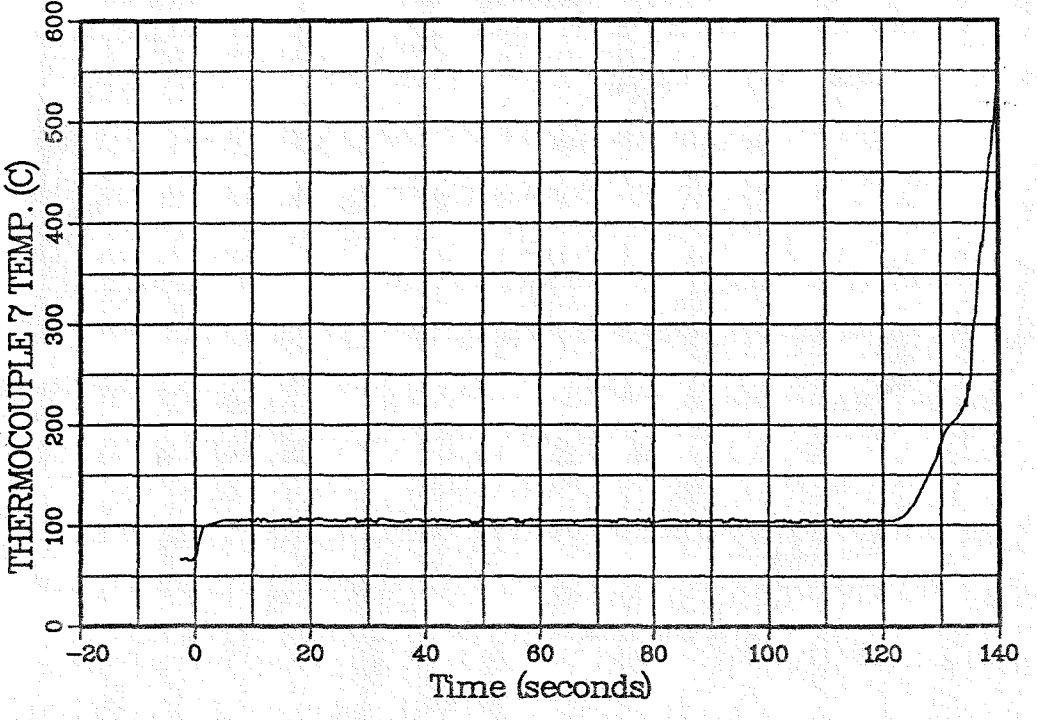

SANDIA NATIONAL LABORATORIES
Fusion Technology
Shot 144201

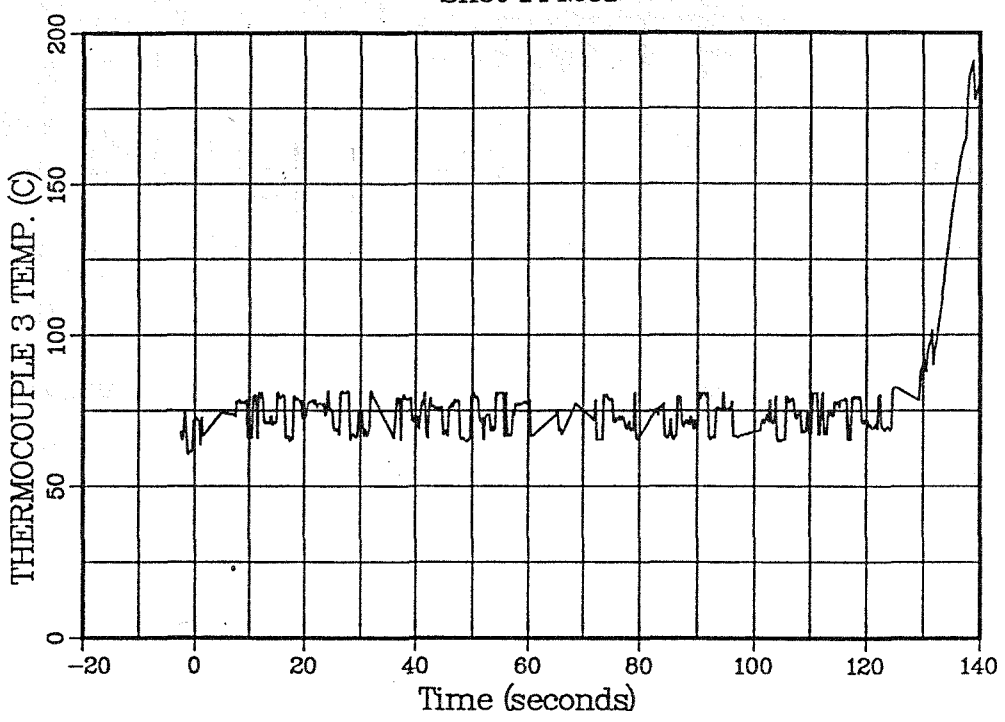

SANDIA NATIONAL LABORATORIES
Fusion Technology
Shot 144201

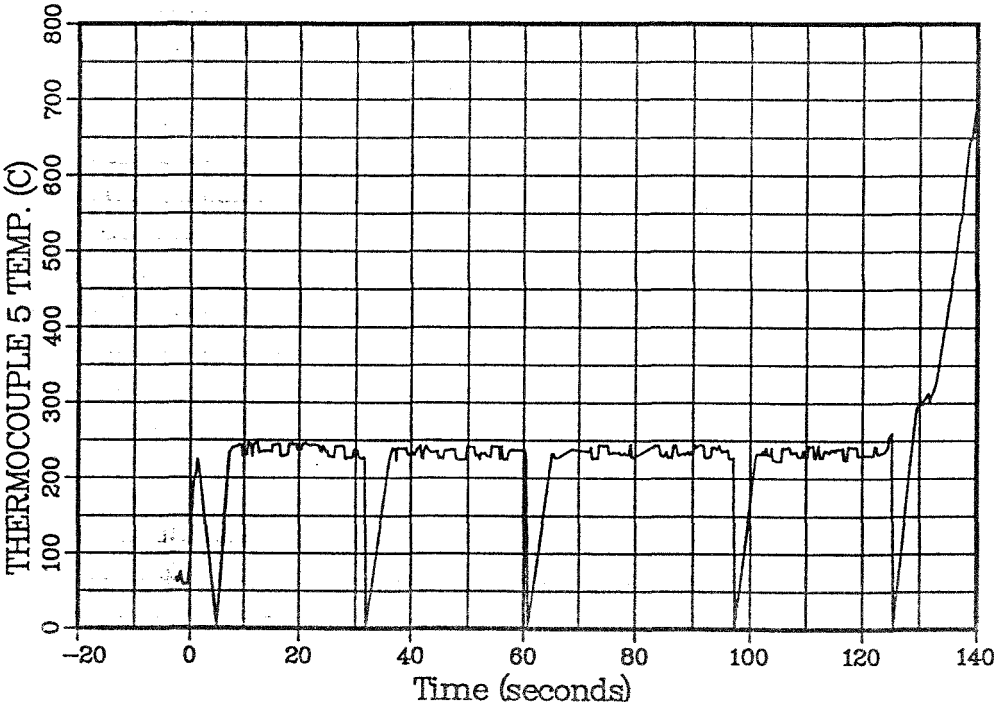

SANDIA NATIONAL LABORATORIES
Fusion Technology
Shot 144201

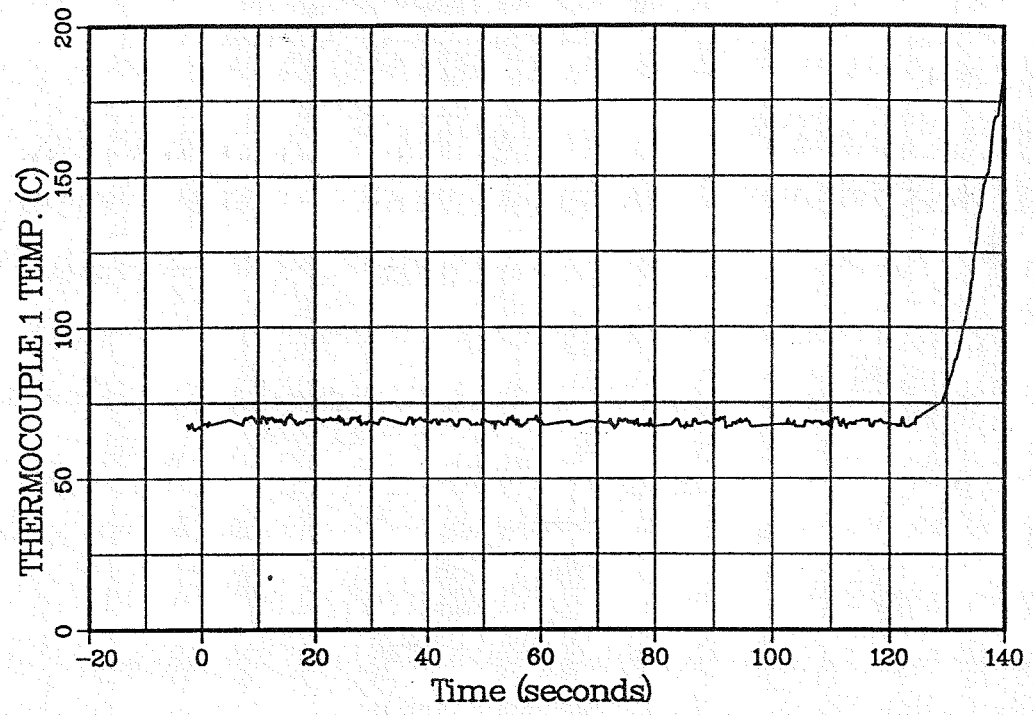

SANDIA NATIONAL LABORATORIES
Fusion Technology
Shot 144201

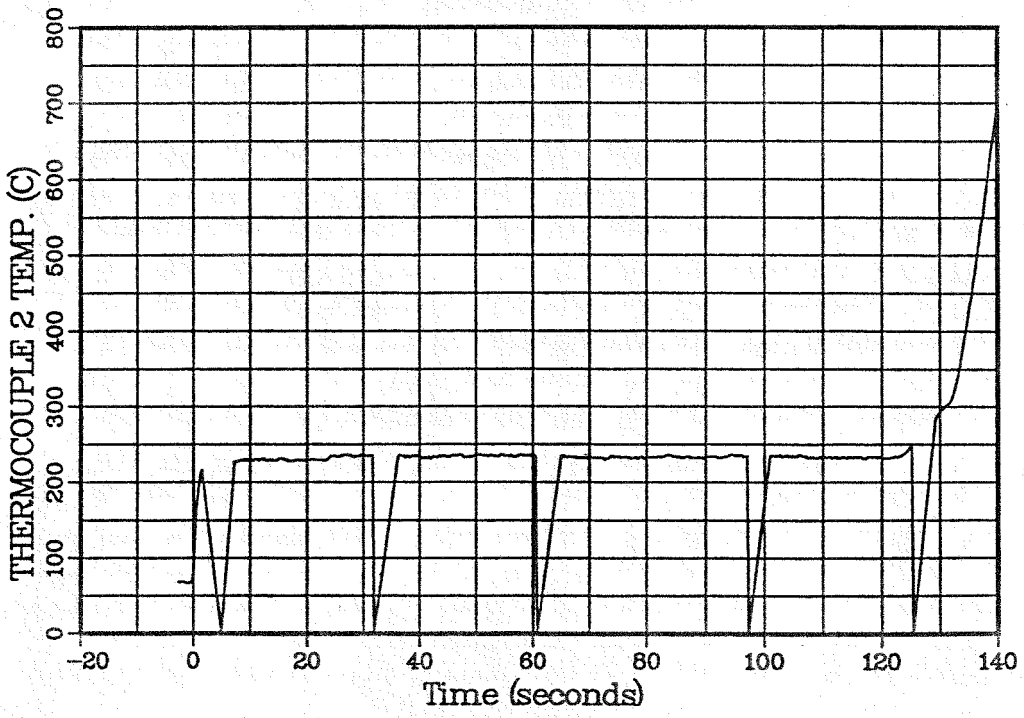

SANDIA NATIONAL LABORATORIES
Fusion Technology
Shot 144201

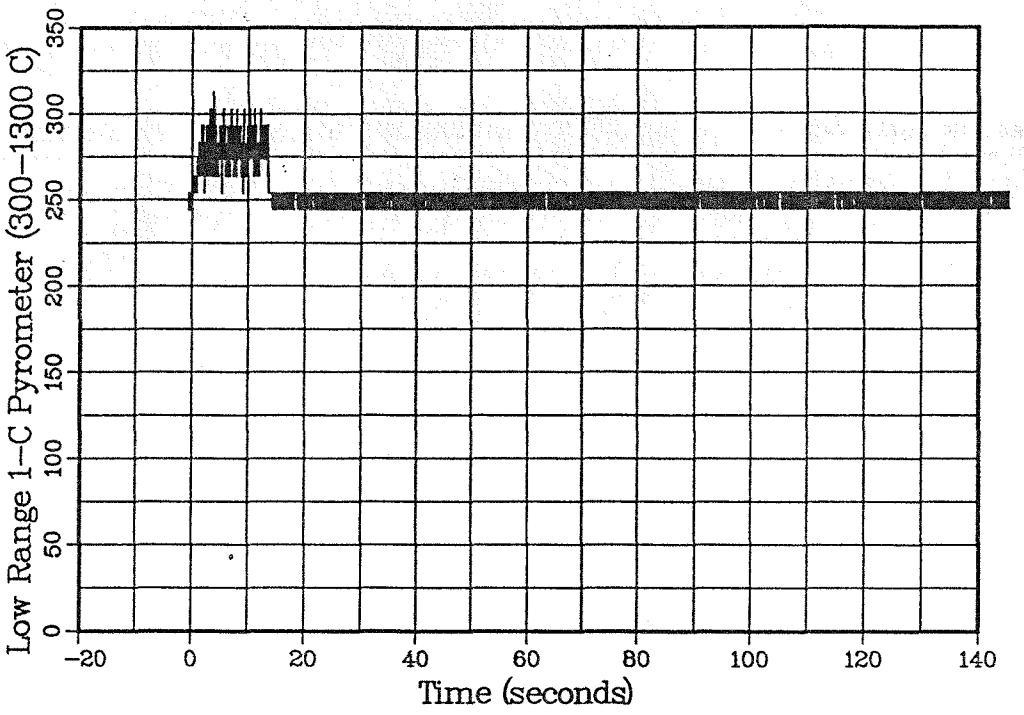

SANDIA NATIONAL LABORATORIES
Fusion Technology
Shot 144201

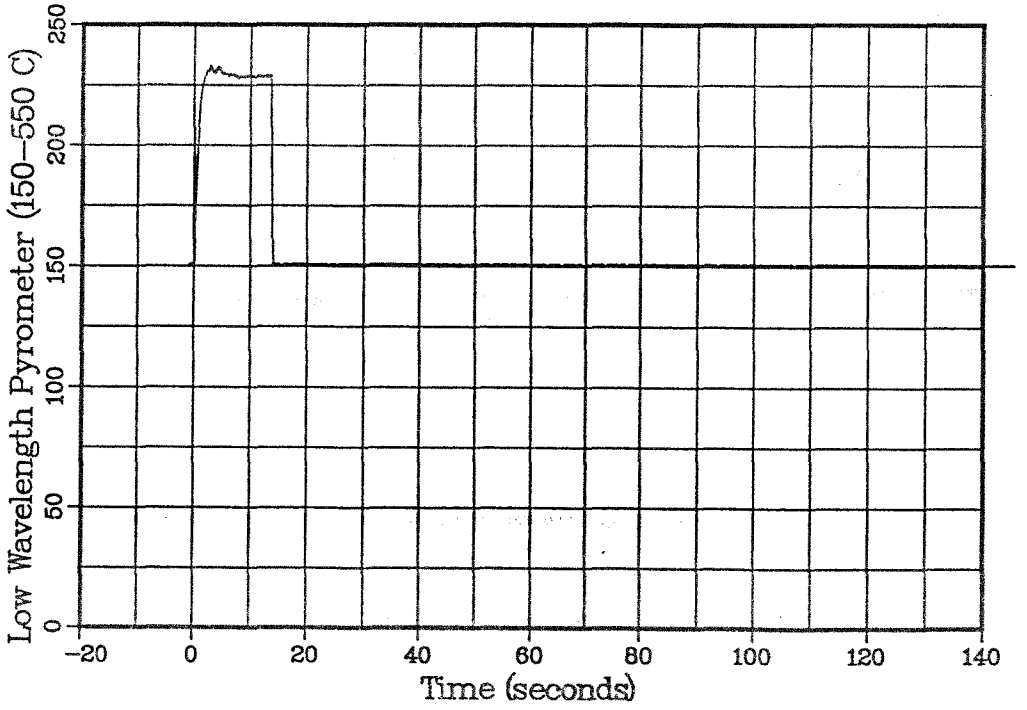

SANDIA NATIONAL LABORATORIES
Fusion Technology
Shot 144201

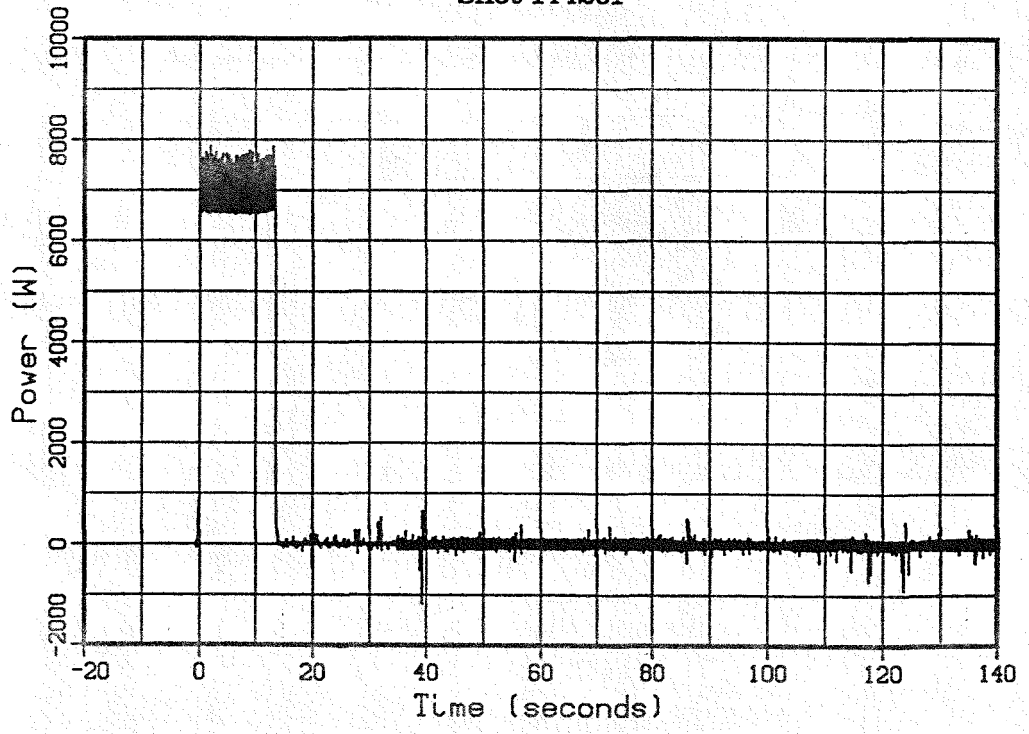

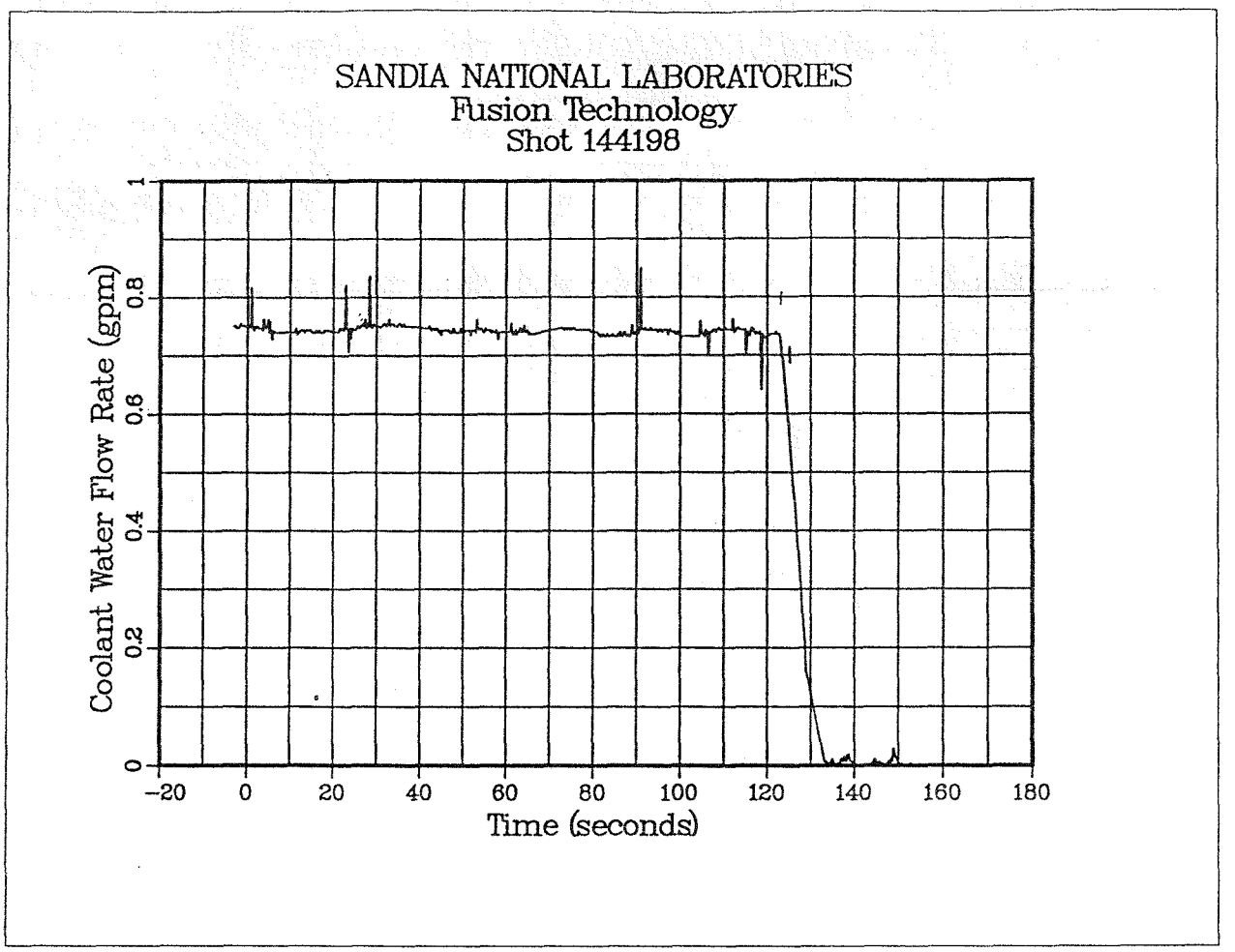
SANDIA NATIONAL LABORATORIES
Fusion Technology
Shot 144198
Coolant Water Flow Rate (gpm)
0
0.2
0.4
0.6
0.8
1
−20
0
20
40
60
80
100
120
140
160
180
Time (seconds)

SANDIA NATIONAL LABORATORIES
Fusion Technology
Shot 144198

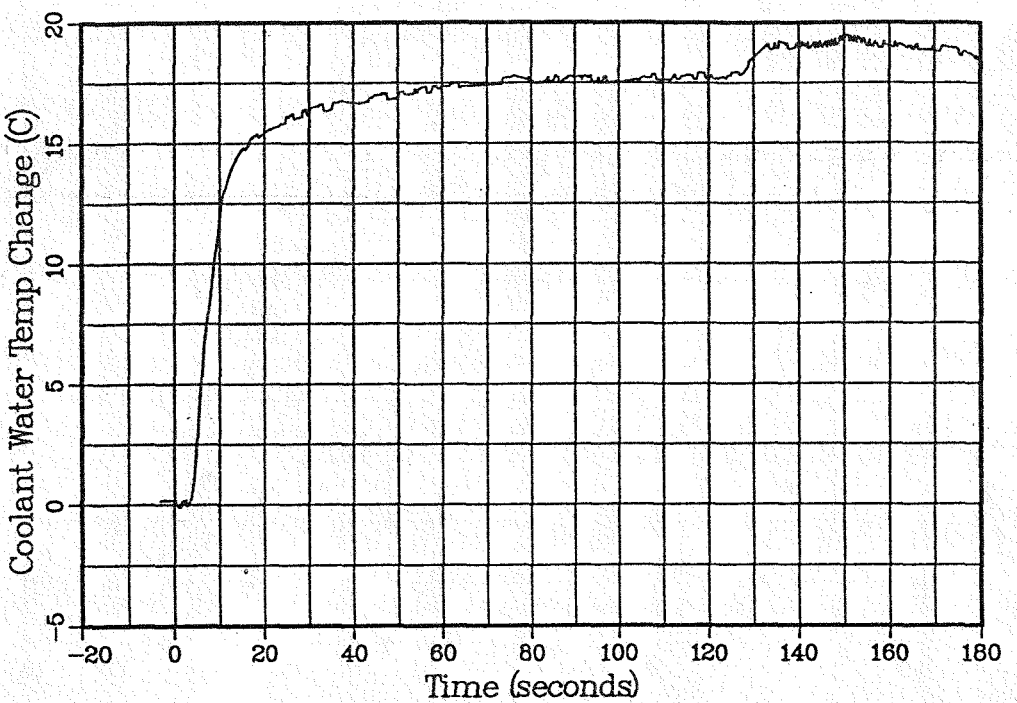

SANDIA NATIONAL LABORATORIES
Fusion Technology
Shot 144198

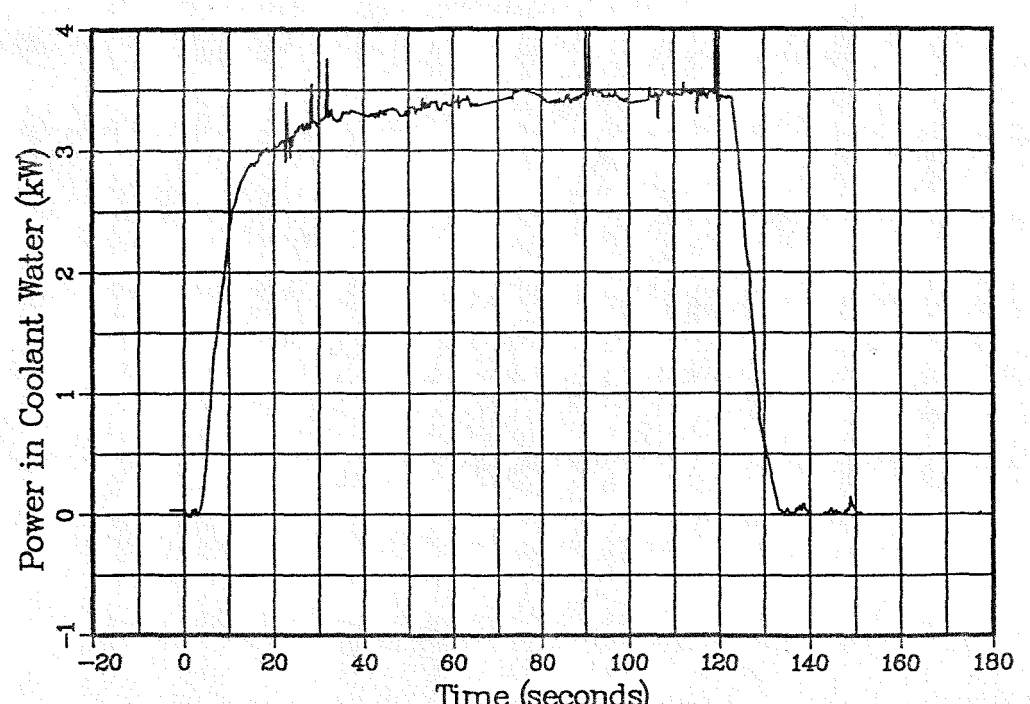

SANDIA NATIONAL LABORATORIES
Fusion Technology
Shot 144198

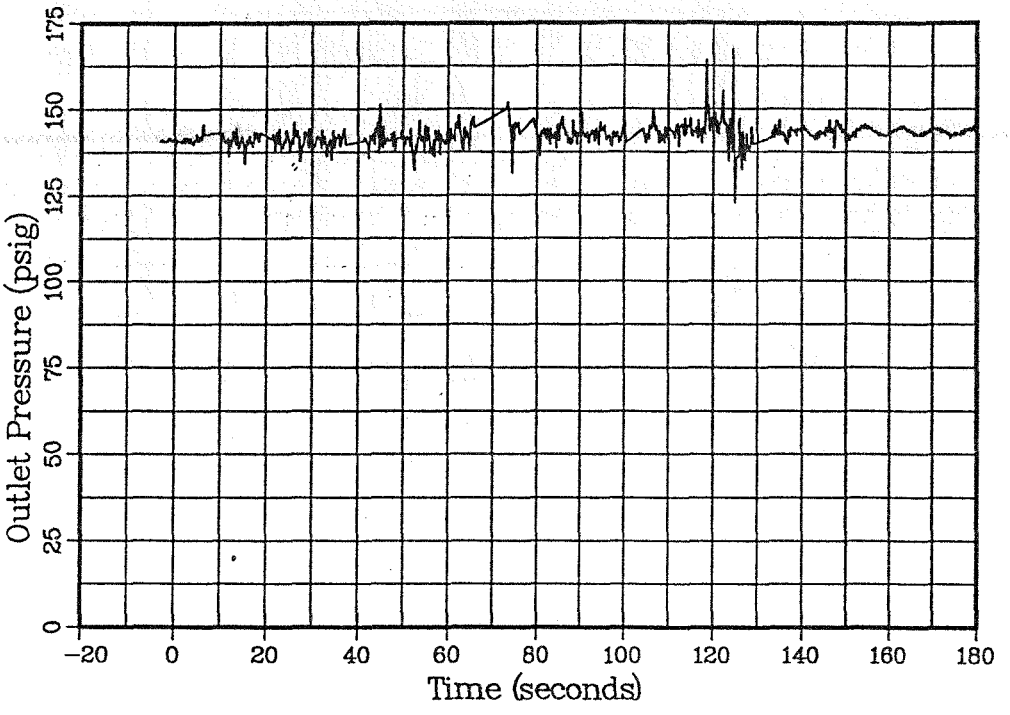

SANDIA NATIONAL LABORATORIES
Fusion Technology
Shot 144198

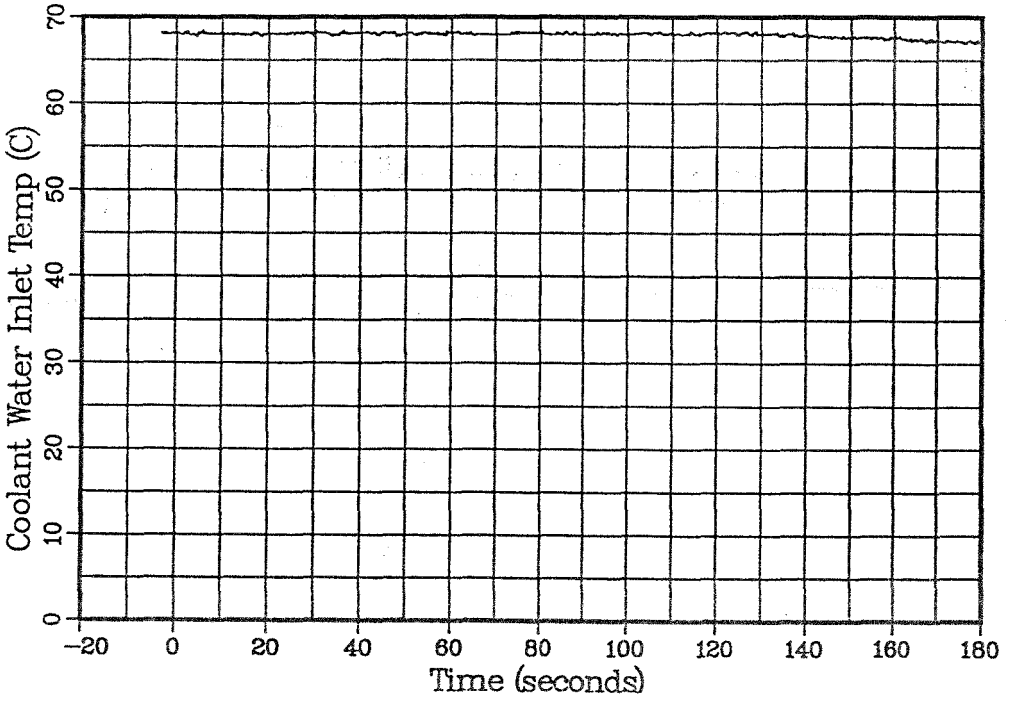

SANDIA NATIONAL LABORATORIES
Fusion Technology
Shot 144198

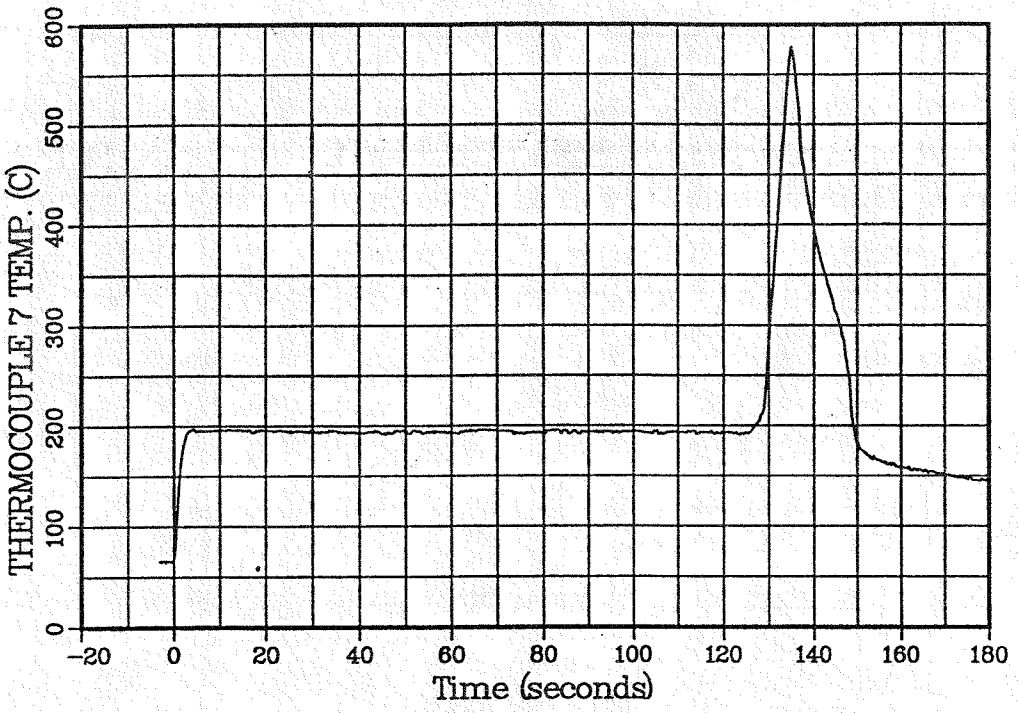

SANDIA NATIONAL LABORATORIES
Fusion Technology
Shot 144198

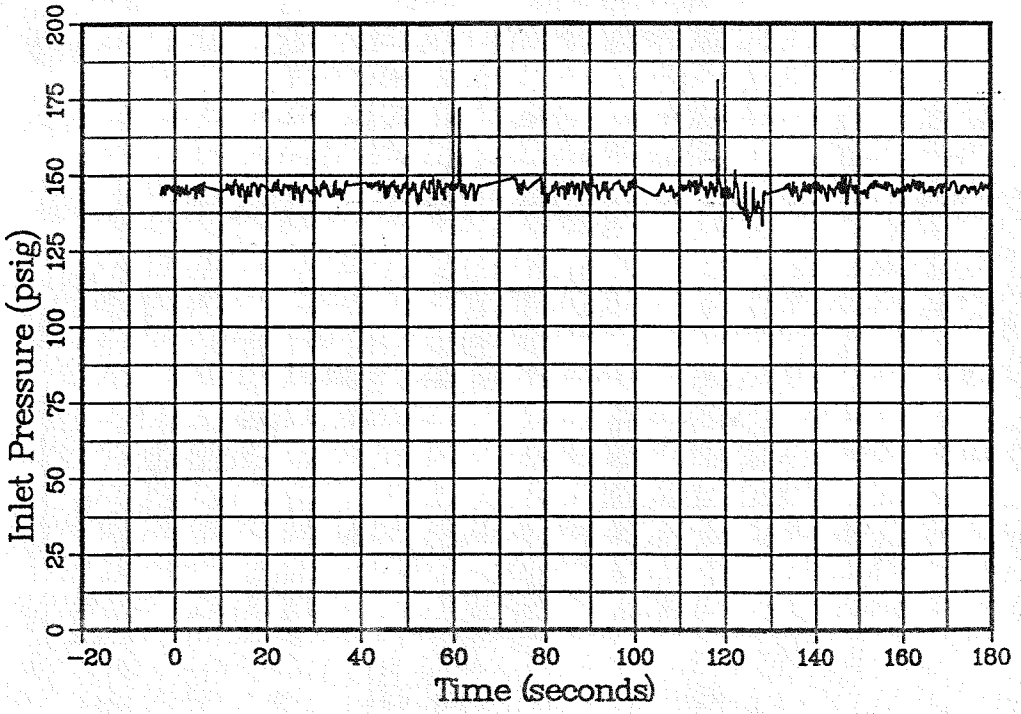

SANDIA NATIONAL LABORATORIES
Fusion Technology
Shot 144198

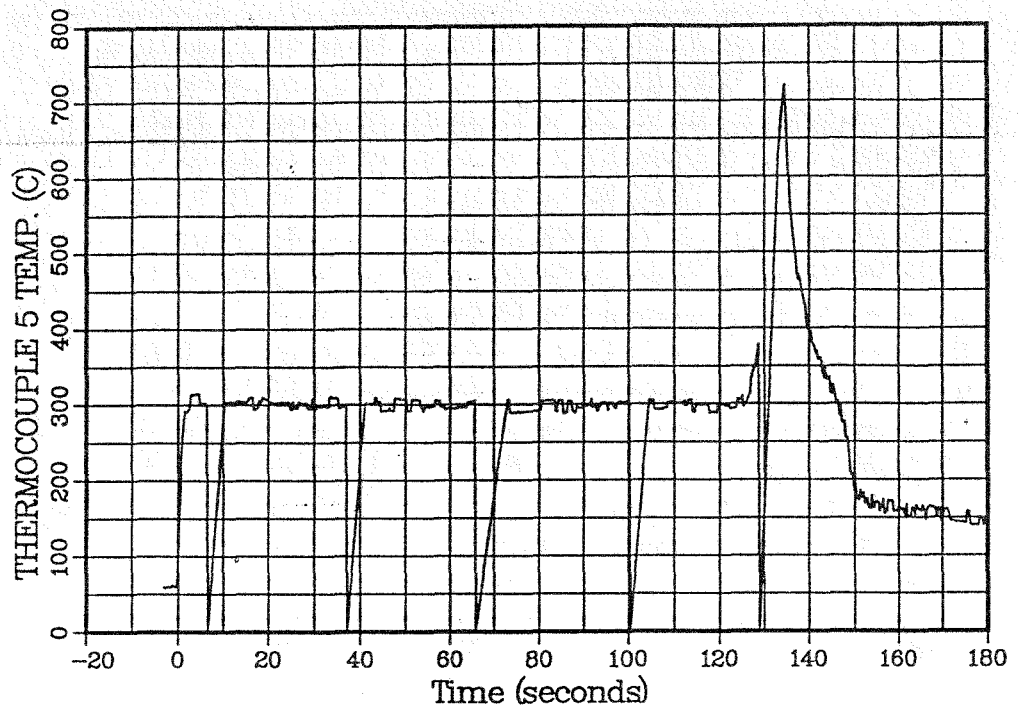

SANDIA NATIONAL LABORATORIES
Fusion Technology
Shot 144198

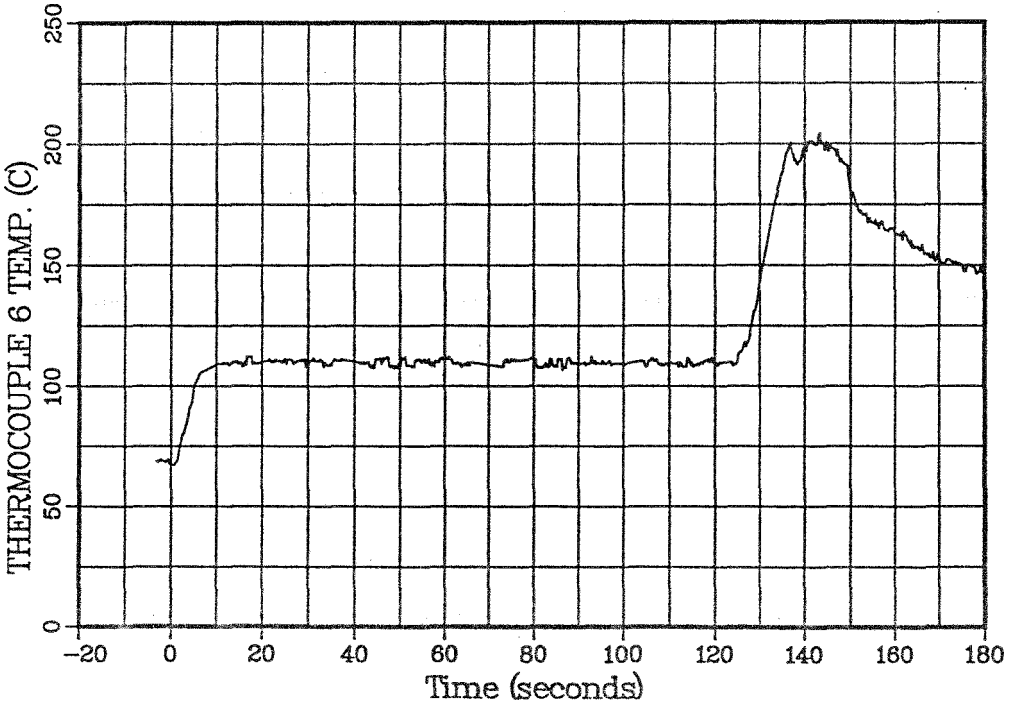

SANDIA NATIONAL LABORATORIES
Fusion Technology
Shot 144198

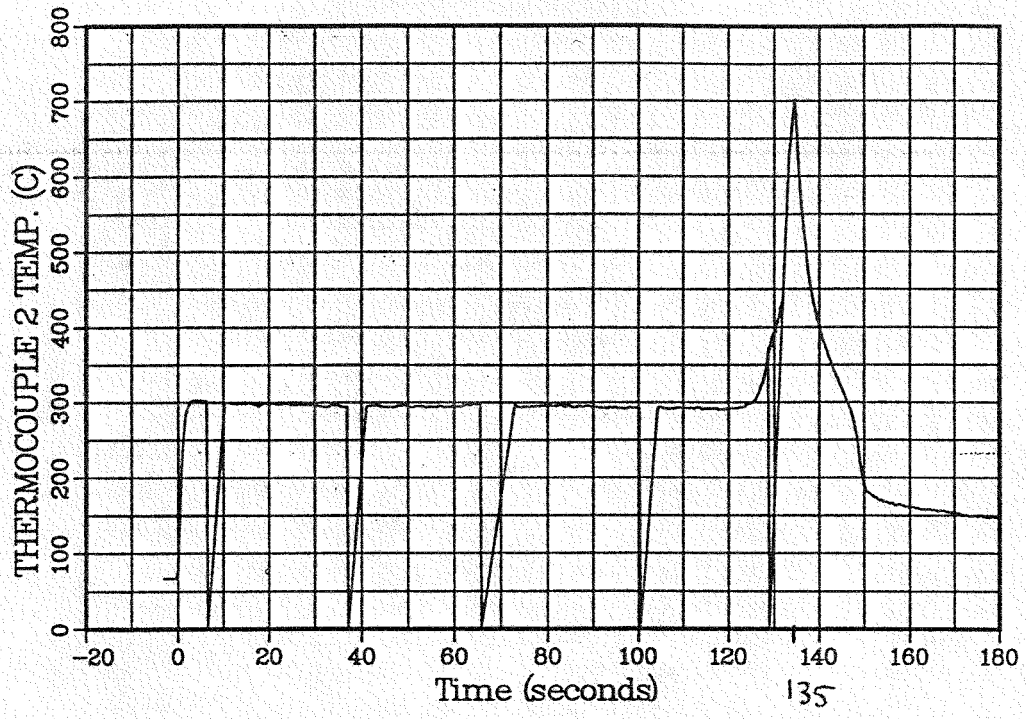

135

SANDIA NATIONAL LABORATORIES
Fusion Technology
Shot 144198

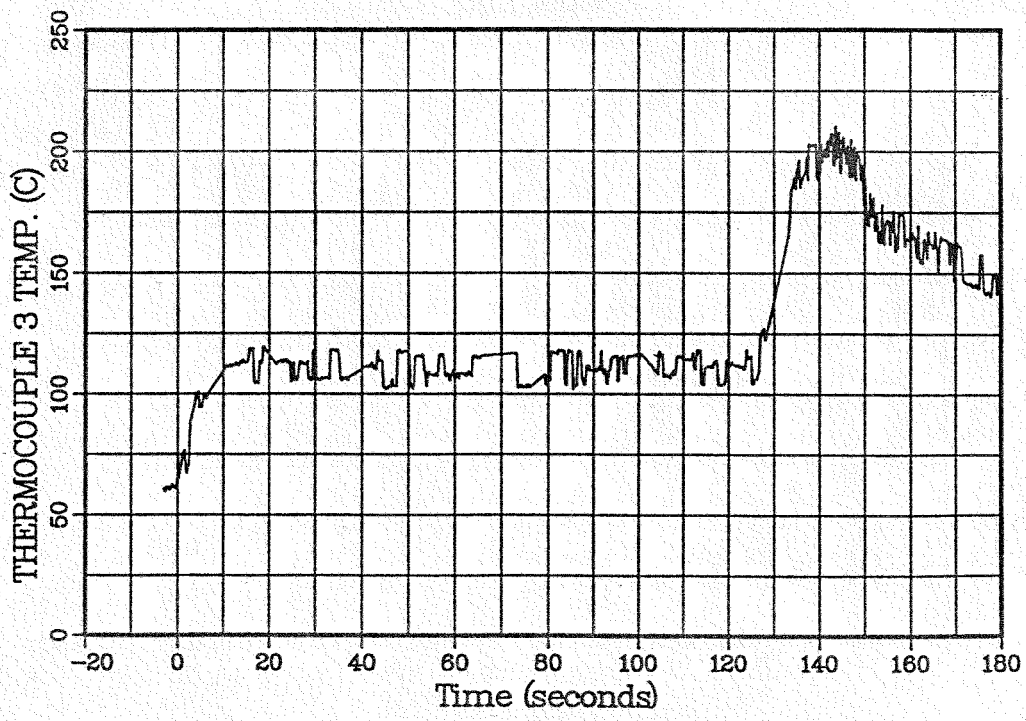

SANDIA NATIONAL LABORATORIES
Fusion Technology
Shot 144198

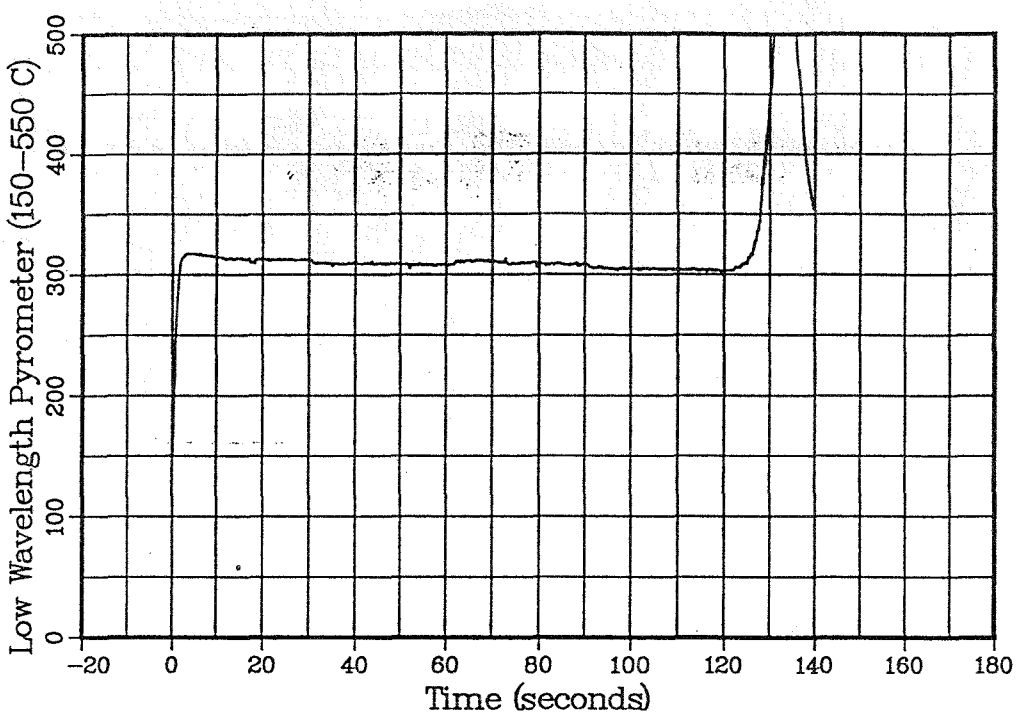

SANDIA NATIONAL LABORATORIES
Fusion Technology
Shot 144198

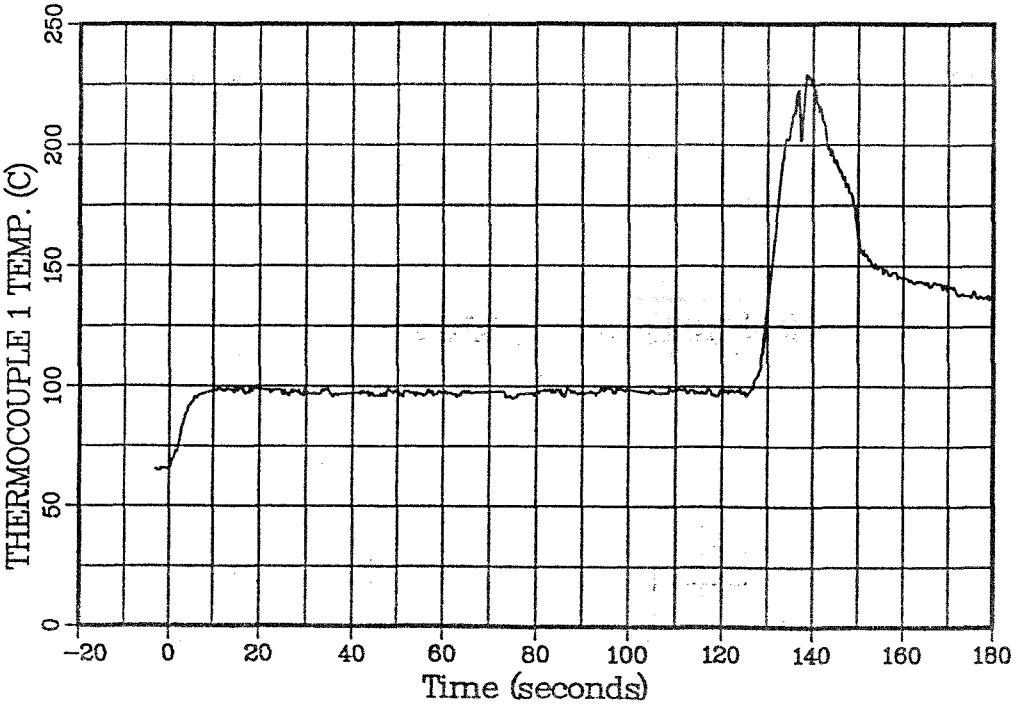

SANDIA NATIONAL LABORATORIES
Fusion Technology
Shot 144198

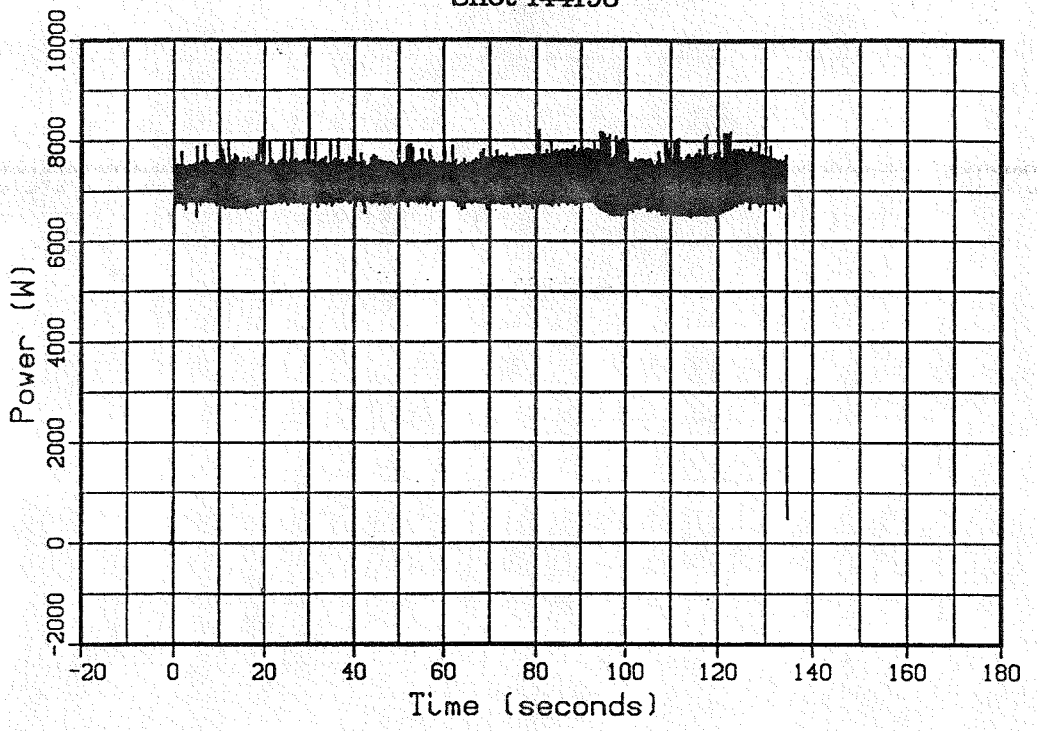

SANDIA NATIONAL LABORATORIES
Fusion Technology
Shot 144198

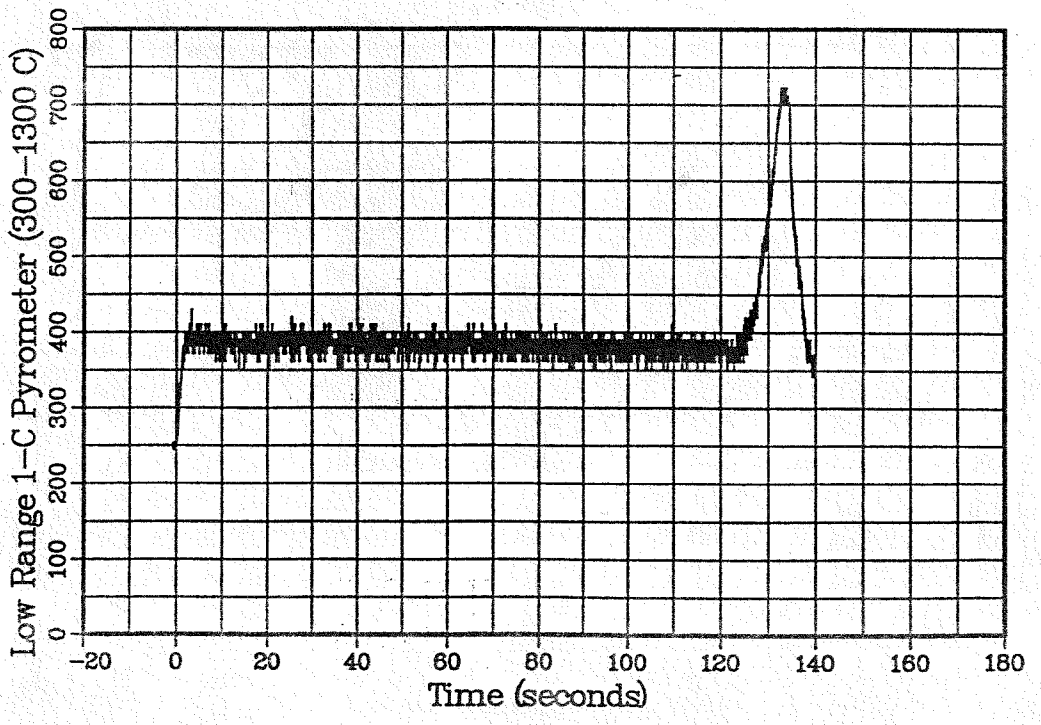

DISTRIBUTION:

Dr. M. Akiba
Japan Atomic Energy Research Institute
801-1 Mukouyama
Naka-Machi, Naka Gun
Ibaraki-ken, 311-01 JAPAN

Dr. Mansori Araki
Japan Atomic Energy Research Institute
NBI Heating Laboratory
801-1 Mukouyama
Naka-Machi, Naka-Gun
Ibaraki-Ken, 311-01 JAPAN

Mr. Luc Bartsoen
Tractebel Energy Engineering
Nuclear Department
Avenue Ariane 7
B-1200 Brussels BELGIUM

Mr. Javier Batencourt
University of Puerto Rico-Mayaguez
Department of Mechanical Engineering
Mayaguez, PR 00680

Dr. Chandu Baxi
General Atomics
P.O. Box 85608
San Diego, CA 92186

Mr. John Beach
Jaycor
700 Comanche Road, NE
Albuquerque, NM 87107

Dr. Arthur Bergles
Rensselaer Polytechnic Institute
Department of Mechanical Engineering
Troy, NY 12180

DISTRIBUTION (continued):

Dr. Robert Block
Rensselaer Polytechnic Institute
Department of Engineering
Troy, NY 12180

Dr. Jean Boscary
Japan Atomic Energy Research Institute
NBI Heating Laboratory
801-1 Mukoyama
Naka-Machi, Naka-Gun
Ibaraki-Ken, 311-01 JAPAN

Dr. Ronald Boyd
Prairie View A&M University
Department of Mechanical Engineering
P.O. Box 397
Prairie View, Texas 77446

Mr. Lee Cadwallader
Lockheed Martin Idaho Technologies
Fusion Safety Program
P.O. Box 1625
Idaho Falls, Idaho 83415-3815

Dr. Antonio Cardella
ITER JCT/The NET Team
c/o Max-Planck Institute Fur Plasma Physik
Boltzmannstr 2
D85748 Garching Bei Munchen, GERMANY

Dr. G. Celata
ENEA Energy Department
Thermal Process Engineering Division
Casaccia-VIA Anguillarese
301,00060 Rome, ITALY

Dr. P. Chappuis
CEA, CE/Cadarache
DRFC/STIF
13108 St. Paul Lez Durance CEDEX, FRANCE

DISTRIBUTION (continued):

Dr. D. Ciric
JET Joint Undertaking
Neutral Beam Test Bed
Abingdon, Oxfordshire OX14 3EA, ENGLAND

Dr. Marvin Cohen
U.S. Department of Energy
Office of Fusion Energy
ER-533, Germantown
Washington, DC 20585

Dr. Ian Cook
AEA Culham Laboratory
Abingdon, Oxon
OX14 3DB
UNITED KINGDOM

Dr. Maurizio Cumo
ENEA Energy Department
Thermal Process Engineering Division
Casaccia-VIA Anguillarese
301,00060 Rome, ITALY

Dr. Stephen D'Amico
Knolls Atomic Power Laboratory
Fluid Dynamics Experiments
P.O. Box 1072
Schenectady, NY 12301

Dr. Masayuki Dairaku
Japan Atomic Energy Research Institute
NBI Heating Laboratory
801-1 Mukouyama
Naka-Machi, Naka-Gun
Ibaraki-Ken, 311-01 JAPAN

Mr. Greg Dale
North Carolina State University
Department of Nuclear Engineering
Box 7909
Raleigh, NC 27695-7909

DISTRIBUTION (continued):

Dr. G. Dell'orco
ENEA, Energy Department
Divisione Ingegneria Sperimentale
C.R.E. Brasimone
40032 Camugnano-Bologna, ITALY
DISTRIBUTION (continued):\

Dr. P. Deschamps
EURATOM-CEA
sur la Fusion Controlee CE-Cadarache
F-13108 Saint Paul Lez Durance CEDEX, FRANCE

Dr. V. Divavin
D.V. Efromov Scientific Research Institute
of Electrophysical Apparatus
St. Petersburg, 189631 RUSSIAN FEDERATION

Dr. Dan Driemeyer
McDonnell Douglas Aerospace
Mail Stop 1067220
P.O. Box 516
St. Louis, MO 63166-0516

Dr. Hans Falter
JET Joint Undertaking
Neutral Beam Test Bed
Abingdon, Oxfordshire OX14 3EA, ENGLAND

Dr. M. Febvre
EURATOM-CEA
sur la Fusion Controlee CE
FRAMATOME< Le Creusot, FRANCE

Dr. G. Gaspari
SIET
VIA Nino Bixio 27
29100 Piacenza, ITALY

DISTRIBUTION (continued):

Dr. Jorge Gonzalez
University of Puerto Rico-Mayaguez
Department of Mechanical Engineering
Mayaguez, PR 00680

Dr. Larry Green
Westinghouse Electric Corporation
Science and Technology Center
1310 Beulah Road
Pittsburgh, PA 15235

Dr. S. Grigoriev
D.V. Efromov Scientific Research Institute
of Electrophysical Apparatus
St. Petersburg, 189631 RUSSIAN FEDERATION

Dr. D. Guilhem
CEA, CE/Cadarache
DER/SPPF
13108 St. Paul Lez Durance CEDEX, FRANCE

Dr. Radmir Guiniatouline
D.F. Efremov Scientific Research Institute
of Electrophysical Apparatus
P.O. Box 42
St. Petersburg 189631 RUSSIAN FEDERATION

Dr. Werner Gulden
NET Team
Max-Planck Institut fur Plasmaphysik
Boltzmannstrasse 2
D-85748 Garching bei Muenchen GERMANY

Dr. T. Hellwig
McDonnel Douglas Aerospace
Mail Stop 1067220
P.O. Box 516
St. Louis, MO 63166-0516

DISTRIBUTION (continued):

Dr. Y. Hirohata
Hokkaido University
Department of Nuclear Engineering
Kita-13, Nishi-8, Kita-ku, Sapporo, 060 JAPAN

Dr. M. Hoffman
University of California
University of Mechanical Engineering
Davis, CA 95616

Dr. Shuichi Ikeda
Japan Atomic Energy Research Institute
NBI Heating Laboratory
801-1 Mukouyama
Naka-Machi, Naka-Gun
Ibaraki-Ken, 311-01 JAPAN

Dr. M. Izenson
Creare, Inc.
P.O. Box 71
Hanover, NH 03755

Dr. Michael Jensen
Rensselaer Polytechnic Institute
Department of Mechanical Engineering
Troy, New York 12180

Dr. Owen Jones
Rensselaer Polytechnic Institute
Department of Nuclear Engineering
Troy, NY 12180

Dr. Barclay Jones
University of Illinois
103 S. Goodwin Avenue
Urbana, IL 61801

Dr. J. Journeaux
EURATOM-CEA
sur la Fusion Controlee CE-Cadarache
F-13108 Saint Paul Lez Durance CEDEX, FRANCE

DISTRIBUTION (continued):

Dr. Y. Katto
Nihon University, Kanda-Surugadai
Department of Mechanical Engineering
Chiyoda-Ku, Tokyo 101, JAPAN

Dr. Boris Kolbasov
Kurchatov Institute
Institute of Nuclear Fusion
Russian Research Center
Kurchatov Square, 1
123182 Moscow RUSSIAN FEDERATION

Dr. D. Kubik
McDonnell Douglas Aerospace
Mail Stop 1067220
P.O. Box 516
St. Louis, MO 63166-0516

Dr. R. Lahey
Rensselaer Polytechnic Institute
Department of Engineering
Troy, NY 12180

Dr. B. Lekakh
Massachusetts Institute of Technology
Department of Nuclear Engineering
Cambridge, MA 02139

Dr. Howard Littman
Rensselaer Polytechnic Institute
Department of Chemical Engineering
Troy, NY 12180

Dr. Glen Longhurst
Lockheed Martin Idaho Technologies
Fusion Safety Program
P.O. Box 1625
Idaho Falls, Idaho 83415-3815

DISTRIBUTION (continued):

Dr. Andrea Mariani
ENEA Energy Department
Thermal Process Engineering Division
Casaccia-VIA Anguillarese
301,00060 Rome, ITALY

Dr. W. Marton
U.S. Department of Energy
Office of Fusion Energy
ER-533, Germantown
Washington, DC 20585

Dr. P. Massmann
JET Joint Undertaking
Neutral Beam Test Bed
Abingdon, Oxfordshire OX14 3EA, ENGLAND

Dr. G. Mayaux
CEA, CE/Cadarache
DER/STIF
13108 St. Paul Lez Durance CEDEX, FRANCE

Dr. Igor Mazul
D.F. Efremov Scientific Research Institute
of Electrophysical Apparatus
P.O. Box 42
St. Petersburg 189631 RUSSIAN FEDERATION

Dr. Kathy McCarthy
Lockheed Martin Idaho Technologies
Fusion Safety Program
P.O. Box 1625
Idaho Falls, Idaho 83415-3815

Dr. Kaichiro Mishima
Kyoto University
Research Reactor Institute
Kumatori-cho, Sannan-gun
Osaka 590-04 JAPAN

DISTRIBUTION (continued):

Dr. Dave Morgan
McDonnel Douglas Aerospace
Mail Stop 1067220
P.O. Box 516
St. Louis, MO 63166-0516

Dr. Kazuyki Nakamura
Japan Atomic Energy Research Institute
NBI Heating Laboratory
801-1 Mukouyama
Naka-Machi, Naka-Gun
Ibaraki-Ken, 311-01 JAPAN

Dr. H. Nariai
University of Tsukuba
Institute of Engineering Mechanics
Tsukuba, Ibaraki 305 JAPAN

Dr. Ralph Nelson
Los Alamos National Laboratory
Engineering and Safety Analysis Group
Los Alamos, NM 87545

Dr. Masuro Ogawa
Japan Atomic Energy Research Institute
NBI Heating Laboratory
801-1 Mukouyama
Naka-Machi, Naka-Gun
Ibaraki-Ken, 311-01 JAPAN

Dr. Dave Petti
Lockheed Martin Idaho Technologies
Fusion Safety Program
P.O. Box 1625
Idaho Falls, Idaho 83415-3815

DISTRIBUTION (continued):

Dr. Steve Piet
U.S. ITER Home Team
U.S. ITER Project Office
University of California at San Diego
9500 Gilman Drive
La Jolla, CA 92093-0035

Dr. Michael Podowski
Rensselaer Polytechnic Institute
Department of Nuclear Engineering
Troy, NY 12180

Dr. Rene Raffray
ITER Garching JWS
c/o Max-Planck-Institut fur Plasmaphysik
Boltzmannstr 2
D-85748 Garching, GERMANY

Dr. John Rosenfeld
Thermacore
780 Eden Road
Lancaster, PA 17601

Dr. Akio Sagara
National Institute of Fusion Science
Furo-cho, Chikusa
Nagoya 464-01 JAPAN

Dr. K. Sato
Japan Atomic Energy Research Institute
801-1 Mukouyama
Naka-Machi, Naka-Gun
Ibaraki-ken, JAPAN 311-01

Dr. Jacques Schlosser
CEA, CE/Cadarache
DRFC/STIF
13108 St. Paul Lez Durance CEDEX, FRANCE

DISTRIBUTION (continued):

Dr. D. Schroeder-Richter
Technische Universitat Berlin
Department of Chemical Engineering SEKR
KT1, Marchstr 18, 10587 Berline GERMANY

Dr. Y. Seki
Japan Atomic Energy Research Institute
Naka Fusion Research Establishment
801-1 Mukouyama
Naka-Machi, Naka-Gun
Ibaraki-Ken 311-02 JAPAN

Dr. Leigh Sevier
General Atomics
P.O. Box 85608
San Diego, CA 92186

Dr. Don Steiner
Rensselaer Polytechnic Institute
Department of Nuclear Engineering
Troy, New York 12180

Dr. S. Suzuki
Japan Atomic Energy Research Institute
801-1 Mukouyama
Naka-Machi, Naka-Gun
Ibaraki-ken, JAPAN 311-01

Dr. Victor Tanchuk
D. V. Efromov Scientific Research Institute
of Electrophysical Apparatus
St. Petersburg, 189631 RUSSIAN FEDERATION

Dr. Kazutoshi Tokunaga
Kyushu University
Research Institute for Applied Mechanics
Kasuga, Fukuoka 816, JAPAN

DISTRIBUTION (continued):

Dr. Cetin Unal
Los Alamos National Laboratory
Engineering and Safety Analysis Group
Los Alamos, NM 87545

Dr. H. Viallet
CEA, CE/Cadarache
DRFC/STIF
13108 St. Paul Lez Durance CEDEX, FRANCE

Dr. G. Vieider
Max-Planck-Institut fur Plasmaphysik
Boltzmannstrasse 2
85748 Garching bei Munchen, GERMANY

Dr. Joel Weisman
University of Cincinnati
Nuclear Engineering Program
Cincinnati, OH 45221

Dr. Clement Wong
General Atomics
P.O. Box 85608
San Diego, CA 92186

Dr. Stan Yin
AECL Research
Thermalhydraulics Development Branch
Chalk River Laboratories
Chalk River, Ontario
Canada K0J 1J0

Dr. Kenji Yokoyama
Japan Atomic Energy Research Institute
NBI Heating Laboratory
801-1 Mukouyama
Naka-Machi, Naka-Gun
Ibaraki-Ken, 311-01 JAPAN

DISTRIBUTION (continued):

Dr. Yu Zeigarnik
Institute of High Temperatures
Academy of Sciences
Moscow, RUSSIAN FEDERATION

Dr. Nelson Zhan
Westinghouse Electric Corporation
Science and Technology Center
1310 Beulah Road
Pittsburgh, PA 15235

Dr. Giuseppe Zummo
ENEA Energy Department
Thermal Process Engineering Division
Casaccia-VIA Anguillarese
301,00060 Rome, ITALY

1	MS0736	N. R. Ortiz, 6400
1	MS1129	T.J. Lutz, 6428
12	MS1129	T. D. Marshall, 6428
1	MS1129	R. E. Nygren, 6428
1	MS1129	M. A. Ulrickson, 6428
1	MS1129	R. D. Watson , 6428
1	MS1129	D. L. Youchison, 6428
1	MS9163	K. Wilson, 8304
1	MS9162	R. Causey, 8347
1	MS1146	J.D. Miller, 9363
1	MS9018	Central Technical Files, 8523-2
5	MS0899	Technical Library, 4414
1	MS0619	Print Media, 12615
2	MS0100	Document Processing, 7613-2 for DOE/OSTI